Plasmonic Fields at Work

Hamans, Ruben Floris

2022

document version
Publisher's PDF, also known as Version of record

Plasmonic Fields at Work

Ruben F. Hamans

The cover of this thesis has been designed by Ferry Nugroho and illustrates the four results chapters: an array of metallic nanoparticles enhances the fluorescence intensity of a single molecule (back, bottom), a gold nanorod catalyzes the conversion of a non-fluorescent molecule into its fluorescent reduced form (front, bottom), the light-driven synthesis of a silver shell around a gold nanorod (back, top), and the plasmonic near-fields of a pentagonally-twinned silver nanowire (front, top). Besides the main themes presented in this thesis, the cover also illustrates some of the activities the author enjoys outside of work.

Printed by: ADC Nederland.

This work has been carried out in the Nanomaterials for Energy Applications group at DIFFER - Dutch Institute for Fundamental Energy Research and in the Photoconversion Materials group at the Vrije Universiteit Amsterdam, Faculty of Science, Department of Physics and Astronomy.

This work has been supported by The Netherlands Organisation for Scientific Research through the NWO Vidi Award 680-47-550.

ISBN: 9789491837463

VRIJE UNIVERSITEIT

Plasmonic Fields at Work

ACADEMISCH PROEFSCHRIFT

ter verkrijging van de graad Doctor of Philosophy aan
de Vrije Universiteit Amsterdam,
op gezag van de rector magnificus
prof.dr. J.J.G. Geurts,
in het openbaar te verdedigen
ten overstaan van de promotiecommissie
van de Faculteit der Bètawetenschappen
op maandag 14 maart 2022 om 15.45 uur
in een bijeenkomst van de universiteit,
De Boelelaan 1105

door

Ruben Floris Hamans

geboren te Roosendaal en Nispen

promotor:	dr. A. Baldi
copromotor:	prof.dr. E.L. von Hauff
promotiecommissie:	prof.dr.ir. E.J.G. Peterman prof.dr. J. Gómez Rivas dr. P. Zijlstra dr. E. Alarcón Lladó prof.dr. E. Cortés dr. G. Tagliabue

To my parents

Summary

Metal nanoparticles are used in a wide range of applications, from catalysis, to advanced solar cells, photothermal cancer therapy, and medical imaging. One of the most striking features of metal nanoparticles is their unique interaction with light, leading to strong absorption and scattering in the ultraviolet, visible, and infrared parts of the electromagnetic spectrum. These so-called plasmon resonances are responsible for a variety of interesting effects, ranging from the ability to focus electromagnetic fields into sub-wavelength hot spots, called plasmonic near-fields, to the generation of highly energetic charge carriers and high temperature gradients at the surface of the nanostructures.

Despite our current understanding of optical resonances in metallic nanoparticles and their applications, several challenges remain. First, the typical size of a plasmonic nanoparticle is much smaller than the features we can observe with conventional optical microscopy techniques. Therefore, we need other, more advanced, methods to study optical properties at the sub-particle level. Second, since plasmon resonances can drive chemistry via a variety of activation pathways, there is debate over which physical mechanism is dominant. Third, with an ever-expanding catalog of colloidal nanoparticles, establishing clear relationships between structural and optical properties is currently a challenge. Overcoming these three issues would allows us to rationally design optical devices and photocatalysts based on plasmonic nanoparticles.

In this thesis we will address these challenges with a wide variety of studies, in which we use plasmonic nanoparticles as antennas, photocatalysts, and electrodes. As we will see, in all chapters *plasmonic near-fields* play an important role. Furthermore, in all chapters we are motivated by the *work* that can be performed by these fields. Therefore, to give a title to - and to encompass the full contents of - this thesis, we can say we will discuss "plasmonic fields at work".

In chapter 2 we first discuss the physics relevant to this thesis. In chapter 3 we describe super-resolution fluorescence microscopy, the technique that will be used in the first two results chapters. We show how this technique can break the limits of conventional microscopy by performing measurements on single fluorescent molecules.

In the first results chapter, chapter 4, we study the interaction between light-emitting materials and periodic arrays of plasmonic nanoparticles. The improved optical properties of these arrays, such as enhanced plasmonic near-fields, can modify the intensity and directionality of nearby light emitters. However, the resonances in such arrays occur at wavelengths comparable to the interparticle distance. Therefore, mapping the interaction between light emitters and plasmonic particle arrays cannot be done with conventional microscopy methods. In this chapter, we map the enhanced emission of single fluorescent molecules coupled to a plasmonic particle array with $\sim$20 nm in-plane resolution by using super-resolution microscopy. Combined with numerical modeling, this approach allows us to pinpoint which physical mechanism is driving the light emission enhancement. These results can guide the rational design of future optical devices based on plasmonic particle arrays.

In chapter 5, we study how plasmon resonances drive chemical reactions at the single particle level. In this chapter, we report a study of a chemical reaction driven solely by plasmonic near-fields. Using super-resolution fluorescence microscopy, we map the position of individual product molecules and demonstrate a clear spatial correlation between the electric field distribution around individual nanoparticles and their super-resolved catalytic activity maps. These results can be extended to systems with more complex electric field distributions, thereby guiding the design of future advanced photocatalysts.

In chapter 6, we study how plasmon resonances drive chemical reactions at the ensemble level. In this chapter, we develop a synthesis of silver shells around gold nanorods in which each plasmon activation mechanism can be independently assessed. Using different illumination wavelengths combined with optical spectroscopy, transmission electron microscopy, thermal characterization, and numerical modeling, we unequivocally identify which physical mechanism is the main driving force behind the silver shell growth. Our strategy to discern between plasmon activation mechanisms can be extended to a variety of light-driven processes, including photocatalysis, nanoparticle syntheses, and drug delivery.

In chapter 7, we study the optical properties of silver nanowires. Their performance often relies on their unique optical properties that emerge from plasmon resonances in the ultraviolet part of the electromagnetic spectrum. In order to tailor the nanowire geometry for a specific application, a correct understanding of the relationship between the wire's structure and its optical properties is therefore necessary. However, while the synthesis of silver nanowires typically leads to structures with pentagonally-twinned geometries, their optical properties are often modeled assuming a cylindrical cross section. In this chapter, we highlight the strengths and limitations of such an approximation by numerically calculating the optical and electrical response of pentagonally-twinned silver nanowires and nanowire networks. We find that our accurate modeling is crucial to deduce structural information from the extinction spectra of nanowire suspensions and to predict the performance of nanowire-based near-field sensors. These results can help assess the quality of nanowire syntheses and guide in the design of optimized silver nanowire-based devices.

Finally, in chapter 8 we summarize the contents of this thesis. We also provide perspective for future work in the field of plasmon-driven chemistry. We suggest specific experiments in which super-resolution microscopy can be used to map the spatial distribution of charge carriers resulting from plasmon decay. Finally, we comment on the mechanism of charge transfer from metallic nanoparticles to adjacent species, such as semiconductors or adsorbed molecules, which is relevant for applications in photocatalysis and photodetection. Here, we believe further research is required.

Contents

Chapter 1

Introduction

Figure 1.1: Pictures of (a) a Gothic stained glass rose window of Notre-Dame de Paris and (b) the Lycurgus cup. Images are taken from Refs. 1,2.

1.1 The plasmon

Colloidal solutions of noble metal nanoparticles have long been used for their vivid colors. Well-known examples include stained glass windows, such those in the cathedral Notre-Dame de Paris, and, perhaps most famously, the Lycurgus Cup, a 4th century Roman glass cage cup (Figure 1.1). In Roman times, the process used to obtain this glass was probably not understood or controlled and the presence of silver and gold nanoparticles with diameters around 50 - 100 nm was likely due to an accidental contamination.[3,4]

Much later, from the 1850s through to the 1870s James Clark Maxwell formulated a set equations that describe how electric and magnetic fields behave, now known as Maxwell's equations.[5,6] In 1908, Gustav Mie solved these equations for a system with spherical symmetry, which gives us the physical framework to calculate and understand many of the optical properties of metallic nanoparticles.[7] The strong interaction between these particles and visible light is due to the exis-

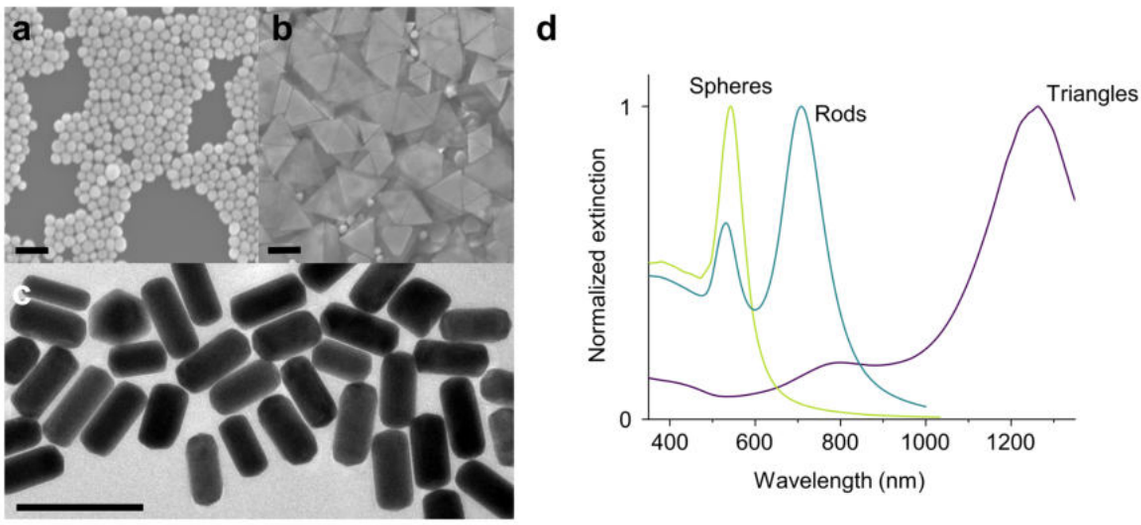

Figure 1.2: Electron microscopy images of (a) gold spheres, (b) gold triangles, and (c) gold rods synthesized during this thesis work and (d) their corresponding extinction spectra. All scalebars are 200 nm.

tence of the so-called localized surface plasmon resonance (LSPR).[8,9] This resonance arises due to the fact that the free electrons inside the metal follow the oscillation of the electric field of light. Similar to a harmonic oscillator, when the driving force is at the right frequency, i.e. when the light is of the right color, the oscillation is resonant. These oscillations in the electron density of a metal are also known as plasma oscillations, hence the use of the word "plasmon" in "localized surface plasmon resonance".

The unique optical properties of metallic nanoparticles can be attributed to the existence of this resonance. At the LSPR wavelength, the ability of a particle to scatter and absorb light is enhanced to the point where the corresponding scattering and absorption cross sections can be larger than their geometrical counterpart. Colloidal suspensions of metallic nanoparticles owe their vivid color to these high cross sections and to the fact that the LSPR appears at a distinct wavelength that can be tuned via the shape, size, and composition of the particles (Figure 1.2).

Beyond their decorative proposes, LSPRs also became of technological interest due to their scattering and absorption properties. The scattering properties of plasmonics nanoparticles allow them to focus light into sub-wavelength volumes, resulting in intense enhancements of the electromagnetic fields at the nanoparticle surface. These so-called plasmonic near-fields allow metallic nanoparticles to be used as nanoscale antennas for light[10,11] and to accelerate light-driven processes. For example, plasmonic near-fields can drive photosensitive chemical reactions[12] or enhance the fluorescence intensity of dyes.[13] They are also the driving force behind surface-enhanced Raman spectroscopy,[14–16] which allows us to identify reaction intermediates and reaction products generated during a catalytic process with a sensitivity down to the single molecule.[17,18]

The absorptive properties of plasmonic nanoparticles were initially deemed detrimental to nanophotonic applications, as they limit the quality factor of the resonance.[19] However, light absorption can also be used advantageously, as it results in the formation of non-equilibrium charge carriers and elevated surface temperatures.[20] Due to their high energy, these so-called 'hot' charge carriers can be used to drive and change the energy landscape of chemical reactions happening on the nanoparticle surface.[21–24] Furthermore, they can be injected into an adjacent semiconductor, allowing plasmonic nanoparticles to be used as sub-bandgap photodetectors.[25,26] The

photothermal effect of the increased nanoparticle surface temperature has also been used advantageously. The accurate spatial control over where heat is applied has been used, for example, for photothermal cancer therapy and for driving chemical reactions selectively at the nanoparticle surface.[27–29]

1.2 Current challenges and scope of this thesis

Despite the above advances in the understanding of optical resonances in metallic nanoparticles and their applications, several challenges remain. The typical size of a plasmonic nanoparticle is of the order of 10 - 100 nm, whereas the wavelengths of their resonances typically lie in the visible to near-infrared part of the electromagnetic spectrum, roughly from a few hundred nm to a few µm, see for example again Figure 1.2. As the resolution of optical techniques such as conventional microscopy is limited to roughly half of the resonance wavelength due to light diffraction, we can immediately recognize a disparity in length scales: when using conventional microscopy, we cannot study the properties of these nanoparticles with sub-particle spatial resolution. In this thesis we will use an extension of fluorescence microscopy, stochastic super-resolution microscopy, which allows us to reach a resolution of 20 - 30 nm. We will use this technique to study the interaction between light-emitting materials and arrays of plasmonic nanoparticles and to map chemical reactions driven by plasmonic near-fields.

The mechanisms by which plasmon resonances can drive chemical reactions is also currently an open question. LSPRs are characterized by i) their ability to focus light into nanoscale regions of high electromagnetic fields, ii) the generation of highly energetic charge carriers, and iii) photothermal nanoparticle heating. As all of these processes happen simultaneously and on ultrafast timescales, it has proven challenging to disentangle these mechanisms experimentally.[30–39] In this thesis we will see how a light-driven synthesis of silver shells around gold nanoparticles, combined with accurate numerical modeling of the electromagnetic fields and of the light propagation inside the reaction volume, allows us to individually assess each of these plasmon activation pathways. Furthermore, we will use super-resolution fluorescence microscopy to map chemical reactions with nanometer spatial resolution driven by one specific plasmon activation mechanism, namely plasmonic near-fields.

Lastly, with the ever-expanding catalog of colloidal nanoparticles, the relationship between structural and optical properties is currently a challenge. A detailed understanding of the structural underpinning of optical resonances is crucial to the characterization of nanoparticle syntheses. In this thesis we study two systems for which the structure-optics relationship is particularly relevant. First, we show how the structural changes that occur during a light-driven synthesis of silver shells around gold nanoparticles influence the particle's resonance wavelength, the intensity of its plasmonic near-fields, and its ability to eject non-equilibrium charge carriers. Second, we study the relationship between the structure and the optical properties of silver nanowires. The polyol synthesis of these nanowires leads to wires with pentagonal cross sections, giving them unique optical properties, such as enhanced near-fields, that can only be fully described when accurately modeling the wire's shape.

1.3 Outline of this thesis

In this thesis we will see a wide variety of studies on the optical properties of metallic nanoparticles. In two chapters we employ super-resolution microscopy to perform studies with nanometer spatial resolution at the single molecule level, one chapter focuses on a plasmon-driven synthesis at the ensemble level, and one chapter focuses on modeling the optical properties of silver

nanowires. As we will see, in all chapters *plasmonic near-fields* play an important role. Furthermore, in all chapters we are motivated by the *work* that can be performed by these fields, such as driving chemistry or enhancing Raman signals. Therefore, to encompass the full contents of this thesis, we can say we will discuss "plasmonic fields at work".

In **chapter 2** we first discuss the physics relevant to this thesis. We derive the existence of the plasmon resonance by considering a small sphere illuminated by a harmonically oscillating electric field. This approach allows us to calculate experimentally relevant parameters such as scattering and absorption cross sections and electric field enhancements. We also discuss how the dielectric function of a metal can be understood in the framework of a free electron gas that oscillates due to an externally applied electric field. We then extend our framework for modeling the optical properties of metallic nanoparticles by discussing Mie theory, which allows us to model spheres of any size, and the finite-difference time-domain method, which allows us to model arbitrary shapes. We conclude by describing how plasmon decay can drive chemical reactions via the generation of highly energetic charge carriers, elevated surface temperatures, and enhanced electromagnetic fields.

Since the first two main results chapters in this thesis employ super-resolution fluorescence microscopy, we dedicate **chapter 3** to discussing this technique. We first describe the working principles of the optical microscope and the fluorescence microscope. We identify a resolution limit of $\sim$250 nm in the visible part of the electromagnetic spectrum due to the diffraction of light and show how this limit can be broken by performing single molecule localization, allowing us to reach a resolution of several (tens of) nanometers. We show how this technique can be used to study catalytic conversions and fluorescence enhancement at the nanoscale level. Finally, we describe the image processing that is performed on the fluorescence microscopy data.

In the first results chapter, **chapter 4**, we study the interaction between light-emitting materials and periodic arrays of plasmonic nanoparticles. These two-dimensional arrays have remarkable optical properties originating from their collective behavior, which results in resonances with narrow linewidths and enhanced electric fields extending far into the surrounding medium. The improved properties of these so-called surface lattice resonances can enhance the intensity of nearby light emitters by modifying their absorption and spontaneous decay rates, and the directivity of their emission. These resonances occur at wavelengths comparable to the interparticle distance in the array. Therefore, mapping the interaction between light emitters and plasmonic particle arrays cannot be done with diffraction-limited conventional microscopy methods. In this chapter, we map the enhanced emission of single fluorescent molecules coupled to a plasmonic particle array with $\sim$20 nm in-plane resolution by using super-resolution microscopy. We find that extended lattice resonances have minimal influence on the spontaneous decay rate of an emitter, but instead can be exploited to enhance the outcoupling and directivity of the emission. These results can guide the rational design of future optical devices based on plasmonic particle arrays.

In **chapter 5**, we study how plasmon resonances drive chemical reactions at the single particle level. In this chapter, we report an in-situ study of a fluorogenic chemical reaction driven solely by plasmonic near-fields. Using super-resolution fluorescence microscopy, we map the position of individual product molecules with $\sim$30 nm spatial resolution and demonstrate a clear correlation between the electric field distribution around individual nanoparticles and their super-resolved catalytic activity maps. These results can be extended to systems with more complex electric field distributions, thereby guiding the design of future advanced photocatalysts.

In **chapter 6**, we study how plasmon resonances drive chemical reactions at the ensemble level. The driving forces of plasmon-driven chemistry, photothermal heating, plasmonic near-fields, and the ejection of highly energetic charge carriers, all typically occur simultaneously and on ultrafast timescales, making them hard to disentangle. In this chapter, we develop a plasmon-assisted synthesis of silver shells around gold nanorods in which each plasmon decay mechanism can be independently assessed. Using different illumination wavelengths combined with extinction spectroscopy, transmission electron microscopy, thermal characterization, and numerical modeling, we unequivocally identify interband holes as the main driving force behind the silver shell growth. Our conclusion is corroborated by single particle studies on gold nanospheres that display isotropic reactivity, consistent with interband hole-driven nanoparticle syntheses. Our strategy to discern between plasmon activation mechanisms can be extended to a variety of light-driven processes, including photocatalysis, nanoparticle syntheses, and drug delivery.

In **chapter 7**, we study the optical properties of silver nanowires. Their performance often relies on their unique optical properties that emerge from localized surface plasmon resonances in the ultraviolet part of the electromagnetic spectrum. In order to tailor the nanowire geometry for a specific application, a correct understanding of the relationship between the wire's structure and its optical properties is therefore necessary. However, while the colloidal synthesis of silver nanowires typically leads to structures with pentagonally-twinned geometries, their optical properties are often modeled assuming a cylindrical cross section. In this chapter, we highlight the strengths and limitations of such an approximation by numerically calculating the optical and electrical response of pentagonally-twinned silver nanowires and nanowire networks. We find that our accurate modeling is crucial to deduce structural information from the extinction spectra of nanowire suspensions and to predict the performance of nanowire-based near-field sensors. These results can help assess the quality of nanowire syntheses and guide in the design of optimized silver nanowire-based devices.

Finally, in **chapter 8** we summarize the contents of this thesis. We also provide perspective for future work in the field of plasmon-driven chemistry. We suggest specific experiments in which super-resolution microscopy can be used to map the spatial distribution of non-equilibrium charge carriers resulting from plasmon decay. Finally, we comment on the mechanism of charge transfer from metallic nanoparticles to adjacent species, such as semiconductors or adsorbed molecules, where we believe further research is required.

1

Chapter 2

Fundamentals of plasmonics

Abstract

The studies in this thesis all involve optical resonances in metallic nanoparticles. In this chapter we discuss the underlying physics of these resonances. We derive the existence of the localized surface plasmon resonance from Maxwell's equations by considering a metallic sphere in a harmonically oscillating electric field. We use the quasi-static approximation for particles much smaller than the wavelength to show the basic physics behind the plasmon resonance. We also discuss how the dielectric function of a metal can be understood in the framework of a free electron gas that oscillates due to an externally applied electric field. We then extend our framework for modeling the optical properties of metallic nanoparticles by discussing Mie theory, which allows us to model spheres of any size, and the finite-difference time-domain method, which allows us to model arbitrary shapes. We conclude by describing how plasmon decay can drive chemical reactions via the generation of highly energetic charge carriers, elevated surface temperatures, and enhanced electromagnetic fields.

2.1 The quasi-static approximation

We can derive the existence of an LSPR by considering a metallic sphere in a harmonically oscillating electric field. If we first assume that the particle is much smaller than the wavelength, the phase of the electric field is practically constant over the whole volume of the nanoparticle and, therefore, the problem can be treated electrostatically (Figure 2.1a). This approximation is also known as the quasi-static approximation.

In general, electromagnetic fields are described by Maxwell's equations:

$$\nabla \cdot \vec{D} = \rho_f, \tag{2.1a}$$

$$\nabla \cdot \vec{B} = 0, \tag{2.1b}$$

$$\nabla \times \vec{E} = -\frac{\partial \vec{B}}{\partial t}, \tag{2.1c}$$

$$\nabla \times \vec{H} = \vec{J}_f + \frac{\partial \vec{D}}{\partial t}, \tag{2.1d}$$

This chapter is partially based on Ref. 40: **Super-Resolution Mapping of Plasmonic Hot Electrons**, Ruben F. Hamans, *Eindhoven University of Technology: Eindhoven*, 2017 and Ref. 41: **Single Particle Approaches to Plasmon-Driven Catalysis**, Ruben F. Hamans, Rifat Kamarudheen, and Andrea Baldi, *Nanomaterials*, 2020, 10, 12, 2377

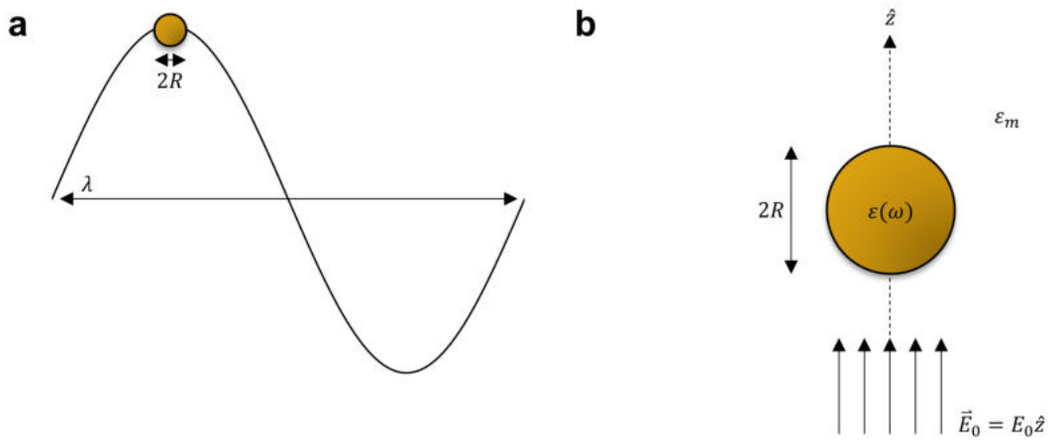

Figure 2.1: (a) Illustration of a sphere with a radius much smaller than the wavelength. (b) A sphere with a radius R subjected to an incident field $\vec{E_0} = E_0\hat{z}$. The dielectric function of the sphere is described by the complex function $\varepsilon = \varepsilon(\omega)$ and the surrounding medium has a dielectric constant ε_m.

where $\vec{E}$ is the electric field, $\vec{D}$ the dielectric displacement, $\vec{B}$ the magnetic induction, $\vec{H}$ the magnetic field, ρ_f the free electric charge density, and $\vec{J_f}$ the free electric current density. $\vec{E}$ & $\vec{D}$ and $\vec{B}$ & $\vec{H}$ are related via

$$\vec{D} = \varepsilon_0\vec{E} + \vec{P}, \tag{2.2a}$$

$$\vec{H} = \frac{1}{\mu_0}\vec{B} - \vec{M}, \tag{2.2b}$$

where ε_0 is the permittivity of free space, $\vec{P}$ the polarization field, μ_0 the permeability of free space, and $\vec{M}$ the magnetization field. For linear media the polarization and magnetization fields are proportional to the electric and magnetic fields, respectively:

$$\vec{P} = \varepsilon_0\chi_e\vec{E}, \tag{2.3a}$$

$$\vec{M} = \chi_m\vec{H}, \tag{2.3b}$$

where χ_e and χ_m are the electric and magnetic susceptibility, respectively. The expressions for the displacement field $\vec{D}$ and the magnetic field $\vec{H}$ then become

$$\vec{D} = \varepsilon_0\varepsilon\vec{E}, \tag{2.4a}$$

$$\vec{H} = \frac{1}{\mu_o\mu}\vec{B}, \tag{2.4b}$$

where $\varepsilon = 1 + \chi_e$ is known as the dielectric function, dielectric constant, or relative permittivity and $\mu = 1 + \chi_m$ as the relative permeability. In the absence of free charges ($\rho_f = 0$), the first Maxwell's equation (Gauss's law) then changes into

$$\nabla \cdot \vec{E} = 0. \tag{2.5}$$

Furthermore, as we are working in an electrostatic approximation, the third Maxwell's equation (Faraday's law) changes into

$$\nabla \times \vec{E} = 0. \tag{2.6}$$

We can now use the vector identity $\nabla \times \nabla\Phi = 0$, which allows us to express the electric field as the gradient of a scalar function, which we call the potential Φ:

$$\vec{E} = -\nabla\Phi. \tag{2.7}$$

In other words, solving the first Maxwell's equation, equation (2.5), in an electrostatic system is equivalent to solving the Laplace equation:

$$\nabla^2\Phi = 0. \tag{2.8}$$

In a spherical coordinate system (r, θ, ϕ), where r is the radial distance, θ the polar angle, and ϕ the azimuthal angle, and under the assumption of azimuthal symmetry ($\partial\Phi/\partial\phi = 0$), the solution to the Laplace equation is[42]

$$\Phi(r,\theta) = \sum_{l=0}^{\infty} \left(A_l r^l + B_l r^{-(l+1)}\right) P_l(\cos\theta), \tag{2.9}$$

where A_l and B_l are coefficients determined by the boundary conditions of the system, and P_l are the Legendre polynomials. We can then set the following boundary conditions:

- The potential remains finite at the origin ($r = 0$), i.e. at the center of the sphere,
- When $r \to \infty$, the electric field must be equal to the applied field E_0,
- The tangential components of $\vec{E}$ are equal at both sides of the sphere,
- The normal components of $\vec{D}$ are equal at both sides of the sphere,

where the latter two are the standard boundary conditions originating from Maxwell's equations in integral form. The first condition sets the coefficients $B_l = 0$ for the potential inside the sphere to avoid diverging terms, resulting in

$$\Phi_{\text{in}} = \sum_{l=0}^{\infty} A_l r^l P_l(\cos\theta), \tag{2.10a}$$

$$\Phi_{\text{out}} = \sum_{l=0}^{\infty} \left(C_l r^l + D_l r^{-(l+1)}\right) P_l(\cos\theta), \tag{2.10b}$$

for the potential inside and outside the sphere, respectively. The second condition yields

$$\lim_{r\to\infty} \Phi_{\text{out}} = \lim_{r\to\infty} \sum_{l=0}^{\infty} C_l r^l P_l(\cos\theta) = -E_0 z = -E_0 r\cos\theta, \tag{2.11}$$

which sets $C_1 = -E_0$ and $C_l = 0$ for $l \neq 1$, leaving us with

$$\Phi_{\text{in}} = \sum_{l=0}^{\infty} A_l r^l P_l(\cos\theta), \tag{2.12a}$$

$$\Phi_{\text{out}} = -E_0 r\cos\theta + \sum_{l=0}^{\infty} D_l r^{-(l+1)} P_l(\cos\theta). \tag{2.12b}$$

The third and fourth condition yield the following expressions:

$$-\frac{1}{R}\left.\frac{\partial\Phi_{\text{in}}}{\partial\theta}\right|_{r=R} = -\frac{1}{R}\left.\frac{\partial\Phi_{\text{out}}}{\partial\theta}\right|_{r=R}, \tag{2.13a}$$

$$-\varepsilon_0\varepsilon\left.\frac{\partial\Phi_{\text{in}}}{\partial r}\right|_{r=R} = -\varepsilon_0\varepsilon_m\left.\frac{\partial\Phi_{\text{out}}}{\partial r}\right|_{r=R}, \tag{2.13b}$$

where R is the radius of the sphere, ε the dielectric function of the sphere, and ε_m the dielectric constant of the surrounding medium. These conditions set $A_l = D_l = 0$ for $l \neq 1$ and give the following expressions for A_1 and D_1:

$$-\frac{1}{R}A_1 R = -\frac{1}{R}\left(-E_0 R + D_1 R^{-2}\right), \tag{2.14a}$$

$$-\varepsilon_0 \varepsilon A_1 = -\varepsilon_0 \varepsilon_m \left(-E_0 - 2D_1 R^{-3}\right), \tag{2.14b}$$

which solve to

$$A_1 = -\frac{3\varepsilon_m}{\varepsilon + 2\varepsilon_m} E_0, \tag{2.15a}$$

$$D_1 = \frac{\varepsilon - \varepsilon_m}{\varepsilon + 2\varepsilon_m} E_0 R^3, \tag{2.15b}$$

thereby obtaining the final expressions for the potentials:

$$\Phi_{\text{in}} = -\frac{3\varepsilon_m}{\varepsilon + 2\varepsilon_m} E_0 r \cos\theta, \tag{2.16a}$$

$$\Phi_{\text{out}} = -E_0 r \cos\theta + \frac{\varepsilon - \varepsilon_m}{\varepsilon + 2\varepsilon_m} E_0 R^3 \frac{\cos\theta}{r^2}. \tag{2.16b}$$

Interestingly, in the expression for Φ_{out} we recognize the first term as being the applied field and the second term as being equivalent to an electric dipole. The potential of an electric dipole is

$$\Phi_{\text{dipole}} = \frac{1}{4\pi\varepsilon_0\varepsilon_m} \frac{\vec{p}\cdot\vec{r}}{r^3}, \tag{2.17}$$

where $\vec{p}$ is the dipole moment. We can, therefore, rewrite equation (2.16b) into

$$\Phi_{\text{out}} = -E_0 r \cos\theta + \frac{1}{4\pi\varepsilon_0\varepsilon_m} \frac{\vec{p}\cdot\vec{r}}{r^3}, \tag{2.18}$$

using

$$\vec{p} = 4\pi\varepsilon_0\varepsilon_m R^3 \frac{\varepsilon - \varepsilon_m}{\varepsilon + 2\varepsilon_m} \vec{E_0}. \tag{2.19}$$

If we then define a polarizability α, which describes the tendency of a material to acquire an electric dipole moment when subjected to an electric field, using $\vec{p} = \varepsilon_0\varepsilon_m\alpha\vec{E_0}$,[9] we obtain

$$\alpha = 4\pi R^3 \frac{\varepsilon - \varepsilon_m}{\varepsilon + 2\varepsilon_m}. \tag{2.20}$$

From equation (2.20) it becomes clear that the polarizability experiences a resonance when

$$\varepsilon = -2\varepsilon_m, \tag{2.21}$$

also known as the Fröhlich condition. This condition requires the real part of the dielectric function of the sphere to be negative, which is a material property commonly found in metals. As can be seen in Figure 2.2a, for metals such as Al, Pd, Ag, Cu, and Au the resonance condition is satisfied for wavelengths in the ultraviolet to visible parts of the electromagnetic spectrum. Note that for Al the Fröhlich condition is satisfied at ∼170 nm when $\varepsilon_m = 1.78$. The magnitude of the polarizability at the resonance wavelength is limited due to the fact that the dielectric function ε contains both a real and an imaginary part. The highest values of α are reached for metals with the lowest losses, i.e. with the lowest values for $\text{Im}[\varepsilon]$. For this reason, Au and Ag are the most commonly used plasmonic metals (Figure 2.2b).

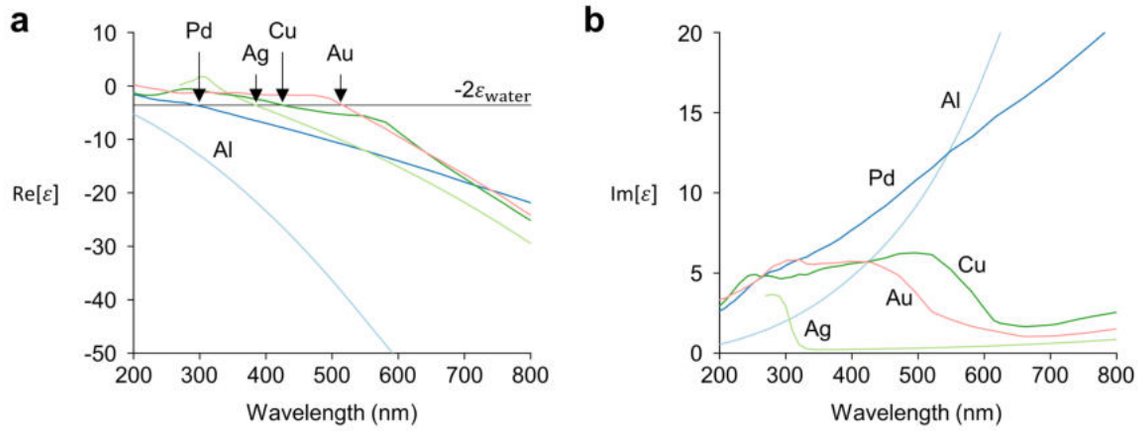

Figure 2.2: (a) Real and (b) imaginary parts of the dielectric functions of Al, Pd, Ag, Cu, and Au. The horizontal line denotes the resonance condition when the surrounding medium is water ($\varepsilon_m = 1.78$). Dielectric functions are taken from Refs. 43–45.

From an experimental point of view it is interesting to note that the resonant enhancement of the polarizability translates into enhancements in the scattering and absorption cross sections σ_{sca} and σ_{abs} of the sphere via[8]

$$\sigma_{\text{sca}} = \frac{k^4}{6\pi}|\alpha|^2, \tag{2.22a}$$

$$\sigma_{\text{abs}} = k\,\text{Im}[\alpha], \tag{2.22b}$$

where $k = 2\pi/\lambda$ is the wavevector. As can be seen in the above equation, σ_{sca} scales with $|\alpha|^2 \propto R^6$, whereas σ_{abs} scales with $\text{Im}[\alpha] \propto R^3$. Therefore, for smaller particles $\sigma_{\text{abs}} > \sigma_{\text{sca}}$, whereas for larger particles (for Au, with a radius larger than ~40 nm) $\sigma_{\text{sca}} > \sigma_{\text{abs}}$. As can be seen in Figure 2.3a, the polarizability is characterized by a peak at the resonance wavelength. Due to equation (2.22), this peak also translates into a peak in the extinction cross section $\sigma_{\text{ext}} = \sigma_{\text{sca}} + \sigma_{\text{abs}}$ (see Figure 2.3b).

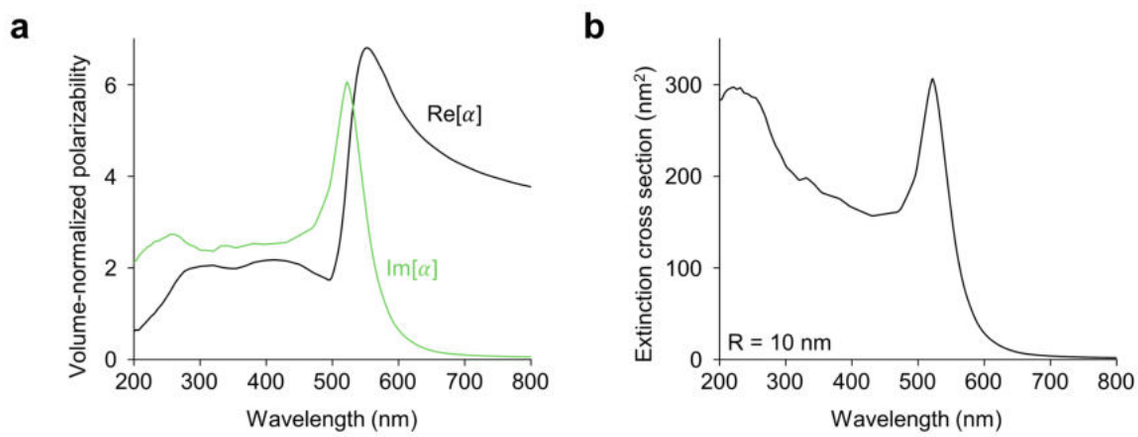

Figure 2.3: (a) Real (black) and imaginary (green) parts of the volume-normalized polarizability $\alpha/(\frac{4}{3}\pi R^3)$ calculated using equation (2.20) and (b) the extinction cross section of an Au sphere with a radius R of 10 nm calculated using equation (2.22). The dielectric function ε is taken from Ref. 45.

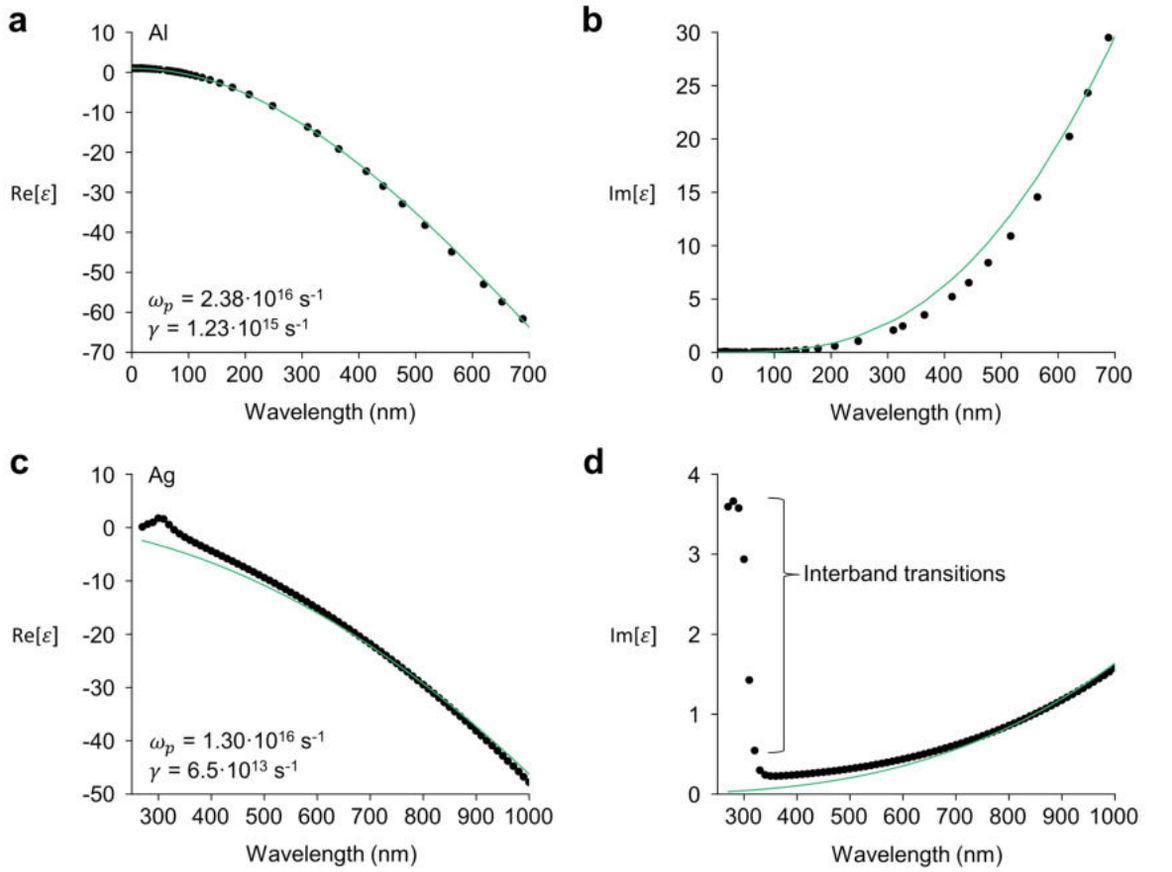

Figure 2.4: (a) Real and (b) imaginary parts of the dielectric function of Al (black points) and a fit to equation (2.26) (green line). (c,d) Same as (a,b), but for Ag. The dielectric functions are taken from Refs. 43,44.

2.2 The dielectric function of a metal

In Figure 2.3 we have used an experimentally-obtained dielectric function (see also Figure 2.2). Over a wide range of frequencies the optical properties of metals can also be described using the plasma model. This model, also known as the Drude model,[46,47] describes a free electron gas against a background of fixed ion cores. The electrons oscillate due to an externally applied electric field $\vec{E}$ and their motion is damped with a characteristic timescale τ or collision frequency $\gamma = 1/\tau$. The equation of motion then is[9]

$$m\frac{\mathrm{d}^2\vec{x}}{\mathrm{d}t^2} = -e\vec{E} - m\gamma\frac{\mathrm{d}\vec{x}}{\mathrm{d}t}, \tag{2.23}$$

where m is the effective mass of the electron, $\vec{x}(t)$ the position of the electron as a function of time, and e the elementary charge. The first term on the right hand side describes the electromagnetic force and the second term is a damping term. The above equation solves to

$$\vec{x}(t) = \frac{e}{m(\omega^2 + i\gamma\omega)}\vec{E}(t), \tag{2.24}$$

where the electric field has a harmonic time dependence with a frequency ω, $\vec{E} = \vec{E}_0\exp(i\omega t)$. The displacement of electrons in a free electron gas with an electron density n gives a macroscopic polarization field

$$\vec{P} = -ne\vec{x}. \tag{2.25}$$

As we have seen before, the polarization field contributes to the dielectric displacement via $\vec{D} = \varepsilon_0\vec{E} + \vec{P} = \varepsilon_0\varepsilon\vec{E}$, see equations (2.2a) and (2.4a), allowing us to extract the dielectric function:

$$\varepsilon(\omega) = 1 - \frac{\omega_p^2}{\omega^2 + i\gamma\omega}, \tag{2.26}$$

where we have defined the plasma frequency

$$\omega_p^2 = \frac{ne^2}{\varepsilon_0 m}. \tag{2.27}$$

Since free electrons have an energy dispersion given by[48]

$$E = \frac{\hbar^2 k^2}{2m}, \tag{2.28}$$

where $\hbar$ is the reduced Planck constant and k the electron wavevector, the Drude model works particularly well for metals where the electronic bands are well-approximated by a quadratic dispersion. An example of such a metal is Al,[49] as can be seen in Figure 2.4a,b, where we fit the experimental dielectric function to equation (2.26). For the noble metals Au and Ag, however, high energy photons can excite electron-hole pairs via interband transitions from an electronic band below the Fermi level to another above the Fermi level.[50,51] These additional losses result in an increased Im[ε] for high photon energies, which is not captured by the plasma model, as highlighted by the example of Ag in Figure 2.4c,d. To include these transitions in the model, additional Lorentzian terms are often added to equation (2.26).[52]

2.3 Mie theory

For large particles the quasi-static approximation is no longer valid due to the phase variations of the electric field inside the particle. In this case, Maxwell's equations need to be solved electrodynamically, i.e. including time dependence. The case of an electromagnetic plane wave impinging on a homogeneous sphere can be solved analytically, resulting in Mie theory or the Mie solution to Maxwell's equations.[7]

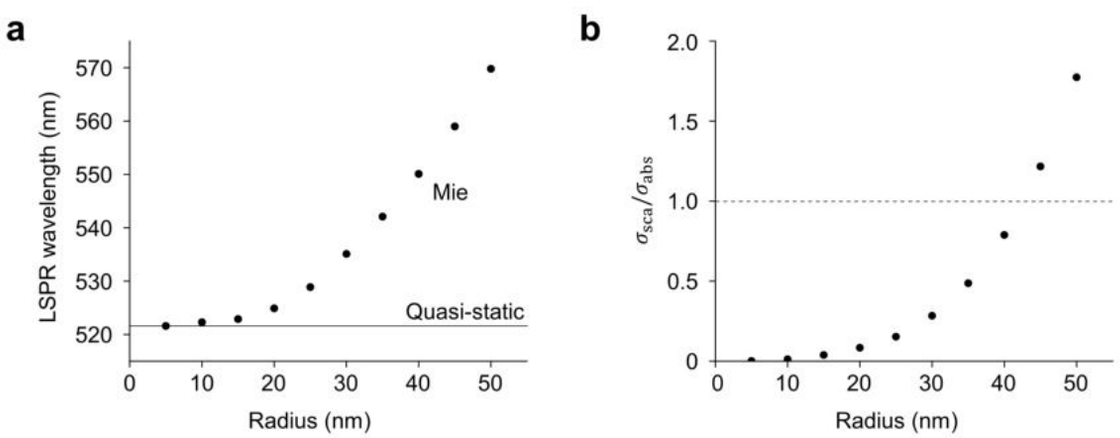

Figure 2.5: (a) LSPR wavelength of an Au sphere as a function of the particle radius calculated in the quasi-static approximation (line) and using Mie theory (points). (b) The Mie theory-calculated ratio between the scattering cross section σ_{sca} and the absorption cross section σ_{abs}. The dielectric function is taken from Ref. 45.

As can be seen in Figure 2.5a, the Mie solution to Maxwell's equations gives an LSPR wavelength that redshifts as the particle size increases. For radii above ∼20 nm the LSPR wavelength significantly deviates from the quasi-static case, which demonstrates the range of validity for this approximation. As can be seen in Figure 2.5b, for the case of Au spheres, scattering starts dominating over absorption for radii above ∼40 nm. For this reason, microscopy techniques that rely on scattering, such as dark-field microscopy, require large nanoparticles in order to identify them from the background. Smaller particles can be imaged using, for example, photothermal imaging, which relies on the absorption cross section.[53]

2.4 Resonance tunability and the FDTD method

From the resonance condition in equation (2.21) it is clear that the LSPR wavelength is sensitive to the dielectric function of the metal (Figure 2.6a) and to the dielectric constant of the surrounding medium (Figure 2.6b). The latter is employed as a mechanism to use plasmonic nanoparticles as sensors: a change in the dielectric constant of the surrounding medium, for example due to the binding of a molecule, can result in a detectable shift of the LSPR.[54] In the previous section we have also seen that the LSPR wavelength is sensitive to the particle size (Figure 2.6c). Lastly, the LSPR wavelength can be tuned by changing the shape of the nanoparticle. For example, nanorods have two resonances, one for electric field polarizations along the short axis of the nanorod and one for polarizations along the long axis. The resonance along the short axis, the transverse resonance, is typically around the same wavelength as the resonance of a small sphere (520 - 530 nm for gold, see Figure 2.5a). The resonance along the long axis, the longitudinal resonance, redshifts with increasing aspect ratio, which allows for tuning over a wide range of wavelenghts (Figure 2.6d).

Since Mie theory assumes a spherical particle, it is no longer valid for non-spherical shapes. Mie theory can be extended to spheroidal particles, known as Mie-Gans theory,[55,56] but for arbitrary shapes computational methods need to be employed. The finite-difference time-domain (FDTD) method solves Maxwell's equations on a discrete spatial and temporal grid.[57] The simulated geometry can be of arbitrary shape and material, as long as all dielectric functions satisfy the Kramers-Kronig relations.[42] A short light pulse from a source is injected into the system in the form of a plane wave or a point dipole. The pulse then propagates through the system until it reaches the boundaries of the simulation volume. These boundaries can be periodic, for simulating periodic structures, or they can consist of absorbing layers, for simulating individual structures. The electromagnetic fields resulting from these simulations can be used to calculate, for example, scattering and absorption cross sections and electric field enhancements. As light is injected in the form of a short pulse, one single simulation contains a broad range of frequencies. By then performing a Fourier transform after the simulation, the resulting parameter of interest can be expressed as a function of frequency or wavelength.

In this thesis, we will often use Mie theory and FDTD simulations to model the optical properties of plasmonic nanoparticles. In particular, in chapters 4 and 6 we use simulations to disentangle different contributions to fluorescence enhancement and to plasmon-driven chemistry, respectively. In chapter 5, we demonstrate that we can use super-resolution fluorescence microscopy to map chemical reactions driven by electric fields with nanometer spatial resolution by comparing our measurements to FDTD simulations. In chapter 7, we show that, to accurately estimate the optical properties of Ag nanowires, it is of paramount importance to simulate particles with a shape that accurately reproduces the shape that is experimentally observed.

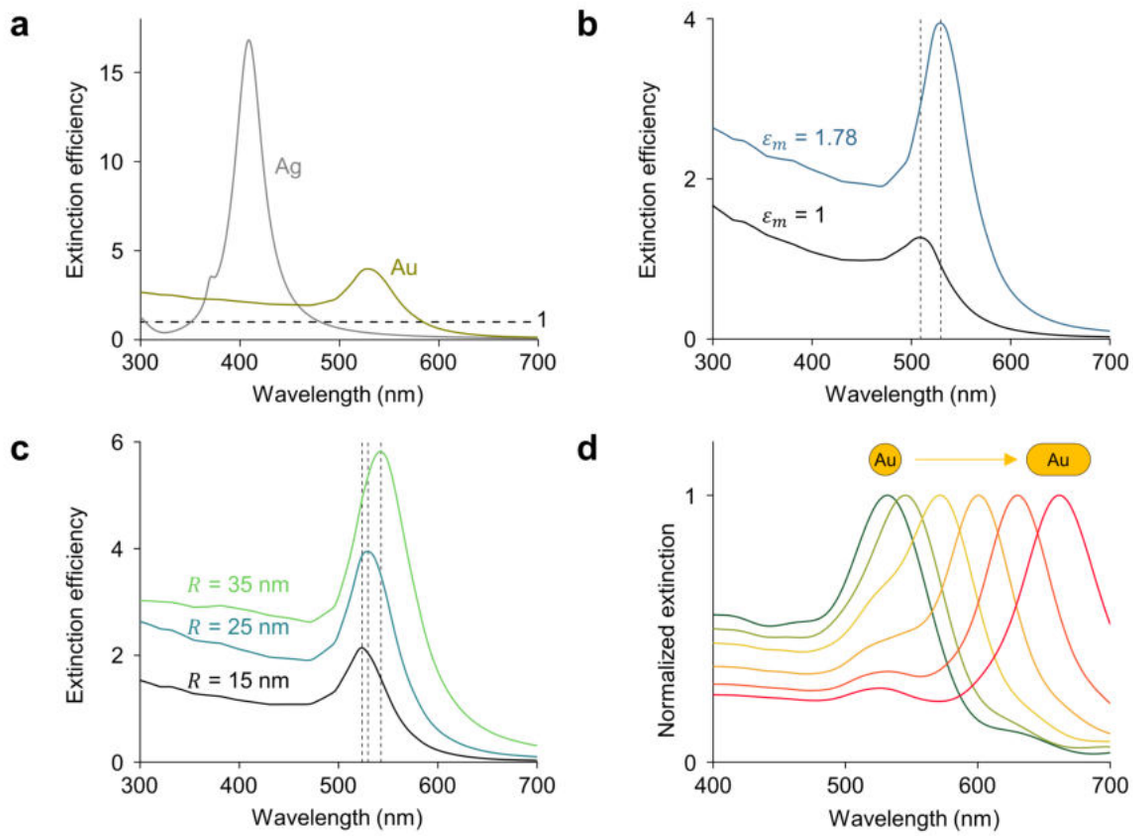

Figure 2.6: (a) Extinction efficiency of a sphere with radius $R = 25$ nm made of gold or silver in air. The extinction cross sections are normalized to the geometrical cross section πR^2 to give the extinction efficiency. The dashed horizontal line denotes an extinction cross section equal to the geometrical cross section. (b) Extinction efficiency of a gold nanoparticle with $R = 25$ nm embedded in air ($\varepsilon_m = 1$, black line) or water ($\varepsilon_m = 1.78$, blue line). The dashed lines denote the LSPR wavelengths, 509 nm and 529 nm. (c) Extinction efficiency of a gold nanoparticle with $R = 15$ nm, 25 nm, or 35 nm. The dashed lines denote the LSPR wavelengths, 523 nm, 529 nm, and 542 nm. (d) Normalized extinction cross section of a gold sphere of $R = 25$ nm, that is elongated in steps of 10 nm to a gold nanorod with a total length of 100 nm. The cross sections are calculated using Mie theory (a-c) or using the FDTD method (d).

2.5 Plasmon decay

The LSPR can either decay radiatively (scattering) or non-radiatively (absorption). The resonant enhancement in the polarizability, as described in section 2.1, also results in a resonant enhancement in the electric fields inside and outside the particle (Figure 2.7). The electric field enhancement is particularly pronounced in the region just outside the nanoparticle, which is why this effect is also referred to as a near-field enhancement. For example, for an Au sphere with a radius $R = 25$ nm the field intensity inside the particle $|\vec{E}|^2$ is enhanced up to ∼7 times with respect to the incident field, and the intensity outside the particle is enhanced up to ∼41 times (Figure 2.7). If now an absorbing species is present in the vicinity of the nanoparticle, it will experience an enhanced electric field. This enhancement is the mechanism behind surface-enhanced Raman spectroscopy[15] and can drive photosensitive reactions[12] or enhance fluorescence intensity.[13]

The absorption process first results in the photon exciting an electron-hole pair in the metal. This process can happen via four different mechanisms.[58] First, for high photon energies, a photon can excite a direct interband transition from one electronic band below the Fermi level to another

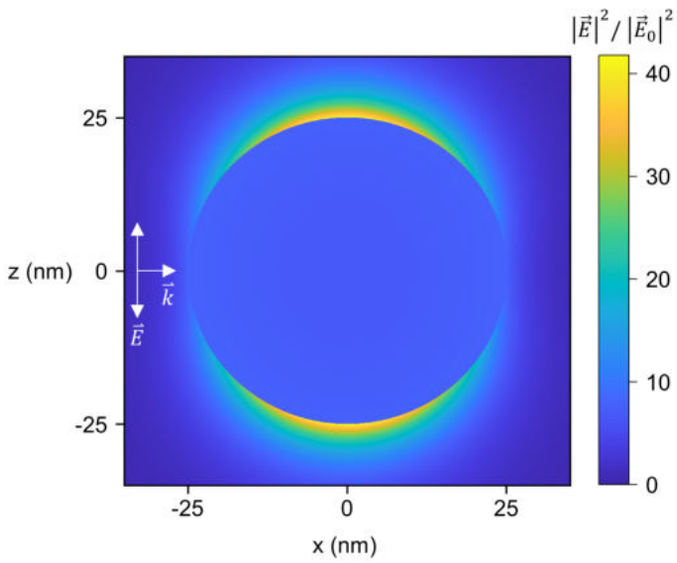

Figure 2.7: Electric field intensity $|\vec{E}|^2$ normalized to the incident field intensity $|\vec{E}_0|^2$ in and around an Au sphere with $R = 25$ nm. The incident field propagates along the x axis and is polarized along the z axis, as indicated by the white arrows. The fields are calculated using Mie theory and the dielectric function is taken from Ref. 45.

above the Fermi level (Figure 2.8a). In Au and Cu, these transitions originate from the d-band, which lies ∼2 eV below the Fermi level. Therefore, the generated hole is more energetic than the electron.[59] The effective mass can be calculated from the energy dispersion via[48]

$$m = \hbar^2 \frac{1}{\partial^2 E / \partial k^2}. \tag{2.29}$$

Due to the low curvature of the d-band, the hole has a large effective mass and, consequently, a low mean free path (< 5 nm).[60] Nevertheless, the asymmetry in the energy distribution between the electron and the hole has important consequences both for driving chemical reactions and for charge transfer across a metal-semiconductor interface. As the holes are more energetic, interband excitation in Au or Cu is particularly suitable for accelerating chemical reactions where the hole-driven process (oxidation) is the rate-limiting step, as we will see in chapter 6.[39] Similarly, these excitations are more suitable for hole transfer from a metal to a p-type semiconductor rather than for electron transfer to an n-type semiconductor.[26,61]

All other carrier generation mechanisms occur via intraband transition, i.e. they involve the transition between states with different wavevectors within the same sp-band. In the second mechanism, the momentum mismatch is compensated by a phonon or defect (Figure 2.8b). The resulting electron and hole, on average, both have an energy $\hbar\omega/2$ relative to the Fermi level. The sp-band is characterized by a higher curvature than the d-band and, therefore, charge carriers generated in this band have a low effective mass and a high mean free path (10 - 40 nm).[60]

Intraband transitions can also occur via electron-electron scattering (Figure 2.8c).[58] In this third process, the photon energy is shared between two electrons and two holes, each with an energy of $\hbar\omega/4$, on average. The momentum mismatch, i.e. the difference between the initial momentum and the final momentum ($\vec{k}_3 - \vec{k}_1 + \vec{k}_4 - \vec{k}_2$), is, in this case, equal to the reciprocal lattice vector $\vec{G}$.

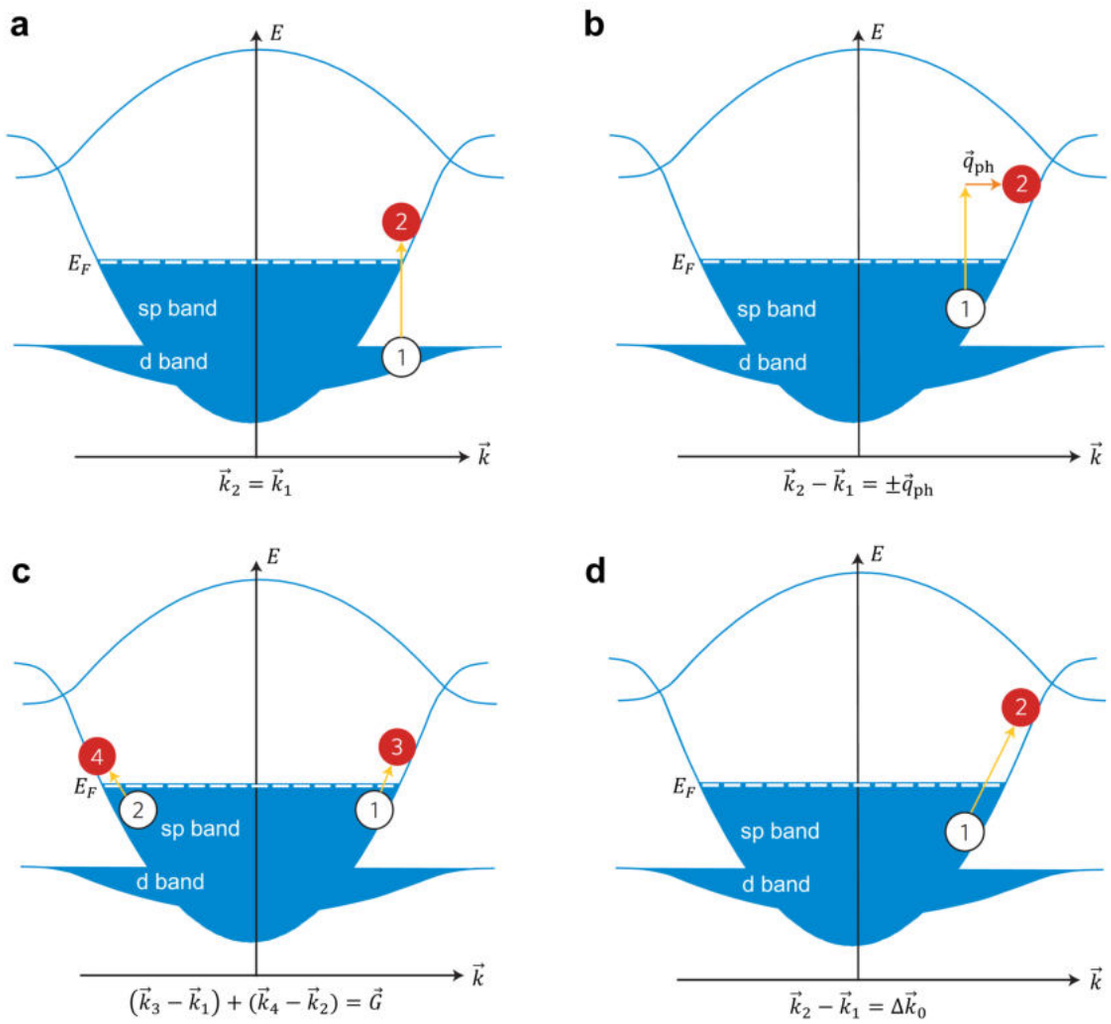

Figure 2.8: (a) Momentum-conserved interband transition from the d-band to the sp-band. (b) Intraband transition where the momentum mismatch $\vec{q}_{ph}$ is compensated by a phonon or defect. (c) Intraband transition assisted by electron-electron scattering. The momentum mismatch $\vec{k}_3 - \vec{k}_1 + \vec{k}_4 - \vec{k}_2$ is equal to the reciprocal lattice vector $\vec{G}$. (d) Intraband transition assisted by surface scattering, where the momentum mismatch $\Delta\vec{k}_0$ is compensated by electromagnetic field confinement. The figure is adapted from Ref. 19.

Lastly, intraband transitions can occur via geometry-assisted damping, also referred to as Landau damping (Figure 2.8d).[58,62] Classically, this process can be understood as an exchange of momentum between the electron and the metal lattice when an electron collides with the surface. Quantum mechanically, this process can be seen as the result of electric field confinement, which results in the Fourier spectrum of the field having wavevectors that are large enough to compensate the momentum mismatch.[58] This phenomenon can also be understood intuitively from the uncertainty principle, where spatial confinement necessitates a broad momentum distribution.[62]

Once non-equilibrium charge carriers are generated, they can transfer to an adjacent semiconductor and be measured as photocurrent or to an adjacent adsorbed species and drive chemical reactions.[21,25,63] If these carriers are not harvested, however, they dissipate their energy to other electrons and, eventually, to the lattice via electron-electron and electron-phonon scattering.[20] The latter results in the nanoparticle and its surrounding medium heating up.

The enhanced fields inside the nanoparticle result in an enhanced absorption of optical power via[64]

$$P_{\text{abs}} = \frac{1}{2}\omega\varepsilon_0|\vec{E}|^2\text{Im}[\varepsilon], \tag{2.30}$$

where P_{abs} is the absorbed power per unit volume. The total power that is absorbed by the nanoparticle then is a volume integral of P_{abs}, which can also be expressed as the absorption cross section σ_{abs} multiplied by the irradiation intensity I. This absorbed power results in a temperature increase ΔT of the nanoparticle. Assuming a spherical particle with a radius R, ΔT is given by:[65]

$$\Delta T = \frac{\sigma_{\text{abs}} I}{4\pi\kappa R}, \tag{2.31}$$

where κ is the thermal conductivity of the surrounding medium. If we take the example of an Au sphere with $R = 25$ nm in water ($\sigma_{\text{abs}} = 6.8{\cdot}10^{-15}$ m^2, $\kappa = 0.61$ W/m/K) irradiated with a 1 mW laser focused to a 1 µm^2 spot, we obtain a ΔT of 35 K.

The rate k of a chemical reaction scales with

$$k \propto \exp\left(-\frac{E_a}{k_B T}\right), \tag{2.32}$$

where E_a is the activation barrier, k_B the Boltzmann constant, and T the temperature. Note that k here denotes a rate constant and should not be confused with the wavevector. The above equation, also known as the Arrhenius equation,[66,67] shows that the temperature increase due to the irradiation of a plasmonic nanoparticle, plasmonic heating, can be used to drive chemical reactions at the nanoparticle surface.[28] If we stick to the previous example of an Au sphere with an increased surface temperature ΔT of 35 K and assume an activation energy of 50 kJ/mol (0.52 eV), we find a rate enhancement of

$$\frac{k(T+\Delta T)}{k(T)} = \frac{k(328\,\text{K})}{k(293\,\text{K})} = 8.9.$$

As can be seen, due to the exponential scaling, even moderate temperature increases can already significantly alter the rate of a chemical reaction.[35]

As all of the above processes (near-field enhancement, non-equilibrium charge carrier generation, and plasmonic heating) happen simultaneously on ultrafast timescales, it has proven to be challenging to disentangle all these mechanisms experimentally.[30–39] In this thesis we will see how super-resolution fluorescence microscopy can be used to map chemical reactions driven by plasmonic near-fields with nanometer spatial resolution (chapter 5). Furthermore, we will see how a light-driven synthesis of core@shell Au@Ag nanoparticles, combined with numerical modeling, can be used to individually assess each plasmon activation mechanism (chapter 6).

Chapter 3

Stochastic super-resolution microscopy

Abstract

In this chapter we discuss the microscopy technique that is used in chapters 4 and 5 of this thesis: stochastic super-resolution microscopy. We first describe the working principles of the optical microscope and the fluorescence microscope. We identify a resolution limit of ∼250 nm due to the diffraction of light and show how this limit can be broken by performing single molecule localization, allowing us to reach a resolution of several (tens of) nanometers. We then describe the image processing that is performed on the fluorescence microscopy data. Finally, we show how single molecule localization can be used to study catalytic conversions and fluorescence enhancement by plasmonics nanoparticles at the nanoscale level.

3.1 Introduction

Microscopes allow us to see objects that are not visible to the naked eye. More specifically, an optical microscope (Figure 3.1a) guides visible light, for example from a halogen lamp, on a thin sample and then collects and magnifies the transmitted light, before guiding it to an eyepiece or a camera.

While there exist numerous configurations of optical microscopes, a typical light path is shown in Figure 3.1b: a lens collects the light from the source and focuses it on the condenser diaphragm. The condenser lens then projects the light onto the sample. This type of illumination, known as Köhler illumination, where the light from the source is not focused on the sample, results in uniform illumination and prevents an image of the light source, for example a lightbulb filament, from being present in the image of the sample. On the other side of the sample, the objective collects the light and, finally, the tube lens focuses the collected light on a detector, for example a camera. Magnification arises from the difference between the focal length of the tube lens, which is constant, and the effective focal length of the objective (Figure 3.1c). The effective focal length f_{eff} can be calculated from the magnification M of the objective using

This chapter is partially based on Ref. 40: **Super-Resolution Mapping of Plasmonic Hot Electrons**, Ruben F. Hamans, *Eindhoven University of Technology: Eindhoven*, 2017 and Ref. 41: **Single Particle Approaches to Plasmon-Driven Catalysis**, Ruben F. Hamans, Rifat Kamarudheen, and Andrea Baldi, *Nanomaterials*, 2020, 10, 12, 2377

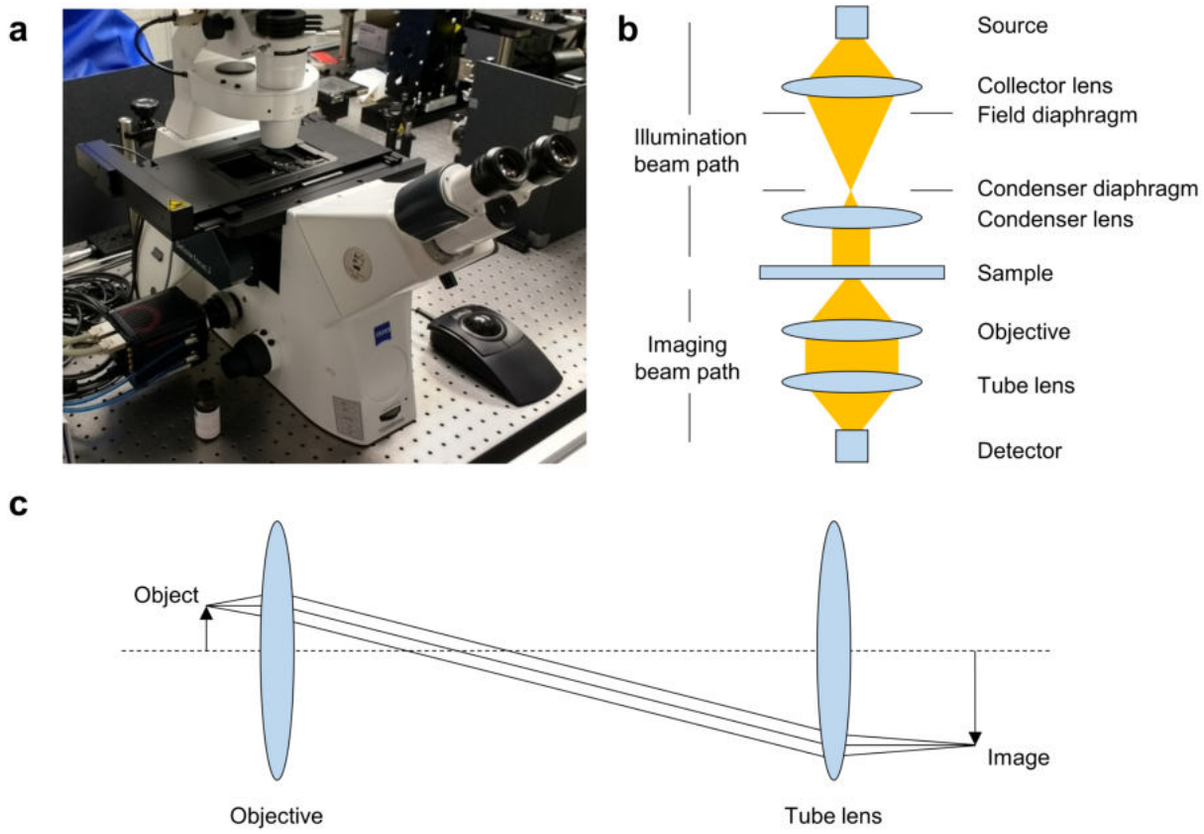

Figure 3.1: (a) Photograph of an optical microscope. This model is a so-called inverted microscope, as the objective is under the sample. (b) Illustration of the illumination and imaging beam paths in a conventional optical microscope. (c) Illustration of the magnification arising from the difference in focal length between the objective and the tube lens.

$$M = \frac{f_{\text{tube}}}{f_{\text{eff}}}, \tag{3.1}$$

where f_{tube} is the focal length of the tube lens. For example, Zeiss microscopes, such as those used in this thesis, have a tube lens with a focal length of 165 mm. A 63× objective would then have an effective focal length of 165 / 63 = 2.6 mm.

The term 'effective' focal length is used here for the objective, as in reality an objective is not a single lens, but consists of multiple optical components. The performance of an objective is usually described sufficiently using its magnification and numerical aperture (NA). The NA is defined as

$$\text{NA} = n \sin \theta_{\text{acc}}, \tag{3.2}$$

where n is refractive index in which the objective is working and θ_{acc} is the acceptance angle, defined as the maximal half-angle of the cone of light that can enter or exit the objective. The NA defines the resolving power of the microscope: as we will derive later in section 3.3, the Rayleigh criterion states that two point sources can no longer be resolved if their separation is smaller than[68]

$$R_{\text{Rayleigh}} = 1.22 \frac{\lambda}{2\text{NA}}, \tag{3.3}$$

where λ is the emitted wavelength. Equation (3.3) shows that the higher the NA, the smaller is the distance at which two point sources are no longer distinguishable, and therefore the higher the microscope resolution. For this reason, to achieve the highest possible resolution, immersion oils are often used to increase the refractive index in which the objective is working, see equation (3.2). Furthermore, if the refractive index of the immersion oil is matched to that of the substrate, for example $n = 1.52$ when using borosilicate glass, no refraction occurs between the sample and the objective, further maximizing the collection efficiency.

3.2 Fluorescence microscopy

A downside of conventional optical microscopy is that it is often limited by the contrast that the sample provides: very thin samples give very little contrast, which results in an image on the detector that is mostly white. Furthermore, conventional optical microscopy is not selective: anything that absorbs or scatters light gives contrast and therefore it can be hard to identify different components in a structure.

Fluorescence microscopy uses light sources with a very narrow emission wavelength, for example a laser, to optically excite so-called fluorophores: molecules capable of re-emitting light at a longer wavelength. During this excitation process the fluorophore goes from its electronic ground state to a higher vibrational level of its first electronically excited state (Figure 3.2a). The excitation then non-radiatively decays to the lowest vibrational level of the first electronically excited state. Finally, the excitation decays back to the electronic ground state by emitting a photon.

As can be seen in Figure 3.2a, the emission spectrum and the absorption spectrum are mirror images of each other, i.e. the color of the excitation source is different from the color of the emitted light, as highlighted by the example of Rhodamine 6G in Figure 3.2b. The absorption of Rhodamine 6G peaks at ∼525 nm, whereas the emission peaks at a lower energy and therefore longer wavelength, ∼550 nm. This spectral shift allows us to use simple optical filters to selectively remove the contribution of our excitation source and therefore construct images in which the emission of the fluorophore appears as a bright spot in a dark background. This removal of the overpowering intensity of the light source greatly increases the sensitivity of the microscopy technique, even allowing us to observe the fluorescence of a single molecule.[71] Furthermore, fluorophores can be labeled to a specific part of a biological structure. Fluorophores with different absorption and emission wavelengths can then be bound to specific parts, which allows us to take multi-color fluorescence images in which each component is identified by a different color (Figure 3.2c).

As can be seen in Figure 3.2d, in a typical fluorescence microscope both the excitation and the collection take place through the microscope objective. Similar to the Köhler illumination shown in Figure 3.1b, the excitation source is not focused on the sample. Instead, a laser beam is focused on the back focal plane of the microscope objective (dashed line in Figure 3.2d), resulting in illumination normal to the sample. This illumination method is also referred to as epifluorescence. In the collection path, the laser beam is filtered out using a dichroic mirror, which reflects the excitation wavelength and transmits the emission wavelength. Any residual contribution from the excitation source is then further filtered out using an emission filter, before the emitted light is focused on a detector by the tube lens.

Since the excitation source travels normal to the sample when using epifluorescence illumination, fluorescent species that are above or below the region that is in focus will also be excited. To avoid the resulting background signal, total internal reflection fluorescence (TIRF) can be used. In this case, the excitation travels towards the glass-sample interface at an angle higher than the

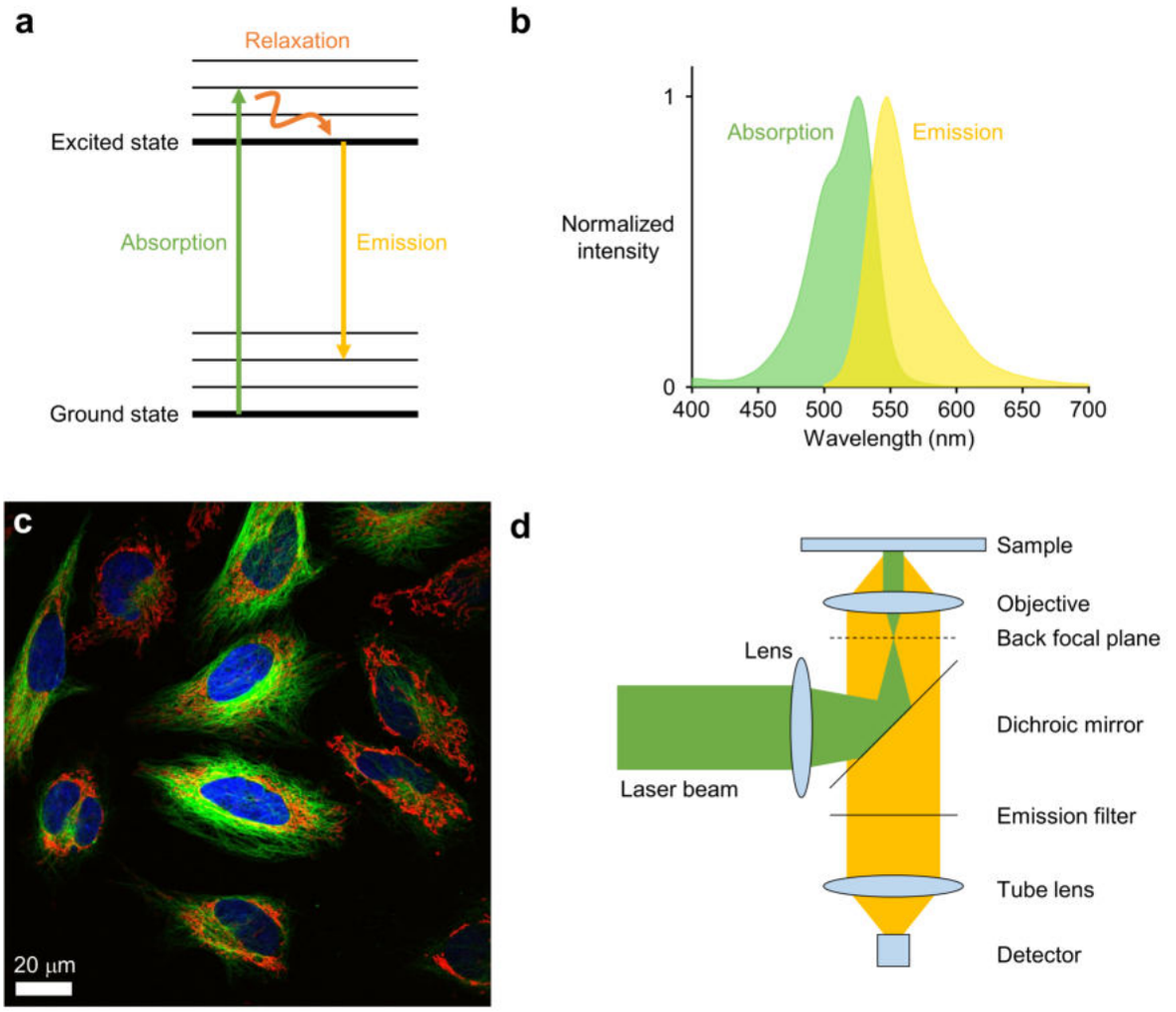

Figure 3.2: (a) Illustration of the process of fluorescence. The think black lines indicate the electronic energy levels and the thin lines the vibrational levels. A photon is absorbed (green arrow) and the excitation decays non-radiatively (orange arrow) to the bottom of the first excited state, before emitting a photon (yellow arrow). (b) Absorption (green) and emission (yellow) spectrum of Rhodamine 6G. (c) Fluorescence image of living HeLa cells. Mitochondria are stained in red (MitoTracker Red), the nucleus in blue (DAPI), and the microtubules in green (Tubulin Tracker Green). (d) Illustration of the beam paths in epifluorescence illumination. Panel (b) is based on data from Ref. 69 and panel (c) is adapted from Ref. 70.

critical angle for total internal reflection (Figure 3.3a). For example, for a glass-water interface the critical angle θ_{TIRF} is

$$\theta_{\mathrm{TIRF}} = \arcsin \frac{n_{\mathrm{water}}}{n_{\mathrm{glass}}} = \arcsin \frac{1.33}{1.52} = 61°.$$

To achieve this high excitation angle, the laser is not focused on the center of the back focal plane of the objective, as is the case for epifluorescence illumination (Figure 3.2d). Instead, the beam is focused on the edge of the back focal plane (Figure 3.3b).

The objective needs to be capable of directing light towards the interface at angles higher than the critical angle, i.e. $\theta_{\mathrm{acc}} > \theta_{\mathrm{TIRF}}$. From equation (3.2), the acceptance angle of an objective with an NA of 1.46 working in an index matching immersion oil ($n = 1.52$) is

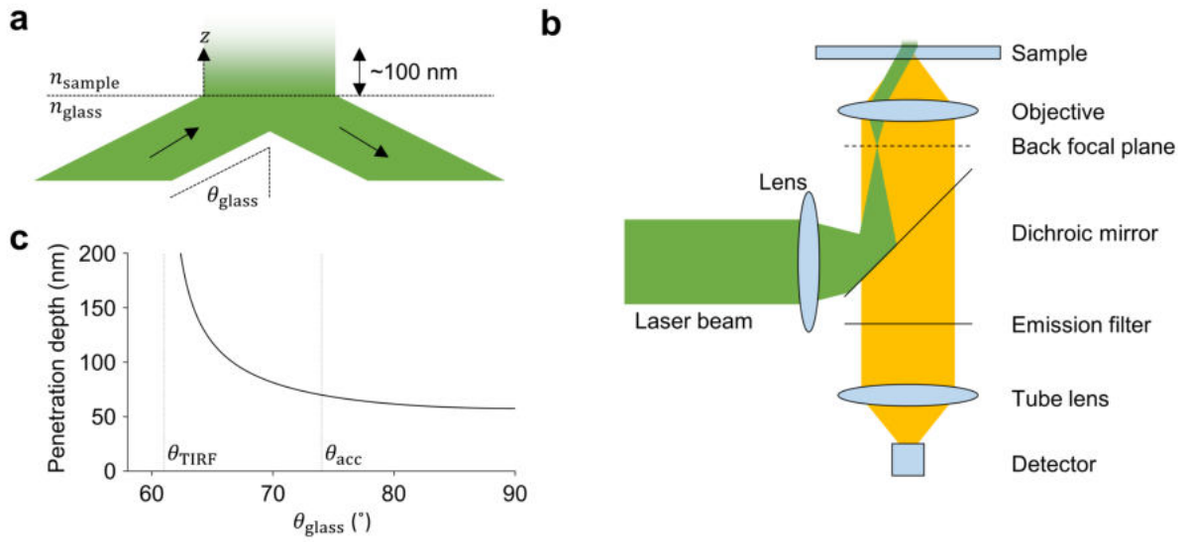

Figure 3.3: Illustration of (a) total internal reflection at the glass-sample interface, where $n_{glass} > n_{sample}$, and (b) the beam paths in TIRF illumination. (c) Plot of equation (3.5) for $\lambda = 532$ nm, $n_{glass} = 1.52$, and $n_{sample} = 1.33$. The critical angle for total internal reflection ($\theta_{TIRF} = 61°$) and the acceptance angle of the objective ($\theta_{acc} = 74°$) for our experimental configuration are highlighted using vertical dashed lines.

$$\theta_{acc} = \arcsin \frac{NA}{n_{glass}} = \arcsin \frac{1.46}{1.52} = 74°.$$

At the glass-sample interface the excitation beam reflects back into the objective. However, the boundary conditions of Maxwell's equations require the normal components of the displacement field $\vec{D}$ and the tangential components of the electric field $\vec{E}$ to be conserved at the interface (see also section 2.1). Therefore, the electric field cannot abruptly go from a finite value to zero, resulting in an evanescent field being present in the sample, with an intensity

$$I = I_0 \exp[-z/d], \tag{3.4}$$

where z is the spatial coordinate normal to the interface (Figure 3.3a), $z = 0$ is at the interface, and d is the penetration depth given by:[72]

$$d = \frac{\lambda}{4\pi}(n_{glass}^2 \sin^2 \theta_{glass} - n_{sample}^2)^{-1/2}, \tag{3.5}$$

where θ_{glass} is the angle of incidence of the excitation beam. As shown in Figure 3.3c, for excitation at 532 nm, $n_{glass} = 1.52$, and $n_{sample} = 1.33$, the above equation gives a penetration depth of ~100 nm. Under these illumination conditions, which correspond to the experimental conditions for the study reported in chapter 5 of this thesis, only fluorescent species that are less than ~100 nm above the glass-water interface are excited, which results in a significant decrease in background signal.

3.3 Single molecule localization

The resolving power of an optical microscope is limited by the Rayleigh condition, see equation (3.3). If we take the example of Rhodamine 6G molecules imaged through an objective with an NA of 1.46, we obtain a resolution of

$$R_{\text{Rayleigh}} = 1.22\,\frac{550\,\text{nm}}{2\times 1.46} \approx 230\,\text{nm}.$$

Therefore, if two Rhodamine 6G molecules are separated by less than 230 nm they can no longer be distinguished from each other. This resolution is incommensurate with the typical lengths scales of the plasmonic nanoparticles or particle arrays used in this thesis, which are of the order of 10 to 100 nm. Therefore, conventional optical microscopy is unsuitable to study plasmonic effects with sub-particle or sub-unit cell resolution.

Before describing how we can improve upon the above-mentioned resolution limit, we first derive the Rayleigh criterion. We consider a plane wave impinging on a screen with a circular aperture and the consequent far-field diffraction pattern on a distant observing screen (Figure 3.4). A focusing lens close to the aperture then allows us to bring the observing screen close to the aperture, without changing the diffraction pattern.

The diffraction that occurs due to the presence of the aperture can be described using Fraunhofer diffraction.[73] According to the Huygens-Fresnel Principle, a differential area $\mathrm{d}S$ in the aperture can be envisioned as being a point source emitting a spherical wave. As monochromatic spherical waves are of the form $\exp[i(\omega t - kr)]/r$, we can write the contribution $\mathrm{d}E$ to the electric field at a point P on the observing screen as

$$\mathrm{d}E = \frac{E_a}{r}\exp[i(\omega t - kr)]\mathrm{d}S, \tag{3.6}$$

where E_a is the source strength per unit area and r the distance between $\mathrm{d}S$ and P. $\mathrm{d}S$ is located at $(0, y, z)$ and P at (X, Y, Z). As P is far away from the aperture, r can be replaced by the distance R from the origin to P in the amplitude term ($\frac{E_a}{r}$), where R is given by:

$$R = (X^2 + Y^2 + Z^2)^{1/2}. \tag{3.7}$$

The phase term, however, needs to be treated more carefully, as k can be a large number.

Expanding the expression for r gives

$$\begin{aligned} r &= (X^2 + (Y-y)^2 + (Z-z)^2)^{1/2} && \text{(3.8a)}\\ &= (X^2 + Y^2 - 2yY + y^2 + Z^2 - 2zZ + z^2)^{1/2} && \text{(3.8b)}\\ &= (R^2 - 2yY + y^2 - 2zZ + z^2)^{1/2} && \text{(3.8c)}\\ &= R\left(1 + \frac{y^2+z^2}{R^2} - 2\frac{yY+zZ}{R^2}\right)^{1/2}. && \text{(3.8d)} \end{aligned}$$

As we are considering a far-field case, R is very large compared to the dimensions of the aperture, making the second term negligible. We then perform a Taylor series around $\frac{yY+zZ}{R^2} = 0$ to obtain

$$r \approx R\left(1 - \frac{yY+zZ}{R^2}\right). \tag{3.9}$$

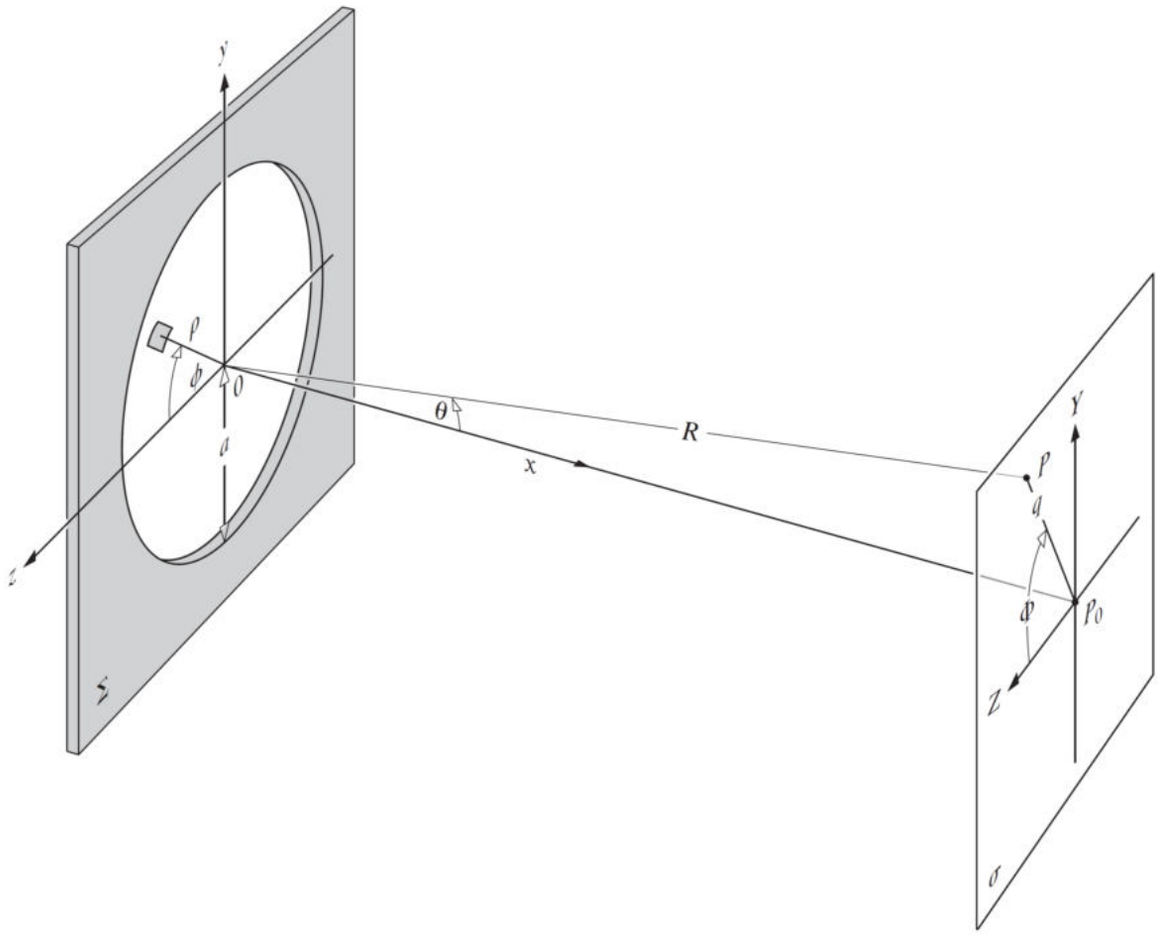

Figure 3.4: Circular aperture geometry. A plane wave impinges on a screen Σ with a circular aperture and the consequent far-field diffraction pattern is observed on a distant observing screen σ. Image taken from Ref. 73.

By using this approximation in equation (3.6) and performing the integral, the total field arriving at P becomes

$$E = \frac{E_a}{R} \exp[i(\omega t - kR)] \iint \exp\left[ik\frac{yY + zZ}{R}\right] \mathrm{d}S, \tag{3.10}$$

where the integral is performed over the area of the aperture. As we are considering a circular aperture, we switch to a spherical coordinate system with

$$y = \rho \sin\phi, \tag{3.11a}$$
$$z = \rho \cos\phi, \tag{3.11b}$$
$$Y = q \sin\Phi. \tag{3.11c}$$
$$Z = q \cos\Phi, \tag{3.11d}$$

Substituting these coordinates in the equation for the field then gives

$$E = \frac{E_a}{R} \exp[i(\omega t - kR)] \int_0^{2\pi} \int_0^a \exp\left[ik\frac{pq\sin\phi\sin\Phi + pq\cos\phi\cos\Phi}{R}\right] \rho \mathrm{d}\rho \mathrm{d}\phi, \tag{3.12a}$$
$$= \frac{E_a}{R} \exp[i(\omega t - kR)] \int_0^{2\pi} \int_0^a \exp\left[ik\frac{pq\cos(\phi - \Phi)}{R}\right] \rho \mathrm{d}\rho \mathrm{d}\phi, \tag{3.12b}$$

where a is the radius of the aperture. Because of axial symmetry, the solution must be independent of Φ and we can solve the above equation for any value of Φ, which we now set to 0.

The solution to the integral over ϕ is a Bessel function. In general, the Bessel function (of the first kind) of order m is given by

$$J_m(u) = \frac{i^{-m}}{2\pi} \int_0^{2\pi} \exp[i(mv + u\cos v)]\mathrm{d}v. \tag{3.13}$$

When using $m = 0$, $v = \phi$, and $u = k\rho q/R$, we obtain

$$E = \frac{E_a}{R} \exp[i(\omega t - kR)]2\pi \int_0^a J_0(k\rho q/R)\rho \mathrm{d}\rho. \tag{3.14}$$

Another property of the Bessel functions is their recurrence relation:

$$\frac{\mathrm{d}}{\mathrm{d}u}[u^m J_m(u)] = u^m J_{m-1}(u). \tag{3.15}$$

For $m = 1$, this gives

$$\int_0^u u' J_0(u')\mathrm{d}u' = uJ_1(u). \tag{3.16}$$

When now using $u' = k\rho q/R$, we obtain

$$E = \frac{E_a}{R} \exp[i(\omega t - kR)]2\pi a^2 (R/kaq) J_1(kaq/R). \tag{3.17}$$

The irradiance at P then becomes

$$I = \frac{1}{2} EE^* = \frac{2\pi^2 a^4 E_a^2}{R^2} \left(\frac{J_1(kaq/R)}{kaq/R} \right)^2 \tag{3.18}$$

When a lens is placed close to the aperture, the numerical aperture can be defined as $\mathrm{NA} = \sin\theta_{\mathrm{acc}} = a/R$ (Figure 3.4), allowing us to write the irradiance as

$$I(p) \propto \left(\frac{2J_1(p)}{p} \right)^2, \tag{3.19}$$

where p is a dimensionless radial coordinate defined as

$$p = 2\pi \frac{\mathrm{NA}}{\lambda} q. \tag{3.20}$$

As can be seen in Figure 3.5, the radiation pattern is characterized by a bright center spot with several rings that become increasingly less intense as p increases. The function $J_1(p)$ has its first zero at $p = 3.8317...$, which gives

$$q_0 \approx \frac{3.8317}{2\pi} \frac{\lambda}{\mathrm{NA}} \approx 1.22 \frac{\lambda}{2\mathrm{NA}}, \tag{3.21}$$

which is the Rayleigh criterion we started this section with, i.e. two point sources can no longer be resolved when the maximum in the diffraction pattern of once source coincides with the first minimum in the other.

An equation such as (3.19) describing the response of an optical system to a point source is also called the point spread function (PSF) of the system. The case treated here has first been derived by Airy and therefore the disk-like shapes as seen in Figure 3.5b are also called Airy disks.[74]

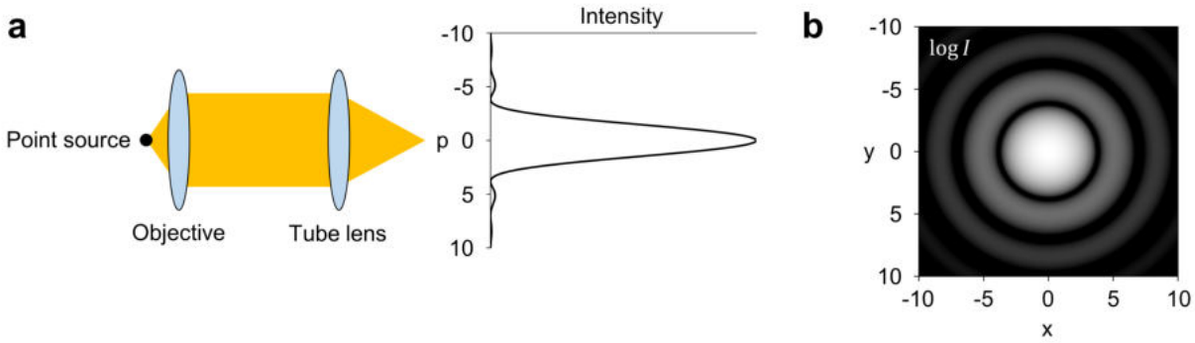

Figure 3.5: (a) Illustration of a point source imaged in an optical microscope and a plot of the intensity in equation (3.19) as a function of the dimensionless spatial coordinate p. (b) Plot of equation (3.19) in Cartesian coordinates, defined using $p^2 = x^2 + y^2$. The colorscale is logarithmic to emphasize the Airy disks.

The above model for the PSF implies that the position of a single molecule can be determined with an accuracy that is much better than just the size of the emission pattern: we can take an experimentally observed fluorescence image of a single molecule and perform a two dimensional fit to the PSF and thereby obtain the center position of the fit, which is then the position of the molecule. In practice, however, fitting to equation (3.19) can be computationally demanding due to the complexity of the Bessel function. Furthermore, due to the noise level in a single molecule fluorescence experiment, only the center spot in Figure 3.5b is typically observed. Therefore, equation (3.19) can be excellently approximated by a Gaussian:

$$I(r) \propto \exp\left(-\frac{r^2}{2\sigma^2}\right), \tag{3.22}$$

where σ is the width of the Gaussian. The Gaussian best describes the Airy disk when $\sigma \approx 0.42\frac{\lambda}{2\mathrm{NA}}$, which results in the fit shown in Figure 3.6.

If we consider each detected photon to be a measurement of the position of the molecule, we can make an initial estimate of the localization precision σ_{loc} of the fit, namely the standard error in the mean:

$$\sigma_{\mathrm{loc}}^2 = \frac{\sigma^2}{N}, \tag{3.23}$$

where N is the number of detected photons. However, there are several sources of noise that worsen the precision with which a molecule can be localized. Firstly, an uncertainty is introduced due to finite pixel size a of the camera that is used to observe the fluorescence: we do not know where on the pixel a photon is detected. This uncertainty changes equation (3.23) into[75]

$$\sigma_{\mathrm{loc}}^2 = \frac{\sigma^2 + a^2/12}{N}, \tag{3.24}$$

which is valid for pixel sizes $a < \sigma$, where a is defined in the image plane, i.e. as the physical size of the pixel divided by the magnification. This equation is used to define an effective standard deviation $\sigma_a^2 = \sigma^2 + a^2/12$. The second source of noise is from background signal that occurs when detected photons do not originate from the fluorescent molecule. Common sources of background noise are background fluorescence (for example from dust or other weakly fluorescing molecules), readout error, and dark current. This noise changes equation (3.24) into[76]

$$\sigma_{\mathrm{loc}}^2 = \frac{\sigma_a^2}{N}\left(\frac{16}{9} + \frac{8\pi\sigma_a^2 b^2}{Na^2}\right), \tag{3.25}$$

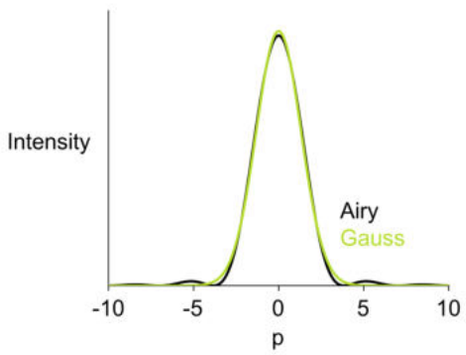

Figure 3.6: Plot of equation (3.19) (black) and corresponding Gaussian fit (green).

where b^2 is the number of background photons, which is calculated as the variance in the residuals between the experimentally observed fluorescence intensity and the fit.

To calculate the typical resolution that can be achieved, we consider a diffraction-limited fluorescent burst, which has a PSF with a width of

$$\sigma \approx 0.42 \frac{\lambda}{2\mathrm{NA}} \approx 79\,\mathrm{nm},$$

where again we consider a molecule emitting at 550 nm, imaged through an objective with an NA of 1.46. The camera used in this thesis (Hamamatsu ORCA-Flash 4.0 V3) has a physical pixel size of 6.5 µm. The objective provides 63× magnification and there is an additional 1.6× magnification in the body of the microscope, yielding a pixel size $a = 64.5$ nm. As can be seen in Figure 3.7, a localization precision of a few (tens of) nanometers can be achieved, significantly improving upon the diffraction limit set in equation (3.3). In our typical experimental conditions the number of detected photons N is 100 to few 100 photons and the background signal b^2 is 5 - 20 photons, resulting in a localization precision around 20 - 30 nm.

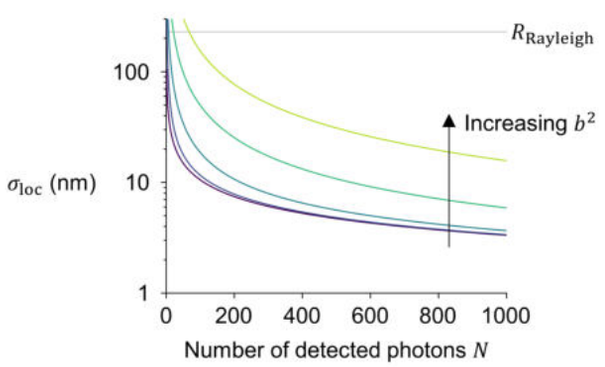

Figure 3.7: Plot of equation (3.25) with $\sigma = 79$ nm, $a = 64.5$ nm, and $b^2 = 0$, 1, 10, 100, 1000. The Rayleigh criterion for a molecule emitting at 550 nm imaged through an objective with an NA of 1.46 is indicated using the black horizontal line.

3.4 Image processing

In both chapters 4 and 5 of this thesis we use ThunderSTORM to process the fluorescence images.[77] This plugin for ImageJ filters the image, finds local maxima, and fits all local maxima and their surroundings to two dimensional Gaussians. These steps will be outlined below.

As a first step in the signal chain, the image is filtered using a wavelet filter (Figure 3.8). This filter allows us to split the image into different so-called wavelet levels, each containing a different range of spatial frequencies.[78] The first wavelet level image mainly contains the high frequency components, including noise. The second wavelet level image contains the lower frequency fluorescent bursts, cleaned from noise (Figure 3.8b). We use this second wavelet level image to determine where the local maxima are.

The second step in the signal chain is finding local maxima in the filtered image. A pixel is considered a local maximum when the following criteria are met:

- The intensity of the pixel is the highest in an 8-connected neighborhood, i.e. in a 3×3 square.

- The intensity of the pixel is higher than a user-specified threshold. Since the points that are to be fitted must lie above noise level in order to obtain good fits, it is useful to look at the first wavelet level image. After all, this image contains most of the noise and can therefore be used to make a quantitative description of when signal can be considered 'above noise level'. Typically, a good threshold lies between 0.5 and 2 times the standard deviation in the pixel intensities of the first wavelet level image. Using high threshold values will result in fewer false detections at the expense of more missed molecules and vice versa.

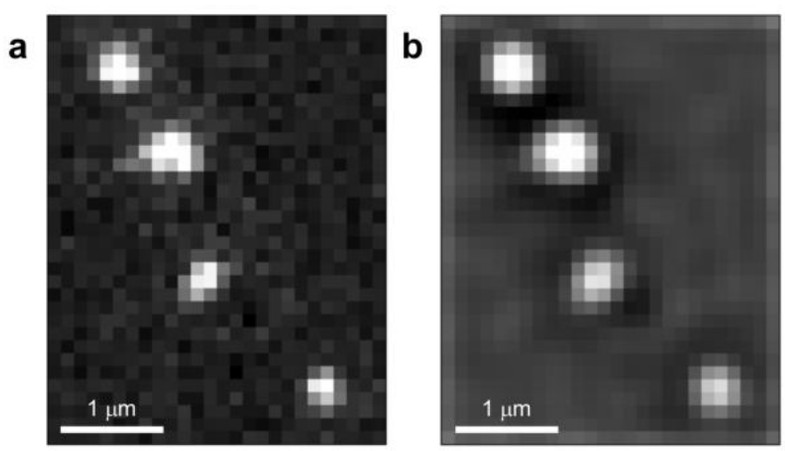

Figure 3.8: (a) Part of a fluorescence image and (b) its second wavelet level, using the filter settings from Ref. 78. The image in panel (b) is used to determine where the local maxima are.

The third step is fitting all local maxima and the surrounding pixels to a two dimensional Gaussian function. The emission pattern of a single molecule is pixelated by the camera or, in other words, each pixel is a local integral of a two dimensional Gaussian. We therefore fit to an integrated

Gaussian of the form[77]

$$I(x,y) = NE_xE_y + I_0, \tag{3.26a}$$

$$E_x = \frac{1}{2}\,\mathrm{erf}\left(\frac{x - x_0 + \frac{1}{2}}{\sqrt{2}\sigma}\right) - \frac{1}{2}\,\mathrm{erf}\left(\frac{x - x_0 - \frac{1}{2}}{\sqrt{2}\sigma}\right), \tag{3.26b}$$

$$E_y = \frac{1}{2}\,\mathrm{erf}\left(\frac{y - y_0 + \frac{1}{2}}{\sqrt{2}\sigma}\right) - \frac{1}{2}\,\mathrm{erf}\left(\frac{y - y_0 - \frac{1}{2}}{\sqrt{2}\sigma}\right), \tag{3.26c}$$

in which I_0 is a vertical offset and erf is the error function defined by

$$\mathrm{erf}\,z = \frac{2}{\sqrt{\pi}}\int_0^z \exp(-t^2)\,\mathrm{d}t. \tag{3.27}$$

After performing the two dimensional fits, we have obtained all the relevant fit parameters for each fluorescent burst: its position (x_0, y_0), intensity N, and PSF width σ. From these parameters we can subsequently calculate the estimated localization precision σ_{loc}, using equation (3.25).

3.5 Drift correction

As single molecule fluorescence experiments are typically long (tens of minutes to a few hours), the sample will drift throughout the experiment, which also translates into a drift in the fitted positions of the fluorescent bursts.

The out-of-plane drift, which would let the sample drift out of focus, is corrected for by the Definite Focus correction system of the Zeiss AxioObserver 7 microscope. This system continuously measures changes in the path length between the objective and the sample using an 850 nm LED and adjusts the focus accordingly. Drift in the lateral direction is corrected for in post processing. A typical single molecule fluorescence experiment contains some constant non-bleaching fluorescent impurities. The light emission from these impurities is also fitted to two dimensional Gaussians and can then be used to construct a drift trajectory, as shown by the example in Figure 3.9. This trajectory is subsequently applied to the coordinates of the fluorescent bursts in the experiment.

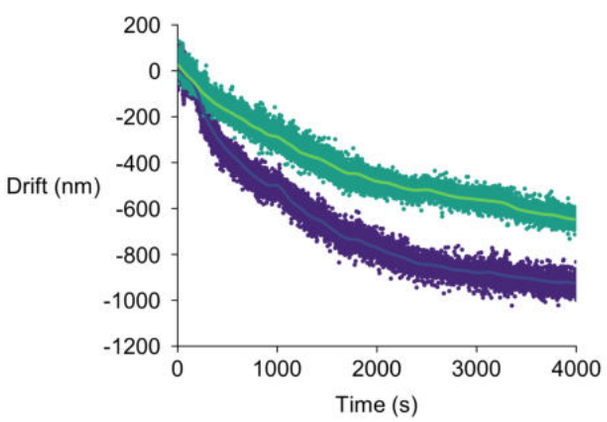

Figure 3.9: Positions of drift markers (dots, x position in purple and y position in green) and the corresponding interpolated trajectories (lines) as a function of time.

3.6 Stochastic super-resolution microscopy

As the name suggests, single molecule localization as described in the previous section requires for a single molecule to be observed at a time. In chapter 4 of this thesis we study the interaction between fluorescent molecules and arrays of plasmonic nanoparticles. In this study, the fluorescent molecules are embedded in a polymer layer above the nanoparticle array. Here, the application of single molecule localization is not immediately straightforward, as all molecules in the laser spot can, in principle, emit simultaneously. The emission patterns of these fluorescent molecules would then overlap, making it impossible to apply single molecule localization. Furthermore, using extremely low dye concentrations would result in the detection of very few events, which does not allow us to build a statistically significant image. To address this issue, we use so-called caged dyes, which are fluorophores that can be photochemically controlled. These molecules initially are in a dark (non-emitting) state and can, therefore, be closely spaced without giving any background signal (Figure 3.10a). Upon excitation with low intensity ultraviolet light, a sparse subset of molecules stochastically switches to a bright (emitting) state (Figure 3.10b). The laser intensity used for the localization of the activated dyes is high enough to eventually lead to photobleaching, the photochemical alteration of the dye such that it is permanently unable to fluoresce. This process avoids the accumulation of bright molecules before a new subset of molecules is activated by the UV light (Figure 3.10a).

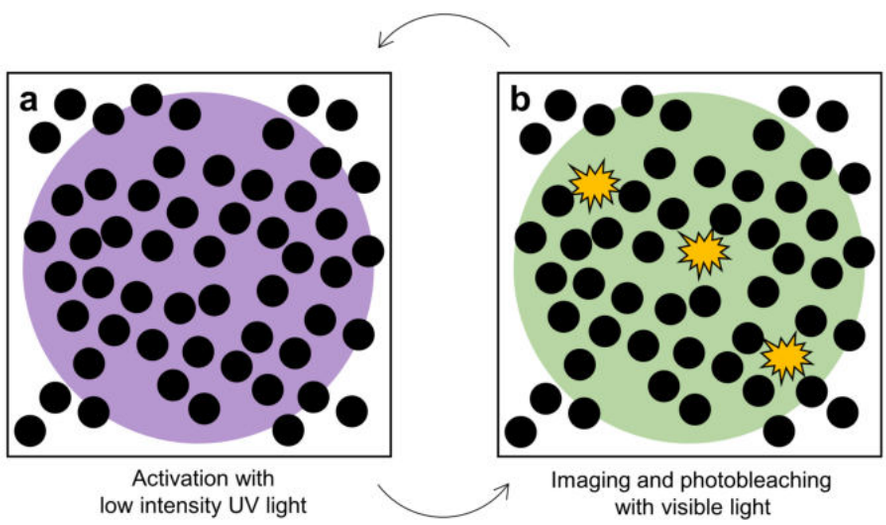

Figure 3.10: Illustration of stochastic super-resolution microscopy. (a) All dye molecules are initially in a dark state. A sparse subset of molecules is activated using low intensity ultraviolet light. (b) These molecules can then be imaged with visible light, using fluorescence microscopy, until they eventually photobleach. The remaining molecules are still in a dark state, and the process can be repeated.

In chapter 5 of this thesis we do not use caged dyes, as we will study fluorogenic catalytic reactions,[79] which are chemical reactions that turn a nonfluorescent reactant molecule into a fluorescent product molecule. After the reaction, the fluorescent product is still adsorbed on the surface of the catalyst and can be imaged through an optical fluorescence microscope. Given the typical brightness of the molecules we use and the intensity of our incident laser, the acquisition time needed to accurately image the emission from a single molecule is between 10 and 100 ms. Once the product molecule has desorbed, it will be in Brownian motion in the liquid surrounding the catalysts. During Brownian motion a molecule is able to move ∼10 µm within a single frame of 100 ms and, therefore, will only contribute to the background signal.[80] By controlling the pH and

the concentrations of the reactants, the typical turnover rate (number of catalytic reactions per second) can be engineered to be slower than the desorption time.[81] In this case, each fluorescent burst that is observed in the microscope can be considered as coming from a single molecule.

Chapter 4

Super-resolution mapping of enhanced emission by collective plasmonic resonances

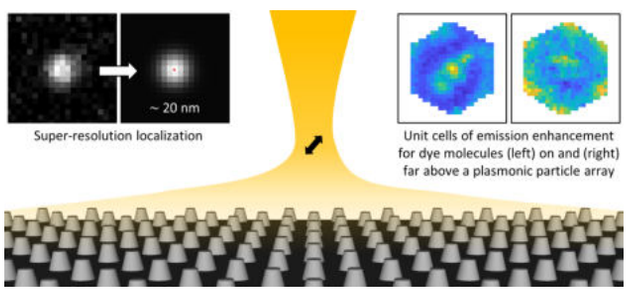

This chapter is based on Ref. 82: ACS Nano 2019, 13(4), 4514-4521.

4.1 Foreword

As we have seen in chapter 2, the polarizability of a metallic nanoparticle is limited in magnitude due to the imaginary part of the dielectric function, or, in other words, due to the fact that metals are lossy. We have also seen that these absorptive properties can be exploited for driving chemical reactions via non-equilibrium charge carriers or plasmonic heating. However, they result in the LSPR having a very low quality factor or high linewidth, which can be detrimental for photonic applications.[19] Placing plasmonic nanoparticles in a periodic array with a lattice constant of the order of the wavelength allows for the formation of collective resonances known as surface lattice resonances (SLRs).[83–85]

The SLR inherits properties from the plasmonic resonances, resulting in strong electric field enhancements,[86–88] but also from in-plane diffraction orders, resulting in narrow linewidths.[89–92] Furthermore, due the relative ease of fabrication and the planar design of plasmonic particles arrays, they can easily be integrated with light-emitting materials such as organic fluorophores. These improved properties make plasmonic particle arrays particularly interesting for controlling light-matter interactions at the nanoscale. Therefore, it is important that we have an extensive understanding of how light emitters interact with these arrays. However, the lattice constant of the array is of the order of its resonance wavelength, resulting in the optical modes having features that are impossible to resolve with conventional optical microscopy.

In this chapter we use stochastic super-resolution microscopy, as described in section 3.6, to investigate the influence of collective plasmonic resonances on the emission of fluorescent molecules with sub-diffraction resolution. Using this technique allows us to measure the intensity of a single fluorescent molecule as a function of its position inside the unit cell of the array. Fluorescence intensity, however, can be modified via several mechanisms. First, as mentioned before, SLRs are characterized by strong electromagnetic field enhancements. If an emitter is placed in this near-field it experiences a higher field intensity, therefore absorbs more light, and will be brighter. In our experiments we are exciting off-resonance, so we expect modifications in the absorption rate of the dyes to be low. Second, the spontaneous decay rate of the dye can be modified due to the presence of a resonant cavity (the plasmonic particle array), also known as the Purcell effect.[93] This effect results in an enhanced radiative quantum yield η:

$$\eta = \frac{F_P \gamma_{\text{rad}}}{\gamma_{\text{nrad}} + F_P \gamma_{\text{rad}}}, \tag{4.1}$$

where F_P is the Purcell factor and γ_{rad} and γ_{nrad} are the radiative and non-radiative decay rates, respectively. Third, the emission radiated by the dye can be reflected by the array, which can result in more radiation being directed towards the microscope objective. This effect we refer to as directivity.

To distinguish between these mechanisms we compare our measurements to FDTD simulations, which allow us to model the Purcell effect and the directivity. Our results show that the Purcell effect is only significant when the distance between the emitter and a nanoparticle is small. This effect is also reproduced when simulating an emitter close to a single particle and, therefore, does not benefit from the array having a collective resonance. Interestingly, we also observe an enhanced intensity in parts of the unit cell that are far away from a nanoparticle. This observation can be reproduced when simulating an array of particles, but not when simulating a single particle. Therefore, the enhanced intensity is due to a directivity enhancement from the whole array: multiple nanoparticles scatter the radiation from the emitter, which then interferes constructively in the direction of the microscope objective.

Abstract

Plasmonic particle arrays have remarkable optical properties originating from their collective behavior, which results in resonances with narrow linewidths and enhanced electric fields extending far into the surrounding medium. Such resonances can be exploited for applications in strong light-matter coupling, sensing, light harvesting, non-linear nanophotonics, lasing, and solid-state lighting. However, since the lattice constants associated with plasmonic particle arrays are of the order of their resonance wavelengths, mapping the interaction between point dipoles and plasmonic particle arrays cannot be done with diffraction-limited methods. Here, we map the enhanced emission of single fluorescent molecules coupled to a plasmonic particle array with ∼20 nm in-plane resolution by using stochastic super-resolution microscopy. We find that extended lattice resonances have minimal influence on the spontaneous decay rate of an emitter, but instead can be exploited to enhance the outcoupling and directivity of the emission. Our results can guide the rational design of future optical devices based on plasmonic particle arrays.

4.2 Introduction

Localized surface plasmon resonances (LSPRs), arising from the coherent oscillation of free electrons in a metallic nanostructure,[8] can be used to manipulate the absorption and emission of light at the nanoscale.[10,94–97] Positioning these metallic nanostructures in a periodic array can lead to the formation of collective lattice modes known as surface lattice resonances (SLRs). SLRs are the result of radiative coupling between the LSPRs of individual nanostructures, enhanced by the in-plane orders of diffraction.[83–85] As SLRs are hybrid plasmonic-photonic modes, they are characterized by a linewidth much narrower than that of an LSPR[89–92] and manifest strong electric field enhancements that spatially extend far into the surrounding medium.[86–88] Due to these improved properties and ease of fabrication, SLRs have been investigated thoroughly for applications in sensing,[98] solid-state lighting,[99] lasing,[100–103] and spectroscopy.[104] Additionally, the planar design of structures supporting SLRs and the versatility for integration with other components and materials such as organic fluorophores,[105,106] two-dimensional materials,[107,108] and carbon nanotubes,[109] have attracted significant attention in using arrays of metallic nanoparticles for controlling light-matter interaction at the nanoscale. Hence, improved functionality of optical devices based on SLRs requires an extensive understanding of the interaction between point dipoles and plasmonic particle arrays at the unit cell level. However, the lattice constant of a plasmonic particle array is of the order of its resonance wavelength, resulting in the optical modes having sub-diffraction limit features and being impossible to resolve with conventional optical microscopy.

Here, we use stochastic super-resolution microscopy[110–112] to separately investigate the influence of localized and extended lattice resonances on single molecule emission with sub-diffraction resolution. We combine these measurements with finite-difference time-domain (FDTD) simulations to gain more physical insight into the underlying mechanisms that modify the emission. We simulate single molecule intensity enhancement as a function of emitter position and disentangle the different contributions by monitoring the Purcell factor, the enhancement in power radiated to the far-field, and the directivity. We find that, despite the extended nature of the SLR, enhanced spontaneous decay rates are only observed in the near-field of the nanoparticles, while the enhanced emission due to the SLR mostly originates from an enhanced directivity.

4.3 Results and discussion

4.3.1 Sample design

We design a plasmonic particle array which supports two spectrally separated lattice resonances, both overlapping with the emission of a fluorescent molecule. This sample geometry allows us to separately investigate the influence of different resonances on the emission of single molecules by proper choice of emission filters. The sample is composed of a hexagonal array of aluminum nanostructures with a lattice constant of 450 nm. To obtain a high scattering cross section, each nanostructure is given the shape of a tall truncated cone, with a base diameter of 140 nm, a top diameter of 80 nm, and a height of 150 nm, as shown in Figures 4.1a,b. The array is fabricated on fused silica using substrate conformal imprint lithography and reactive ion etching, as this technique allows fabrication over large areas with high reproducibility.[113] The extinction spectrum of the array shows two peaks that both overlap with the emission of the caged dye[114] that is used as the fluorescent probe in our study, as shown in Figure 4.1c (see the Methods section 4.5 of this chapter and Figure 4.5). To gain more physical insight into the resonances associated with these peaks, we use FDTD simulations to obtain electric field distributions at the two peaks' wavelengths (see Methods section 4.5 and Figure 4.6). The resulting electric field distributions demonstrate the distinctive characteristics of both resonances: the broad resonance centered at 655 nm shows fields that are highly localized to the nanoparticle surface (Figures 4.1d,e) and we will therefore refer to it as the LSPR. Note that this LSPR is still a hybrid plasmonic-photonic mode, as its dispersion is not fully flat,[115] and therefore does not correspond to the localized surface plasmon resonance of the individual nanoparticles, which is expected to be much broader.[116] The narrow resonance centered at 580 nm, contrary to the LSPR, shows fields that extend far into the surrounding medium (Figures 4.1f,g) and we will therefore refer to it as the SLR. A detailed description of the origin of these lattice resonances and their electromagnetic properties was already provided in previous work.[115–118] In many other systems based on plasmonic particle arrays, quasiguided modes are also supported,[119] as a high index polymer layer on top of the array can serve as a waveguide. For simplicity, we suppress these modes by using a polymer with a refractive index lower than that of the immersion oil of the microscope objective.

While our microscopy technique allows for a resolution of ∼20 nm in the x,y-plane of the sample, we also achieve sub-diffraction resolution in the z-direction by confining the dye molecules to a 50 nm thick layer, placed at a height at which it spatially overlaps with the electric field distribution of the LSPR or the SLR.[115]

To investigate the effect of the LSPR on single molecule emission (sample S1 in Figure 4.1h), we place a 50 nm thick dye-doped polymer layer at the bottom of the nanostructures (z = 0-50 nm), as this position maximizes the overlap with the field in Figure 4.1d. To investigate the effect of the SLR (sample S2 in Figure 4.1i), we place a dye layer at z = 250-300 nm, where it overlaps with the extended field in Figure 4.1f. The Methods section 4.5 of this chapter describes the fabrication of these multi-layered polymer structures.

4.3.2 Localizing and simulating single emitters coupled to a plasmonic particle array

The samples are imaged in an inverted optical fluorescence microscope, as illustrated in Figure 4.2a. At the beginning of each experiment, we first take a transmitted white light image of the array. From this image we localize all nanostructures in the field-of-view of 133 µm by 133 µm by fitting all local maxima in the image to a two-dimensional Gaussian.[75] Due to the high signal-to-noise ratio that can be achieved in the transmitted light image, this fitting procedure results in an estimated localization precision of 7 nm in the x,y-plane of the sample.[75,77] After acquiring

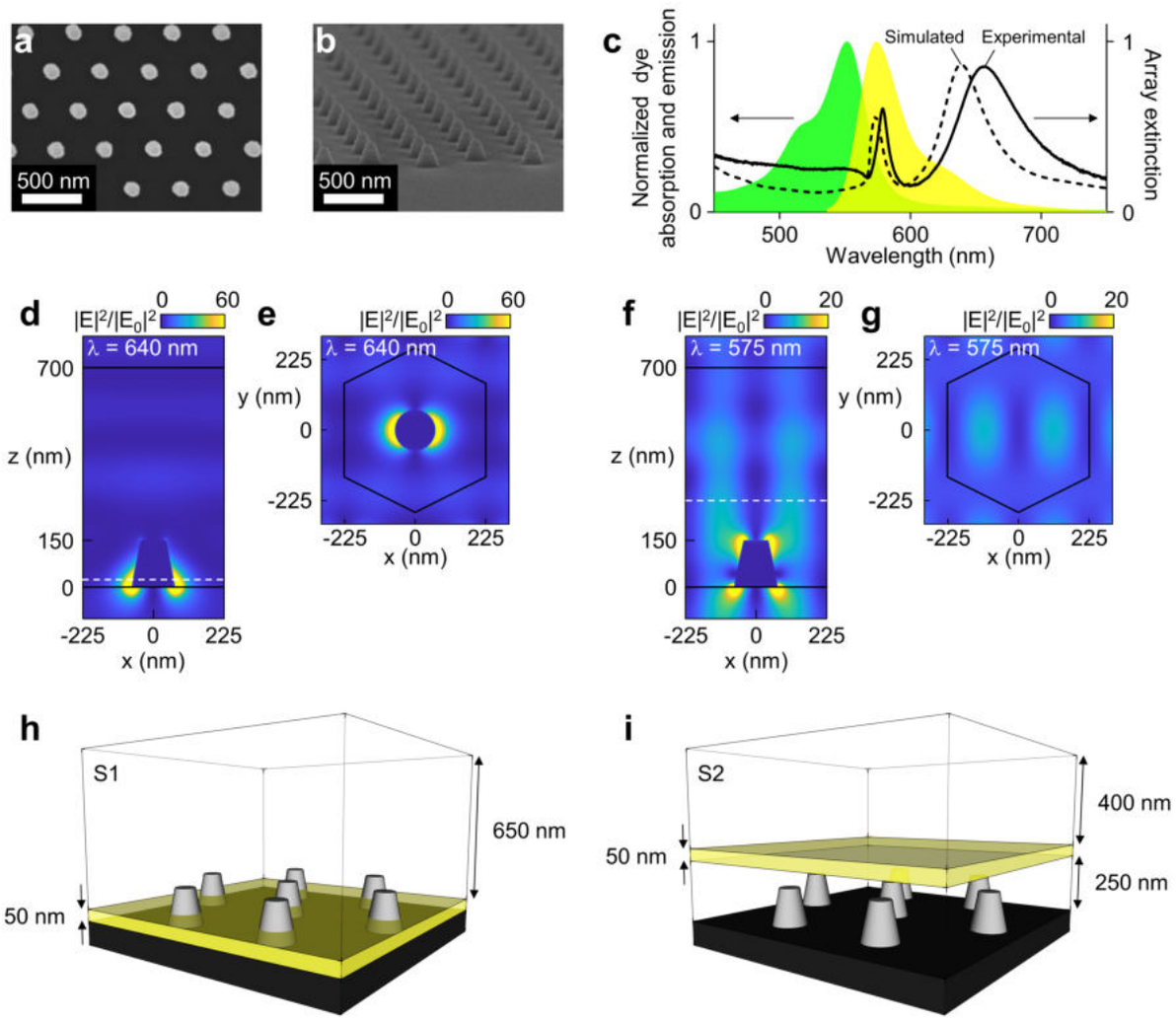

Figure 4.1: Design and optical properties of the investigated samples.(a) Top view scanning electron microscope (SEM) image of the hexagonal array of aluminum nanostructures. (b) Side view SEM image of the same array. (c) Experimental (solid line) and simulated (dashed line) extinction spectra of the array and normalized absorption (green) and emission (yellow) spectra of the dye in the uncaged state. The absorption and emission spectra were obtained from the dye manufacturer.[114] (d) Simulated (x,z) spatial distribution of the electric field intensity $|E|^2$ normalized to the incident field $|E_0|^2$ at the wavelength corresponding to the LSPR in the simulated extinction spectrum, $\lambda_{LSPR} = 640$ nm. Dielectric interfaces are marked using black lines. (e) Same as (d), but monitored in the (x,y) plane at z = 25 nm, as marked by the dashed white line in (d). The black hexagon marks the unit cell of the array. (f) Same as (d), but for the wavelength corresponding to the SLR, $\lambda_{SLR} = 575$ nm. (g) Same as (f), but monitored in the (x,y) plane at z = 275 nm, as marked by the dashed white line in (f). (h) Schematic of sample S1: the transparent box indicates a dye free PMMA layer (n = 1.49) and the yellow box indicates a 50 nm thick PVP layer (n = 1.56) at z = 0 - 50 nm doped with a caged dye. (i) Schematic of sample S2: same as sample S1, but with the PVP layer containing the dye placed at z = 250 - 300 nm.

the transmitted light image, the sample is illuminated with a 532 nm cw laser to image the fluorescence, as illustrated in Figure 4.2a. Throughout the experiment we correct for in-plane drift by tracking fluorescent impurities and for out-of-plane drift by using a built-in focus correction system.

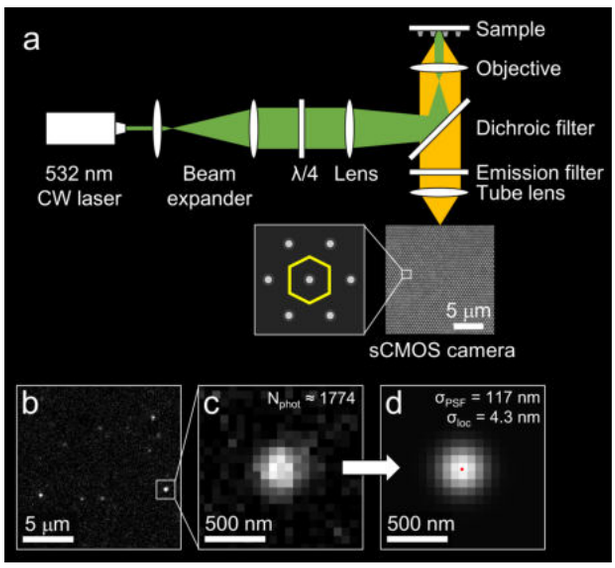

Figure 4.2: Super-resolution localization of single emitters coupled to a plasmonic particle array. (a) Schematic depiction of the setup: the sample is illuminated at normal incidence with a 532 nm cw laser through the objective of a fluorescence microscope and the emission is imaged on a sCMOS camera. The sCMOS camera image is a cropped transmitted white light image of the plasmonic particle array. The zoom-in drawing schematically illustrates the hexagonal unit cell of the array (yellow hexagon). (b) 250 × 250 pixel cut-out of an example frame of a fluorescence measurement on sample S2 after background subtraction, showing multiple single emitters in the field of view. (c) Zoom of (b), showing the diffraction-limited emission profile of one emitter. The number of photons N_{phot} in each fluorescent event is calculated from the number of photoelectrons per camera count. (d) Two-dimensional Gaussian fit of the emission profile in (c). The fitted molecule position, defined as the center of the 2D Gaussian, is illustrated with the red dot. For this particular event, the width of the fitted Gaussian σ_{PSF} is 117 nm and the estimated localization precision σ_{loc} is 4.3 nm.

The dye-doped polymer layers contain a caged dye,[114] which only becomes fluorescent upon illumination. Using caged dyes allows for a high concentration of dye in the layer, while maintaining a low density of fluorescent events in a single frame, see for example Figure 4.2b. By keeping the number of fluorescent events per frame low, we can assume that the observed diffraction-limited spots are single molecules, see section 3 of the Supporting Information. We localize these stochastic bursts of single molecule fluorescence by fitting them to a two-dimensional Gaussian, see Figures 4.2c,d. This fitting procedure results in an estimated localization precision of 15 nm for measurements on sample S1 and 11 nm for measurements on sample S2. As the estimated localization precision scales with $1/\sqrt{N_{\mathrm{phot}}}$,[75] where N_{phot} is the number detected of photons, the slightly worse localization precision for sample S1 is due to the worse overlap of the dye emission with the LSPR, see Figure 4.1c. Since we detect molecules over a large field-of-view, we can average over thousands of nanostructures by redefining the positions of all molecules relative to their nearest nanostructure. This procedure results in all molecule positions falling in a single unit cell, as indicated by the yellow hexagon in Figure 4.2a. The total estimated localization precision now becomes the sum of the error in localizing the nanostructures and the error in localizing the molecules, resulting in 22 nm for sample S1 and 18 nm for sample S2. A more detailed description of the setup and the image processing can be found in the Methods section 4.5 of this chapter and section 4.6.4 of this chapter's supporting information.

For each molecule, we also measure the emission intensity as the total number of detected photons. From all intensities, we can then build a two-dimensional map of the emission intensity as a function of emitter position, where the bin sizes are equal to the estimated localization precision. This map is subsequently normalized with the mean intensity of a molecule detected outside of the array to obtain the experimentally observed enhancement in emission intensity I_{exp}.

The measured changes in intensity are a superposition of modifications in the absorption rate of the dye, their spontaneous decay rate, and the directivity of their emission. To disentangle these contributions, we compare our measurements to FDTD simulations of single electric dipoles coupled to a finite plasmonic particle array (see Methods section 4.5and section 4.6.5 of this chapter's supporting information). The simulated enhancement in emission intensity I_{sim} is obtained by performing a near-field to far-field transformation on the field monitored in the direction of the objective, in which we neglect all waves propagating at angles that fall outside the numerical aperture of the objective of our microscope (NA = 1.4).

From the three underlying contributions, we neglect modifications in the absorption rate, as the laser wavelength of 532 nm is not resonant with the array, see Figure 4.1c. We quantify the modification in spontaneous decay rate by monitoring the Purcell factor F_P, which corresponds to the enhancement in the total power radiated by the dipole. As the system investigated here contains aluminum, which is lossy at optical wavelengths, not all photons emitted by the dipole radiate to the far-field. To quantify these losses in the metal, we also monitor the enhancement in total power radiated to the far-field F_{rad}. We define the directivity enhancement D from these simulated values as the ratio between I_{sim} and F_{rad}, as F_{rad} considers the enhancement in all power radiated to the far-field and I_{sim} only the enhancement in the power radiated towards the objective. Since the directivity enhancement D is calculated from I_{sim}, the resulting values for D are also defined for an NA of 1.4.

4.3.3 Enhanced emission of single molecules coupled to a plasmonic particle array

Since sample S1 contains dye molecules preferentially coupled to the LSPR, we use an emission filter that transmits at the LSPR wavelength, see dashed line in Figure 4.3a. In this sample we observe strong intensity enhancements of up to ∼100% for positions corresponding to the center of a nanostructure, as shown in Figure 4.3b. Although no dye molecules can be present inside the metallic nanostructures, their apparent position in the far-field can be located at the center of the unit cell due to mislocalization effects:[120,121] when a dye molecule is close to a nanostructure, it can excite the LSPR of the nanostructure, which can subsequently radiate to the far-field. This effect results in the fitted position of the molecule being 'pulled' towards the nanostructure. Although the amount of mislocalization decreases with increasing emitter-nanostructure separation, it can still be present for separations of several tens of nanometers.[120] Due to the localized nature of the LSPR, molecules that are close to a nanostructure experience both a strong emission enhancement and strong mislocalization, resulting in the intensity peak at the center of Figure 4.3b.

The simulated far-field intensity I_{sim} agrees well with the experiment, showing high intensity for dipoles close to a nanostructure, see Figure 4.3c. The contributions leading to this enhanced emission can be evaluated by comparing Figures 4.3d-f. Since in this sample some emitters are at nanometer distance from a nanostructure, the change in spontaneous decay rate can become significant.[122] Our simulations confirm this observation, showing Purcell factors up to 5 for small emitter-nanostructure distances, see Figure 4.3d. Despite such high enhancements, the power radiated to the far-field shows lower peak values, see Figure 4.3e. This decrease indicates that although the molecule experiences strong emission enhancement, a substantial fraction is absorbed by the nanostructures.[96] For small emitter-nanostructure distances we also observe en-

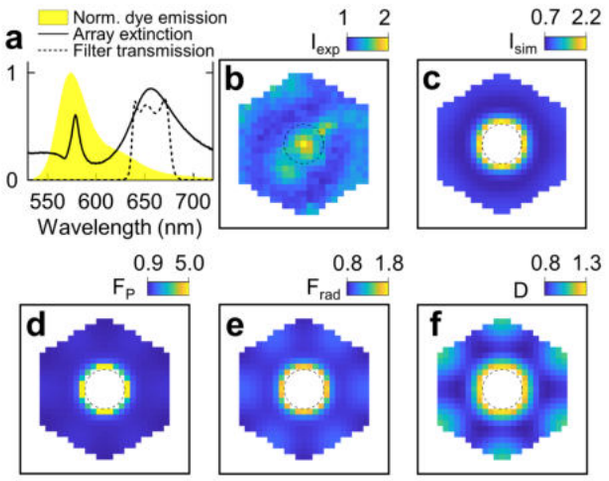

Figure 4.3: Enhanced emission of single molecules coupled to the LSPR. (a) Normalized dye emission (yellow), array extinction (solid line), and emission filter transmission (dashed line). (b) Two-dimensional histogram of the experimentally observed emission enhancement I_{exp}. Simulated (c) emission enhancement I_{sim}, (d) Purcell factor F_P, (e) enhancement in power radiated to the far-field F_{rad}, and (f) directivity enhancement D. Figure (b) has 22×22 nm^2 bins and Figures (c-f) have 20×20 nm^2 bins. The dashed lines denote the base of the nanostructure.

4

hanced directivity, see Figure 4.3f. As can be seen when comparing the maximum values in panels e and f of Figure 4.3, the emission enhancement in this sample is a superposition of a modified spontaneous decay rate and a slight change in directivity. We also perform a control measurement on sample S1 with an emission filter that targets the SLR wavelength and we simulate the emission enhancement at the same wavelength (see Figure 4.11). Interestingly, we obtain a similar emission enhancement map as in Figure 4.3b, due to the similar spatial profile of the near-fields at the bottom of the nanoparticles for both the SLR and LSPR (see Figures 4.1d and 4.1f).

In sample S2 the emitters preferentially couple to the SLR and we therefore map their emission using a filter that transmits at the SLR wavelength, see dashed line in Figure 4.4a. In contrast to sample S1, which shows highly localized emission enhancement, we now observe a much more fine structure in the intensity map, see Figure 4.4b. The highest enhancement is observed at the corners of the unit cell, where the distance to a nanostructure is maximal. The simulations of the far-field intensity I_{sim} accurately reproduce this feature, as shown in Figure 4.4c. However, the relative weights of the underlying contributions have now shifted substantially. The Purcell factor F_P shows values around unity across the whole unit cell of the array, see Figure 4.4d, indicating negligible change in the spontaneous decay rate. This observation can be understood from the fact that the Purcell factor scales with the ratio between the quality factor and the mode volume of the resonance.[93] Even though the quality factor is larger for the SLR than for the LSPR, see Figure 4.1c, the SLR is not confined to the nanostructure surface, see Figure 4.1f. In other words, due to its extended volume, the SLR has minimal influence on an emitter's spontaneous decay rate. The power radiated to the far-field shows values similar to the Purcell factor, see Figure 4.4e, indicating low absorption in the metal due to the large emitter-nanostructure separation in this sample. In contrast to F_P and F_{rad} both showing values around unity, the directivity is enhanced over the whole unit cell of the array due to constructive interference of radiation directed towards the objective, see Figure 4.4f. From these observations we can conclude that, while SLRs cannot be used to enhance the spontaneous decay rate of emitters, they could be exploited in applications where enhanced directivity over large volumes is required.

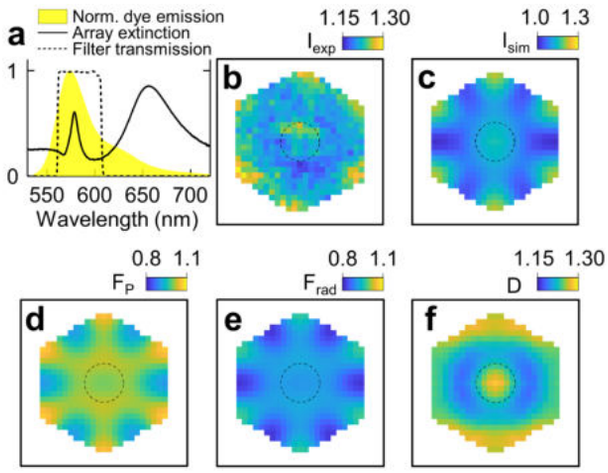

Figure 4.4: Enhanced emission of single molecules coupled to the SLR. (a) Normalized dye emission (yellow), array extinction (solid line), and emission filter transmission (dashed line). (b) Two-dimensional histogram of the experimentally observed emission enhancement I_{exp}. Simulated (c) emission enhancement I_{sim}, (d) Purcell factor F_P, (e) enhancement in power radiated to the far-field F_{rad}, and (f) directivity enhancement D. Figure (b) has 18 × 18 nm^2 bins and Figures (c-f) have 20 × 20 nm^2 bins. The dashed lines denote the base of the nanostructure.

For sample S2 we also perform control measurements and simulations, now at the LSPR wavelength (see Figure 4.12). Interestingly, the extended nature of the SLR is now lost, as the enhancement remains limited to molecules in the middle of the unit cell. While both F_P and F_{rad} remain largely unchanged due to the large emitter-nanostructure separation, the directivity enhancement D shows values up to ∼1.8 for molecules placed right above a nanostructure. Such directivity enhancement is due to light emitted towards the underlying nanoparticle and reflected back into the objective. A similar directivity enhancement is in fact expected for the case of emitters placed above individual aluminum particles (see section 4.6.8 in this chapter's supporting information).

To further investigate the collective nature of the lattice resonances and their influence on single molecule emission, we compare our experiments and simulations on extended arrays to simulations on a single nanostructure. As can be seen in Figures 4.13 and 4.14, simulations of dipoles coupled to a single particle can describe most behavior observed in sample S1, both at the SLR and the LSPR wavelength. This result can be understood from the fact that emission enhancement in this sample mostly happens when the dipole is very close to the surface of a nanostructure, where it is not influenced by other nanostructures far away. The emission enhancement we experimentally observe on sample S2, however, is described poorly by simulations on a single particle, see Figures 4.15 and 4.16. The emission enhancement at the unit cell corners observed in Figure 4.4b is not reproduced with a single particle, confirming that this is indeed the result of constructive interference between the scattering from multiple particles. Further discussion on the comparison between the results on the extended array and those on a single particle can be found in section 4.6.8 in this chapter's supporting information.

4.4 Conclusion

We have demonstrated how stochastic super-resolution microscopy in conjunction with FDTD simulations can be used to study the enhanced emission of single molecules coupled to a plasmonic particle array at the nanometer scale. Combining these methods enables us to disentangle and quantify the different mechanisms leading to the observed emission enhancement. We find that

although plasmonic particle arrays have resonances with fields extending far into the surrounding medium, their ability to influence the spontaneous decay rate of an emitter remains limited to small emitter-nanostructure separations. Instead, collective resonances allow us to engineer the radiation pattern of an emitter to obtain directional emission. Our approach of experimentally mapping emission enhancement with sub-diffraction resolution and numerically disentangling the underlying contributions can inform the rational design of optical devices based on plasmonic particle arrays.

4.5 Methods

4.5.1 Fabrication of multi-layered polymer structures

Multi-layered polymer structures are fabricated by using combinations of polymers and solvents that do not affect each other. We use polymethylmethacrylate (PMMA, Molecular Weight ∼350,000 g/mol) with a refractive index of 1.49 dissolved in toluene for the polymer layers without dye and polyvinylpyrrolidone (PVP, Molecular Weight ∼360,000 g/mol) with a refractive index of 1.56 dissolved in 2-propanol for the layers with dye. For the extinction spectrum shown in Figure 4.1c, we use a single layer of polyvinylacetate (PVAc, Molecular Weight ∼500,000 g/mol, dissolved in acetonitrile) with a refractive index of 1.48.

For both samples, the 50 nm thick PVP layer is obtained by spin coating a 1 wt.% solution at 4000 rpm. For sample S1, the 650 nm thick PMMA layer is obtained by spin coating a 6 wt.% solution at 1000 rpm. For sample S2, the bottom 250 nm thick PMMA layer is obtained by spin coating a 4 wt.% solution at 1700 rpm and the top 400 nm thick layer by spin coating a 4 wt.% solution at 600 rpm. The spin coating time is set to 1 minute and the acceleration to 500 rpm/s for all layers.

As can be seen in Figure 4.5, the resonance wavelengths remain unchanged when changing between polymer layers, due to the small thickness of the PVP layer and the small difference in refractive index between PVAc (used for the extinction spectrum in Figure 4.1c) and PMMA (used for the super-resolution measurements).

4.5.2 Extinction measurements

To obtain the extinction spectrum in Figure 4.1c, a fiber coupled laser-based white light source (Energetiq LSDS) is first collimated using a lens. The sample is placed at normal incidence with respect to the collimated beam and the transmitted light is collected with a lens focused on a multimode fiber (Ocean Optics QP600-2-VIS/BX) connected to a spectrometer (Ocean Optics USB2000+). A drop of immersion oil is placed on top of the polymer to mimic the oil-immersion objective that is used for the super-resolution measurements.

The extinction is defined as $1 - T/T_{\text{source}}$, where T is the collected spectrum when the beam passes through the array and T_{source} the collected spectrum when the beam passes through an empty part on the same substrate.

4.5.3 FDTD simulations of electric field distributions

All simulations are performed using "FDTD Solutions" by Lumerical.[123] The hexagonal periodicity of the array is introduced in the simulations by placing two nanostructures as shown in Figure 4.6 and by applying periodic boundary conditions. The nanostructures are defined as truncated cones with the dimensions mentioned in the manuscript (150 nm high, 80 nm diameter at the top, and 140 nm diameter at the bottom). The 700 nm thick polymer layer is defined as a lossless dielectric with a refractive index of 1.48 and literature values are used for the complex dielectric function of aluminum and fused silica.[43] The background index is set to that of the immersion oil, 1.52. A plane wave source polarized along the x axis is injected from the top (pointing from the immersion oil to the substrate) and the resulting electric field distribution is monitored in the (x,z) plane and the (x,y) plane.

4.5.4 Super-resolution measurements

Due to the finite absorption at 532 nm of the dye in its caged state and the high absorption at the same wavelength in the uncaged state,[114] one 532 nm cw laser (CNI MGL-FN-532) is used to

both uncage and localize the dye. The concentration of dye (300 nM in the solution used for spin coating) and laser power density (6.4 W mm^{-2}) are optimized to give a low enough activation rate («1 per μm^2 in any given frame) while retaining high signal-to-noise ratio.

The setup illustrated in Figure 4.2a is based around a Zeiss AxioObserver 7 inverted optical fluorescence microscope. The laser beam is expanded using two lenses and its polarization is changed to circular using a $\lambda/4$ plate. The beam is then focused on the back focal plane of the oil-immersion objective (Zeiss Plan-Apochromat 63x/1.4 Oil DIC M27), resulting in illumination normal to the sample.

For the measurement on sample S1 a longpass dichroic filter is used (Chroma AT565DC) with a bandpass emission filter that transmits $\lambda = 650 \pm 20$ nm (Thorlabs FB650-40). For the measurement on sample S2 a custom made dichroic filter is used (Semrock, reflection at $\lambda = 532$ nm and transmission from $\lambda = 550$ nm to $\lambda = 700$ nm) with a bandpass emission filter that transmits $\lambda = 585 \pm 20$ nm (Semrock 585/40 BrightLine).

The signal is imaged on a Hamamatsu ORCA-Flash 4.0 V3 sCMOS camera with 2048 × 2048 pixels and an effective pixel size of 64.5 nm (6.5 µm physical size, used with a 63× magnification objective and an additional 1.6× magnification in the body of the microscope). The integration time is 100 ms and for each experiment 10,000 frames are acquired. The Gaussian fitting is performed in ThunderSTORM.[77] The image processing is described in more detail in section 4.6.4 in this chapter's supporting information.

4.5.5 FDTD simulations of single dipoles

The enhanced emission of single molecules is simulated by placing an electric dipole in a finite array of nanostructures. Using periodic boundary conditions is no longer appropriate for these simulations, as this would imply having dipole sources coherently emitting at the same position in each unit cell. The finite array consists of 20 × 20 nanostructures and the z-coordinate of the dipole is in the middle of the dye layer, i.e. z = 25 nm for sample S1 and z = 275 nm for sample S2, measured from the substrate.

The Purcell factor F_P is obtained by monitoring the radiated flux out of a box surrounding only the dipole. The enhancement in power radiated to the far-field F_{rad} is obtained with a box surrounding the whole particle array. The transmission through these monitors is normalized to a simulation without nanostructures and averaged over three orthogonal dipole orientations. The resulting values are directly plotted in Figures 4.3d, 4.3e, 4.4d, and 4.4e. Because of symmetry, simulations are only performed for dipole positions in the first quadrant (positive x and y coordinates) and the results are mirrored to obtain the whole unit cell.

The far-field intensity enhancement I_{sim} is obtained by performing a near-field to far-field transformation on the field monitored above the dipole. All waves propagating at angles higher than the NA of the objective are then filtered out and the remaining waves are projected on an image plane. The resulting far-field emission profile is pixelated to mimic the finite-sized pixels of the camera (see Figures 4.9 and 4.10). The far-field intensity I_{sim} plotted in Figures 4.3c and 4.4c is defined as the sum over all pixels in an 11 × 11 pixel region around the center (see Figure 4.10), normalized to a simulation without nanostructures and averaged over three orthogonal dipole orientations.

The directivity enhancement D plotted in Figures 4.3f and 4.4f is defined as I_{sim} divided by F_{rad}, as F_{rad} considers all power radiated to the far-field and I_{sim} only the power radiated towards the objective.

4.6 Supporting information

4.6.1 Extinction spectra of all the samples

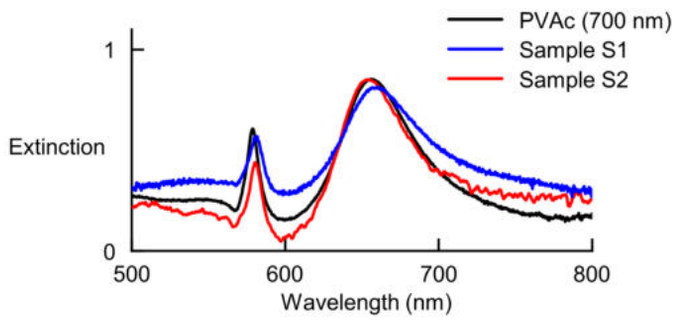

Figure 4.5: Extinction spectra of the array covered with different combinations of polymers. The array covered with 700 nm PVAc is used for the extinction spectrum shown in Figure 4.1c.

4.6.2 FDTD simulations of the electric field distributions

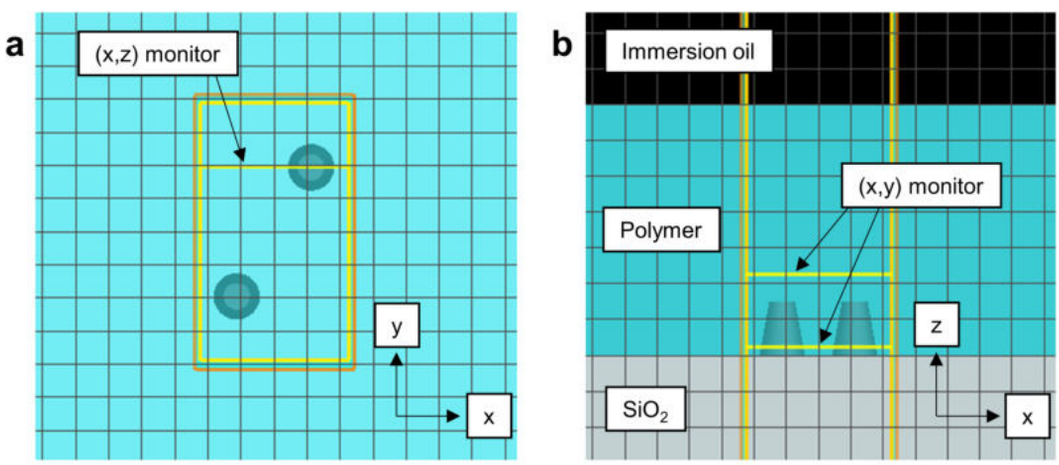

Figure 4.6: Design of the FDTD simulations presented in Figures 4.1d-g, shown in the (a) x,y-plane and (b) in the x,z-plane. Some components (e.g. the plane wave source and the additional mesh around the nanostructures) have been hidden for clarity. A transmission monitor is placed in the SiO_2 to obtain the simulated extinction spectrum in Figure 4.1c.

4.6.3 The observed diffraction-limited spots are single molecule events

The field-of-view of our camera is 133 µm by 133 µm and every diffraction-limited spot fills an area A equal to

$$A = \pi \left(1.22 \frac{\lambda}{2\,NA}\right)^2 = 2.03 \cdot 10^{-13}\,\mathrm{m}^2,$$

where λ is the emission wavelength (584 nm) and NA the Numerical Aperture of the microscope objective (NA = 1.4).

The total number of diffraction-limited sites k in our field-of-view then is

$$k = \frac{(133 \cdot 10^{-6})^2}{2.03 \cdot 10^{-13}} = 8.70 \cdot 10^4$$

If we now start distributing n molecules randomly over the field-of-view, the probability that a molecule A and a molecule B are exactly in the same position equals $1/k$, so the probability that these two molecules are not in the same position is 1-1/k.

The probability p that molecule A is not in the same position as all other n-1 molecules then becomes

$$p = \left(1 - \frac{1}{k}\right)^{n-1}$$

This allows us to calculate the expectation value E for the number of molecules that do not share their position with another molecule:

$$E = np = n\left(1 - \frac{1}{k}\right)^{n-1}$$

If we now were to distribute $n = 200$ molecules, we would find that $E = 199.54$. As the typical number of events in a frame is around 200, we can treat our experimentally observed diffraction-limited spots as single molecule events with $> 99\%$ certainty.

4.6.4 Image processing for super-resolution measurements

Background subtraction

After acquisition the images are background subtracted with a Python script. The background of a frame i is defined as the average over frames $i-100$ to $i+100$, excluding frame i itself. For the frames at the beginning and end of the experiment, the background range is reduced accordingly, e.g. the background of frame $i = 53$ is the average of frames 1 to 153, again excluding frame 53 itself.

Filtering and fitting

After background subtraction, the image is filtered in the software package ThunderSTORM[77] using a wavelet filter. This filter splits the image into different wavelet levels, each containing a different range of spatial frequencies. The first level mainly contains the high frequency components of the image including noise. As the level increases, the spatial frequencies of the components become lower and lower. The filter is set as recommended by Ref. 78 and the second wavelet level is used for further analysis.

The next step is to find local maxima in the filtered image. A pixel is considered a local maximum when the following criteria are met:

- The intensity of the pixel is the highest in an 8-connected neighborhood, i.e. in a 3×3 pixel square.
- The intensity of the pixel is higher than a user-specified threshold. Since the points that are to be fitted must lie above noise level in order to obtain good fits, it is useful to look at the first wavelet level. After all, the first wavelet level contains most of the noise and therefore can be used to make a quantitative description of when signal can be considered 'above noise level'. Typically, a good threshold lies between 0.5 and 2 times the standard deviation of the first wavelet level. Using high threshold values will result in less false detections at the expense of more missed molecules and vice versa. For measurements on sample S1 a threshold of 1.5 times the standard deviation is used and for the measurements on sample S2 2 times is used.

The local maxima and the surrounding pixels are subsequently fitted to a Gaussian function using maximum likelihood estimation, again using ThunderSTORM.[77] A fitting radius of 5 pixels is used, i.e. all pixels with a distance $\leq$5 pixels from a local maximum are included in the fitting procedure. Since the emission profile of a molecule is pixelated by the camera, we use an integrated Gaussian as a fitting function.

The localization precision σ_{loc} can be estimated by:[75,77]

$$\sigma_{\text{loc}}^2 = \frac{\sigma_{\text{PSF}}^2 + a^2/12}{N} + \frac{8\pi\sigma_{\text{PSF}}^4 b^2}{a^2 N^2},$$

where σ_{PSF} is the standard deviation of the fitted Gaussian, a the effective pixel size (64.5 nm), N the number of detected photons, and b the standard deviation in the residuals between the experimental emission profile and the fit.

Calculating σ_{loc} for all events results in the histograms in Figure 4.7. The total localization precision used for defining the bin sizes in Figure 4.3b and 4.4b of the manuscript is the peak value in Figure 4.7 for the nanostructures plus the peak value for the emitters.

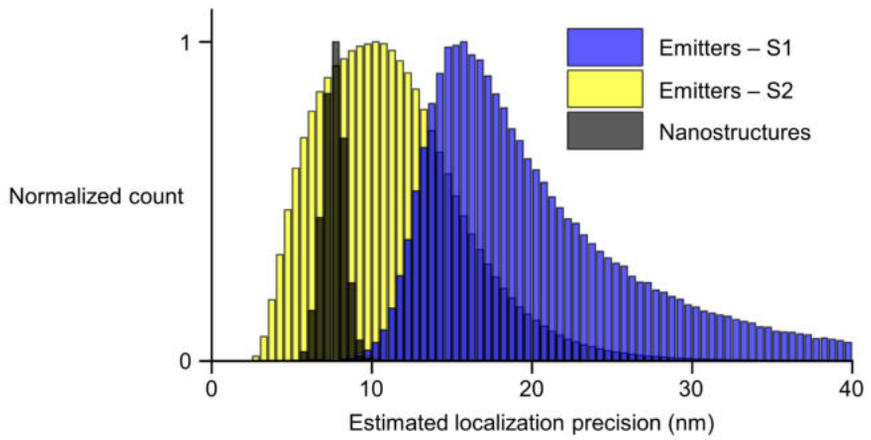

Figure 4.7: Histograms of the estimated localization precision for (blue) the positions of the emitters in sample S1, (yellow) the positions of the emitters in sample S2, and (black) the positions of the nanostructures.

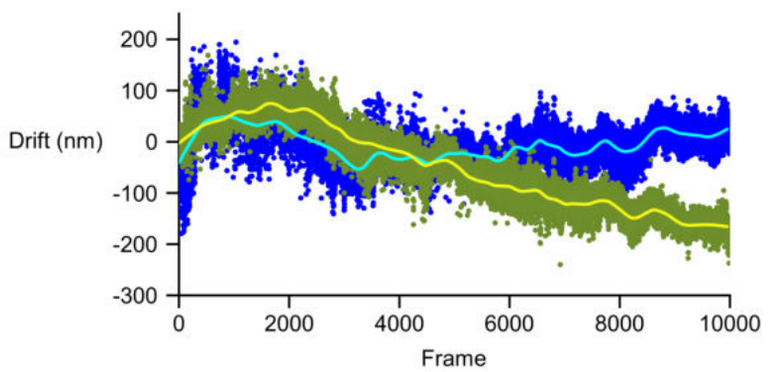

Figure 4.8: Drift markers (blue dots for x coordinates, green dots for y coordinates) and drift trajectory (light blue line for x, yellow line for y) for the experiment on sample S2.

Drift correction

Each experiment consists of 10,000 frames and therefore takes several tens of minutes to acquire, during which the sample might drift. Drift in the vertical direction, which would let the sample drift out of focus, is corrected for by the Definite Focus correction system of the Zeiss AxioObserver 7 microscope. This system continuously measures changes in the path length between the objective and the sample using an 850 nm LED and adjusts the focus accordingly.

Drift in the lateral direction is corrected for in post processing using ImageJ and ThunderSTORM.[77] In the raw data, i.e. before background subtraction, there are always some constant fluorescent impurities. These are fitted to two-dimensional Gaussians and can then be used to form a drift trajectory, see for example Figure 4.8. This trajectory is subsequently applied to the coordinates acquired on the background subtracted data.

Post processing

As the Gaussian fitting procedure is also applied to a transmitted light image of the array, two lists of coordinates are obtained: one list containing the positions of all emitters and one containing the positions of all nanostructures. For every emitter the coordinate of the nearest nanostructure is found using Matlab and the relative coordinate of the emitter is then defined as the coordinate

of the emitter minus the coordinate of the nearest nanostructure. This results in all relative coordinates falling into the unit cell of the array (see zoom-in drawing in Figure 4.2a). These relative coordinates allow us to make a two-dimensional histogram of the number of molecules M detected in a certain position in the unit cell, where the bin size is set equal to the estimated localization precision.

Every bin in the abovementioned histogram contains a list of molecules with an intensity I_i defined as the number of detected photons in the event, where the number of photons is calculated from the number of photoelectrons per camera count and $i = 1, 2, \ldots, M$. We now define a mean intensity $\bar{I}$ equal to

$$\bar{I} = \frac{\sum_{i=1}^{M} I_i}{M}$$

This calculation is done for every bin in the two-dimensional histogram (i.e. M and the list I_i are different for each bin), resulting in a spatial distribution of mean molecule intensities. This histogram is subsequently normalized to the mean intensity of a molecule detected outside of the array, resulting in the experimentally observed intensity enhancement I_{exp}.

4.6.5 Simulating the far-field intensity

An example of the emission profiles resulting from the near-field to far-field transformation can be found in Figure 4.9. To mimic the finite-sized pixels of the sCMOS camera, the simulated emission profiles are also pixelated with 64.5 nm pixels resulting in, for example, Figure 4.10. The far-field intensity I_{sim} is defined as the sum over all pixels in an 11 × 11 pixel region around the center, normalized to a simulation without nanostructures and averaged over three orthogonal dipole orientations.

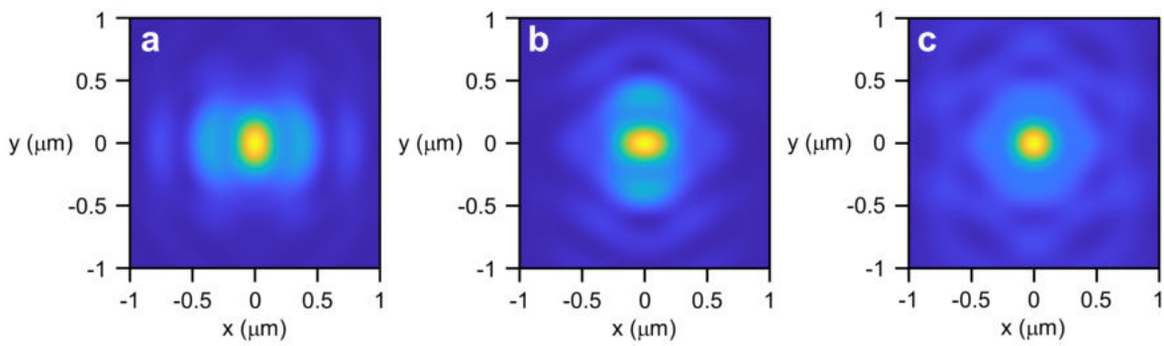

Figure 4.9: Emission profile obtained from performing a near-field to far-field transformation on the field monitored above the dipole. The dipole is orientated along the (a) x axis, (b) y axis, or (c) z axis.

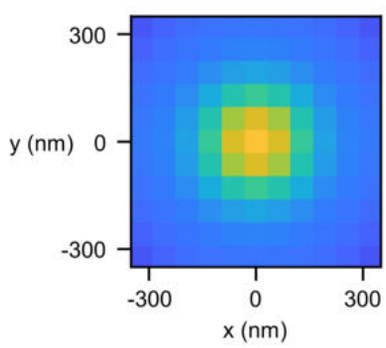

Figure 4.10: Pixelated emission profile (pixel size = 64.5 nm) of Figure 4.9c.

4.6.6 Sample S1 measured and simulated at the SLR wavelength

In sample S1 molecules are placed at the bottom of the nanostructures, see Figure 4.1h, where they preferentially couple to the LSPR. However, the SLR also has a significant electric field in this position, see Figure 4.1f. If we filter the emission in this sample at the SLR wavelength, see Figure 4.11a, we observe similar patterns as in Figure 4.3, see Figure 4.11: the emission is mainly enhanced when the emitter-nanostructure separation is small. This enhancement is the result of an enhanced spontaneous decay rate, which is slightly lower at this wavelength than at the LSPR wavelength, and an enhanced directivity, which is similar for both wavelengths.

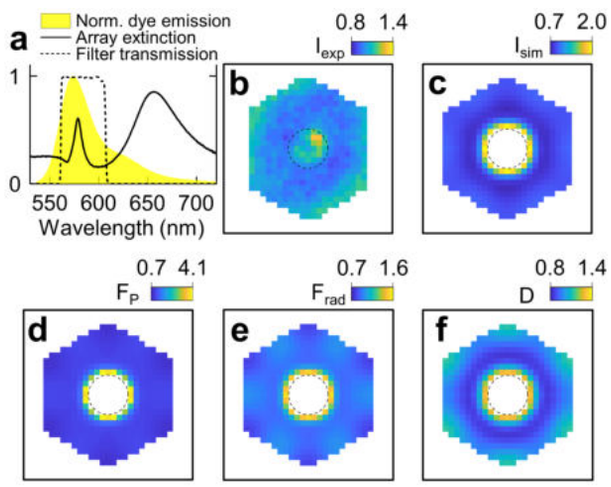

Figure 4.11: Enhanced emission of single molecules preferentially coupled to the LSPR, while filtering at the wavelength of the SLR. (a) Normalized dye emission (yellow), array extinction (solid line), and emission filter transmission (dashed line). (b) Two-dimensional histogram of the experimentally observed emission enhancement I_{exp}. Simulated (c) emission enhancement I_{sim}, (d) Purcell factor F_P, (e) enhancement in power radiated to the far-field F_{rad}, and (f) directivity enhancement D. Figures (b-f) have 20×20 nm^2 bins. The dashed lines denote the base of the nanostructure.

4.6.7 Sample S2 measured and simulated at the LSPR wavelength

In sample S2 molecules are placed 250 nm above the substrate, see Figure 4.1i in the manuscript, where they preferentially couple to the SLR. However, the emission at the LSPR wavelength can also be modified at this position due to the ability of the nanostructures to scatter and absorb light at this wavelength. If we filter the emission in this sample at the LSPR wavelength, see Figure 4.12a, we observe patterns that are very different from those in Figure 4.4, see Figure 4.12: the Purcell factor remains low due to the large emitter-nanostructure separation, but molecules that are placed right above a nanostructure experience a high directivity due to scattering by the underlying particle. This results in high far-field intensities in the middle of the unit cell, both in the experiment and the simulations. The extended nature of the SLR, however, is lost, as the enhancement remains limited to molecules in the middle of the unit cell.

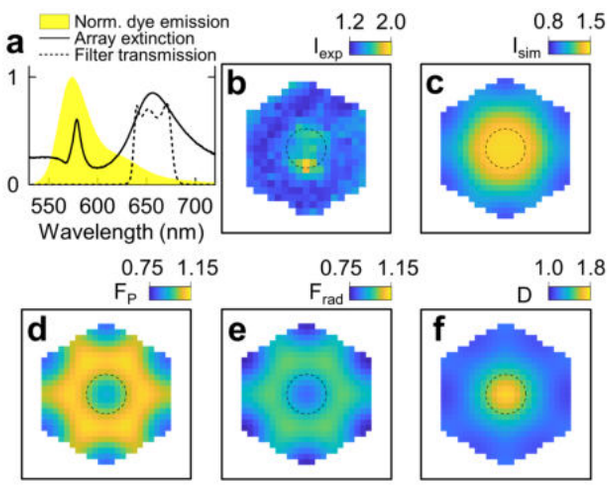

Figure 4.12: Enhanced emission of single molecules preferentially coupled to the SLR, while filtering at the wavelength of the LSPR. (a) Normalized dye emission (yellow), array extinction (solid line), and emission filter transmission (dashed line). (b) Two-dimensional histogram of the experimentally observed emission enhancement I_{exp}. Simulated (c) emission enhancement I_{sim}, (d) Purcell factor F_P, (e) enhancement in power radiated to the far-field F_{rad}, and (f) directivity enhancement D. Figure (b) has 25 × 25 nm^2 bins and Figures (c-f) have 20 × 20 nm^2 bins. The dashed lines denote the base of the nanostructure.

4.6.8 Simulations on single particles

Figures 4.13 and 4.14 compare the experimentally observed intensity enhancement on sample S1 to simulations on a full array and on a single particle. The wavelength corresponds to the SLR wavelength for Figure 4.13 and the LSPR wavelength for Figure 4.14. For both wavelengths the single particle simulations are able to reproduce most behavior observed on the full array, which can be understood from the fact that emission enhancement in this sample mostly happens when the dipole is very close to the surface of a nanostructure, where it is not influenced by other nanostructures far away. The only feature that is not captured well in the single particle simulations, is the enhanced directivity at the corners of the unit cell (compare Figure 4.13h with 4.13i and 4.14h with 4.14i), which is the result of scattering from multiple particles. This feature, however, does not result in an increased far-field intensity, as the Purcell factor is <1 in those same positions.

Figures 4.15 and 4.16 are the same as 4.13 and 4.14, but for sample S2. At the SLR wavelength (Figure 4.15), we experimentally observe high intensities at the corners of the unit cell. As mentioned in the manuscript, the Purcell factor shows values around unity due to the large mode volume of the SLR, whereas the directivity is enhanced over the whole unit cell. When simulating with a single particle, the maps for both F_P and F_{rad} (Figures 4.15e,g) are qualitatively different from those simulated on a full array (Figures 4.15d,f), but still show values around unity. The simulations on the full array only show a higher difference between F_P and F_{rad}, as the presence of more particles increases absorptive losses. A bigger mismatch is observed in the directivity (Figure 4.15i), which for a single particle is <1 in most of the unit cell, indicating a decreased directivity. This decrease results in a far-field intensity enhancement (Figure 4.15c) that is also <1 in most the unit cell and does not show the enhanced emission at the corners of the unit cell. Therefore, these simulations confirm that the observed emission enhancement in Figure 4.4 is the result of constructive interference between the scattering from multiple particles.

For sample S2 at the LSPR wavelength (Figure 4.16), we experimentally observe high intensities for molecules right above a nanostructure. As mentioned in section 4.6.7, this can be understood as scattering from the underlying particle. Although again qualitatively different, the maps for F_P and F_{rad} show values around unity for both the simulations on the full array (Figure 4.16d,f) and those on a single particle (Figure 4.16e,g). The directivity enhancement simulated on a single particle also shows a peak value of $\sim$1.8 at the center of the unit cell, indicating that the experimentally observed intensity enhancement in Figure 4.12b (same as Figure 4.16a) is dominated by scattering from the underlying particle.

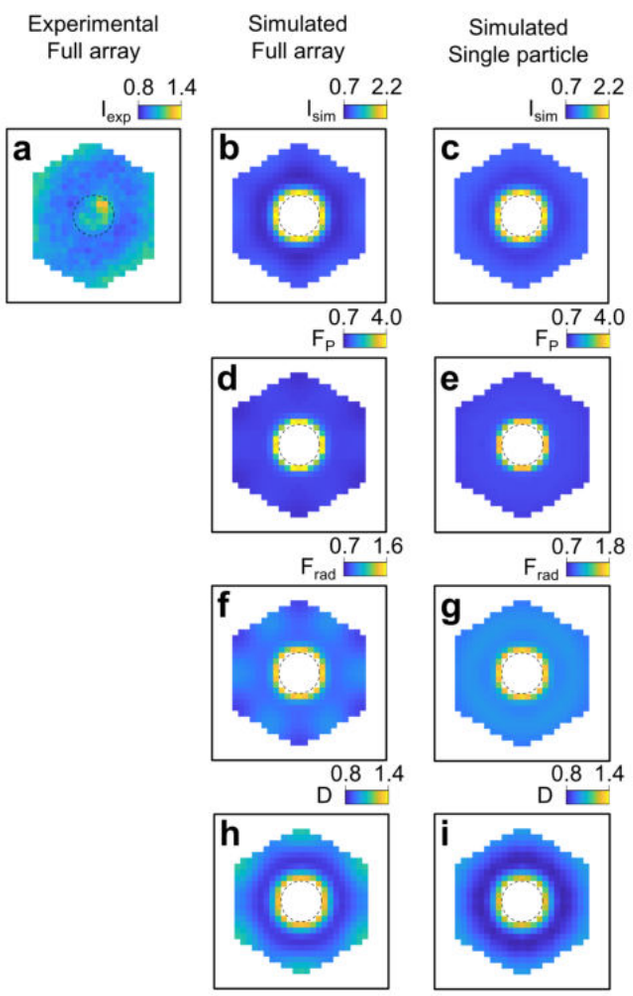

Figure 4.13: Experiment and simulations on sample S1 at the SLR wavelength. (a) Two-dimensional histogram of the experimentally observed emission enhancement I_{exp}. Simulated (b,c) emission enhancement I_{sim}, (d,e) Purcell factor F_P, (f,g) enhancement in power radiated to the far-field F_{rad}, and (h,i) directivity enhancement D. Figures (b,d,f,h) are simulated on an array of 20 × 20 particles and Figures (c,e,g,i) on a single particle. All panels have 20 × 20 nm^2 bins.

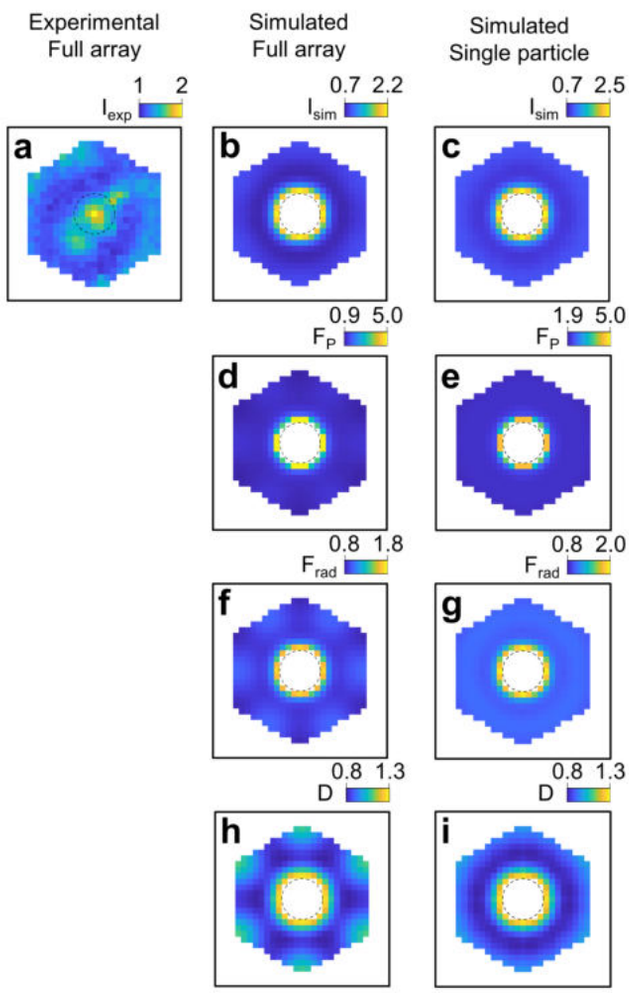

Figure 4.14: Same as Figure 4.13, but at the LSPR wavelength. Figure (a) has 22 × 22 nm^2 bins and Figures (b-i) have 20 × 20 nm^2 bins.

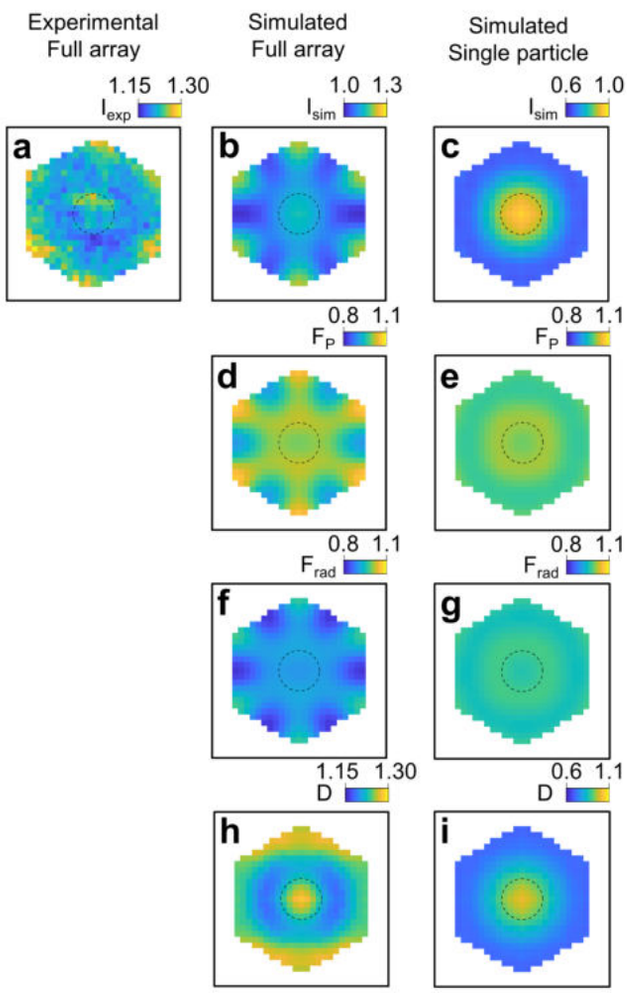

Figure 4.15: Same as Figure 4.13, but for sample S2 at the SLR wavelength. Figure (a) has 18 $\times$ 18 nm^2 bins and Figures (b-i) have 20 $\times$ 20 nm^2 bins.

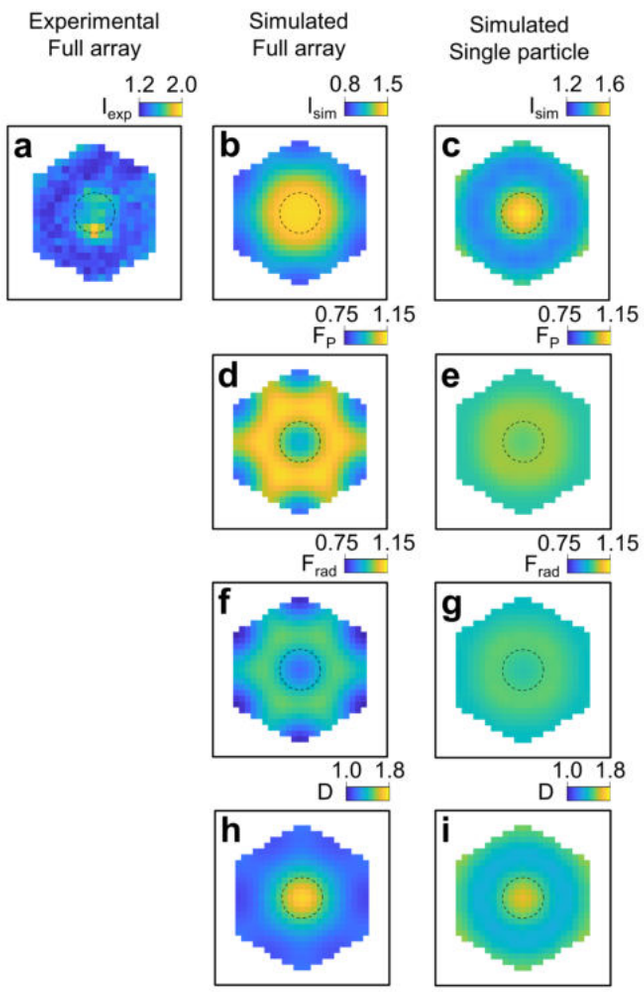

Figure 4.16: Same as Figure 4.13, but for sample S2 at the LSPR wavelength. Figure (a) has 25 $\times$ 25 nm^2 bins and Figures (b-i) have 20 $\times$ 20 nm^2 bins.

Chapter 5

Super-resolution mapping of a chemical reaction driven by plasmonic near-fields

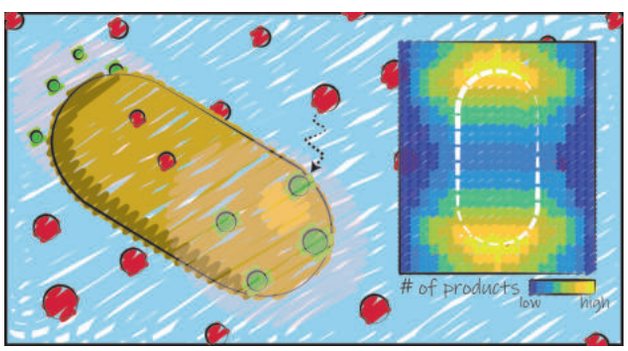

This chapter is based on Ref. 124: Nano Letters 2021, 21(5), 2149-2155.

5.1 Foreword

We have seen in section 2.5 that scattering from a plasmonic nanoparticle results in intense near-fields and that absorption leads to the generation of non-equilibrium charge carriers and to plasmonic heating. In this chapter, we begin our investigation of how these phenomena can be exploited to activate chemical processes at the nanoscale. In particular, here we study how plasmonic near-fields can drive photocatalytic reactions within nanoscopic regions at the surface of metal nanoparticles.

Since the catalytic properties of metal nanoparticles are strongly dependent on variations in, for example, their size, shape, defects, and local surfactant concentration,[125] several features remain hidden when performing ensemble-averaged measurements. In particular, (i) even nearly monodisperse nanoparticle ensembles show different reaction pathways for the same catalytic conversion,[79] (ii) catalytic activity depends on the available surface facets[126] and the presence of defects,[127,128] both of which can vary from particle to particle, and (iii) the structure of a catalyst changes during operation, resulting in spatiotemporal variations in catalytic activity.[80,129–131] Furthermore, in ensemble experiments it is challenging to study if the locations at which photochemical reactions take place correlate with the light polarization or with the spatial distribution of non-equilibrium charge carriers.[132–134] For all these reasons, single particle and single molecule experiments can provide unprecedented insights into the catalytic and photocatalytic properties

of metal nanoparticles.[41]

In this chapter, we use super-resolution fluorescence microscopy to map the activation of a purely near-field-driven chemical reaction under in-situ conditions and on individual nanoparticles. In particular, we irradiate gold nanorods that catalyze the conversion of the nonfluorescent molecule resazurin to its highly fluorescent reduced form resorufin.[79] We first characterize the dependence of the turnover rate on the incident laser power and find that the reaction mechanism is a photodriven disproportionation.[135] We then simulate the plasmonic near-fields around individual nanorods and show that the ratio between the electric field intensities on the nanorod tips depends on the orientation of the particle with respect to the polarization of the incident field. Lastly, we demonstrate a clear correlation between these simulations and the experimental super-resolved catalytic activity maps of individual particles. Our work shows for the first time a super-resolved spatial distribution of photocatalytic activity on individual nanoparticles driven by plasmonic near-fields.

Abstract

Plasmonic nanoparticles have recently emerged as promising photocatalysts for light-driven chemical conversions. Their illumination results in the generation of highly energetic charge carriers, elevated surface temperatures, and enhanced electromagnetic fields. Distinguishing between these often-overlapping processes is of paramount importance for the rational design of future plasmonic photocatalysts. However, the study of plasmon-driven chemical reactions is typically performed at the ensemble level and, therefore, limited by the intrinsic heterogeneity of the catalysts. Here, we report an in-situ single particle study of a fluorogenic chemical reaction driven solely by plasmonic near-fields. Using super-resolution fluorescence microscopy, we map the position of individual product molecules with ∼30 nm spatial resolution and demonstrate a clear correlation between the electric field distribution around individual nanoparticles and their super-resolved catalytic activity maps. Our results can be extended to systems with more complex electric field distributions, thereby guiding the design of future advanced photocatalysts.

5.2 Introduction

Localized surface plasmon resonances (LSPRs) arise from the coherent oscillation of free electrons upon illumination of metallic nanoparticles.[8] These resonances can enhance the rate of chemical reactions and change their potential energy landscape.[21–24] For example, LSPRs have been used to enhance the rate of NH_3 decomposition on copper-ruthenium nanoparticles[31] and to increase the selectivity of CO_2 hydrogenation on rhodium nanocubes.[136] At least three mechanisms have been proposed to explain the observed enhancements: i) the generation of non-equilibrium charge carriers driving redox reactions, ii) photothermal nanoparticle heating inducing faster chemical turnover according to the Arrhenius equation, and iii) focusing of light into nanoscale regions of high electromagnetic fields (near-fields) that accelerate photosensitive reactions.[20] All these mechanisms take place on ultrafast timescales and can contribute simultaneously to the enhancement of a chemical reaction, making them very difficult to disentangle experimentally.[20,34,35]

Recent studies have begun elucidating the mechanism underlying a wide range of plasmon-driven processes by carefully characterizing the rate of chemical reactions under different illumination parameters, while measuring the temperature inside the reactor.[30–33,39] These experiments are often performed at the ensemble level, resulting in measurements that are averaged over many particles. The photocatalytic properties of nanoparticles, however, are intrinsically heterogeneous due to the distribution in particle sizes and orientations with respect to the incoming light,[81,137] the heterogeneity of active sites,[138] and the dynamic restructuring of catalytic surfaces.[80,129,130] For this reason, in-situ measurements of the catalytic activity of single nanoparticles with single molecule accuracy and nanometer spatial resolution are necessary.[41,79,125,133] In this context, super-resolution fluorescence microscopy has emerged as an effective approach thanks to its ability to interrogate individual catalytic nanoparticles at the single molecule level.[79] For example, super-resolution microscopy has been used to characterize chemical reactions that are accelerated by plasmonic hot charge carriers.[139,140] However, the efficiency of hot charge carrier extraction is typically very low due to their extremely short lifetimes.[62,141] Recently, several studies have proposed an alternative mechanism to explain their plasmon-driven catalysis enhancement, in which the plasmonic near-field induce direct optical excitations of adsorbate molecules.[142–145] To demonstrate this mechanism, which is not limited by fast electron-electron scattering and could therefore result in high conversion efficiencies, it is important to spatially correlate the photocatalytic activity of individual metal nanoparticles with their plasmonic near-fields.

Here, we utilize super-resolution microscopy to map the activation of a purely field-driven chemical reaction under in-situ conditions. In particular, we irradiate gold nanorods that catalyze the conversion of the nonfluorescent molecule resazurin to its highly fluorescent reduced form resorufin.[135] The power dependence of the turnover rate and the spatial distribution of the catalytic events unequivocally indicate that the activation mechanism is solely due to the plasmonic near-fields.

5.3 Results and discussion

We first synthesize gold (Au) nanorods with a length of 118 ± 10 nm and a width of 54 ± 4 nm using a previously reported seed-mediated process (Figure 5.5).[137] These dimensions result in a longitudinal LSPR at 718 nm, which is spectrally separated from the emission of the reaction product resorufin and thereby minimizes mislocalization effects.[120,121,146,147] We then coat the nanorods with a ∼16 nm mesoporous SiO_2 ($mSiO_2$) shell using a previously reported growth method (Figure 5.1a and Figure 5.5).[148,149] The mesoporous shell with ∼2.5 nm pores[149] temporarily traps the reaction products and thereby facilitates their detection, which would otherwise be hindered by fast product desorption and fluorescence quenching on Au.[127] Interestingly, our Au@$mSiO_2$ nanorods show no catalytic activity in the dark, suggesting that the mesopores do not extend all the way to the metallic surface (Figure 5.6).

We dropcast the Au@$mSiO_2$ nanorods on a coverslip, resulting in an average interparticle spacing of ∼6 µm, which allows each rod to be resolved spatially in the microscope. The coverslip is then built into a flowcell supplying a continuous flow of 200 nM resazurin and the assembly is mounted on an inverted fluorescence microscope (Figure 5.7).

At the beginning of each experiment, we first take a transmitted white light image of the sample. We fit all local transmission minima to two-dimensional Gaussians and thereby localize all nanoparticles with a ∼6 nm precision (Figure 5.8).[75,77,82] We then irradiate an area of the sample of ∼100×100 µm^2 with a 532 nm cw laser in a total internal reflection (TIRF) configuration (Figure 5.7). This laser wavelength simultaneously excites the reaction product resorufin and the transverse plasmon resonance of the nanorods (Figures 5.1b,c). The nanorod photoluminescence closely follows its longitudinal plasmon resonance ($\lambda = 718$ nm),[150] which is outside the spectral range of the emission filter. Therefore, in our experimental configuration, we do not need to perform background subtraction to remove the nanorod photoluminescence and we only observe stochastic bursts of fluorescence corresponding to the generation of resorufin molecules.[135] Similar to the localization procedure for the nanoparticles, we localize these bursts (Figures 5.1d,e) by fitting them to two-dimensional Gaussians (Figure 5.1f), resulting in a localization precision of ∼24 nm (Figure 5.9). Combined with the error in the nanoparticle locations, the overall localization precision of the experiment is ∼30 nm.

Resazurin (Rz) can be converted to resorufin (Rf) via two different mechanisms:[151] i) a reductive deoxygenation catalyzed by Au, which requires the presence of hydroxylamine (NH_2OH) as a reducing agent[79]

$$2\,\mathrm{Rz} + \mathrm{NH_2OH} + \mathrm{OH^-} \xrightarrow{\mathrm{Au}} 2\,\mathrm{Rf} + \mathrm{NO2^-} + 2\,\mathrm{H_2O} \tag{5.1}$$

or ii) a photodriven disproportionation[135]

$$3\,\mathrm{Rz} + \mathrm{H_2O} \xrightarrow{\hbar\omega} \mathrm{Rf} + 2\,\mathrm{Rz^\bullet} + 2\,\mathrm{OH^-} \tag{5.2}$$

where $Rz^\bullet$ indicates an oxidized radical of resazurin.

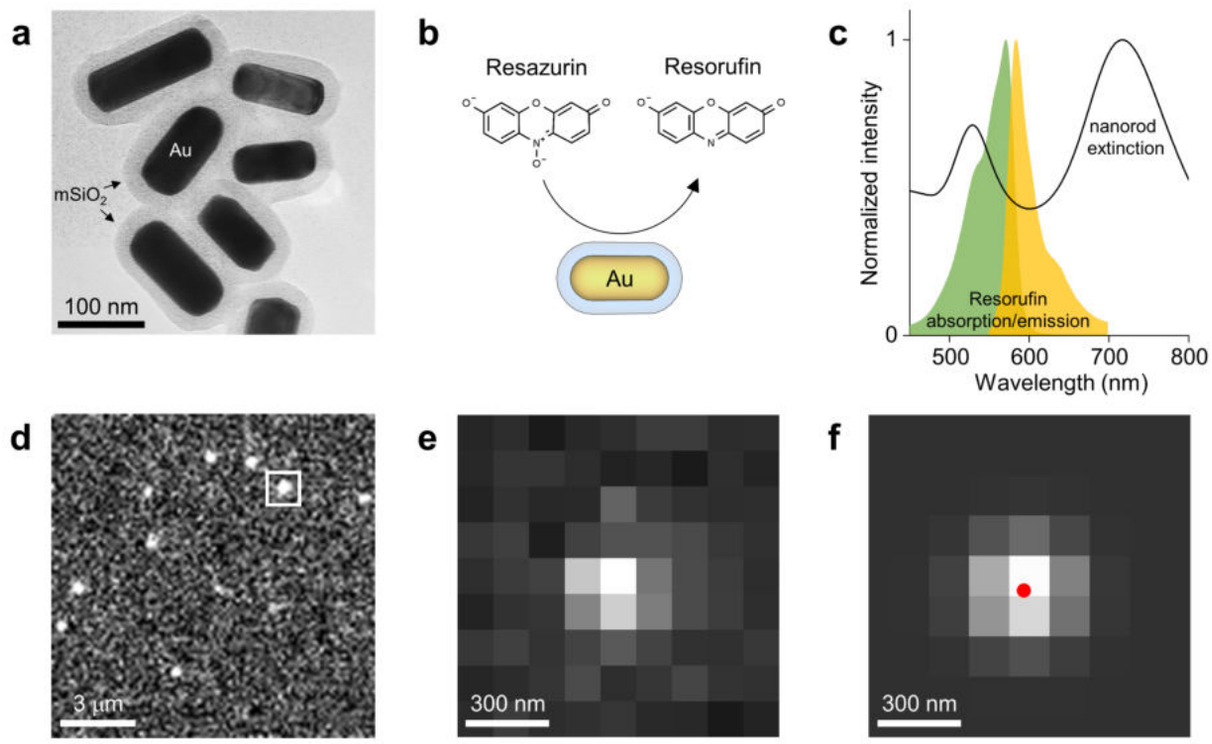

Figure 5.1: In-situ super-resolution catalysis on individual gold nanorods. (a) Transmission electron microscopy (TEM) image of the Au@mSiO$_2$ nanorods after ligand removal. (b) Illustration of the catalytic conversion of resazurin to resorufin. (c) Normalized extinction of a colloidal solution of Au@mSiO$_2$ nanorods after ligand removal (black line) and absorption (green) and emission (yellow) of the reaction product resorufin. (d) Example frame showing the fluorescence of resorufin molecules generated on several catalysts. The image displayed here is cropped from the total field-of-view of 133 × 133 µm^2. (e) Zoomed-in area denoted by the white box in (d), showing the emission of one resorufin molecule. (f) Two-dimensional Gaussian fit of panel (e). The resulting molecule position is denoted by the red dot.

The first mechanism occurs under dark conditions, but can be enhanced by exciting the plasmon resonance of the catalysts.[139] The second mechanism does not occur under dark conditions and does not strictly require a catalytic surface, but exhibits faster dynamics in the presence of Pd or Au nanoparticles.[135] These two reaction pathways are characterized by different dependencies of the turnover rate (number of detected products per catalyst per second) on the laser power. The reductive deoxygenation in equation (5.1) shows a quadratic power dependence, which has been attributed to the presence of two photoexcited species on the nanoparticle surface.[139] In the absence of a catalytic surface, the photodriven disproportionation in equation (5.2) also shows a quadratic dependence, as each reaction involves two photoexcited resazurin molecules.[135] In the presence of a catalytic surface, however, the turnover rate of the second mechanism increases linearly, suggesting a different reaction pathway involving a single photoexcited resazurin molecule.[135]

To discern between these reaction pathways, we measure the turnover rate as a function of laser power both in the absence and presence of the reducing agent NH_2OH (Figure 5.2a). To exclude fluorescent impurities, we only consider events detected within 100 nm of a Au@mSiO$_2$ catalyst. The observed trend of the turnover rate on the laser power does not strongly depend on this distance threshold (Figure 5.10). Every 10,000 frames (corresponding to ∼20 minutes) we reduce the laser power in steps of 20 mW from 200 mW to 100 mW and then, to check the reversibility

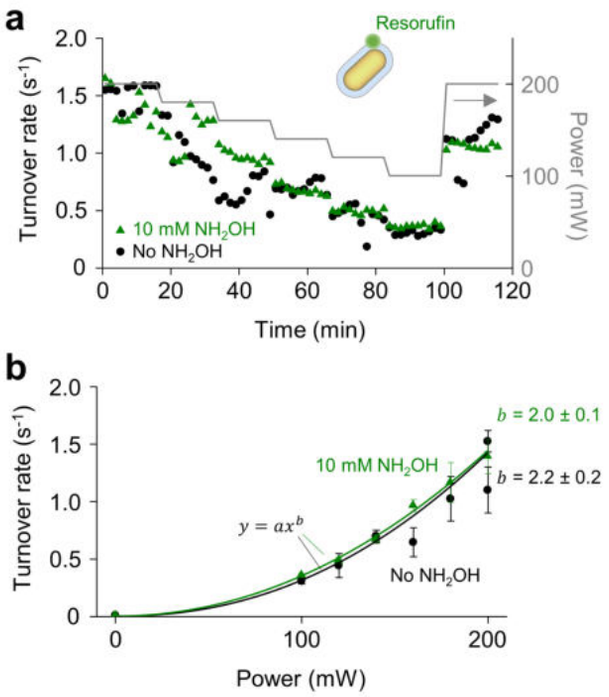

Figure 5.2: Kinetics of the resazurin to resorufin conversion. (a) Mean turnover rate as a function of time in the absence (black circles) and presence (green triangles) of 10 mM NH_2OH. Every point is an average over 1000 frames and 485 particles (black circles) or 331 particles (green triangles). (b) Turnover rate as a function of laser power in the absence (black circles) and presence (green triangles) of 10 mM NH_2OH. Each point is the average of ten points in panel (a). Error bars are standard deviations. Solid lines are a fit to $y = ax^b$, where y is the turnover rate, x is the laser power, and a and b are fitting parameters.

5

of the laser power dependence, we increase the power back to 200 mW as the final step (right y-axis in Figure 5.2a). We observe a decrease in turnover rate with decreasing laser power, which is almost fully reversible (Figure 5.2a). We also find that this decrease in turnover rate is not due to a decrease in the detectability of the reaction products, as the amount of events that are not localized on a catalyst, such as fluorescent bursts from impurities or reaction products that read-sorb on the glass coverslip, does not vary with laser power (Figure 5.11). As our $mSiO_2$ shells are both thin and porous, we attribute the incomplete recovery of the initial catalytic activity to the partial dissolution of SiO_2 in water,[149,152] which decreases the ability of the shell to temporarily trap the reaction products.

Plotting the turnover rate as a function of laser power and fitting the results to a power law ($y = ax^b$) reveals a quadratic dependence both in the presence and absence of 10 mM NH_2OH (Figure 5.2b). Intermediate NH_2OH concentrations also show no influence on the turnover rate (Figure 5.12). Therefore, we can conclude that our catalysts are inactive for the reductive deoxygenation, as the presence of NH_2OH does not alter the reaction kinetics. Furthermore, the catalysts are also inactive for the photodriven disproportionation mediated by a catalytic surface, as we observe a quadratic rather than a linear dependence of the turnover rate on laser power. The quadratic power dependence in the absence of NH_2OH indicates that in our system the conversion of resazurin to resorufin is not mediated by electron transfer with Au. Instead, we exploit the capability of Au nanoparticles to focus light into sub-wavelength volumes (near-fields) and thereby accelerate photodriven reactions in the vicinity of their surface.

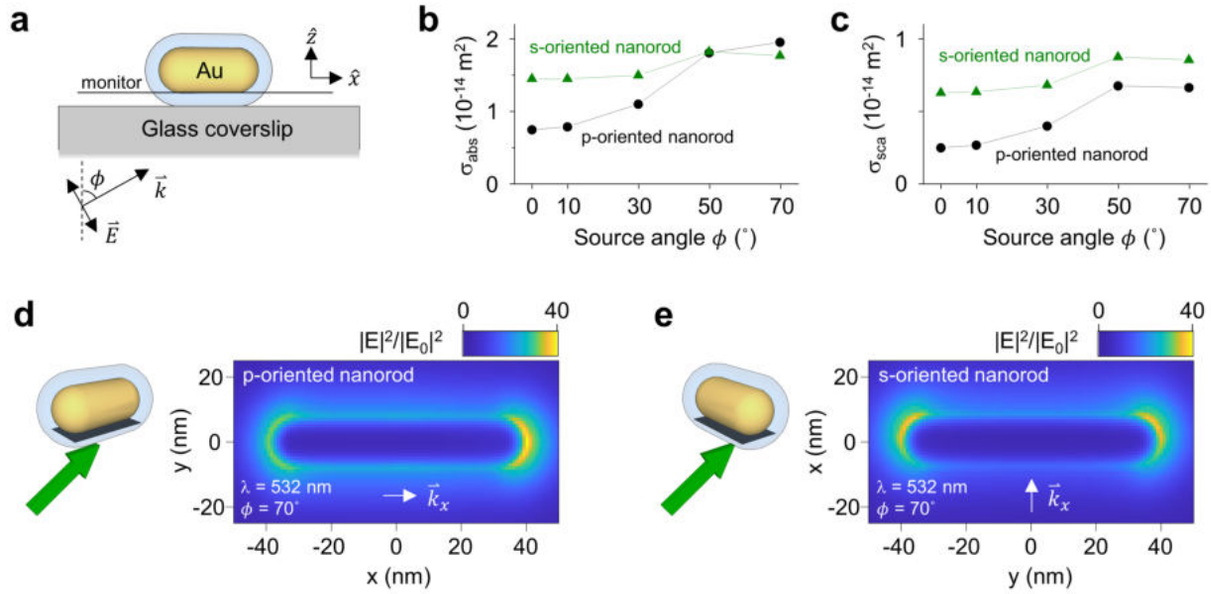

Figure 5.3: FDTD simulations on Au@mSiO$_2$ nanorods. (a) Illustration of the simulation. A p-polarized field $\vec{E}$ with wavevector $\vec{k}$ is injected on an Au@mSiO$_2$ nanorod on a glass coverslip. The source angle ϕ is defined as the angle between $\vec{k}$ and $\hat{z}$. The electric field is monitored at the bottom of the nanorod. (b,c) Absorption (b) and scattering (c) cross sections at 532 nm as a function of source angle. The nanorod is p-oriented (black circles), as in panel (a), or s-oriented (green triangles). The critical angle for TIRF is 61°. (d,e) Electric field intensity $|E|^2$ normalized to the incident field intensity $|E_0|^2$ at 532 nm monitored at the bottom of the Au nanorods for a source angle of 70°. The nanorod is p-oriented (d), as in panel (a), or s-oriented (e).

Since in our system no electron transfer takes place between Au and resazurin, we can rule out any contribution from non-equilibrium charge carriers generated through plasmon excitation. We further verify this statement by simultaneously exciting the longitudinal plasmon resonance of the Au@mSiO$_2$ nanorods using a 730 nm cw laser. While at this energy resazurin is not photo-excited (Figure 5.13), the charge carriers generated by absorption in Au have enough energy to occupy the lowest unoccupied molecular orbital of resazurin.[135] However, we observe no change in the kinetics of the reaction when comparing the reaction rate with or without the excitation of the longitudinal resonance of the rods (Figure 5.13). Furthermore, due to the low power density and large interparticle spacing used in our study, localized and collective photothermal contributions can also safely be ruled out (Figure 5.14), thereby leaving the plasmonic near-fields as the sole contributor to the resazurin-to-resorufin conversion.

The observation that in our system the conversion of resazurin to resorufin is driven by the plasmonic near-fields suggests that a correlation should exist between the spatial distribution of the electric field around the nanorods and the regions where we observe high catalytic activity. We therefore first simulate the optical response of our nanorods under 532 nm irradiation using a finite-difference time-domain (FDTD) method. We simulate an Au@mSiO$_2$ nanorod on a glass coverslip and we inject a p-polarized field through the glass coverslip (Figure 5.3a and Figure 5.15). The long axis of the rod is pointing along the x axis (Figure 5.3a), which we will refer to as p-oriented, or along the y-axis, which we will refer to as s-oriented. We monitor the absorption and scattering cross section, σ_{abs} and σ_{sca}, and the total electric field intensity inside and outside the rod for various injection angles of the source. For a source angle of 0°, which corresponds to injection normal to the coverslip, the cross sections at 532 nm are higher for the s-oriented rod (Figures 5.3b,c). This behavior is expected, as 532 nm illumination overlaps with the transverse

resonance of Au nanorods (Figure 5.15), which is preferentially excited when the polarization of the field is perpendicular to the long axis of the rod. However, as the source angle increases, a second transverse resonance with charges oscillating along the z axis is excited.[153] As the rod is always oriented in the x,y-plane, this resonance is excited independent of the rod orientation when the source is off-axis, resulting in the cross sections for p-oriented and s-oriented rods becoming increasingly similar as the source angle increases (Figures 5.3b,c).

As TIRF illumination corresponds to excitation at very high angles (between 61° and 74° in our experimental geometry), the absorption and scattering cross sections of a nanorod do not depend strongly on the in-plane particle orientation. However, the spatial distribution of the electric field does show distinguishing features. We observe electric field hot spots at the bottom of the nanorod (Figures 5.3d,e) and relatively weak field enhancement at the nanorod center (Figure 5.15). For the p-oriented rod the field intensity is ∼1.3× higher on the tip away from the incident light than on the tip facing the source (Figure 5.3d). We do not observe this difference for the s-oriented rod, as this orientation is perpendicular to the propagation direction of the field, which leads to an identical distribution of enhanced fields at the opposing ends of the nanorod (Figure 5.3e).

The above observations suggest that for varying in-plane orientations we expect similar turnover rates, but different spatial distributions of catalytic events. Since the dimensions of our catalysts are only a few times larger than our resorufin product localization precision, quantitative comparison between the simulated electric field and the catalysis maps is challenging. Additionally, due to partial spectral overlap of the nanorod extinction with the resorufin emission, the latter can couple to the nanorod, resulting in the apparent position of the molecule being 'pulled' toward the nanorod center (Figure 5.16).[120,121] However, despite these limitations, our spatial resolution is sufficient to discriminate between the catalytic activity of the two tips of the rods. Therefore, to correlate the observed catalytic activity to the simulated electric field, we look at the in-plane angular distribution of catalytic events.

For each nanorod, we define the positions of the catalytic events relative to the position of the rod, which is known from the transmitted white light image. We then assign an angle θ to each catalytic event, defined as the angle between the position of the event and the x axis (Figure 5.4a). Instead of plotting the detected products on a single particle as a two-dimensional map (Figure 5.4b), this definition of θ allows us to plot the detected products as an angular distribution (dots in Figure 5.4c). For these angular distributions we use a bin size of $\pi/10$, which is commensurate with the typical error in θ (Figure 5.17). We then fit this distribution to a function given by the sum of two Gaussian peaks, corresponding to the two tips of the nanorod. The first peak models the catalytic activity of the front tip with a negative y coordinate and is characterised by an amplitude A_1 and an in-plane orientation θ_0. The second peak, corresponding to the back tip with a positive y coordinate, has an amplitude A_2 and an in-plane orientation $\theta_0 + \pi$ (Figure 5.18). Fitting the angular distribution of catalytic events allows us to extract the particle orientation θ_0 and the reactivities of the two nanorod tips, A_1 and A_2 (Figure 5.4c).

When $\theta_0 \approx 0$, the particle is p-oriented. In this orientation A_1 corresponds to the reactivity of the tip away from the incident light, where the field is higher than on the tip facing the source (Figure 5.3d), and therefore we expect $A_1 > A_2$. When $\theta_0 \approx \pi/2$, the particle is s-oriented. In this orientation the field enhancement on the two tips is equal (Figure 5.3e), and we expect $A_1 \approx A_2$. Lastly, when $\theta_0 \approx \pi$, the particle is again p-oriented. However, A_1 now corresponds to the reactivity of the tip facing the source and we expect $A_1 < A_2$. The example shown in Figures 5.4a-c corresponds to a particle with $\theta_0 = 175°$ and for which A_1 is therefore smaller than A_2, as shown by the clear peak intensity difference in Figure 5.4c. Other examples of nanorods with

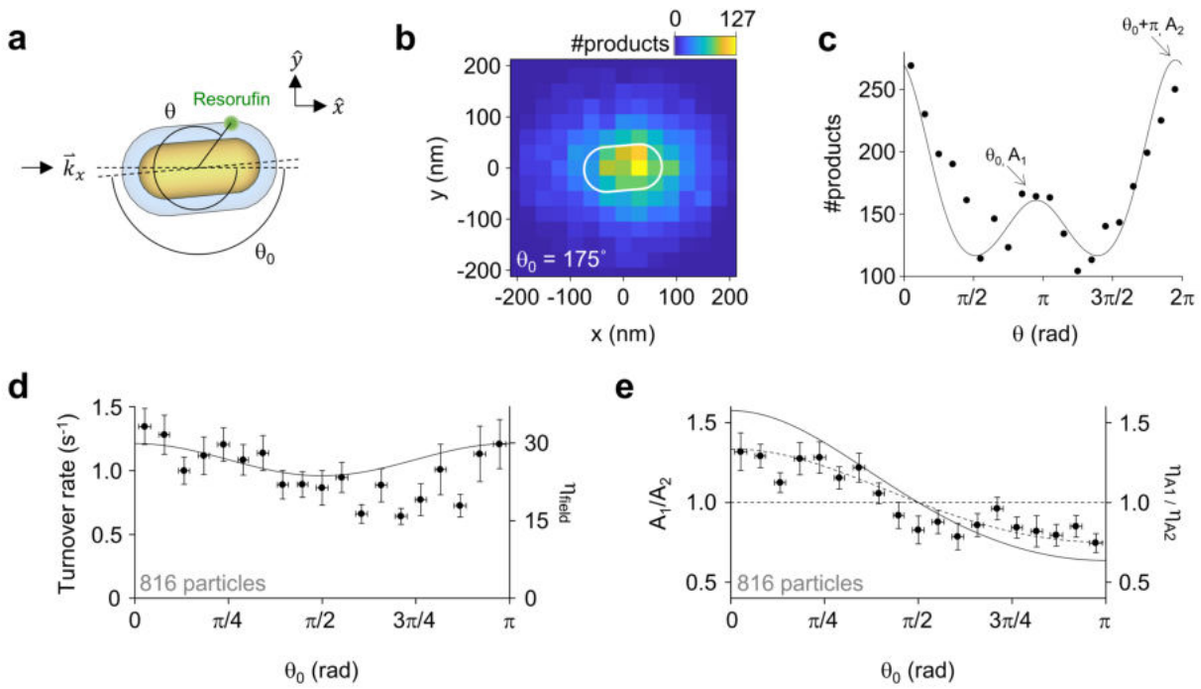

Figure 5.4: Analyzing catalysis maps as a function of particle orientation. (a) Illustration of the definition of the angle θ and the particle orientation θ_0. The x component of the wavevector $\vec{k}$ is also illustrated. (b,c) Two-dimensional histogram (b) and angular distribution (c) of the products detected within 200 nm of a single Au nanorod. The bin sizes are 30×30 nm^2 (b) and $\pi/10$ (c). Panel (b) also contains a white outline depicting the fitted position and orientation of the Au@mSiO$_2$ nanorod catalyst. The orientation θ_0 is extracted from the fit in panel (c). (d) Mean turnover rate as a function of particle orientation (circles) and the simulated electric field enhancement (line), as defined in equation (5.3). (e) Mean ratio between the peaks in the angular distribution (circles) and the ratio between the simulated electric field enhancements on the two tips (lines) as a function of particle orientation. In the simulation we consider the whole mSiO$_2$ shell (solid line) or the outer 5 nm of the shell (dashed line). In panels (d) and (e) the data from both the experiments with and without NH_2OH are used, resulting in a total of 816 particles. The points correspond to a bin with a width of $\pi/19$, the x error bars are standard deviations, and the y error bars are standard errors in the mean.

different in-plane orientations can be found in Figure 5.19.

In Figure 5.4d, we bin together particles with similar in-plane orientations and plot the measured turnover rates as a function of θ_0, where the bin size is commensurate with the typical fitting error in θ_0 (Figure 5.18). Since the turnover rate scales quadratically with the electric field intensity (Figure 5.2b), we compare these values to the square of the average simulated electric field intensity outside the nanoparticle. We calculate this value η_{field} by integrating over all mesh cells outside the particle, but within the mSiO$_2$ shell:

$$\eta_{\text{field}} = \frac{1}{V} \iiint_{r<16\,\text{nm}} \frac{|E|^4}{|E_0|^4} \mathrm{d}V, \tag{5.3}$$

where V is the integrated volume, r is the distance from a mesh cell outside of the nanoparticle to the particle surface, E is the electric field, and E_0 is the incident field.

We find that both the turnover rate and the average field enhancement show only a weak dependence on the particle orientation (Figure 5.4d), as also expected from the similar scattering

cross sections of p-oriented and s-oriented nanorods at the experimental illumination angle (Figure 5.3c). Interestingly, however, we find a clear angular dependence of the peak ratio $\frac{A_1}{A_2}$ on θ_0 (Figure 5.4e). We compare this value to the ratio between the simulated field enhancement η_{A1} in the half-space occupied by the tip corresponding to A_1 and the field enhancement η_{A2} in the half-space occupied by the tip corresponding to A_2.

The measured ratio between the photocatalytic activity of the two tips of the nanorods ($\frac{A_1}{A_2}$) matches qualitatively with the simulated ratio between the electric field intensity enhancements on the two tips ($\frac{\eta_{A1}}{\eta_{A2}}$), as both show a transition from values > 1 for in-plane orientations $\theta_0 < \pi/2$ to values < 1 for $\theta_0 > \pi/2$ (Figure 5.4e). Interestingly, if we assume that all molecules are detected within the outer 5 nm of the $mSiO_2$ shell, we obtain a quantitative agreement (dashed line in Figure 5.4e). This assumption is justified by the fact that the mesopores likely do not extend all the way to the metallic surface, as our catalysts are inactive in the dark, and by the fact that fluorescence quenching can occur for molecules generated in the vicinity of the Au surface. Such quantitative agreement does not take into account the potential mislocalization of the resazurin emission, due to coupling to the nanorod plasmon resonance.[120,121,146,147] Although these effects are likely to be small (Figure 5.16), a proper quantitative agreement should rely on exact calculations of these effects for our experimental particle-molecule geometries.

5.4 Conclusion

In summary, we use super-resolution fluorescence microscopy for the in-situ study of a plasmon-driven chemical reaction. We begin by identifying the reaction mechanism as a photodriven disproportionation by measuring the photocatalytic turnover rate at the single molecule level for various illumination intensities and reducing agent concentrations. We then use single molecule localization to show a clear correlation between the simulated electric field distribution and the super-resolution catalysis maps. Our photochemical approach to map scattered near-fields in-situ and with sub-particle spatial resolution can be extended to systems with different chemical compositions and complex field distributions and can thereby guide the design of future advanced materials for photocatalysis, biomolecule sensing, and photonic devices.

5.5 Supporting information

5.5.1 Synthesis of the Au@mSiO$_2$ catalysts

All the chemicals are used as received, without any further purification. Hexadecyltrimethylammonium bromide (CTAB) (98%), $NaBH_4$ (99%), $HAuCl_4$ trihydrate (99.9%), $AgNO_3$ (99.9999%), ascorbic acid (99%), HCl (37% in water), NH_2OH (50% in water), tetraethyl orthosilicate (TEOS) (99.999%), K_2HPO_4 (98%), and KH_2PO_4 (99%) were purchased from Sigma Aldrich. Sodium oleate (NaOL) (97%) was purchased from TCI. Ethanol (dried, $< 0.01\%$ H_2O) was purchased from Merck. NaOH (98%) was purchased from Alfa Aesar. Resazurin (99%) was purchased from Thermo Fisher. Ultrapure water obtained from a Milli-Q Integral Water Purification System by Merck Millipore was used for all aqueous solutions.

Au nanorod synthesis

We synthesize Au nanorods using a previously reported seed-mediated growth method.[137] Au seeds are synthesized by mixing 5 mL 0.5 mM $HAuCl_4$ and 5 mL 0.2 M CTAB. 600 µL of fresh 0.01 M $NaBH_4$ is diluted to 1 mL and subsequently added under vigorous stirring. The stirring is stopped after 2 minutes and the seeds are aged at room temperature for at least 30 minutes before use. Ideally, the seeds are used within a few hours to avoid CTAB crystallization.

To synthesize the rods, 3.5 g CTAB and 0.617 g NaOL are dissolved in 125 mL water and kept at 30 °C. 12 mL 4 mM $AgNO_3$ is added and the solution is kept undisturbed for 15 minutes. After adding 125 mL 1 mM $HAuCl_4$, the solution is stirred for 90 minutes to reduce the Au^{3+} to Au^{+}.[137] Then, 750 µL HCl (37% in water) is added to adjust the pH. After 15 minutes of stirring, 625 µL 64 mM ascorbic acid is added. After 30 seconds of vigorous stirring, 200 µL of the above seeds solution is added. The resulting mixture is stirred again for 30 seconds and then left overnight undisturbed at 30 °C.

Mesoporous SiO$_2$ coating

The nanorods are coated with mesoporous SiO_2 ($mSiO_2$) by adapting a previously reported method.[148,149] 40 mL of the above nanorods are centrifuged at 5500 × g for 30 minutes and redispersed in 40 mL 5 mM CTAB. The nanorods are then centrifuged again and redispersed in 5 mL 5 mM CTAB.

To 3 mL of the above nanorods 7 mL water is added to achieve a final CTAB concentration of 1.5 mM. 100 µL 0.1 M NaOH is added to adjust the pH. Then, while continuously stirring at 30 °C, three injections of 30 µL 0.9 M TEOS in ethanol are done separated by 45 minute time intervals. After the final injection, the solution is kept stirring at 30 °C for ∼40 hours.

After synthesis, the solution is diluted with water to a total volume of 40 mL. This solution is then centrifuged three times at 7000 × g for 15 minutes and redispersed in 40 mL ethanol to remove excess SiO_2 and CTAB. We observe a slight red shift of the resonance (Figure 5.5a), due to the increase in refractive index around the nanorods.

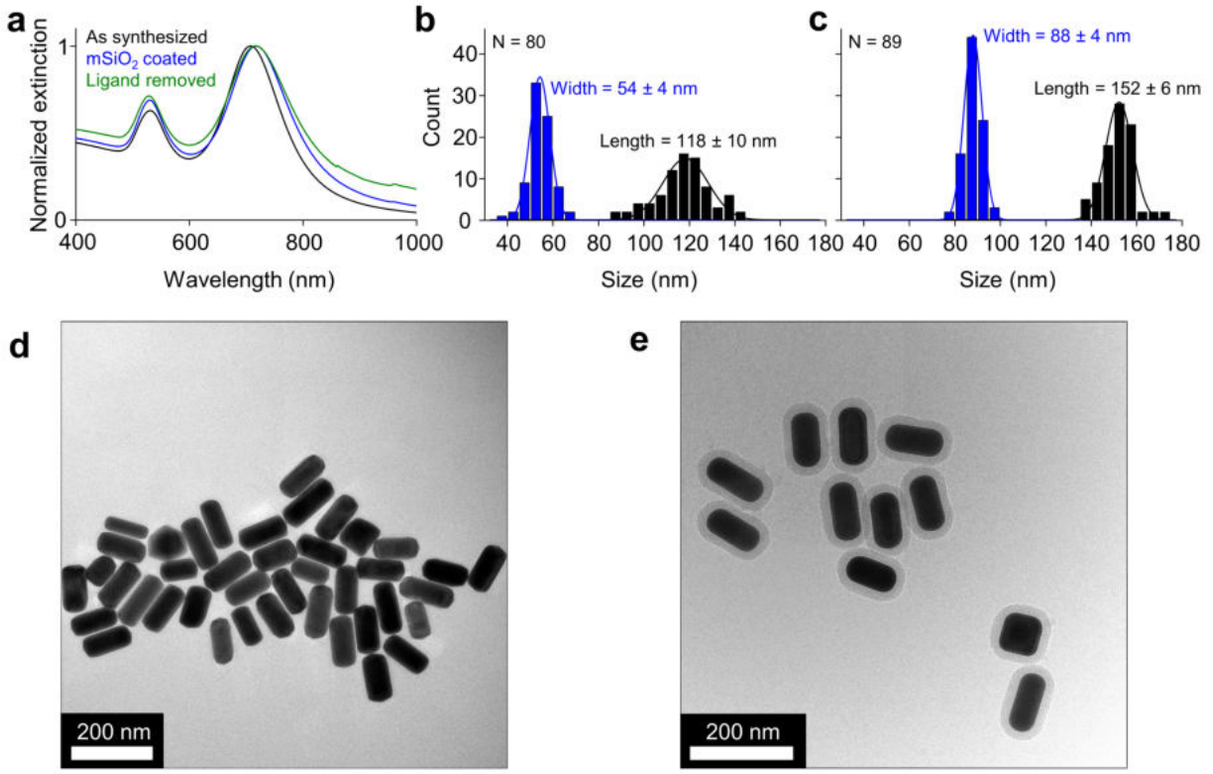

Figure 5.5: (a) Normalized UV-Vis spectra of the rods before (black) and after (blue) $mSiO_2$ coating, and after ligand removal (green). The longitudinal resonances are at 708 nm (black), 717 nm (blue), and 718 nm (green). The transverse resonances are at 531 nm (black), 530 nm (blue), and 529 nm (green). (b) Size distribution of 80 nanorods before $mSiO_2$ coating. (c) Size distribution of 89 nanorods after ligand removal. The reported values for the length and width result from Gaussian fits of the distributions, see the lines in panels (b) and (c). The reported errors are the standard deviations of the fitted Gaussians. (d,e) Representative TEM images of the nanorods before $mSiO_2$ coating (d) and after ligand removal (e).

5

Ligand removal

To further remove CTAB and thereby unblock the mesopores, 85 µL HCl (37% in water) is added to 10 mL of the above Au@$mSiO_2$ nanorod solution in ethanol.[154] This solution is ultrasonicated for 30 minutes in a Branson 5800 ultrasonic bath. After sonication, the solution is diluted to 40 mL with ethanol and centrifuged twice at 7000 × g for 15 minutes and redispersed in 40 mL ethanol. Finally, the solution is centrifuged at 7000 × g for 15 minutes again and redispersed in 10 mL ethanol. We observe a slight resonance broadening (Figure 5.5a), which we attribute to a slight loss in sample uniformity due to HCl etching.

Size distributions

To obtain the nanorod and $mSiO_2$ shell dimensions, we measure size distributions from transmission electron microscopy (TEM) images before $mSiO_2$ coating (Figure 5.5b) and after ligand removal (Figure 5.5c) using ImageJ. Representative TEM images can be found in Figures 5.5d,e.

5.5.2 The Au@mSiO$_2$ nanorods show no catalytic activity in the dark

We characterize the catalytic activity of the Au@mSiO$_2$ nanorods in the dark using UV-Vis spectrocopy. The white light source of the spectrometer (Perkin Elmer Lambda 1050) is not expected to induce any catalytic activity due to its low power density. We prepare a cuvette with 1 mL 50 mM pH 7.3 potassium phosphate buffer with 10 µM resazurin and 20 mM NH_2OH. We then add 100 µL of the Au@mSiO$_2$ nanorods after ligand removal at an optical density of ∼0.35 and consecutively measure absorption spectra for 2 hours. The absorption of resazurin is characterized by a peak at 602 nm (Figure 5.6a) and the absorption of resorufin by a peak at 572 nm (Figure 5.1c). As can be seen in Figure 5.6b, the Au@mSiO$_2$ nanorods show no catalytic activity in the dark.

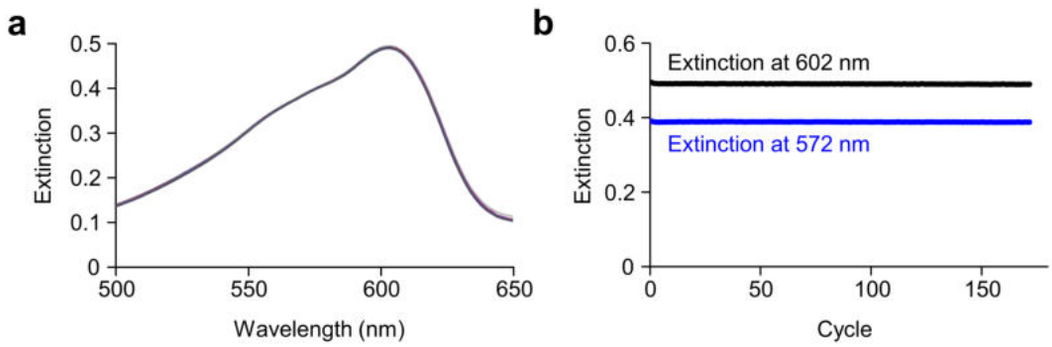

Figure 5.6: (a) 172 consecutive absorption spectra of 100 µL Au@mSiO$_2$ nanorods added to 1 mL 50 mM pH 7.3 potassium phosphate buffer with 10 µM resazurin and 20 mM NH_2OH. (b) Extinction peaks of resazurin at 602 nm (black) and resorufin at 572 nm (blue) as a function of time.

5.5.3 Microscopy setup

The flowcell consists of a 22 mm × 40 mm coverslip and a 22 mm × 30 mm coverslip separated by a silicone gasket in a Warner Instruments RC-30 flowcell. All reactant solutions are supplied at 50 µL min^{-1} in a 50 mM potassium phosphate buffer at pH 7.3.

The optical setup is based around a Zeiss AxioObserver 7 inverted optical fluorescence microscope. The laser beam from a 532 nm cw laser (CNI MGL-FN-532) is focused into a Thorlabs P3-488PM-FC-2 single mode polarization-maintaining fiber using a Thorlabs PAF2-7A FiberPort. The fiber is connected to a Zeiss TIRF slider, which focuses the laser on the edge of the back focal plane of an oil-immersion objective (Zeiss Alpha Plan-Apochromat 63×/1.46NA). The emission is filtered using a dichroic mirror (Semrock, reflection at $\lambda = 532$ nm and $\lambda = 730$ nm and transmission from $\lambda = 550$ nm to $\lambda = 700$ nm) and a band-pass filter that transmits $\lambda = 585 \pm 20$ nm (Semrock 585/40 BrightLine). The signal is imaged on a Hamamatsu ORCA-Flash 4.0 V3 sCMOS camera with 2048 × 2048 pixels (6.5 µm physical size), which is reduced to 1024 × 1024 pixels using 2 × 2 binning, resulting in an effective pixel size of 129 nm (63× magnification objective and an additional 1.6× magnification in the body of the microscope). The integration time is 100 ms.

During the experiment we correct for in-plane drift by tracking fluorescent impurities and for out-of-plane drift using a focus correction system built into the microscope. Image filtering and Gaussian fitting are performed in ThunderSTORM.[77,82] Events for which the fitted Gaussian has a width $\sigma < 35$ nm are filtered out, as these are false detections (hot pixels). Events that appear in consecutive frames are merged. An illustration of the setup can be found in Figure 5.7.

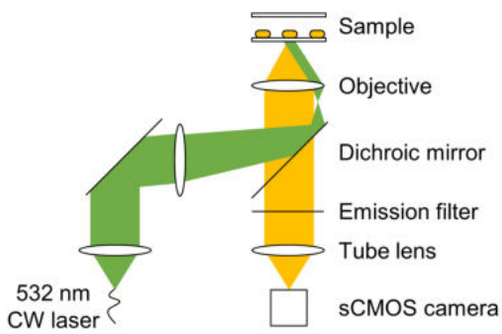

Figure 5.7: Illustration of the optical setup.

5.5.4 Localization of the catalysts in the microscope

The catalysts are localized using a transmitted white light image (Figure 5.8a). This image is inverted (Figure 5.8b), so that the catalysts appear as local maxima instead of local minima. Each local maximum is then fitted to a two-dimensional Gaussian using ThunderSTORM,[77] see also Figures 5.1e,f. The localization precision σ_{loc} is calculated using[75,77]

$$\sigma_{\mathrm{loc}}^2 = \frac{\sigma_{\mathrm{PSF}}^2 + a^2/12}{N} + \frac{8\pi\sigma_{\mathrm{PSF}}^4 b^2}{a^2 N^2}, \tag{5.4}$$

where σ_{PSF} is the standard deviation of the fitted Gaussian, a is the effective pixel size (129 nm), N is the number of detected photons, and b is the standard deviation in the residuals between the experimental emission profile and the fit. This calculation results in an average estimated localization precision of ∼6 nm (Figure 5.8c).

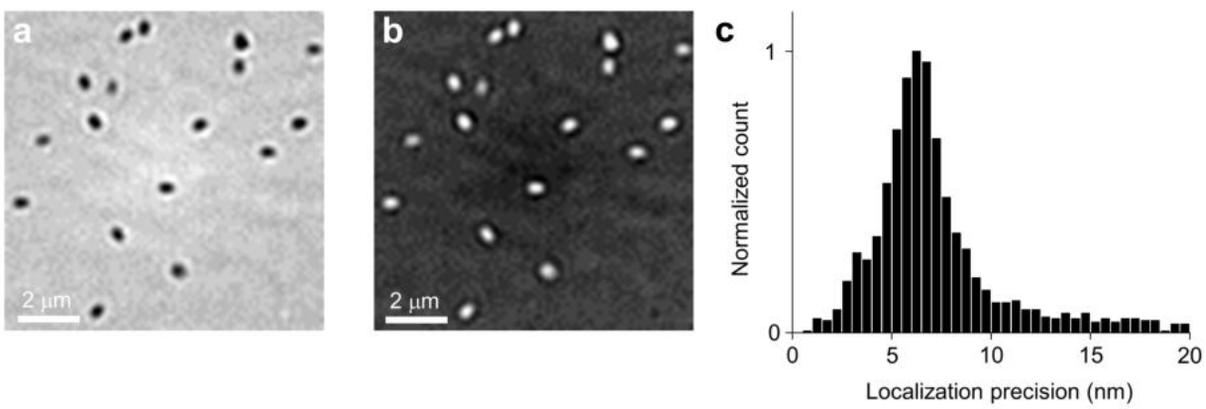

Figure 5.8: (a,b) Transmitted white light image of the catalysts before (a) and after (b) color inversion. The image displayed here is cropped from the total field-of-view of 133 × 133 µm^2. (c) Histogram (485 particles) of the estimated localization precision of the catalyst positions, calculated using ThunderSTORM.[77]

5.5.5 Localization precision of the resorufin molecules

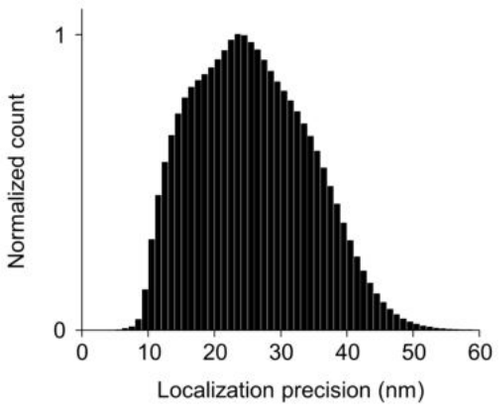

Figure 5.9: Histogram ($\sim 6 \cdot 10^6$ events) of the estimated localization precision of the molecule positions, calculated using ThunderSTORM.[77]

5.5.6 The observed power dependencies do not strongly depend on the distance threshold

In our analysis of the dependence of the turnover rate on the laser power (Figure 5.2) we only consider events detected within 100 nm of the catalysts. The observed dependencies do not significantly change for thresholds ranging from 50 nm to 500 nm, as indicated by the relatively constant value of the fitted power law exponent b (Figure 5.10).

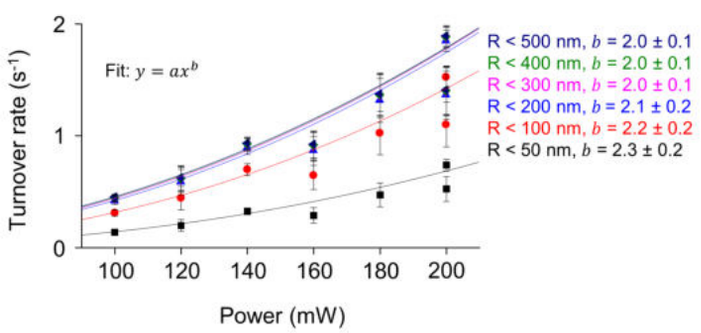

Figure 5.10: Turnover rate as a function of laser power in the absence of NH_2OH for different values of the distance threshold R. Solid lines are a fit to $y = ax^b$, where y is the turnover rate, x is the laser power, and a and b are fitting parameters.

5.5.7 The observed power dependencies are not due to a change in product detectability

As the 532 nm laser also excites the reactions products, changing its power density could result in a change in the product detectability. When fitting the experimental data we fit all local maxima in all frames, *i.e.* we do not preselect regions of interest at the catalyst locations. By using this procedure we detect reaction products at the catalyst positions, but we also detect fluorescent impurities or reaction products that readsorb on the coverslip (Figure 5.11, top). Since we know the catalyst positions from the transmitted light image (Figure 5.8), we can filter out these impurities by only considering events detected within 100 nm of a catalyst (Figure 5.11, middle). Conversely, we can filter out detections on the catalysts and only consider fluorescent impurities (Figure 5.11, bottom). We find that the number of detected impurities per frame does not change within the range of laser powers that we use and that, therefore, the product detectability remains unaltered.

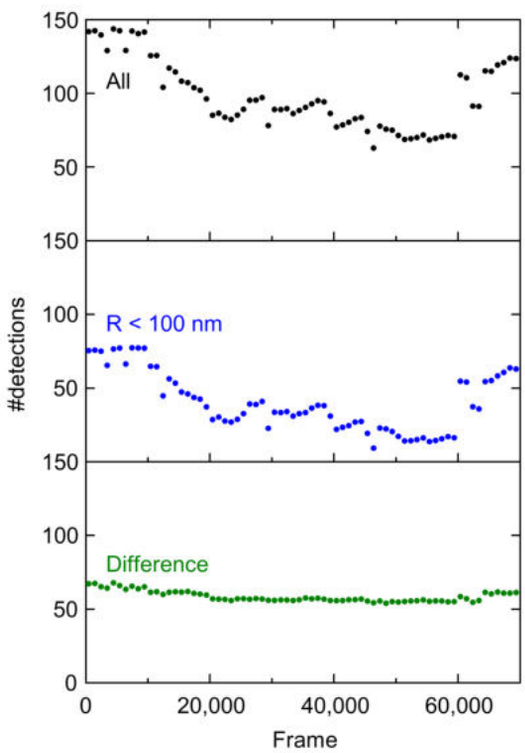

Figure 5.11: (top) Total number of detections per frame in the experiment without NH_2OH reported in Figure 5.2. (middle) Number of detections within 100 nm of a catalyst. (bottom) Difference between the total number of detections and the detections within 100 nm of a catalyst.

5.5.8 NH_2OH does not influence the reaction kinetics

In this experiment we flow in 200 nM resazurin together with a certain concentration of NH_2OH in a 50 mM pH 7.3 potassium phosphate buffer over a sample of Au@mSiO_2 nanorods. We acquire 10,000 frames (∼20 minutes) for every concentration. When switching between reactants, we allow the system to settle for at least 15 minutes before acquiring the next 10,000 frames.
As can be seen in Figure 5.12, the turnover rate does not vary with NH_2OH concentration.

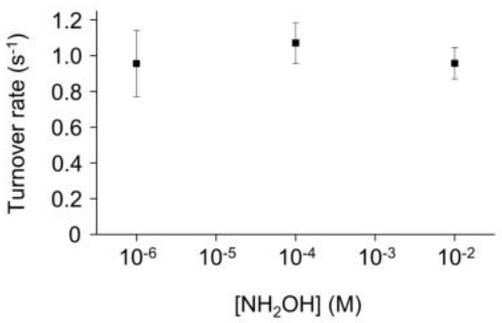

Figure 5.12: Mean turnover rate (averaged over 369 particles) as a function of NH_2OH concentration. Error bars are standard deviations.

5.5.9 Independently exciting the LSPR of the Au@mSiO$_2$ nanorods does not alter the reaction kinetics

In this experiment we flow in 200 nM resazurin together with a certain concentration of NH_2OH in a 50 mM pH 7.3 potassium phosphate buffer over a sample of Au@mSiO$_2$ nanorods. We acquire 20,000 frames (∼40 minutes) for every concentration. During the first 10,000 frames we only use a 532 nm cw laser to excite the resorufin molecules and the transverse LSPR of the nanorods. During the second 10,000 frames, we also use a 730 nm cw laser to excite the longitudinal LSPR of the Au@mSiO$_2$ nanorods. The 730 nm cw laser only excites the LSPR and does not excite the resazurin molecules (Figure 5.13a). When switching between reactants, we allow the system to settle for at least 15 minutes before acquiring the next 20,000 frames.

According to previous density functional theory calculations, the energy gap between the Fermi level of Au and the lowest unoccupied molecular orbital of resazurin is smaller than 1 eV,[135] so a non-equilibrium electron excited in Au under 730 nm (1.7 eV) irradiation should have enough energy to occupy this energy level and reduce resazurin. However, for any NH_2OH concentration, the 730 nm cw laser does not change the kinetics of the reaction (Figure 5.13b). Therefore, this experiment is further evidence that in our system no electron transfer takes place between Au and resazurin.

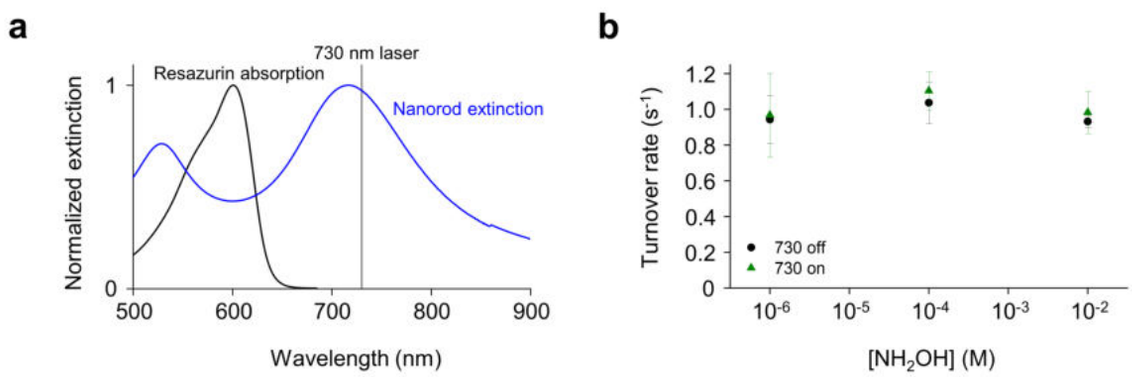

Figure 5.13: (a) Resazurin absorption (black) and Au@mSiO$_2$ nanorod extinction (blue). The 730 nm laser (black vertical line) only excites the nanorods and not the resazurin. (b) Mean turnover rate (averaged over 369 particles) for different NH_2OH concentration with the 730 nm laser turned off (black circles) or on (green triangles). The power density for the 730 nm laser is $2.0 \cdot 10^6$ W m^{-2}. Error bars are standard deviations.

5.5.10 Photothermal contributions are negligible

The temperature increase ΔT_{local} on a single nanorod can be calculated using[155]

$$\Delta T_{\text{local}} = \frac{\sigma_{\text{abs}} I}{4\pi\beta\bar{\kappa}R_{\text{eq}}}, \tag{5.5}$$

where σ_{abs} is the absorption cross section of a single nanorod ($2 \cdot 10^{-14}$ m^2), I is the illumination intensity ($1.3 \cdot 10^7$ W m^{-2}), β is the thermal capacitance coefficient of a nanorod, $\bar{\kappa}$ is the average thermal conductivity of the surrounding medium, and R_{eq} is the radius of a sphere with a volume equal to the volume of the nanorod (38 nm). The thermal capacitance coefficient β is defined as

$$\beta = 1 + 0.96587 \ln^2\left(\frac{l}{w}\right), \tag{5.6}$$

where l and w are the length and width of the nanorod. With $l = 118$ nm and $w = 54$ nm, this equation gives $\beta = 1.59$. The average thermal conductivity of the surrounding medium $\bar{\kappa}$ can, in first approximation, be defined as

$$\bar{\kappa} = \frac{\kappa + \kappa_s}{2}, \tag{5.7}$$

where κ is the thermal conductivity of the medium (0.6 W m^{-1} K^{-1} for water) and κ_s is the thermal conductivity of the substrate (1.38 W m^{-1} K^{-1} for glass). These parameters result in a local temperature increase $\Delta T_{\text{local}} \approx 35$ mK.

However, the simultaneous illumination of many nanoparticles can lead to macroscopic collective heating effects, which can be orders of magnitude larger than the local temperature increase. If we approximate our dropcasted catalysts as a periodically spaced infinite array illuminated by a Gaussian beam, the collective temperature increase ΔT due to photon absorption can be calculated using[156]

$$\Delta T = \frac{\sigma_{\text{abs}} P}{\bar{\kappa}} \sqrt{\frac{\ln 2}{4\pi}} \frac{1}{HA} \left(1 - \frac{4\sqrt{\ln[2]A}}{\pi H}\right), \tag{5.8}$$

where P is the power of the illumination (100 mW), H is the full width at half maximum of the Gaussian beam (100 µm), and A is the unit cell area of the lattice.
In our samples the interparticle spacing is typically > 2 µm, and on average ~ 6 µm. For example, in Figure 5.8, an area of $\sim$100 µm^2 contains 17 particles, with an average interparticle spacing of $\sqrt{100/17} = 2.4$ µm. As we are approximating our dropcasted catalysts as a periodically spaced infinite array, this interparticle spacing yields a unit cell area $A > 4$ µm^2. The estimated temperature increase, ΔT, for these interparticle spacings is $\sim$1 - 2 K, see Figure 5.14.

According to the Arrhenius equation, the rate constant $k(T)$ of a chemical reaction increases exponentially with temperature:

$$k \propto \exp\left[-\frac{E_a}{k_B T}\right], \tag{5.9}$$

where E_a is the reaction activation energy and k_B is the Boltzmann constant. Assuming an initial temperature of 300 K and an activation energy of 38.2 kJ mol^{-1},[157] a 2 K increase would then give a rate enhancement

$$\frac{k(302)}{k(300)} = 1.1. \tag{5.10}$$

In our experiments we are varying the laser power and the interparticle spacing can locally be higher than 2 µm, so a rate enhancement of 1.1 is an upper limit. Therefore, photothermal effects cannot explain the large variations (up to 5-fold) in turnover rate observed in Figure 5.2.

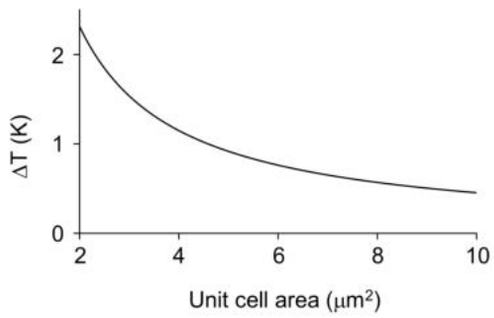

Figure 5.14: Temperature increase ΔT as a function of the unit cell area A.

5.5.11 Design of the FDTD simulations, FDTD spectra at normal incidence, and electric fields monitored at the nanorod center

FDTD simulations are performed using Lumerical FDTD.[123] The glass coverslip is simulated as a semi-infinite lossless dielectric with a refractive index of 1.52. The Au nanorod is simulated as a 118 nm by 54 nm spherically-capped cylinder with a dielectric function taken from literature.[45] The 16 nm $mSiO_2$ shell is simulated as a spherically-capped cylinder with a refractive index of 1.4. The surrounding medium has a refractive index of 1.333. A p-polarized total-field scattered-field source is injected upwards, from inside the coverslip towards the nanorod. The absorption and scattering cross sections are monitored by placing a transmission box inside and outside the source, respectively. The electric field is monitored in three dimensions and we plot x,y slices. A fine mesh of 1 nm^3 is used across the whole volume of the source.

Figure 5.15a shows the absorption and scattering spectra obtained in FDTD simulations with the source impinging at normal incidence. By summing these spectra, we obtain a simulated extinction cross section that matches well with the experimentally measured nanorod extinction (Figure 5.15b). Figures 5.15c,d show the electric field enhancement at the nanorod center for a source angle of 70°. These enhancements are lower than those observed at the bottom of the nanorod (Figure 5.3).

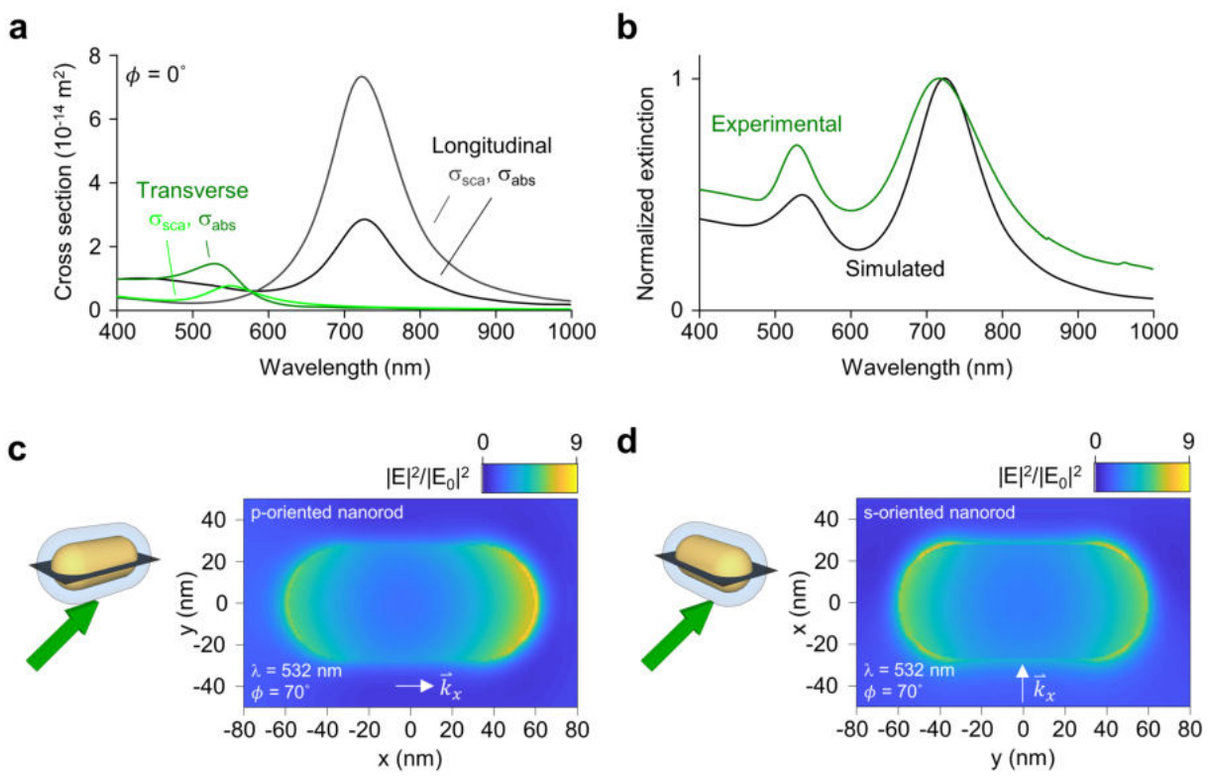

Figure 5.15: (a) Absorption and scattering cross sections when the nanorod is p-oriented (black and dark grey, respectively) or s-oriented (dark green and light green, respectively). The source angle ϕ is 0°. (b) Comparison between the experimental bulk extinction spectrum (green) and the simulated extinction spectrum (black). (c,d) Electric field intensity $|E|^2$ normalized to the incident field intensity $|E_0|^2$ at 532 nm, monitored at the center of the nanorod. The nanorod is p-oriented (c) or s-oriented (d). The source angle ϕ is 70°.

5.5.12 Mislocalization effects

In a semiclassical picture, when a fluorescent molecule emits light in the vicinity of a plasmonic nanoparticle, the emitted photons can excite the LSPR of the nanoparticle, which can subsequently radiate to the far-field. Therefore, the apparent position of the molecule can be pulled toward the center of the nanoparticle, resulting in mislocalization. The extent of mislocalization can be minimized by spectrally detuning the emission of the fluorophore and the LSPR.[120,121,146] For example, Taylor et al. have used fluorophores emitting at ∼532 nm to optically reconstruct the geometry of gold nanorods with an LSPR of ∼790 nm, suggesting mislocalization in their system is minimal.[146] In our experiments, the fluorophore emission and the LSPR are similarly spectrally separated (Figure 5.16), suggesting that also here mislocalization effects should be minimal.

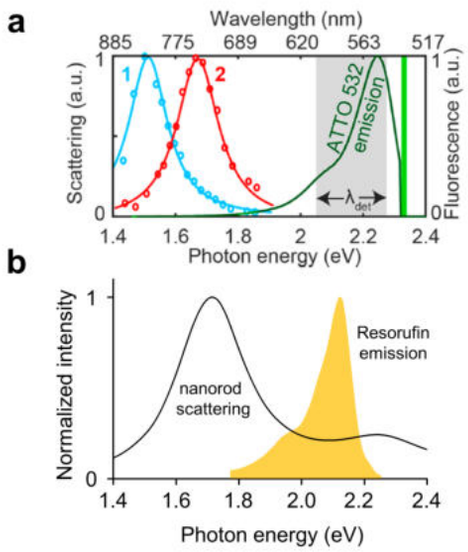

Figure 5.16: Comparison between the spectral positions of the fluorophore emission and the LSPR in (a) the work by Taylor et al. and (b) this work. Both panels are plotted on the same energy and wavelength scale. Panel (a) is adapted from Ref. 146.

Furthermore, any residual mislocalization would mainly influence the radial coordinate of the detected events rather than their angle, especially for events that are detected at the tips of the nanorod, which dominate the values A_1 and A_2. Therefore, this effect would not strongly influence the single particle angular distributions (Figure 5.4c).

If many events are shifted toward the nanorod center, this would increase the vertical offset A_0 in our fits of the angular distribution of catalytic events. Although an increased vertical offset could influence the exact values of A_1 and A_2, the trend of A_1/A_2 as a function of the particle orientation θ_0 should remain unaltered. For this reason, quantitative comparison between the FDTD simulations and the spatial distribution of catalytic events is challenging and a proper agreement should rely on exact calculations of the mislocalization effects in our experimental particle-molecule geometries.

5.5.13 Error in the angle θ of a catalytic event

The angle θ of a catalytic reaction is defined as in Figure 5.4a and can be calculated using

$$\theta = \arctan\left[y/x\right], \tag{5.11}$$

where x and y are the Cartesian coordinates of the event. Note that in reality we use the four-quadrant inverse tangent in MATLAB to fully resolve all angles between 0 and 2π. This difference has no influence on the error analysis.

The error σ_θ in θ can be calculated using

$$\sigma_\theta^2 = \left(\frac{\partial\theta}{\partial x}\right)^2 \sigma_x^2 + \left(\frac{\partial\theta}{\partial y}\right)^2 \sigma_y^2, \tag{5.12}$$

where σ_x and σ_y are the errors in the Cartesian coordinates.

If we then plot histograms of σ_θ for individual particles (Figure 5.17a) we find distributions that peak around ∼0.2 rad. For each particle we calculate the median σ_θ, which we find to be ∼0.3 rad (Figure 5.17b), which justifies our use of $\pi/10$ as the bin size in the angular distributions (see for example Figure 5.4c).

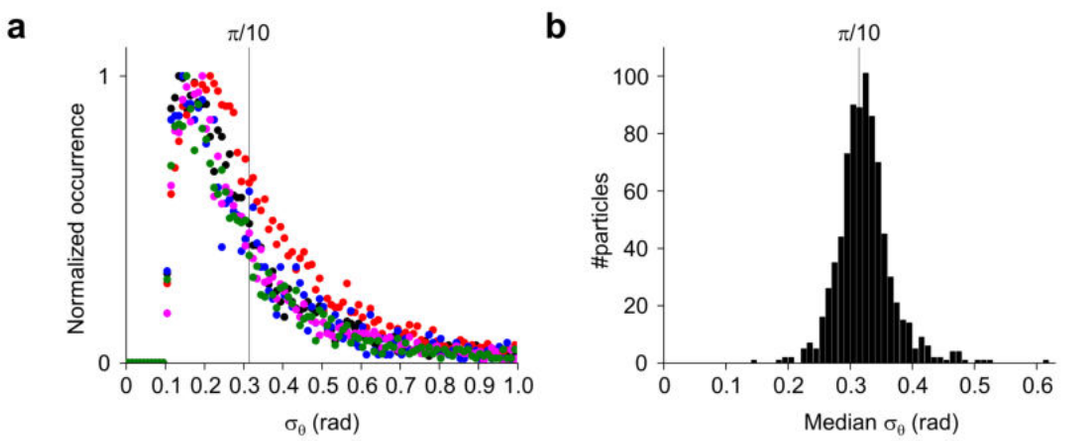

Figure 5.17: (a) Histogram of σ_θ for five example particles. (b) Histogram of the median σ_θ for all particles. The bin size of $\pi/10$ that is used in the angular distributions of catalytic activity is highlighted in both panels with a vertical line.

5.5.14 Fitting function, θ_0 histogram, and fitting error in θ_0

We fit the angular distribution of catalytic events to

$$\begin{aligned} &A_0 + A_1 \exp\left[-\frac{(\theta-\theta_0)^2}{0.9}\right] + A_2 \exp\left[-\frac{(\theta-\theta_0-\pi)^2}{0.9}\right] \\ &+ A_2 \exp\left[-\frac{(\theta-\theta_0-2\pi)^2}{0.9}\right] + A_2 \exp\left[-\frac{(\theta-\theta_0+\pi)^2}{0.9}\right], \end{aligned} \tag{5.13}$$

where A_0 is a vertical offset, A_1 and A_2 are the peak amplitudes, θ is the angle as defined in Figure 5.4a, and θ_0 ($0 < \theta_0 < \pi$) is the orientation of the particle. The peak with amplitude A_2 appears several times to ensure continuity at $\theta = 0$ and $\theta = 2\pi$ for all values of θ_0. We pick 0.9 as the peak width, as this results in a width similar to that of a $\cos^2$ function, see Figure 5.18a. We can exclude systematic errors in detecting the catalyst positions, as this would result in an uneven distribution of θ_0 values, which is not what we observe, see Figure 5.18b. The fitting error in θ_0 is typically well below $\pi/19$ (Figure 5.18c), which is the bin size we use for Figures 5.4d,e.

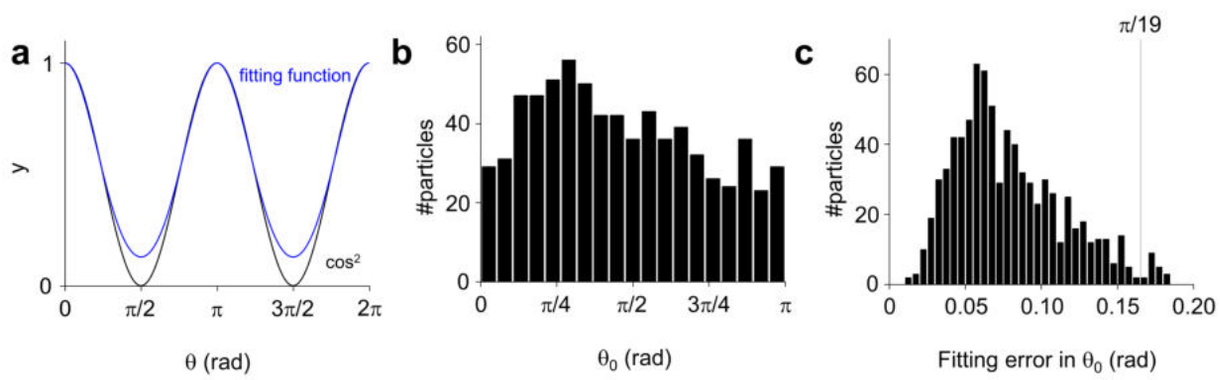

Figure 5.18: (a) $\cos^2\theta$ (black) compared to the fitting function for the angular distributions (blue). The parameters for the fitting function are $A_0 = 0$, $A_1 = 1$, $A_2 = 1$, $\theta_0 = 0$. (b) Histogram of the obtained values for θ_0. The bin size is $\pi/19$. (c) Histogram of the fitting errors in θ_0. The bin size is 5 mrad. The bin size of $\pi/19$ that is used in Figures 5.4d,e is highlighted with a vertical line.

5.5.15 Single particle catalysis maps and angular distributions

In Figures 5.4a-c we show how we extract the particle orientation from the two-dimensional super-resolution catalysis map. Further examples are shown below in Figure 5.19.

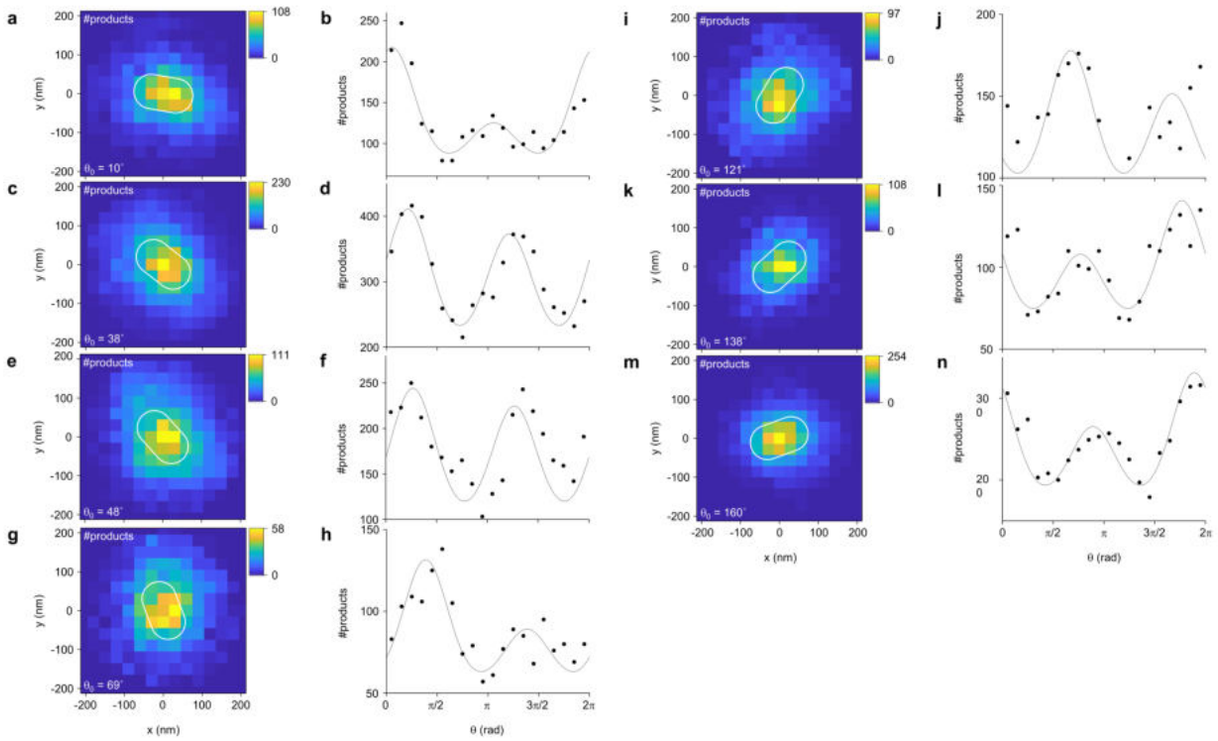

Figure 5.19: Further examples of single particle catalysis maps (a,c,e,g,i,k,m) and the corresponding angular distributions (b,d,f,h,j,l,n). Panels (a,c,e,g,i,k,m) contain a white outline depicting an Au@mSiO$_2$ nanorod. The orientation θ_0 is extracted from the fits in panels (b,d,f,h,j,l,n). Bin sizes are 30 $\times$ 30 nm^2 (a,c,e,g,i,k,m) and $\pi/10$ (b,d,f,h,j,l,n).

Chapter 6

Distinguishing among all possible activation mechanisms of a plasmon-driven chemical reaction

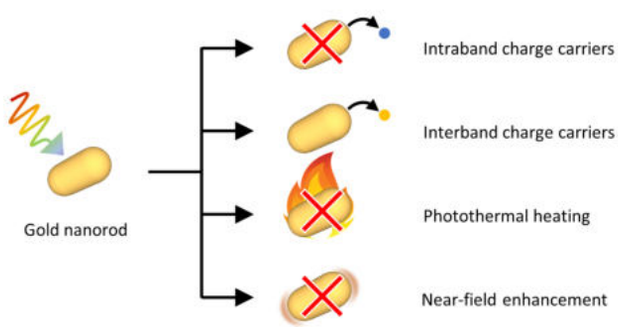

This chapter is based on Ref. 39: ACS Energy Letters 2020, 5(8), 2605-2613.

6.1 Foreword

In section 2.5 and in the previous chapter we have described and studied the different mechanisms by which a plasmon resonance can drive chemical reactions: near-fields, non-equilibrium charge carriers, and plasmonic heating. As all of these mechanisms happen simultaneously and on ultrafast timescales, they are difficult to disentangle experimentally.[30–39] In this chapter, we continue our investigation of how these phenomena can be exploited to activate chemical processes. In particular, here we study the light-driven growth of an Ag shell around Au nanorods and individually address the role of each possible activation mechanism of the reaction.

We first perform the shell growth under dark conditions and characterize it using UV-vis spectroscopy and transmission electron microscopy (TEM). We therefore establish a clear and reproducible relationship between the optical and structural properties of Au@Ag core@shell nanorods with different shell thicknesses. We then perform the shell growth under 532 nm illumination, corresponding to the transverse resonance of the nanorods, and, in a separate experiment, under 730 nm illumination, corresponding to the longitudinal resonance. We pay particular attention to the laser power we use, as we make sure that the amount of absorbed power and, therefore, the temperature increase are the same for both light-driven syntheses. We find that under 730 nm illumination the kinetics of the reaction remain unchanged, whereas under 532 nm illumination

the reaction follows a similar pathway, but at a much faster rate. Although we also perform thermocouple and infrared camera measurements, we can immediately rule out thermal contributions due to the equal amount of absorbed power between the two light-driven syntheses.

To evaluate the contribution of plasmonic near-fields, we perform FDTD simulations. The morphology of the nanorods at different growth stages are extracted from TEM images and are used as an input for the simulations. We find that the electric field intensity increases, whereas the rate enhancement decreases as the reaction progresses. Therefore, contributions of plasmonic near-fields to the shell growth can be ruled out.

To investigate the role of non-equilibrium charge carriers we perform FDTD simulations of the absorbed power. We find that the total amount of absorbed power increases as the reaction progresses, whereas the amount of power absorbed within 4 nm of the surface decreases with a similar trend as the rate enhancement. This observation points to d-band holes generated via interband transitions, which have a mean free path of $\sim$4 nm, as the driving force behind this chemical reaction.

We further corroborate this statement with single particle experiments, in which we characterize the anisotropy of the Ag shell. Intraband carriers are preferentially emitted along the polarization direction of the incident field, whereas interband carriers are emitted isotropically.[58] We observe an isotropic shell growth, which is further evidence for interband carriers driving this chemical reaction.

Abstract

Localized surface plasmon resonances (LSPRs) in metal nanoparticles can drive chemical reactions at their surface, but it is often challenging to disentangle the exact activation mechanism. The decay of LSPRs can lead to photothermal heating, electromagnetic hot spots, and the ejection of non-thermalized charge carriers, but all these processes typically occur simultaneously and on ultrafast timescales. Here, we develop a plasmon-assisted Au@Ag core@shell nanorod synthesis in which each plasmon-decay mechanism can be independently assessed. Using different illumination wavelengths combined with extinction spectroscopy, transmission electron microscopy, thermal characterization, and finite-difference time-domain simulations, we unequivocally identify interband holes as the main driving force behind the silver shell growth. Our conclusion is corroborated by single-particle studies on gold nanospheres that display isotropic reactivity, consistent with interband hole-driven nanoparticle syntheses. Our strategy to discern between plasmon-activation mechanisms can be extended to a variety of light-driven processes including photocatalysis, nanoparticle syntheses, and drug delivery.

6.2 Introduction

Understanding and engineering light-matter interactions is fundamental to a wide variety of photochemical processes from photovoltaics,[158] to (nano)lithography,[159] chemical sensing,[160] drug-delivery,[161] nanoparticle syntheses,[162] and heterogeneous photocatalysis.[23] For example, illumination of metal nanoparticles can tune their activity and selectivity towards industrially relevant catalytic processes, as demonstrated for the epoxidation of propylene on copper nanoparticles[163] and the hydrogenation of carbon dioxide on rhodium nanocubes.[136] Similarly, irradiation of gold and silver nanospheres can be used to photochemically transform them into larger anisotropic structures with very high yield.[164,165] These examples demonstrate how light can act as an ingredient to tailor and accelerate kinetically challenging multi-electron chemical reactions that are unattainable in the dark.[166]

Light-activated processes occurring on metal nanostructures are typically attributed to the excitation of localized surface plasmon resonances (LSPRs).[20] LSPRs are light-driven oscillations of free charge carriers in metal nanostructures that give rise to strong scattering and absorption.[63] Their radiative decay (scattering) generates intense electromagnetic fields at the vicinity of the nanoparticle surface, typically known as near-fields, which can activate photosensitive reactions.[12] On the other hand, the non-radiative decay (absorption) of LSPRs can drive chemical reactions via photothermal heating, that can accelerate temperature-sensitive reactions according to the Arrhenius relation,[27] or via hot charge carriers generated by intraband[22] and interband transitions,[62,167,168] which can activate redox reactions. In most light-driven processes, however, it is often challenging to disentangle and quantify the relative contributions of these mechanisms[30,31,36–38] due to several factors, such as the extremely short lifetimes of hot charge carriers,[20] the low quantum efficiency of photochemical processes,[167] the similar linear power response of photochemical reactions to near-fields and hot charge carriers,[169] non-linear two photon[12] and two electron[166] processes, the typically complex light and heat transport in the reaction volume leading to both nanoscopic and macroscopic temperature rises,[30,170] and the simultaneous generation of interband and intraband carriers under visible light excitation in metals such as gold and copper.[62]

Here, we develop a light-driven Au@Ag core@shell nanorod (NR) synthesis in which each plasmon-activation mechanism can be independently assessed. We first characterize the silver shell growth rate and reaction evolution in the dark, using in situ extinction spectroscopy and transmission electron microscopy. We then compare the growth rate in the dark to the one measured under excitation of either the transverse or the longitudinal plasmon resonances of the gold nanorods,

using a 532 nm or a 730 nm laser, respectively. The laser intensities in the two cases are tuned to obtain the same total amount of absorbed optical power in the reaction volume and therefore the same magnitude of photothermal effects. We find that the silver shell growth rate under excitation of the longitudinal resonance equals the one in the dark and therefore shows no plasmonic enhancement. On the other hand, excitation of the transverse resonance displays strongly enhanced reaction rates at the beginning of the reaction, and this enhancement drastically decreases as the silver shell approaches a thickness of about 4 nm. The striking rate disparity of silver shell growth under identical total absorbed optical power in 532 nm and 730 nm illumination demonstrates the non-thermal nature of the enhancement mechanism, which is later independently confirmed by direct thermal measurements and numerical calculations.

Furthermore, using finite-difference time-domain (FDTD) simulations, we show that the intensity of the near-fields increases with increasing silver shell thickness. As a consequence, near-field enhancements cannot explain the observed time evolution of the reaction rate when using 532 nm light. The absence of any rate enhancement under 730 nm irradiation, which corresponds to an energy just below the interband threshold of gold,[50] shows that low energy plasmonic intraband charge carriers do not contribute to the reaction. Under 532 nm irradiation of gold, however, most of the energy is used to generate hot interband holes,[62] suggesting they are the main contributor for the observed rate enhancement. Strikingly, these holes have typical mean free paths of a few nanometers,[60] corresponding to the silver shell thickness at which plasmon-driven effects are effectively quenched, thereby confirming our interpretation. Finally, we corroborate the nature of the hot charge carriers by monitoring the shell growth at the single-particle level using dark-field scattering spectroscopy. Here, we observe an isotropic nature of the silver shell growth under polarized laser irradiation, which is in agreement with the predicted angular distribution of interband hot holes.[58]

6.3 Results and discussion

6.3.1 Silver shell growth in the dark

Gold nanorods with a length of 78 ± 10 nm and a diameter of 25 ± 5 nm are colloidally synthesized using a seed-mediated growth technique (see sections 6.5.1 and 6.5.4 of this chapter's supporting information).[171] We choose these nanorod dimensions so that we can excite both interband and intraband charge carriers when illuminating at their transverse resonance with a 532 nm laser ($\lambda_{\text{transverse}}$ = 514 nm), while selectively exciting only intraband charge carriers while illuminating at their longitudinal resonance with a 730 nm laser ($\lambda_{\text{longitudinal}}$ = 744 nm) (Figure 6.6). No interband charge carriers can be generated in gold for excitation wavelengths above ∼700 nm.[50]

To discriminate the mechanisms underlying our plasmon-driven chemistry, we use an Au@Ag core@shell nanorod synthesis adapted from a previously reported method.[30] Briefly, aqueous solutions of bis(p-sulphonatophenyl)phenylphosphine dihydrate dipotassium (BSPP), AgNO3, and ascorbic acid are added to a gold nanorod suspension, to yield a final optical density of 0.36 (see Methods section 6.5.1 and Figure 6.1a). The growth of the core@shell nanoparticle occurs via the reduction of Ag^+ to Ag^0 and the concomitant oxidation of ascorbic acid on the gold nanorod surface.[172] The Ag:BSPP ratio is tuned to 2.5, in order to slow down the silver shell growth in dark conditions. The suspension is kept in a temperature-controlled cuvette holder and is actively cooled to 6 °C using a water bath, along with magnetic stirring at 300 rpm.

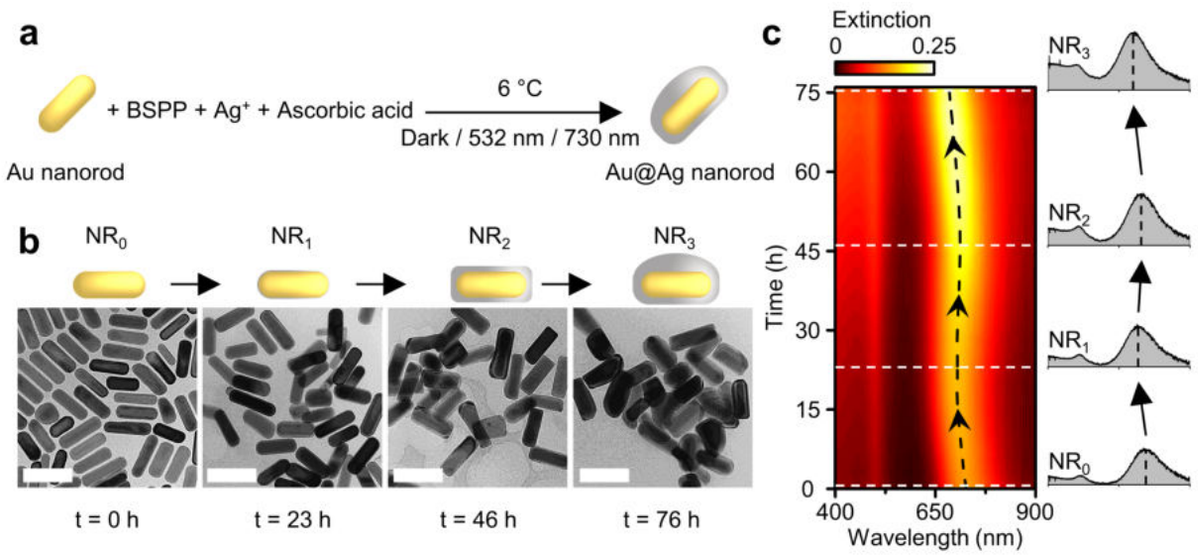

Figure 6.1: Core@shell growth in the dark. (a) Schematic representation of the Au@Ag core@shell nanorod synthesis. (b) TEM images and representative sketches of Au@Ag core@shell nanorods grown in dark conditions at times t = 0 h (NR_0), 23 h (NR_1), 46 h (NR_2), and 76 h (NR_3). The scale bars correspond to 100 nm. (c) Colormap of the time evolution of the extinction spectrum of the Au@Ag core@shell nanorod solution in the dark. The extinction spectra are measured through the 4 mm path length of the cuvette. White dashed lines correspond to the times at which TEM images are taken. The black dashed line indicates the shift in plasmon resonance with time.

We first perform the core@shell synthesis in the dark for 76 h and monitor the silver shell growth using transmission electron microscopy (TEM) and in situ extinction spectroscopy (Figure 6.1b,c). TEM images of the synthesis after 23 h show the growth of a ∼1 nm conformal silver shell around the gold nanorods (Figure 6.6). This nanorod structure is henceforth referred to as NR_1, with NR_0 corresponding to the initial bare gold nanorods. The growth of a 1 nm conformal silver shell induces a blue shift of the longitudinal plasmon resonance of ∼24 nm, as shown in Figure 6.1c. The initial conformal shell growth is followed by the formation of a cuboidal structure with sharp corners and a silver shell that reaches a thickness of about 4 nm after 46 h (NR_2). The formation of cuboidal nanorods is accompanied by a red shift of ∼9 nm of their longitudinal plasmon resonance. Finally, over the course of 76 hours, the reaction proceeds further leading to even thicker and often asymmetric silver shells (NR_3), which gives rise to a blue shift of the longitudinal plasmon resonance of ∼30 nm. Our proposed correlation between the measured spectral changes and the morphology of the growing core@shell nanostructures identified by TEM measurements is consistent with the FDTD calculations (Figure 6.6).

6.3.2 Silver shell growth under plasmon excitation

After studying the silver shell growth dynamics and shape evolution in the dark, we repeat the synthesis under two different laser illumination conditions. In a 10 × 4 mm cuvette, a 500 µL nanorod growth mixture is illuminated using a 240 mW 532 nm or a 55 mW 730 nm continuous wave (cw) laser, in separate experiments. These laser powers are chosen so that the total optical power absorbed inside the reaction volume is the same in both irradiation experiments, as determined by modeling the photon propagation inside the nanorod suspension using Monte Carlo calculations (Figure 6.7).[170]

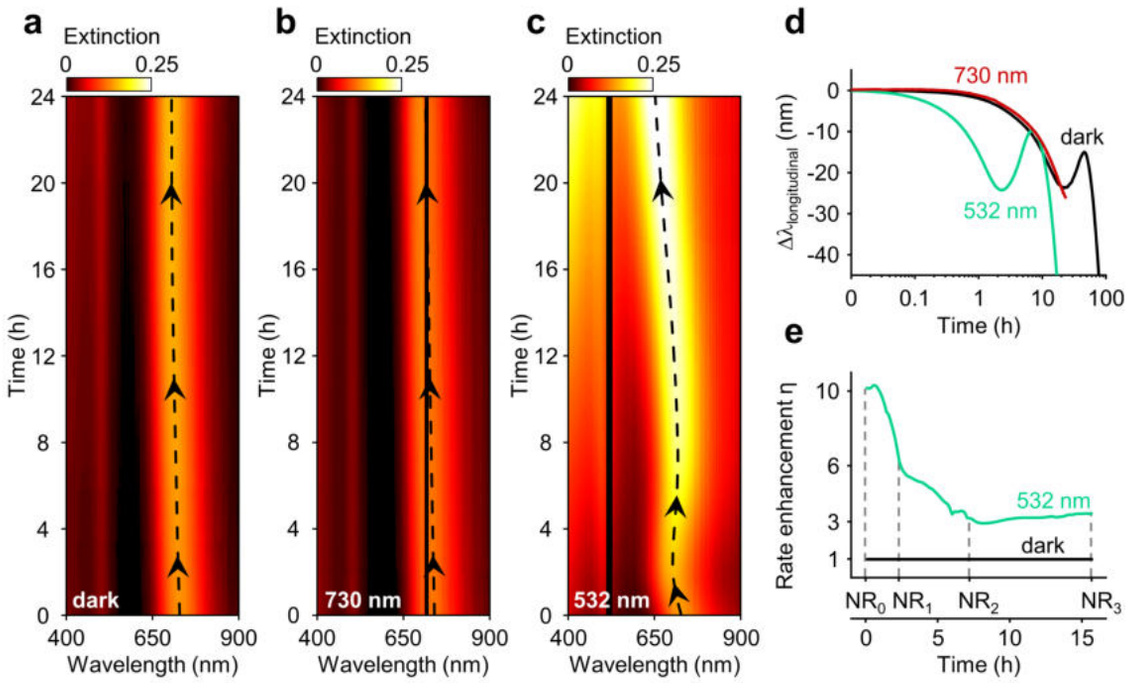

Figure 6.2: Core@shell growth under illumination. (a, b, c) Time evolution of the extinction spectra of Au@Ag core@shell nanorods over a period of 24 h under (a) dark conditions, (b) 55 mW 730 nm laser illumination, and (c) 240 mW 532 nm laser illumination. The black vertical lines in panels b and c correspond to the laser wavelengths which are blocked by notch filters. The black dashed lines indicate the shift in plasmon resonances with time. (d) Time evolution of the longitudinal plasmon resonance under different illumination conditions. (e) Rate enhancement of silver shell growth under 240 mW 532 nm (green) illumination compared to the experiment in dark, plotted as a function of the reaction time under 532 nm illumination.

From our in situ extinction spectroscopic measurements during 24 hours of illumination with the 730 nm laser, we find a spectral evolution similar to the one measured in dark conditions (Figure 6.2a,b). Similar to the reaction in the dark, the longitudinal and transverse plasmon resonances blue shift by ∼25 nm and ∼3 nm, respectively, along with an increase in extinction (see also Figure 6.8). TEM images after 24 h also exhibit similar silver shell growth as in the dark (Figure 6.8).

On the contrary, during 24 h illumination with the 532 nm laser, the in situ extinction measurements display remarkable spectral changes when compared to the experiments in the dark and under 730 nm irradiation (Figure 6.2c). The longitudinal plasmon resonance initially blue shifts from 743 nm to 721 nm in 2 h, followed by a 14 nm red shift of the resonance in the next 5 h, and then again a blue shift of 65 nm at the end of 24 h. The transverse resonance also blue shifts by 15 nm along with the appearance of a new peak at ∼420 nm (see also Figure 6.8).

We assess the growth kinetics by tracking the changes in the longitudinal plasmon resonance during the experiments in the dark and under 532 nm and 730 nm illuminations (Figure 6.2d). The similar growth kinetics for the 730 nm illumination and the dark experiments show that no significant plasmon-driven silver shell growth occurs under these illumination conditions. Strikingly, the spectral changes under 532 nm illumination over a period of 24 h and under dark conditions over a period of 76 h are very similar, indicating a similar reaction pathway, albeit with a rate of spectral changes that is significantly faster for the 532 nm illumination experiment.

To quantify such rate enhancement, η, we first find the time, t_{dark}, at which a certain LSPR wavelength is reached in the dark. We then find the time, $t_{532\,\mathrm{nm}}$, at which the same LSPR wavelength is reached under 532 nm illumination (Figure 6.9). From these values, we define the rate enhancement as $\eta = \partial t_{\mathrm{dark}}/\partial t_{532\,\mathrm{nm}}$ (Figure 6.2e). We observe an initial tenfold rate enhancement that quickly decreases and stabilizes to roughly a threefold enhancement at growth stage NR_2, corresponding to a silver shell thickness of ∼4 nm.

In the following sections we will show how the observed large rate enhancement under 532 nm irradiation can be unequivocally attributed to the generation of hot holes in the gold cores via interband transitions, and to which extent other plasmonic activation mechanisms are contributing to the photochemical rate.

6.3.3 Photothermal effects

The non-radiative decay of LSPRs leads to local temperature increases on the gold nanorod surface, $\Delta T_{\mathrm{local}}$, which under cw irradiation can be quantified using:[27,155]

$$\Delta T_{\mathrm{local}} = \frac{\sigma_{\mathrm{abs}} I}{4\pi\beta\kappa R_{\mathrm{eq}}} \tag{6.1}$$

where σ_{abs} is the absorption cross section of the nanorod, I is the illumination intensity (optical power per unit area), β is the thermal capacitance coefficient of a nanorod, κ is the thermal conductivity of the surrounding medium, and R_{eq} is the radius of a sphere equivalent to the volume of the nanorod. Under our laser intensities, we calculate that localized photothermal effects are negligible with $\Delta T_{\mathrm{local}} \approx$ 1 - 3 mK (Figure 6.10).

The simultaneous illumination of a large number of nanoparticles in ensemble experiments, however, can lead to the rise of non-localized, macroscopic collective heating effects accompanied by large temperature gradients and non-trivial heat transport via conduction and convection. These collective photothermal effects can be several orders of magnitude larger than the localized ones and could in principle increase our reaction temperature by tens of kelvin.[30,156,170,173] In our experiments, however, the power absorbed inside the reaction volume is the same under 532 nm and 730 nm illumination (Figure 6.7) and similar photothermal effects will therefore be generated in both irradiation experiments. As plasmonic enhancements are only observed for 532 nm illumination and not for 730 nm illuminations, we can confidently eliminate the contributions of photothermal effects in our silver shell growth.

Moreover, infrared camera and thermocouple measurements on the nanoparticle suspensions under plasmon excitation reveal experimental temperature increases in the reaction volume smaller than 1 K (Figure 6.10). Such a low temperature rise, which is corroborated by numerical modeling of the heat propagation inside the reaction volume (Figure 6.10), cannot explain the observed tenfold increase in the reaction rate.

6.3.4 Near-field enhancement

After ruling out any photothermal contribution to the silver shell growth, we investigate the effect of near-field enhancements using FDTD simulations. We calculate the electric field enhancement generated under 532 nm excitation using a three-dimensional electric field monitor around Au and Au@Ag nanorods corresponding to the four growth stages identified experimentally (Figure 6.3a). To avoid artefacts due to a finite mesh size at the nanoparticle surface, we calculate the average near-field enhancement, ⟨NFE⟩, at distances between 0.5 nm to 10 nm away from the nanoparticle surface (Figure 6.11) using:

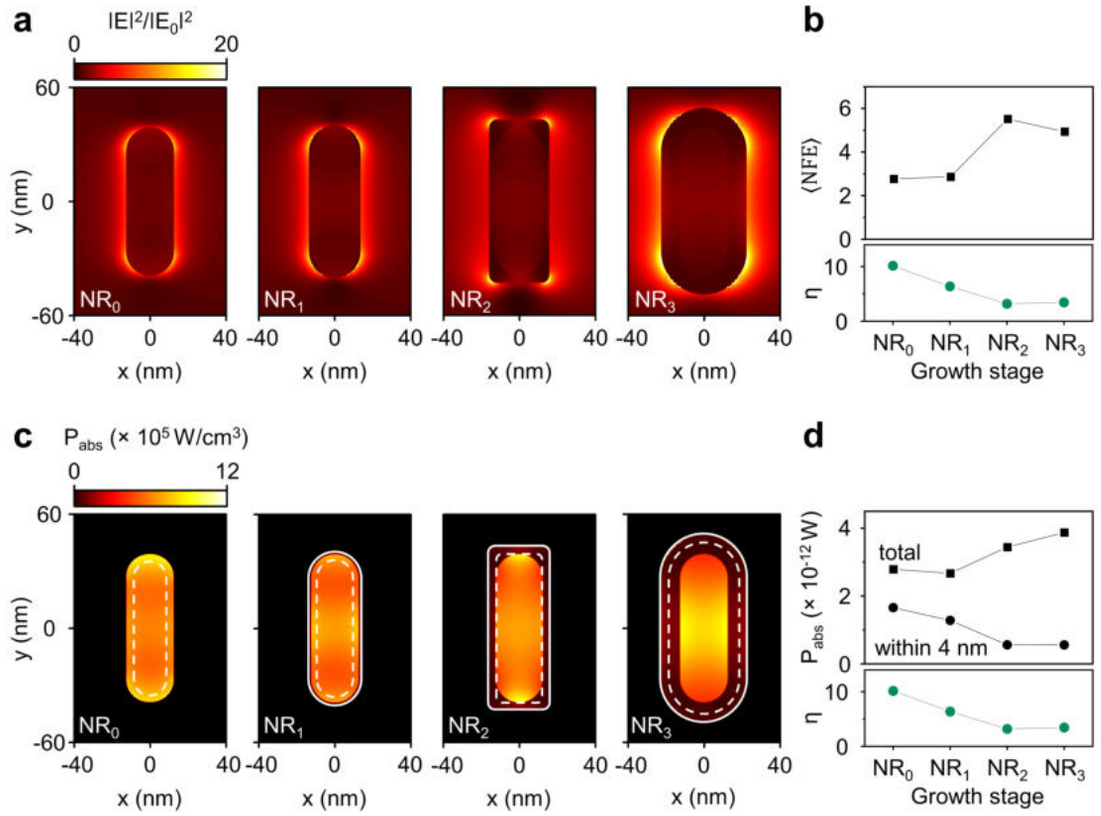

Figure 6.3: Near fields and hot charge carrier contributions. (a) 2D slices of the FDTD calculated electric field enhancements monitored at the center of the Au@Ag core@shell nanorods visualized at different silver shell growth stages corresponding to NR_0, NR_1, NR_2 and NR_3, under 532 nm illumination. (b) (top panel) Average near-field enhancement, $\langle NFE \rangle$, calculated by integrating the electric field intensities between distances of 0.5 nm and 10 nm from the nanoparticle surface at different silver shell growth stages. (c) 2D slices of the FDTD calculated absorbed power distribution monitored at the center of the core@shell nanorod at different silver shell growth stages, under 532 nm illumination. The white solid lines depict the boundaries of the core@shell nanorod and the white dashed lines correspond to a distance of 4 nm inwards from the nanorod surface. (d) (top panel) Total power absorbed (black squares) and power absorbed inside a 4 nm range inwards from the nanorod surface (black circles) under our experimental laser intensity plotted as a function of the silver shell growth stage. The bottom panels in Figure 6.3b and 6.3d correspond to the experimentally measured plasmonic rate enhancement at different silver shell growth stages under 532 nm illumination, extracted from the full time evolution shown in Figure 6.2e. The lines connecting the symbols in Figure 6.3b and 6.3d are guides to the eye.

$$\langle \mathrm{NFE} \rangle = \frac{1}{V} \iiint_{0.5\,\mathrm{nm} < r < 10\,\mathrm{nm}} \frac{|E|^2}{|E_0|^2} \mathrm{d}V \tag{6.2}$$

where V is the integrated volume, r is the distance from a mesh cell outside of the nanorod to the nanorod surface, E is the electric field, and E_0 is the incident field. The calculated average near-field enhancement at the nanorod surface increases with the silver shell growth, as shown in Figure 6.3b. The time evolution of $\langle \mathrm{NFE} \rangle$ is in sharp contrast with the experimentally measured decrease in rate enhancement over the course of the reaction (Figure 6.3b, bottom panel), allowing us to rule out the role of near-fields as the dominant contributor to our plasmon-driven reaction.

6.3.5 Hot charge carriers

The absence of any plasmonic rate enhancement for silver shell growth under 730 nm illumination (Figure 6.2d) indicates that the generated intraband carriers are not sufficiently energetic to activate the core@shell growth. The carriers generated under 532 nm illumination, however, are able to significantly influence the reaction rate (Figure 6.2e). Partially thermalized hot carriers have energies close to the Fermi level, with the electron temperature of the thermalized distribution being mainly determined by the total absorbed optical power and not by the excitation wavelength.[134,174] The reaction rates observed under different illumination wavelengths therefore suggest that the main driving force behind the enhancement under 532 nm illumination is due to non-thermalized (first generation) carriers. To investigate the role of interband and intraband charge carriers generated under 532 nm illumination, we calculate the power absorbed inside the nanorods at different stages of the silver shell growth using FDTD simulations (Figure 6.3c). Carriers generated in the sp-band of gold, i.e. intraband electrons, intraband holes, and interband electrons have high carrier velocities and typical mean free paths (MFPs) of 10 – 40 nm.[60] As these MFPs are similar to the nanorod size, all of these carriers could potentially contribute to the growth of the silver shell. Interband holes in the d-band, however, have significantly lower carrier velocities and MFPs typically smaller than 5 nm.[60] To discriminate the role of interband and intraband charge carriers, we therefore compare the observed rate enhancement with the total power absorbed inside the nanorod and the power absorbed within 4 nm from the nanorod surface for the different silver shell growth stages (Figure 6.3d).

The total power absorbed inside the nanorod under 532 nm illumination (Figure 6.3d, black squares) increases with increasing silver shell growth. The power absorbed within 4 nm from the nanorod surface (Figure 6.3d, black circles), however, decreases with increasing silver shell thickness. In our light-driven synthesis under 532 nm irradiation, the measured plasmonic rate enhancement decreases roughly 3× from the growth stage NR_0 to NR_2 (see Figure 6.2e or bottom panels in Figure 6.3b,d), which is quantitatively similar to the trend calculated for power absorbed within 4 nm from the nanorod surface (Figure 6.3d). This agreement strongly implies that the experimentally observed plasmonic enhancement has to be attributed to charge carriers with an MFP of ∼4 nm, i.e. hot d-band holes generated in the plasmonic gold cores. This interpretation is also consistent with the low losses in silver at 532 nm,[44] which results in carriers being primarily generated in gold. Such photogenerated carriers have to travel through the silver shell in order to perform redox reactions at the nanorod surface, which increases their recombination probability as the silver shell grows beyond a few nanometers in thickness.

The silver shell growth reaction involves the reduction of silver ions and the oxidation of ascorbic acid at the surface of the metal nanoparticles. However, the drastic decrease of plasmonic rate enhancement when the silver shell thickness approaches a value comparable to the mean free path of d-band holes (∼4 nm) indicates that the consumption of holes by ascorbic acid is the rate-limiting step of the plasmon-driven process.[162,167,174,175] Note that no silver shell growth is observed in a control experiment under 532 nm irradiation in the absence of ascorbic acid. Our results can therefore be interpreted in the framework of a reduced activation barrier for ascorbic acid oxidation under 532 nm illumination as compared to the reaction in the dark or under 730 nm illumination (Figure 6.4).[176] Under 730 nm laser irradiation, only intraband absorption can occur and the photon energy (= 1.70 eV) will be on average evenly distributed between short-lived, hot electrons and holes with mild reducing and oxidizing potentials.[174] Upon 532 nm irradiation, however, the photon energy (= 2.33 eV) is preferentially absorbed via interband transitions giving rise to a larger fraction of hot holes with high chemical potentials and therefore low activation energies towards the oxidation of ascorbic acid.[62,174]

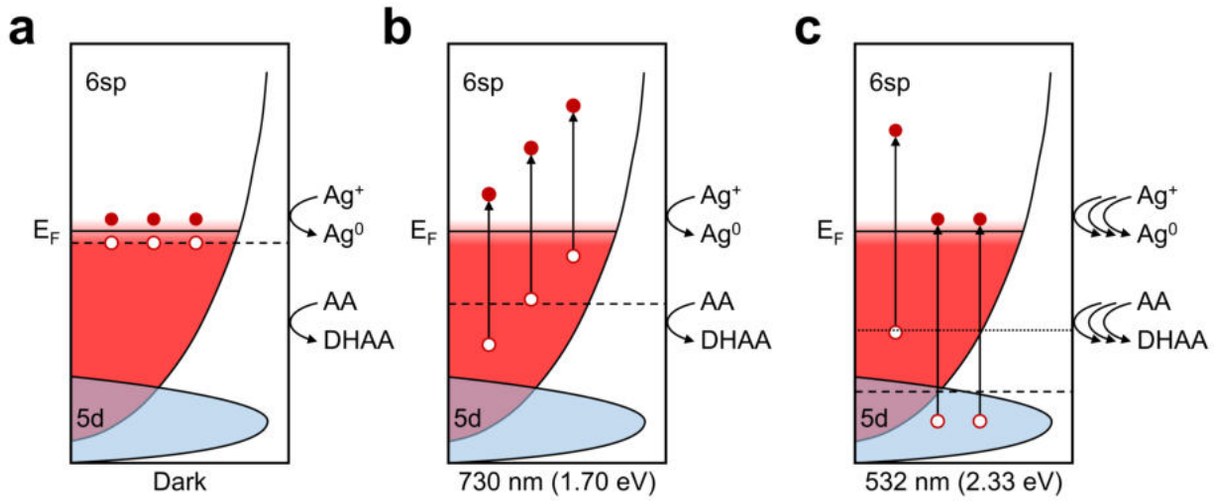

Figure 6.4: Hot hole-assisted silver shell growth. Schematic representation of the energy levels for the plasmon-driven oxidation of ascorbic acid (AA) to dehydroascorbic acid (DHAA) and subsequent reduction of Ag^+ to Ag^0 on gold nanorods under (a) dark conditions, (b) 730 nm illumination, and (c) 532 nm illumination. The red and white circles denote electrons and holes respectively. The dashed lines in panel b and c represent the average energy of non-thermalized holes under plasmon excitation. The dotted line in panel c represents the average energy of non-thermalized intraband holes, which are the only ones contributing to the plasmon-enhanced reactivity for shell thicknesses >4 nm.

A much lower but still significant residual rate enhancement of ∼3× with respect to the dark is observed at the growth stages NR_2 and NR_3, which points to the role of non-thermalized intraband hot holes, characterized by a relatively high potential energy (dotted line in Figure 6.4c) and long mean free paths. Ab initio calculations for 20 nm radius gold nanospheres (equivalent to the volume of our gold nanorods) have previously shown that, under 532 nm illumination, the amount of generated interband carriers is twice the amount of intraband ones.[62] In our experiments, while both interband and intraband holes contribute to the silver shell growth in the beginning (NR_0), only intraband holes can reach the nanorod surface and drive the oxidation of ascorbic acid when the silver shell thickness grows above ∼4 nm (NR_3). By comparing the plasmonic rate enhancement at the growth stages NR_0 and NR_3, and by considering that only intraband holes contribute at NR_3, we find a ratio of 2:1 for interband and intraband holes, which is in qualitative agreement with theoretical predictions.

6.3.6 Single-particle studies confirm the role of interband holes

Thanks to their high chemical potentials, non-thermalized (first generation) carriers in metal nanoparticles are the major contributors to plasmon-driven charge injection in photodetection and photocatalytic processes.[168] The angular distribution of these charge carriers strongly depends on their photogeneration mechanism, with interband charge carriers being uniformly distributed inside the nanoparticles and intraband charge carriers closely following the polarization of the incident light.[58] Such angular dependence suggests an alternative method to distinguish hot charge carrier processes driven by interband and intraband transition events. Here we use the same photochemistry used in our ensemble nanorod experiments to study the spatial profile of laser-driven silver shell growth, by measuring the dark-field scattering spectra of several individual Au@Ag core@shell nanospheres grown under polarized laser excitation. We choose spheres over nanorods for single particle measurements as it is challenging to follow the transverse plasmon resonance of nanorods, due to their extremely low scattering cross-sections. Furthermore, the use of spherical gold nanoparticles ensures a homogeneous surface chemistry and allows us to com-

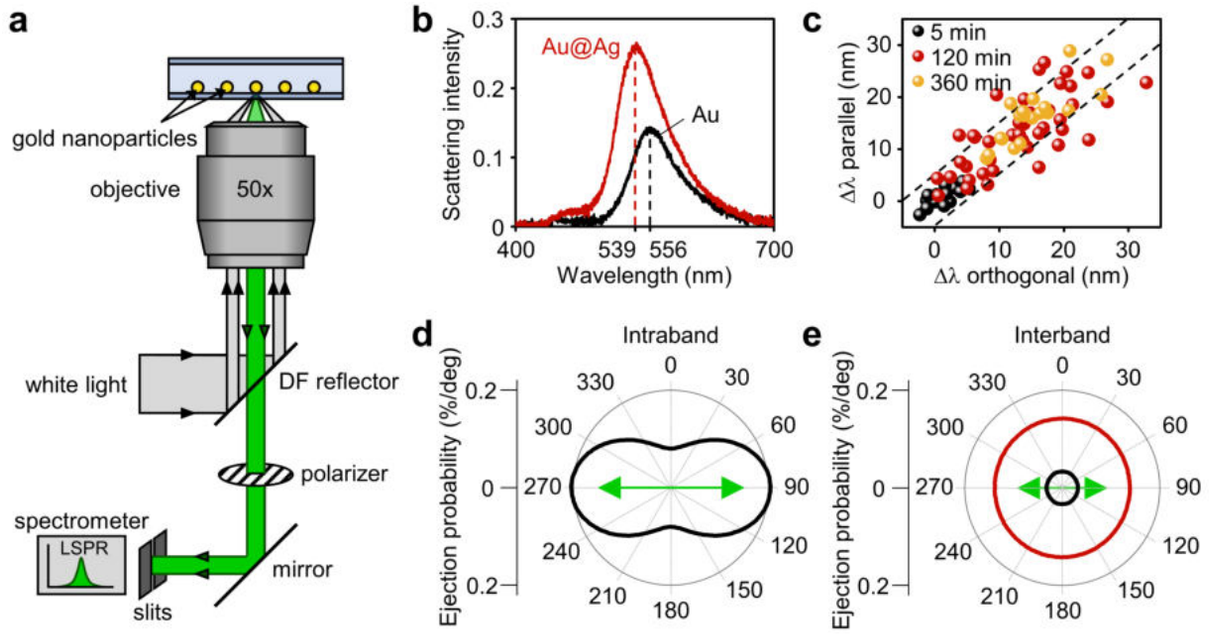

Figure 6.5: Spatial profile of hot charge carriers in single nanoparticles. (a) Illustration of the dark-field microscope used for single-particle studies of light-driven Au@Ag core@shell nanosphere synthesis. (b) Dark-field scattering spectra of a single gold nanoparticle (black curve) and corresponding Au@Ag core@shell nanoparticle (red curve) synthesized under 532 nm laser illumination. (c) Measured LSPR blue shift of several Au@Ag core@shell nanoparticles at polarizations parallel and perpendicular to the laser polarization. The blue shifts are measured from experiments with three different illumination periods of 5 min (black circles), 120 min (red circles), and 360 min (yellow circles). The dashed lines correspond to a difference of silver shell thickness of ± 1 nm at the orthogonal polarizations. (d, e) Calculated polar plots displaying the spatial ejection probability of (d) intraband (MFP = 30 nm for both electrons and holes) and (e) interband (MFP = 30 nm for electrons and 5 nm for holes) charge carriers. The red and black lines represent the spatial profile of electrons and holes respectively. The green arrow represents the laser polarization.

pare orthogonal laser polarizations without adjusting for the different longitudinal and transverse absorption cross-sections of a nanorod. Briefly, a dilute suspension of 66 nm gold nanospheres is drop casted on a glass slide and allowed to dry, followed by the assembly of a flow cell around the nanoparticles using a glass slide and epoxy glue. The flow cell is then mounted on to a dark-field microscope (Figure 6.5a), where the scattering spectra of single nanoparticles are measured before and after their laser irradiation (see section 6.5.2). A silver growth solution is injected in to the flow cell, followed by 532 nm cw laser illumination of several nanoparticles at an intensity of 166 W cm^{-2}. The spectral sensitivity of our dark-field setup allows us to detect spectral shifts down to ∼1 nm, corresponding to a silver shell thickness variation of ∼2 Å. In our experiments, the laser intensity is chosen so as to generate negligible local temperature increases of ∼60 mK and collective heating effects of ∼0.1 K (Figure 6.12). Several experiments are performed by varying the illumination times from 5 min to 6 h.

In Figure 6.5b, we plot the measured plasmon resonance of a typical single gold nanoparticle before and after silver shell growth. After laser irradiation, the plasmon resonance blue shifts by 17 nm indicating the formation of a ∼4 nm silver shell according to Mie theory calculations (Figure 6.13). No silver growth is observed in the absence of laser irradiation or in the absence of gold nanoparticles, confirming the plasmonic contribution to the silver shell growth (Figure 6.14). To investigate the morphology of the core@shell nanoparticles, we place a polarizer in the

dark-field scattering pathway of the nanoparticles (Figure 6.5a). By measuring the plasmon resonance of the nanoparticle before and after illumination at polarizations parallel and orthogonal to the laser polarization, we can estimate the silver shell growth along different directions. We find similar LSPR blue shifts at orthogonal polarizations indicating that the light-induced Au@Ag core@shell nanoparticle growth is isotropic (Figure 6.5c). We compare this isotropic growth to Monte Carlo simulations of the angular distribution of non-thermalized carriers reaching the nanoparticle surface (see section 6.5.3 and Figure 6.15). In this model we generate carriers with a spatial distribution proportional to the absorbed power and we assign a propagation direction to each carrier. The propagation length follows an exponential distribution with the mean free path as the characteristic length. The propagation angle follows the predicted distributions for interband or intraband carriers.[58,168] We only evaluate carriers that reach the nanoparticle surface ballistically, by neglecting scattering at the nanoparticle surface and with other carriers. Carriers generated via intraband transitions have $\cos^2\theta$ and $|\cos^3\theta|$ contributions in their angular distribution, as they are accelerated along the direction of the optical field.[58,168] Here, θ is the angle between the laser polarization vector and the carrier propagation vector. This angular dependence is reflected in the angular distribution of hot carriers reaching the surface (Figure 6.5d). Conversely, carriers generated via interband transitions have an isotropic angular distribution, as the wavevector of the field does not appear in the matrix element of the Hamiltonian describing the transition.[58,168] This lack of angular dependency results in an isotropic distribution of hot carriers reaching the surface (Figure 6.5e). The observation of isotropic silver shell growth therefore suggests that the reduction of Ag^+ ions is not directly driven by non-thermalized intraband electrons.

Furthermore, by grouping the experimentally measured resonance shifts according to the illumination time, we find that the silver shell growth occurs predominantly between 0 – 2 h, and that further growth is negligible at longer time scales (Figure 6.5c). An average blue shift of 16 ± 5 nm is observed after 6 h of illumination, suggesting a growth of 3.5 ± 1 nm silver shell around the gold nanospheres, according to Mie calculations. Similar to our bulk experiments, in which plasmonic enhancement is quenched after the growth of a ∼4 nm shell, the suppression of silver shell growth after 4 nm thicknesses also points to the quenching of d-band holes reaching the nanoparticle surface, due to their extremely short mean free path.

6.4 Conclusion

In summary, we have designed a light-driven Au@Ag core@shell nanoparticle synthesis in which all mechanisms of plasmon activation can be independently assessed. By proper choice of the illumination conditions and by accurate characterization and modeling of the structural, optical, and thermal properties of our growing core@shell nanoparticles, we exclude photothermal and near-field effects and identify d-band holes in gold as the main driving force behind the silver shell growth. Single-particle studies corroborate our conclusions from ensemble experiments, showing a quickly decreasing reaction rate with increasing shell thickness and isotropic silver growth under polarized illumination. Despite the low reduction potential of silver ions, our experiments suggest that plasmonic electrons in gold nanoparticles under 532 nm irradiation are able reduce silver ions only after the corresponding holes have been scavenged through the oxidation of ascorbic acid. The observed relative contribution of intraband and interband activation mechanisms in our plasmon-driven reaction is strongly dependent on the chemical properties of the species involved, including their reduction and oxidation potentials, their binding energies to the metal catalysts, and the evolving surface chemistry of the growing nanoparticle. Our strategy of combining an accurate choice of illumination parameters with detailed numerical modeling of the irradiated plasmonic nanostructures can be extended to the study of a variety of plasmon-driven processes in which several mechanisms simultaneously contribute to the observed reaction rate, from nanoparticle syntheses, to heterogeneous photocatalysis, and photothermal drug delivery.

6.5 Supporting information

6.5.1 Syntheses

Materials and methods

L-Ascorbic acid (≥99%), bis(p-sulphonatophenyl)phenylphosphine dihydrate dipotassium salt (97%), silver nitrate (99.9999%), cetyltrimethylammonium chloride (CTAC, 25 wt.% in H_2O), gold(III) chloride trihydrate (≥99.9%), potassium bromide (≥99%), sodium borohydride (99%), cetyltrimethylammonium bromide (CTAB, ≥98%) are purchased from Sigma Aldrich. All the solutions are prepared using deionized Milli-Q water (18.2 MΩ cm at 25 °C).

Synthesis of gold nanorods

Gold nanorods are synthesized by adapting a previously reported colloidal seed mediated technique.[171] Spherical gold seeds are synthesized first by mixing aqueous solutions of HAuCl4 (5 mL, 0.5 mM) and CTAB (5 mL, 200 mM) in a round bottom flask (RBF). Ice-cold NaBH4 (0.6 mL, 10 mM) is added to the RBF in one shot, under vigorous stirring. The solution is aged for 30 min at room temperature.

To synthesize the nanorods, CTAB (1.8 g) and KBr (0.7 g) are dissolved in 50 mL of warm water in another RBF, followed by cooling the flask to 30 °C. $AgNO_3$ (2.4 mL, 4 mM), HAuCl4 (50 mL, 1 mM), and ascorbic acid (0.9 mL, 64 mM) are added to the above solution at intervals of 15 min. The solution is mixed well after each addition step. Finally, the gold seed solution (0.16 mL) is added to the above mixture and stirred for 30 s, and left undisturbed for 12 h at 30 °C. The nanorods are washed multiple times in 25 mM CTAC solutions by centrifugation at 8000 × g for 25 minutes. The washed nanoparticles are finally dispersed in Milli-Q water.

Synthesis of Au@Ag core@shell nanorods

Au@Ag core@shell nanorods are synthesized by adapting a previous report.[30] Gold NRs (60 µL) are mixed with water (960 µL) to obtain a final optical density of ∼0.36. Aqueous solutions of BSPP (30 µL, 375 mM), $AgNO_3$ (30 µL, 150 mM), and ascorbic acid (90 µL, 1.5M) are added sequentially to the above suspension. The suspension is mixed well after the addition of each reactant.

500 µL of the above suspension is transferred in to a 10 × 4 mm quartz cuvette with a magnetic stir bar. The cuvette is then placed inside a Quantum Northwest Qpod 2e/MPKIT temperature-controlled cuvette holder at 6 °C, under constant stirring at 300 rpm. The temperature of the cuvette holder is maintained using an external water bath.

Depending on the experiment, we either keep this suspension in the dark or under illumination by a 532 nm or 730 nm cw laser. In situ extinction measurements are performed by aligning a halogen white light source to a fiber spectrometer, through the 4 mm path length of the cuvette.

Synthesis of gold nanospheres

Gold nanospheres of 66 nm diameter are synthesized by adapting a previously reported colloidal seed mediated technique.[177] $HAuCl_4$ (5 mL, 0.5 mM) and CTAB (5 mL, 200 mM) aqueous solutions are mixed together in an RBF, followed by the addition of $NaBH_4$ (0.6 mL, 10 mM) in one shot. The solution is then immediately stirred for 2 min. The solution is kept undisturbed at 27 °C for 3 h, to synthesize CTAB capped Au nanoclusters.

In a clean RBF, CTAC (40 mL, 200 mM), ascorbic acid (30 mL, 100 mM), and the CTAB capped gold nanoclusters (1 mL) are added in sequence and mixed at 27 °C. $HAuCl_4$ (40 mL, 0.5 mM) is then added to the above mixture in one shot, under constant stirring for 15 min, to form 10 nm gold nanoseeds. These nanoseeds are initially centrifuged (18,000 × g, 90 min) and redispersed in water. These gold nanoseeds are centrifuged again (18,000 × g, 60 min) and redispersed in a CTAC solution (1 mL, 20 mM).

In another RBF, CTAC (40 mL, 100 mM), ascorbic acid (2.6 mL, 10 mM), and 10 nm gold nanoseeds (0.1 mL) are added in sequence and mixed at 27 °C. $HAuCl_4$ (40 mL, 0.5 mM) is then added to the above mixture using a syringe pump at a rate of 40 mL/h, under constant stirring. The final product is centrifuged thrice (7200 × g, 10 min) in 20 mM CTAC and finally dispersed in Milli-Q water.

Synthesis of individual Au@Ag core@shell nanospheres on a glass substrate

Single-particle studies on the growth of core@shell nanoparticles are performed inside a glass flow cell. Glass slides and coverslips are first treated with 2 M KOH at 80 °C for 20 min, followed by sonication in water, to render their surfaces hydrophilic. A few microliters of a very dilute suspension (optical density < 0.01) of 66 nm gold nanospheres is drop casted on to the coverslip followed by atmospheric drying. A flow cell is fabricated around the nanospheres by gluing the coverslip on to a glass slide with two 1 mm holes, using a two-part epoxy. The two holes on the glass slide act as the inlet and outlet for the silver shell growth solution. The silver growth solution which is injected into the flow cell using a syringe pump is similar to the one used in ensemble experiments, except that the silver to ascorbic acid ratio was reduced to 1:1, in order to prevent any spontaneous silver formation in the dark. The plasmon resonance of selected individual nanoparticles is recorded using the dark-field microscope, followed by 532 nm cw laser irradiation for varying amounts of time, to synthesize the Au@Ag core@shell nanospheres.

6.5.2 Instrumentation

In situ extinction spectroscopy of Au@Ag core@shell nanorod synthesis is performed by placing a tungsten halogen light source (Ocean Optics HL-2000) and a spectrometer (Ocean Optics HR 4000) normal to the laser irradiation pathway. A 365 nm long pass filter coupled with neutral density filters is placed in front of the light source to remove any ultraviolet light which could trigger self-nucleation of silver nanoparticles. In all experiments, including in the dark, the growth of Au@Ag core@shell nanorods is followed in real time with visible light transmission spectroscopy, using a low intensity tungsten halogen light source. In order to rule out any contribution to the reaction rate of the halogen lamp, we performed a control experiment in the absence of continuous illumination and measuring the plasmon resonance at intervals of 1 hour. We did not find any difference in the optical properties of the solution when compared to the one under continuous illumination with the low intensity halogen lamp. Ex situ extinction spectroscopy is performed using a Perkin Elmer Lambda 1050 UV-Vis-NIR spectrometer. 532 nm laser excitation of gold nanorods is performed using a CNI-MGL-532 cw laser, whose power can be varied from 0 – 470 mW. 730 nm laser irradiation is performed using a Crystalaser DL730-050-0 cw laser, whose power can be varied from 0 – 55 mW. Laser powers are measured using a thermopile sensor (Newport, 919P-030-18) which is connected to a power meter (Newport, 2936-R). The laser beam profile and diameters for ensemble experiments are measured using a CCD camera beam profiler (Thorlabs). The mean diameter of the 532 nm (240 mW) and 730 nm (55 mW) laser spots are 1.5 mm and 1.7 mm, respectively. TEM measurements are performed by centrifuging the core@shell nanorods and then drop casting them on carbon membranes supported on a Cu grid, which is then taken to a JEOL JEM-2001 transmission electron microscope. Thermal characterizations are performed using a Fluke Ti200 infrared camera and a K-type thermocouple (CHAL-005) connected to a data logger (OM-ELUSB-TC), both obtained from Omega Engineering Limited.

Dark-field single-particle spectroscopy is performed on a Zeiss Axio Observer microscope equipped with a scanning x,y piezo-stage. The plasmon resonance of nanoparticles before and after illumination are measured by illuminating them with an LED lamp (Zeiss Illuminator microLED) focused through an EC epiplan 50× objective (NA = 0.75) via a dark-field reflector. The back scattered light from the nanoparticles is collected with the same objective and guided to an Andor Newton EMCCD camera coupled to an Andor Shamrock 500i spectrometer. For laser illumination experiments, a collimated Gaussian beam (∼308 µm diameter) is directed on to the coverslip containing gold nanoparticles using the same objective but using a bright-field reflector cube. The laser beam (CNI laser, MGL-FN-532) power is kept at 43 mW. The laser power at the sample is measured by keeping the Newport thermopile sensor close to the microscope objective.

6.5.3 Optical calculations

The absorption and scattering cross-sections, electric field enhancements, and the absorbed power inside the Au and Au@Ag core@shell nanorods are calculated using Lumerical FDTD.[123] All simulations are performed with a background refractive index of 1.333, corresponding to water. A total-field scattered-field (TFSF) light source with a wavelength range of 400-950 nm is used in the simulations. For gold, we use the dielectric function from Johnson and Christy[45] and for silver, we use dielectric functions from Yang et al.[44] The mesh size is set to 0.25 × 0.25 × 0.25 nm^3. Gold nanorods corresponding to growth stage NR_0 are modelled as rounded cylinders with a length of 78 nm and a width of 25 nm. Au@Ag core@shell nanorods are modeled by replicating the structures obtained from TEM measurements. The growth stage NR_1 is modeled with a conformal 1 nm silver shell around the aforementioned gold nanorod. Growth stage NR_2 is modeled as a cuboidal Au@Ag core@shell nanorod, with a silver shell thickness of 3.5 nm on the side, 4 nm on the tips and a 3 nm radius of curvature, while growth stage NR_3 is approximated using a 10 nm conformal silver shell.

Monte Carlo modelling of photon propagation inside the reaction vessel is performed using a Monte Carlo script in MATLAB and the heat transfer simulations are performed using COMSOL. A detailed description of these procedures have been reported previously.[30,170]

Monte Carlo modelling of the hot carrier propagation is performed using MATLAB. 10^8 carriers are placed in a 66 nm sphere, with a spatial distribution proportional to the electric field intensity $|E|^2$ inside the nanoparticle. Each carrier is then given a random displacement (r, θ, ϕ) in spherical coordinates, where r is the propagation length, θ the azimuthal angle, and ϕ the polar angle. The propagation length r obeys an exponential probability distribution with a $1/e$ equal to the mean free path. For interband carriers, θ follows a random distribution in which every angle is equally probable. For intraband carrier, θ follows an angular distribution $R_{\text{eff}}(\theta)$:[58]

$$R_{\text{eff}}(\theta) \propto a\left(\frac{3}{4}\cos^2\theta + \frac{1}{4}\right) + 2(1-a)|\cos^3\theta|$$

where a is the fraction of carriers generated via phonon/defect scattering. For spherical particles, a ≈ 0.45.[58] Lastly, ϕ obeys a random distribution in which all angles are equally probable. The carriers plotted in Figs. 4d,e are those that have their final position outside of the nanoparticle. For simplicity, we neglect any losses due to momentum mismatch at the interface.

Mie calculations[7] of gold nanospheres and Au@Ag core@shell nanospheres in a homogenous environment are performed using a script in Matlab based on the formalism laid by Bohren and Huffman.[8]

6.5.4 Morphological and optical characterization of Au & Au@Ag core@shell nanorods

In this section, we present the morphological and optical characterizations of bare gold nanorods and the Au@Ag core@shell nanorods at different growth stages. We also correlate the spectral shifts observed during the silver shell growth experiment with their morphological changes, which is further corroborated using finite-difference time-domain (FDTD) calculations.

The colloidally synthesized bare gold nanorods (NR_0) exhibit a transverse and longitudinal resonance at 514 nm and 744 nm, respectively (Figure 6.6a). The size distribution of the gold nanorods is calculated by measuring the length and diameter of individual nanorods in transmission electron micrographs, using ImageJ software. Similar size distributions from TEM images have been calculated for different growth stages NR_1 and NR_2 (Figure 6.6a). For the growth stage NR_3, analyzing size distribution is difficult due to the anisotropic shell growth. The correlations regarding the spectral shifts in Figure 6.1c with the morphological changes is further corroborated using FDTD calculations (Figure 6.6b,c,d).

We first simulate the extinction of gold nanorods with a conformal silver shell around them. The silver shell thickness is varied between 0 - 2 nm in our simulations (Figure 6.6b). We observe an increasing blue shift of the longitudinal plasmon resonance with increasing silver shell thickness, which is consistent with the experimentally measured spectral features at the growth stage NR_1. We then simulate the extinction cross-section of cuboidal Au@Ag core@shell nanorods with varying corner sharpness representing the growth stage between NR_1 and NR_2. As a starting point, a 1.2 nm conformal silver shell is considered. We vary the corner radius from 13.7 nm – 3.7 nm corresponding to the transition from a conformal shell to cuboidal shell. A red shift of the plasmon resonance is observed (Figure 6.6c), corroborating our correlation of the measured spectral red shifts with the TEM images at the growth stage NR_2. After growth stage NR_2, a blue shift of the plasmon resonance is observed as the silver shell thickness increases, which is simulated using a conformal silver shell over a gold nanorod with shell thicknesses ranging from 4 to 10 nm, in Figure 6.6d.

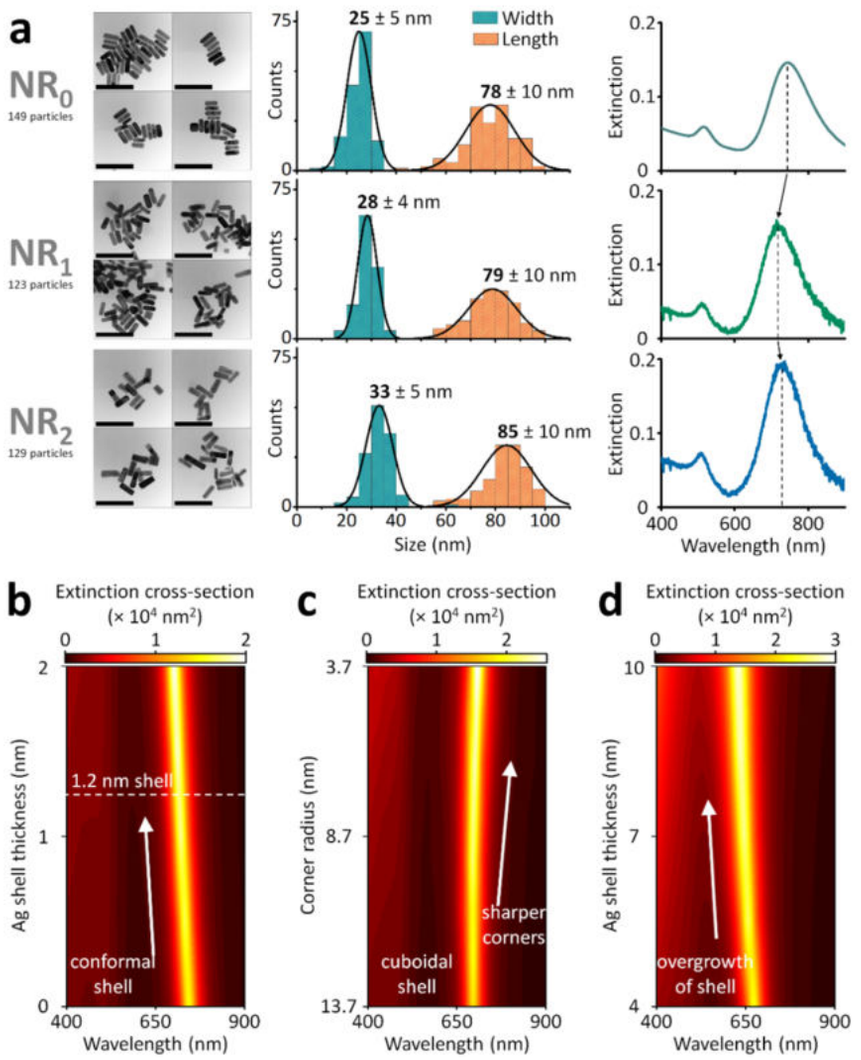

Figure 6.6: (a) TEM images, size distribution, and extinction spectra of bare gold nanorods (NR_0, 1st row), gold nanorods with 1 nm conformal silver shell (NR_1, 2nd row), and gold nanorods with a 4 nm cuboidal silver shell (NR_2, 3rd row). The scalebars correspond to 200 nm. The black line is the histograms are the corresponding Gaussian fits. (b, c, d) FDTD calculated extinction cross sections of gold nanorods suspended in water with a dimension of 78 × 25 nm and (b) a conformal silver shell with thicknesses varying from 0 – 2 nm, (c) a cuboidal silver shell with corner radii varying from 3.7 nm – 13.7 nm, and (d) a conformal silver shell with thicknesses varying from 4 – 10 nm.

6.5.5 Modeling photon propagation in our reaction volume

Since our nanorods display strong absorption and scattering properties at their plasmon resonances, the photon propagation inside the reaction volume can be properly calculated only by solving the complete radiative transfer equation.[30] We employ a Monte Carlo model to model the photon propagation inside the nanorod solution, which has been previously described.[30] Briefly, photons with a spatial distribution corresponding to the experimental laser spatial profile are injected in to the simulated reaction volume. The simulation region is meshed into cuboidal volumes. Each voxel occupies a volume of $12.5 \times 4 \times 10$ µm^3. The nanorod density that we employ in our experiments is 8.2×10^9 nanorods/mL. As such, each voxel is expected to contain approximately 4 nanorods. The photons get scattered and absorbed with probabilities depending on their FDTD calculated scattering and absorption cross sections. The photons absorbed in each mesh cell is calculated and plotted in Figure 6.7. Multiple photon scattering events and reflection and transmission events at the simulation boundaries are also considered in our calculations.

The calculated average absorption and scattering cross sections of the nanorods at 532 nm illumination are 1300 nm^2 and 78 nm^2, respectively, while under 730 nm illumination the average absorption and scattering cross sections are 7700 nm^2 and 3500 nm^2. Intuitively, the larger illumination power required using a 532 nm laser (240 mW) compared to while using a 730 nm laser (55 mW) can be understood by the larger absorption cross section and scattering cross section at 730 nm compared to 532 nm of the nanorods. To ensure that the total absorbed power is the same under the two illuminations, in our Monte Carlo calculation we take into account the different absorption and scattering cross sections, the effect of multiple scattering events, and the slightly different beam diameters of the 532 nm (1.5 mm) and 730 nm (1.7 mm) lasers.

Even though the spatial profile of photon absorption under 532 nm and 730 nm illumination are different, the total power absorbed inside the reaction volume, and therefore any photothermal heating, under these two conditions will be similar.

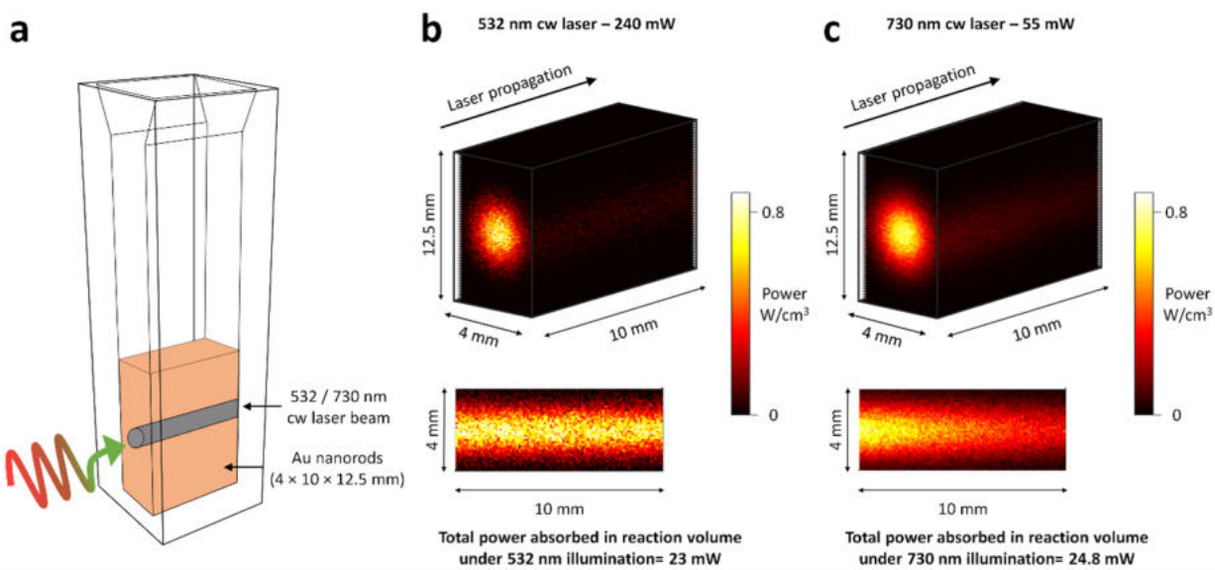

Figure 6.7: (a) Schematic illustration of illumination of our reaction vessel containing gold nanorods. (b, c) Calculated photon absorption inside the reaction volume under (b) 532 nm and (c) 730 nm laser illumination. On the bottom, heat map of calculated photon absorption at the center of the reaction volume is displayed.

6.5.6 Ex situ extinction measurements and morphological characterization under different illumination conditions at t = 0 h and 24 h.

In this section, we present ex situ extinction spectra of Au@Ag core@shell nanorods kept in the dark, under 730 nm illumination, and under 532 nm illumination at time, t = 0 h and t = 24 h. TEM images and corresponding size distributions after 24 h of experiment are also presented.

The ex situ extinction spectra of nanorod growth solutions kept in dark and under 730 nm illumination show similar transverse and longitudinal resonance changes (Figure 6.8a,b) after 24 h, while the solution irradiated using a 532 nm laser shows drastic changes (Figure 6.8c). The TEM images and the size distributions of Au@Ag core@shell nanorods after 24 h of synthesis under dark and 730 nm laser illumination look very similar, as can be observed from Figure 6.8a,b. For 532 nm illumination, analyzing size distribution is difficult due to the anisotropic shell growth.

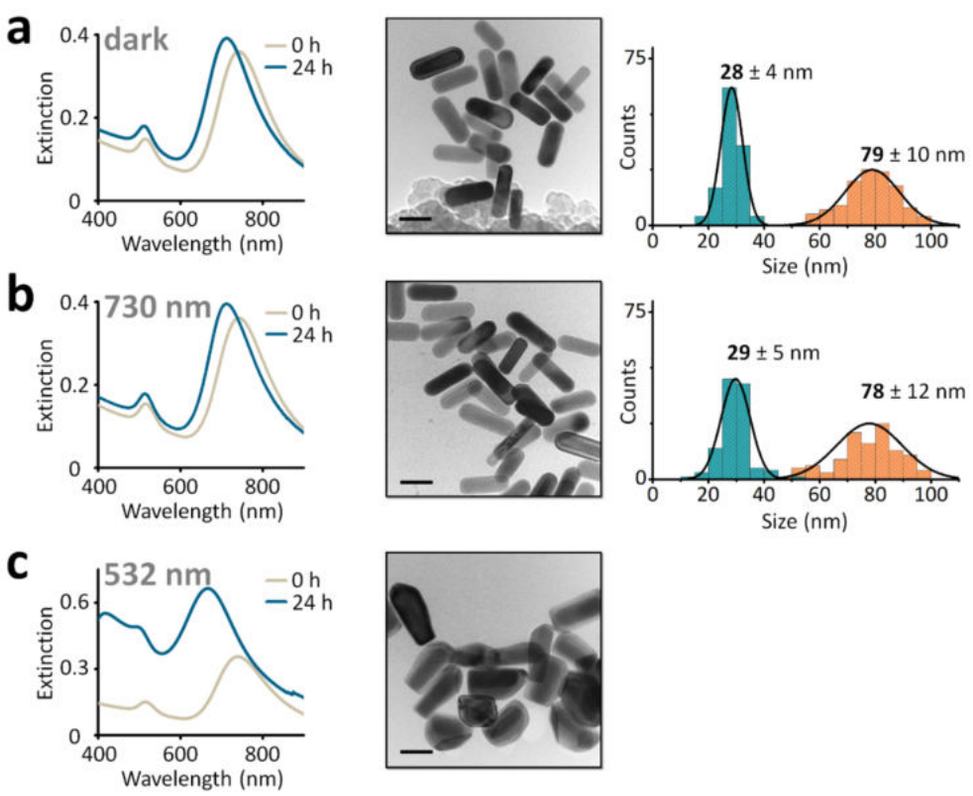

Figure 6.8: Extinction spectra of the Au@Ag core@shell nanorod synthesis at t = 0 h and t = 24 h in (a) dark conditions, (b) 730 nm, and (c) 532 nm laser illumination. TEM images of Au@Ag core@shell nanorods and associated size distributions measured after 24 h of experiment are also presented. Scalebars in the TEM images correspond to 50 nm. The black line in the histograms are the corresponding Gaussian fits.

6.5.7 Evaluating plasmonic rate enhancement

To obtain a rate enhancement from the longitudinal LSPR as a function of time (Figure 6.2d), we first separate the time evolution in three parts: 1) start to first local minimum in the LSPR, 2) first local minimum to the next local maximum in the LSPR, 3) local maximum to the end. We remove part of the 532 nm illumination measurement, so that both datasets end at the same LSPR wavelength (Figure 6.9a). As the local minimum and maximum in the two datasets are not at the exact same wavelengths, we normalize each part of the dataset from 0 to 1 (Figure 6.9b). For each normalized LSPR wavelength we then find the time at which this LSPR is reached in the dark, and the time at which this LSPR is reached under 532 nm illumination (Figure 6.9c). To obtain the rate enhancement in Figure 6.2e, we take the derivative of the time in the dark with respect to the time under 532 nm illumination, i.e. the derivative of Figure 6.9c below.

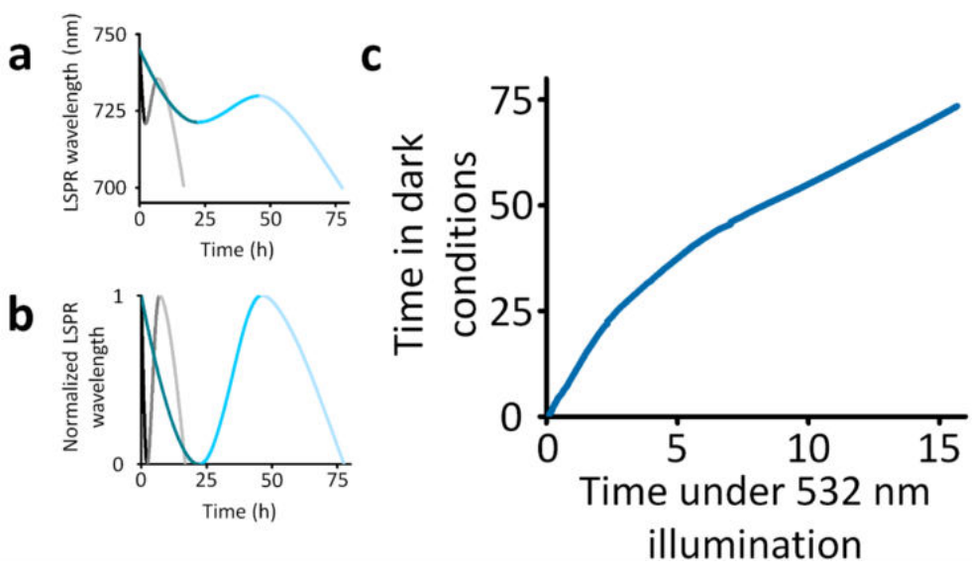

Figure 6.9: (a) Longitudinal LSPR as a function of time for the experiment in the dark (blue) and under 532 nm illumination (grey). (b) Same as panel (a), but each section is normalized from 0 to 1. (c) Time at which a certain LSPR in panel (b) is reached in the dark as a function of the time at which that same LSPR is reached in the 532 nm illumination experiment.

6.5.8 Thermal characterization under laser illumination

Illumination of ensemble nanoparticle suspensions can generate both localized and collective photothermal heating effects.

Localized plasmonic heating

The localized photothermal temperature increase ΔT_{local} on nanorods can be calculated using (see also the aforementioned equation (6.1)):[155]

$$\Delta T_{\text{local}} = \frac{\sigma_{\text{abs}} I}{4\pi\beta\kappa R_{\text{eq}}}$$

Assuming a nanorod geometry parallel to the incident light polarization in FDTD simulations, we calculate absorption cross-sections σ_{abs} of $1.32{\cdot}10^{-11}$ cm^2 and $2.18{\cdot}10^{-10}$ cm^2 at 532 nm and 730 nm wavelengths, respectively. Under our illumination geometries, the maximum power density I at the center of the Gaussian laser beam is 13.38 W/cm^2 and 2.25 W/cm^2 for 532 nm (power = 240 mW, $1/e^2$ beam diameter = 1.511 mm) and 730 nm (power = 55 mW, 1/e2 beam diameter = 1.765 mm) experiments, respectively.

The thermal capacitance coefficient β for a nanorod is defined as:[155]

$$\beta = 1 + 0.96587 \ln^2 \frac{l}{w}$$

where l and w are the length and width of the nanorod. We calculate a β of 2.25 for our gold nanorods of dimension 78 × 25 nm.

The thermal conductivity κ of water is 0.6 W/m/K. The equivalent radius R_{eq} of the nanorod, which is calculated by equating the volume of the nanorod to that of a sphere, in our case is ∼20 nm.

Using the above values, we find a maximum temperature increase of 1.04 mK under 532 nm illumination and 2.87 mK under 730 nm illumination, on the nanorods. Such negligible local temperature increases cannot explain the plasmon-driven silver shell growth in our experiments.

Collective heating effects

Under typical illumination geometries, multiple nanoparticles are illuminated simultaneously which leads to the generation of macroscopic collective heating effects along with heat convection. We characterize these global heating effects by measuring the temperature on the cuvette walls using an infrared camera and by measuring the temperature of the nanoparticle suspension using a thermocouple. Since thermocouples are photosensitive, in our measurements, they are placed inside the liquid suspension above the laser beam.

We also model heat dissipation inside the reaction vessel by first calculating photon absorption inside the reaction volume using Monte Carlo simulations (Figure 6.7), and then we use the calculated absorbed power as an input in COMSOL. In our COMSOL simulations, we fix the temperature at the outer boundary of the quartz cuvette at 6 °C, corresponding to our set temperature in our experiments.

In the infrared camera (IR) measurements, we set an emissivity of 0.93 corresponding to quartz to measure the temperature of the external surface of the cuvette. Infrared camera measurements in Figure 6.10 display temperatures of 9 – 10 °C, despite setting the cuvette holder to 6 °C. This disparity is attributed to the accuracy of ±2 K of the IR camera, according to the website

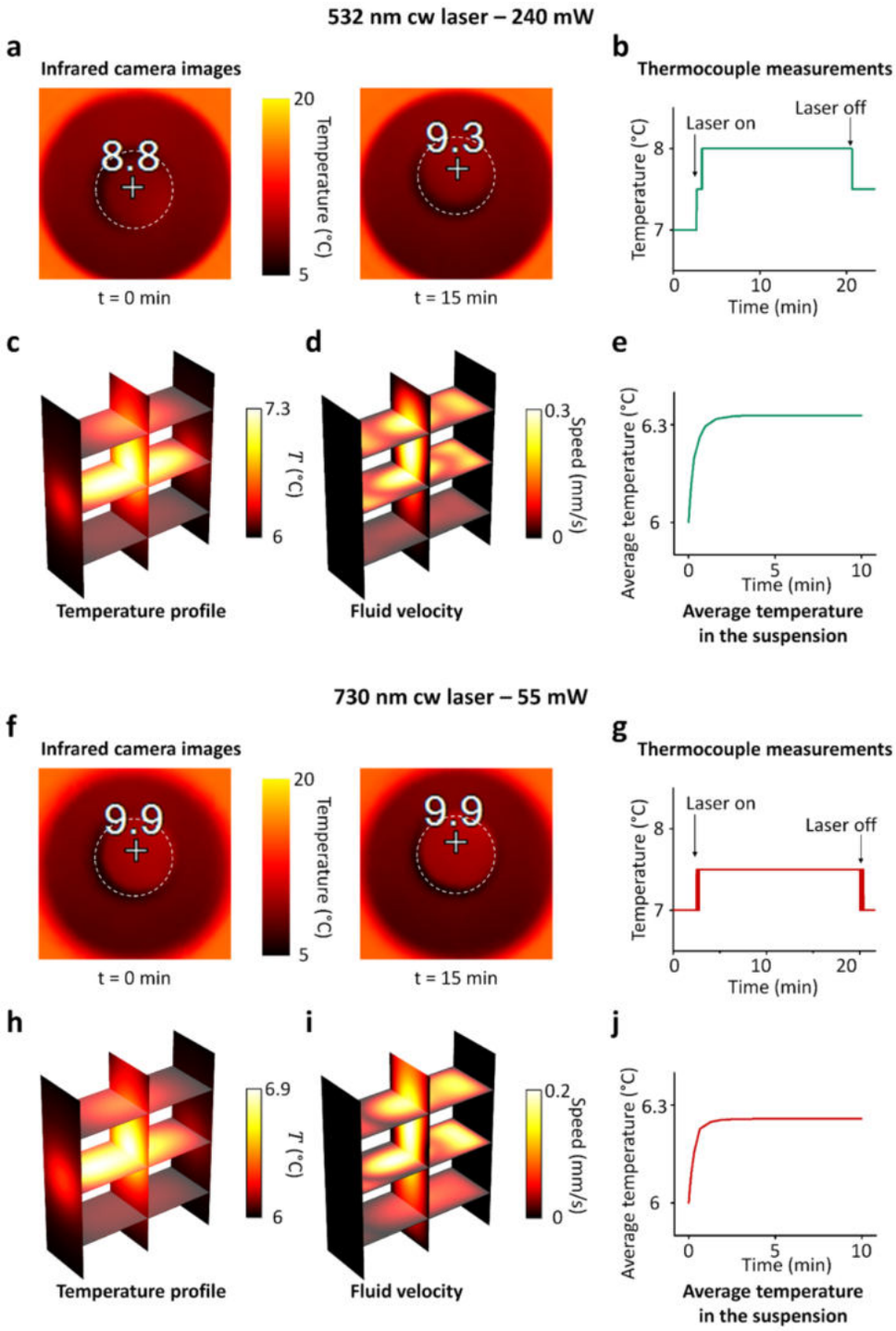

Figure 6.10: (a) Infrared camera measurement at t = 0 min and 15 min, (b) thermocouple temperature measurements as a function of time, COMSOL calculated (c) heat map of temperature profile, (d) heat map of fluid velocity and (e) evolution of average temperature of the nanorod suspensions under 240 mW 532 nm cw illumination. (f, g, h, i, j) Similar thermal characterization for 55 mW 730 nm cw illumination. The white dashed lines in the infrared camera images denote the optical window of the cuvette holder, where the quartz cuvette with the gold nanorod suspension is held.

of the camera manufacturer. The IR measurements indicate a temperature increase of ∼0.5 K under illumination, on the quartz cuvette walls. In the thermocouple measurements, tempera-

ture increases of 1 K and 0.5 K are observed for 532 nm and 730 nm illumination, respectively. The thermocouple measurements have an accuracy of ±2.2 K, according to the website of the thermocouple manufacturer.

The thermal characterizations shown in Figure 6.10 indicate similar temperature increases of ∼1 K for the nanoparticle suspension under 532 nm and 730 nm illumination. Since the magnitude of photothermal effects is similar under green and red laser illumination experiments, one would expect similar silver shell growth kinetics, if the synthesis was driven by photothermal heating. As we observe silver shell growth only under 532 nm irradiation experiments, we can rule out the role of photothermal heating.

After calculating the photon absorption inside the reaction volume using Monte Carlo simulations (Figure 6.7), we use the calculated absorbed power as an input in COMSOL to model heat dissipation inside the reaction vessel. In our COMSOL simulations, we fix the temperature at the outer boundary of the quartz cuvette at 6 °C, corresponding to our set temperature in our experiments. From the COMSOL simulations, we predict a similar average temperature increase inside the reaction volume under 532 nm and 730 nm illumination of ∼0.3 K. The temperature increases calculated here are consistent with the thermocouple and infrared camera measurements we performed in the illuminated reaction vessel. Such small temperature increases cannot explain the silver shell growth rate enhancement we observe under 532 nm illumination.

6.5.9 Quantifying near-field enhancements

We simulate the electric field enhancements in the vicinity of the nanorod surface at different growth stages, using FDTD. In Figure 6.11, we plot the average near-field enhancement ⟨NFE⟩ by integrating the electric fields at various distances from 0.5 to 2, 5, and 10 nm from the nanorod surface.

In our simulations we observe artifacts in the electric field at the nanorod surface, due the roundness of the nanorod tips, resulting in certain mesh cells containing both the metal and the surrounding medium. To avoid these artifacts, we integrate the ⟨NFE⟩ from 0.5 nm from the surface to various distances away from the surface (Figure 6.11), since the fields will decay homogeneously away from the surface. In all these cases, we observe a similar trend where ⟨NFE⟩ increases with silver shell growth, while experimentally we observe a decreasing plasmonic rate enhancement (Figure 6.2d,e), safely allowing us to rule out near-field contributions.

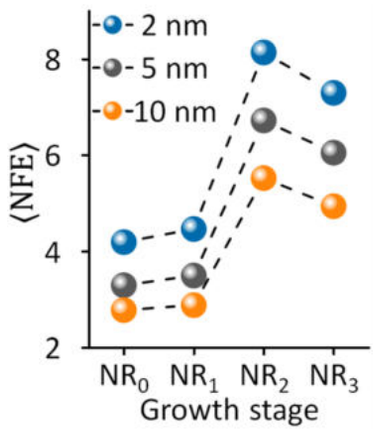

Figure 6.11: Average near-field enhancements around the nanorod surface plotted as a function of the silver shell growth stage. The fields are integrated at distances from 0.5 nm to 2 nm (blue), 5 nm (gray), and 10 nm (orange) from the nanorod surface.

6.5.10 Temperature calculations in single-particle studies

In this section, we demonstrate that temperature effects are negligible in our single particle studies.

Localized plasmonic heating

To calculate the localized temperature increases under illumination in our single particle studies, we use the following equation:[65]

$$\Delta T_{\text{local}} = \frac{\sigma_{\text{abs}} I}{4\pi\kappa R} \tag{6.3}$$

where the absorption cross section σ_{abs} of our 66 nm gold nanospheres is $1.371{\cdot}10^{-14}$ m^2 and the laser intensity I is kept at $165{\cdot}10^4$ W/m^2. Since the gold nanospheres lie at the interface of glass (κ_{glass} = 1 W/m/K) and water (κ_{water}= 0.6 W/m/K), an average thermal conductivity κ of 0.8 W/m/K is chosen for the calculations. The radius of the nanospheres is 33 nm.

Using the above values, we find a negligible local temperature increase of 62 mK on the nanoparticle that is located at the centre of the Gaussian beam. Such low heating effects are not enough to grow a silver shell around the gold spheres.

Collective heating effects

To calculate the temperature increases under collective heating effects, we use the following equation that has been previously used for two-dimensional nanoparticle arrays:[156]

$$\Delta T_{\text{collective}} = \frac{\sigma_{\text{abs}} P}{\kappa} \sqrt{\frac{\ln 2}{4\pi}} \frac{1}{HA} \left(1 - \frac{4\sqrt{\ln(2) A}}{\pi H}\right)$$

where P is the power of illumination, H is the full width at half maximum (FWHM) of the Gaussian laser beam, and A is the unit cell area of the nanoparticle lattice.

Although our nanospheres are dispersed randomly on a glass substrate (Figure 6.12), in order to numerically estimate the temperature increases, we assume that these particles are arranged in a square lattice in order to use the above equation. From the dark-field images of the nanoparticles, we observe that the average interparticle distance is larger than 10 µm. Even in the case of the closest spaced nanoparticles, we measure at least an interparticle distance of 3 µm (Figure 6.12). Assuming an interparticle spacing of 3 µm (therefore A becomes 9 µm^2), and using experimentally measured P and H of the laser beam of 43 mW and 153.9 µm, respectively, we calculate a negligible temperature increase of 0.12 K.

In reality, the average interparticle spacing is much higher than 3 µm, so, therefore, we expect even lower temperature increases due to collective heating effects.

Figure 6.12: Dark-field scattering of gold nanoparticles dispersed on a glass substrate.

6.5.11 Mie theory calculations for the growth of Au@Ag core@shell nanospheres

We calculate the scattering cross-section of Au@Ag core@shell nanospheres using Mie theory[7,8] to estimate the silver shell thickness in our single-particle studies. In our calculations, we use dielectric functions for gold and silver reported by Johnson & Christy and Yang et al, respectively.[44,45] We model a conformal silver shell with thickness from 0 – 5 nm, over a 66 nm gold nanospheres.

From these Mie calculations, we observe increasing blue shift of the plasmon resonance with increasing shell thicknesses. From Figure 6.13, for a plasmon resonance blue shift of 17 nm observed in Figure 6.5b, we can estimate the growth of a 4 nm silver shell over the gold nanosphere.

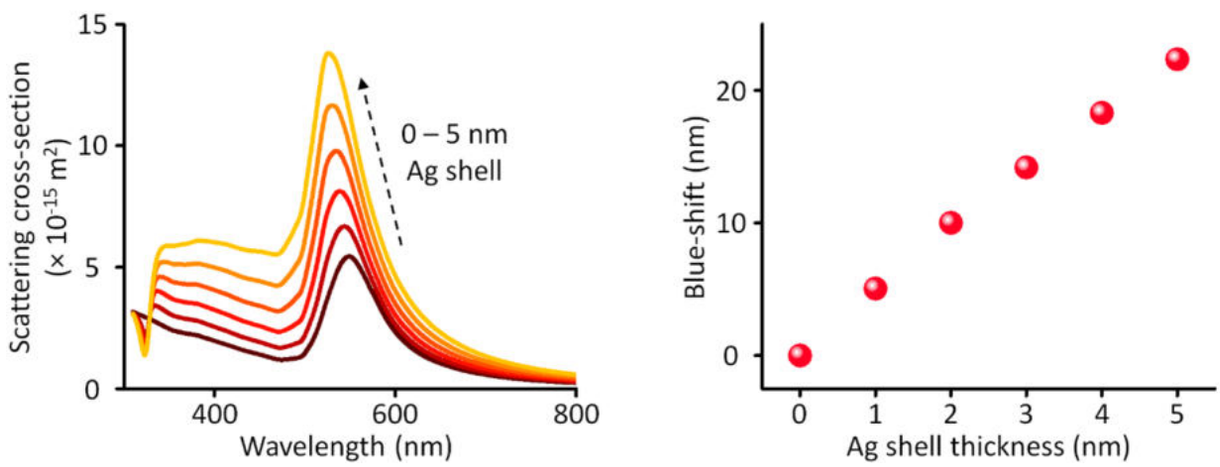

Figure 6.13: (left) Scattering cross-section of Au@Ag core@shell nanospheres, where the silver shell thickness is varied between 0 to 5 nm. (right) From the data on the left plot, the blue shift of plasmon resonance is plotted as a function of silver shell thickness.

6.5.12 Control experiments to confirm the plasmonic nature of silver shell growth

Several control experiments for the dark-field single-particle studies were performed to confirm the plasmonic nature of the core@shell nanosphere growth.

Single particle experiments were performed in the absence of laser irradiation to characterize the silver shell growth under dark conditions (Figure 6.14a). In these experiments, the plasmon resonance of the gold nanoparticles is measured at the beginning and at the end of the experiment, while flowing the silver shell growth solution. No significant silver shell growth is observed under dark conditions even after 6 h, as observed from the similar scattering spectra at the beginning and at the end of the experiment. Such control experiments show that plasmon excitation is necessary for the silver shell growth under our reaction conditions.

In order to rule out the possibility of any gold nanoparticle deformation under illumination, we irradiate the nanoparticles with a 532 nm laser (Figure 6.14b). A solution consisting of BSPP and ascorbic acid is injected in to the flow cell, but in the absence of any Ag^{+} ions. Under illumination, the gold nanoparticles do not show any spectral change as observed in Figure 6.14b, thus allowing us to rule out any nanoparticle deformation under laser irradiation.

In order to verify if any silver nucleation occurs in the absence of gold nanospheres, we fabricate a flow cell without depositing any gold nanoparticles on the coverslip. We flow the silver growth solution through the flow cell and simultaneously illuminate it with a 532 nm cw laser. From Figure 6.14c, we do not observe the formation of any bright scatterers after illumination, suggesting that no large silver nanoparticles are formed on the surface.

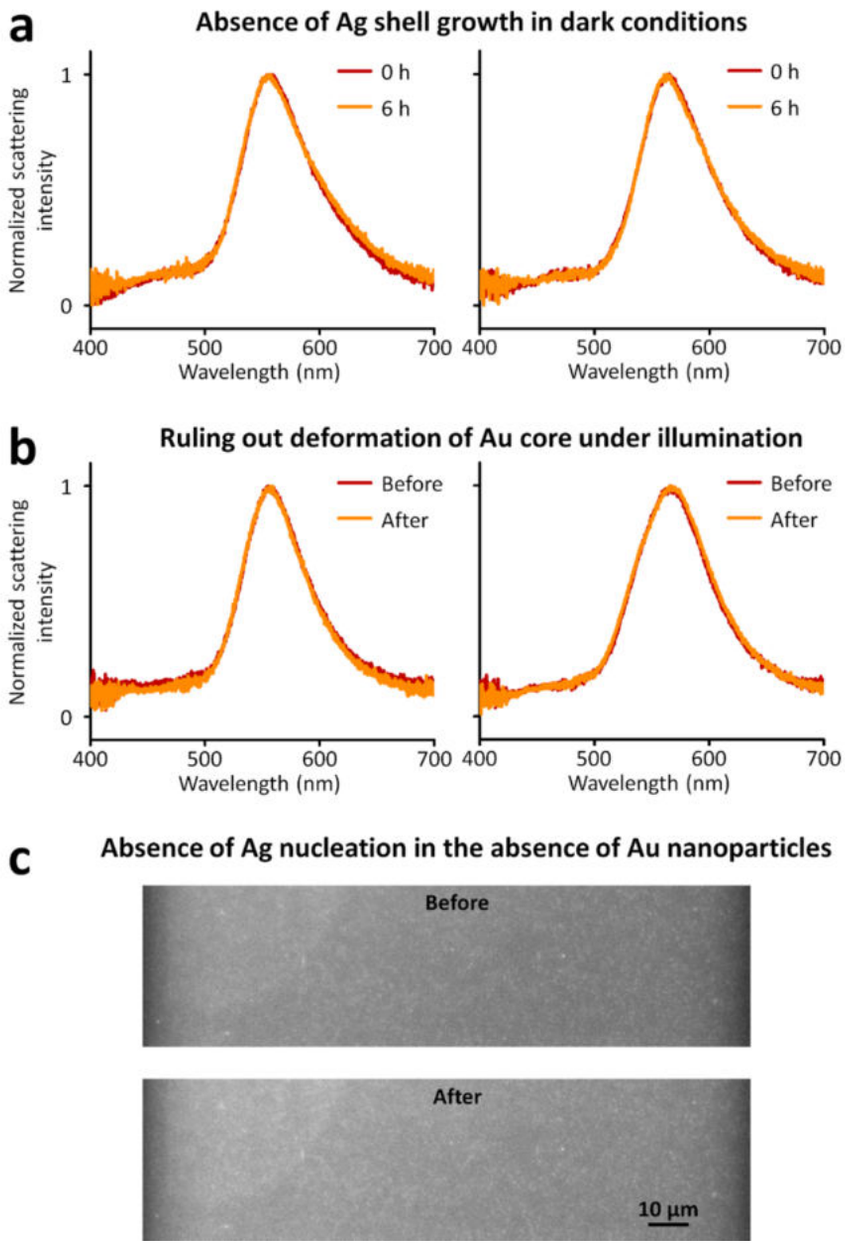

Figure 6.14: (a) Normalized scattering spectra of two different single gold nanoparticles at time t = 0 h and t = 6 h, when kept in the dark while flowing silver growth solution. (b) Normalized scattering spectra of two different single gold nanoparticles before and after laser illumination for a period of 2 h, in the absence of Ag^+ ions in the growth solution. (c) Dark-field image of the quartz cover slip before and after 532 nm illumination for 2 h, while flowing the silver growth solution.

6.5.13 Monte Carlo simulations of hot carrier propagation

We first simulate the power absorbed P_{abs} at 532 nm in a 66 nm gold sphere (Figure 6.15a). 10^8 carriers are then placed in the sphere with a spatial distribution proportional to P_{abs}, which is proportional to $|E|^2$: $P_{\text{abs}} = \frac{1}{2}\omega\varepsilon_0|E|^2\text{Im}[\varepsilon]$, where ω is the photon frequency and $\text{Im}[\varepsilon]$ the imaginary part of the dielectric function ε. Each carrier is given a random displacement (r, θ, ϕ) in spherical coordinates, where r is the propagation length, θ the azimuthal angle, and ϕ the polar angle. The propagation length r obeys an exponential probability distribution with a $1/e$ equal to the mean free path. These random numbers for r are easily generated using inverse transform sampling.

For interband carriers, θ follows a random distribution in which every angle is equally probable. For intraband carriers, θ follows an angular distribution $R_{\text{eff}}(\theta)$:[58]

$$R_{\text{eff}}(\theta) \propto a\left(\frac{3}{4}\cos^2\theta + \frac{1}{4}\right) + 2(1-a)|\cos^3\theta|$$

where, a is the fraction of carriers generated via phonon/defect scattering. For spherical particles, $a \approx 0.45$.[58] Generating random numbers from this angular distribution is not trivial, as the inverse cumulative distribution function of $R_{\text{eff}}(\theta)$ cannot be calculated analytically. Instead, we approximate $R_{\text{eff}}(\theta)$ with a superposition of Gaussian distributions centered at 0, π, 2π, and a width σ of 0.6 radians (Figure 6.15b).

Lastly, ϕ obeys a random distribution in which all angles are equally probable. The carriers plotted in Figure 6.5d,e are those that have their final position outside of the nanoparticle. For simplicity, we neglect any losses due to momentum mismatch at the interface, so the carriers plotted in Figure 6.5d,e can also be interpreted as those that reach the nanoparticle surface.

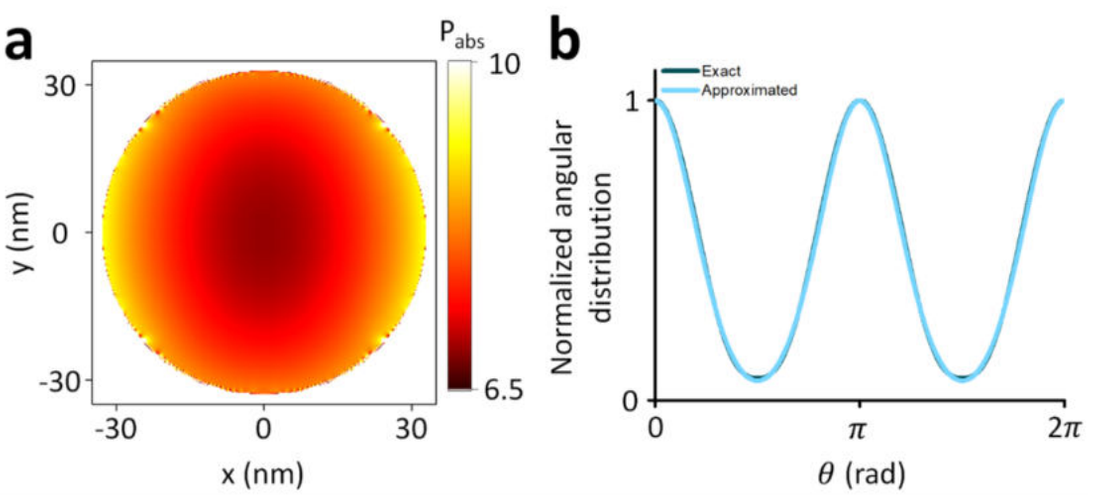

Figure 6.15: (a) Two-dimensional slice of the absorbed power at the center of the nanoparticle. The units for P_{abs} are normalized and can be converted to W/m^3 by multiplying with the power that is experimentally injected on an area equivalent to the simulated source area. The polarization is along the y axis. (b) Normalized angular distribution R_{eff} (labeled 'exact') and the approximation used in the simulation (labeled 'approximated').

Chapter 7

On the optical properties of silver nanowires

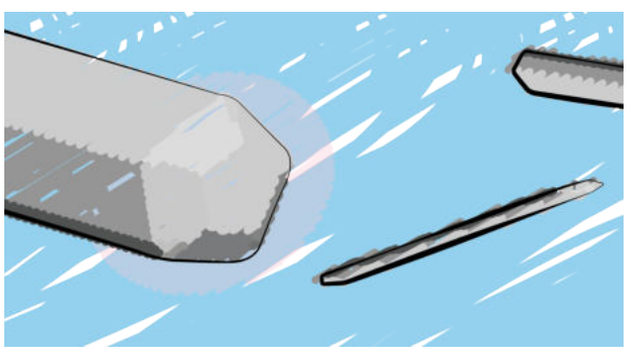

This chapter is based on Ref. 178: ChemRxiv 2022, 10.26434/chemrxiv-2022-vw6vh.

7.1 Foreword

In the previous chapters we have studied the work of plasmonic near-fields in the context of fluorescence enhancement (chapter 4) and plasmon-driven chemistry (chapter 5 and 6). Furthermore, we have seen the power of a detailed understanding of the relationship between structure and optical properties, which allowed us to pinpoint the driving force behind a light-driven synthesis (chapter 6). In this chapter, we study another plasmonic nanostructure for which this relationship is particularly relevant, namely silver nanowires (AgNWs). These wires are used in a variety of applications, ranging from transparent conductive layers to Raman substrates and sensors. Their performance often relies on their unique optical properties that emerge from localized surface plasmon resonances in the UV. The colloidal, large scale synthesis of silver nanowires typically leads to structures with pentagonally-twinned geometries, but their optical properties are often modeled assuming a cylindrical cross section for simplicity. In this chapter, we study the consequences of such an approximation for different optoelectronic applications and highlight the importance of a realistic modeling of the geometry of the Ag nanowires to capture all aspects of their optical properties.

AgNWs are characterized by an extinction spectrum with sharp peaks in the UV. In colloidal syntheses, the degradation of nanowires is accompanied by a broadening of these peaks and by an increase in the extinction in the visible. This increase in residual extinction is often due to the formation of silver nanoparticles as byproducts of the reaction or as the result of nanowire decomposition. Therefore, the synthesis of AgNWs is typically followed by lengthy and expensive

purification steps to increase the relative nanowire yield and, consequently, improve the transparency in the visible. Here, however, we find that some of the residual extinction is inevitable, as it arises due to a silver mirror-like reflection of the long wires. For this reason, the best strategy to obtain AgNW-based transparent electrodes with a high transparency in the visible is not always purification, but the synthesis of thinner wires, which reflect light much less efficiently, while maintaining good electrical conductivity.

The optical model of an infinitely long cylinder can already reproduce the residual extinction in the visible. However, to accurately reproduce the peaks in the UV, the pentagonal geometry of the wire's cross section needs to be included in the model. We find that the radius of curvature of the edges of the wire describes the amount of extinction peaks and how spectrally separated they are. Our observations demonstrate that UV-vis spectroscopy is a powerful tool to evaluate the quality of an AgNW synthesis: the existence of byproducts can be identified by comparing the extinction peaks in the UV to the residual extinction in the visible and the roundness of the wires can be evaluated by the exact shape of the resonance peak.

Using our improved optical model we can define accurate design recommendations for AgNW-based devices. Thanks to their low extinction in the visible, networks of AgNWs are particularly interesting for transparent electrode applications, such as for smart windows, touch screens, organic light-emitting diodes (OLEDs), and solar cells. In these cases, transparency is mostly desired in the visible range (450 - 650 nm) for smart windows, touch screens, or OLEDs or in the above bandgap range (<1100 nm for Si) for solar cells. As the extinction peaks of the wires are in the UV, where the human eye is not sensitive and solar irradiation is not intense, we find that the geometrical size of the AgNWs (their diameter) is more important than the exact shape of their cross section. AgNWs are also used as substrates for surface-enhanced Raman spectroscopy, in which the plasmonic near-fields are responsible for amplifying the Raman signal. As we have seen in chapter 6, electric field enhancement increases in the presence of sharper corners and we find that the use of a pentagonal cross section is instrumental in predicting the performance of AgNW-based near-field devices, such as Raman substrates.

Abstract

Silver nanowires are used in many applications, ranging from transparent conductive layers to Raman substrates and sensors. Their performance often relies on their unique optical properties that emerge from localized surface plasmon resonances in the ultraviolet. In order to tailor the nanowire geometry for a specific application, a correct understanding of the relationship between the wire's structure and its optical properties is therefore necessary. However, while the colloidal synthesis of silver nanowires typically leads to structures with pentagonally-twinned geometries, their optical properties are often modeled assuming a cylindrical cross section. Here, we highlight the strengths and limitations of such an approximation by numerically calculating the optical and electrical response of pentagonally-twinned silver nanowires and nanowire networks. We find that our accurate modeling is crucial to deduce structural information from experimentally measured extinction spectra of colloidally-synthesized nanowire suspensions and to predict the performance of nanowire-based near-field sensors. On the contrary, the cylindrical approximation is fully capable of capturing the optical and electrical performance of nanowire networks used as transparent electrodes. Our results can help assess the quality of nanowire syntheses and guide in the design of optimized silver nanowire-based devices.

7.2 Introduction

Silver nanowires (AgNWs) and nanowire networks show high optical transparency in the visible together with high electrical conductivity, making them appealing for a variety of applications, ranging from transparent electrodes,[179–181] to pressure, temperature, and strain sensors,[182–184] substrates for Raman spectroscopy,[185] and catalysis.[186,187] As their optical and electrical properties strongly depend on their size and shape,[188] it is of paramount importance to tailor their dimensions to the intended application. Numerical simulations allow to predict the optical response of AgNWs and can therefore guide the design of nanowire-based optoelectronic devices. Usually, the optical extinction cross sections of silver nanowires are simulated by approximating them to ellipsoids or to infinitely long cylinders using Mie theory.[189–193] However, the typical method by which AgNWs are produced, the so-called polyol synthesis,[194,195] leads to nanowires with a pentagonal cross section.[180,196–198] This difference between simulated and synthesized geometries leads to the prediction of extinction spectra that are inaccurate and miss crucial optical features. Moreover, the distribution and intensity of the scattered electric fields surrounding the nanowires, the so-called near-fields, are strongly shape dependent. The use of proper geometrical models of the nanowires is therefore important for all applications relying on an accurate prediction of the near-fields, such as surface enhanced Raman scattering (SERS), photocatalysis, and optical sensing.[199–203]

Here, we use a finite difference time domain (FDTD) method to calculate the light scattering, absorption, and extinction of AgNWs with realistic pentagonal cross sections. The simulated extinction spectra accurately reproduce all key features observed experimentally for colloidally-synthesized nanowires. We show that the residual extinction in the visible is a physical limit due to the geometry of the system and not, as often assumed, an indication of the presence of synthetic byproducts. Interestingly, the number and relative intensity of the plasmonic peaks in the ultraviolet are extremely sensitive markers of the nanowire diameter and of the radius of curvature of their edges. On the contrary, we show that silver nanowire networks used as transparent electrode have optical transparencies and electrical conductivities that are insensitive to the exact shape of the modeled nanowires and mainly depend on the magnitude of their geometrical cross section. Finally, we compare near-field maps for circular and pentagonal cross sections and highlight the importance of a proper model of the nanowire shape to predict field enhancements.

7.3 Results and discussion

7.3.1 Comparison between measured and simulated extinction spectra

We first compare the experimental extinction spectrum of a solution of 25 nm radius AgNWs stabilized by polyvinylpyrrolidone (PVP) and suspended in water,[204] to the one calculated with two-dimensional Mie theory assuming an infinitely long cylinder surrounded by a homogeneous medium (Figure 7.1a).[8,205] The silver dielectric function is taken from the literature[44] and the refractive indices of PVP and water are 1.56 and 1.333, respectively. The thickness of the PVP surfactant layer is 5 nm.[206] The polarization of the incoming field is either parallel ($\vec{E}_{\parallel}$) or perpendicular ($\vec{E}_{\perp}$) to the wire.

For a parallel illumination, we observe a near-zero absorption cross section σ_{abs} in the visible region that rises for $\lambda < 350$ nm thanks to interband transitions in silver (Figure 7.1b).[51] The scattering cross section σ_{sca} shows a broadband response for $\lambda > 350$ nm, similar to the reflectivity of an Ag mirror (Figure 7.4). For a perpendicular illumination, both σ_{abs} and σ_{sca} show peaks in the ultraviolet (UV) corresponding to the transverse plasmon resonance of the wire (Figure 7.1b).

From σ_{abs} and σ_{sca} we define the extinction cross section $\sigma_{\text{ext}} = \sigma_{\text{abs}} + \sigma_{\text{sca}}$. In colloidal suspensions, the AgNWs are randomly oriented with respect to the polarization of the incoming light. To reproduce the measured optical properties of colloidal silver nanowires we therefore average σ_{ext} over the two incoming polarizations $\vec{E}_{\parallel}$ and $\vec{E}_{\perp}$. The resulting extinction spectrum is shown in Figure 7.1c and shows two notable features. Firstly, the wire shows an extinction peak in the UV corresponding to the transverse plasmon resonance. This resonance also appears in the experimental extinction spectrum (solid line in Figure 7.1c). However, the cylindrical shape is not able to accurately reproduce the characteristic double peak in the UV that is typically observed experimentally.[204,207–211] Varying the radius of the infinite cylindrical wire merely results in a shift of the transverse plasmon resonance peak, but not in the appearance of a double peak (Figure 7.5).

Secondly, the wire exhibits significant extinction for wavelengths $\lambda > 500$ nm (Figure 7.1c and 7.6), which severely limits the transparency that can be achieved when using these wires as transparent electrodes. This residual optical extinction in the visible is often attributed to the presence of byproducts in the colloidal synthesis of AgNWs.[196,208,212] While byproducts such as spherical particles can certainly contribute to visible light scattering and absorption, here we show that light extinction also emerges as a physical limit of the nanowire system, caused by the Ag mirror-like scattering when the incoming polarization is parallel to the wire. The limited visible transparency can, therefore, not be indefinitely improved by purifying the products at the end of the synthesis.

To more accurately reproduce the pentagonal geometry of the AgNWs, we perform simulations using a finite-difference time-domain method (see Methods section 7.5). We use the same dielectric function,[44] which is now fit to a set of functions that satisfy the Kramers-Kronig relations (Figure 7.7). Figure 7.1d shows the typical pentagonally-twinned cross section of an AgNW with radius R. We also introduce the radius of curvature R_{curv} to account for smooth nanowire edges. To observe the influence of the pentagonal geometry we vary R_{curv} from $R_{\text{curv}} = R = 25$ nm (perfect cylinder) to $R_{\text{curv}} = 5$ nm (pentagon with sharp corners) in steps of 5 nm, while maintaining R = 25 nm. As can be seen in Figure 7.1e, the decrease in R_{curv} first results in a redshift of the resonance and the appearance of a lower wavelength shoulder ($R_{\text{curv}} = 20$ nm). The resonance then further redshifts and the lower wavelength shoulder becomes a well-defined peak ($R_{\text{curv}} =$ 15 - 10 nm), until eventually the spectrum splits even further into three peaks ($R_{\text{curv}} = 5$ nm). The comparison with a typical experimental extinction spectrum clearly indicates that polyol-made AgNWs have pentagonal cross sections with partially smoothed edges (Figure 7.1f and 7.6).

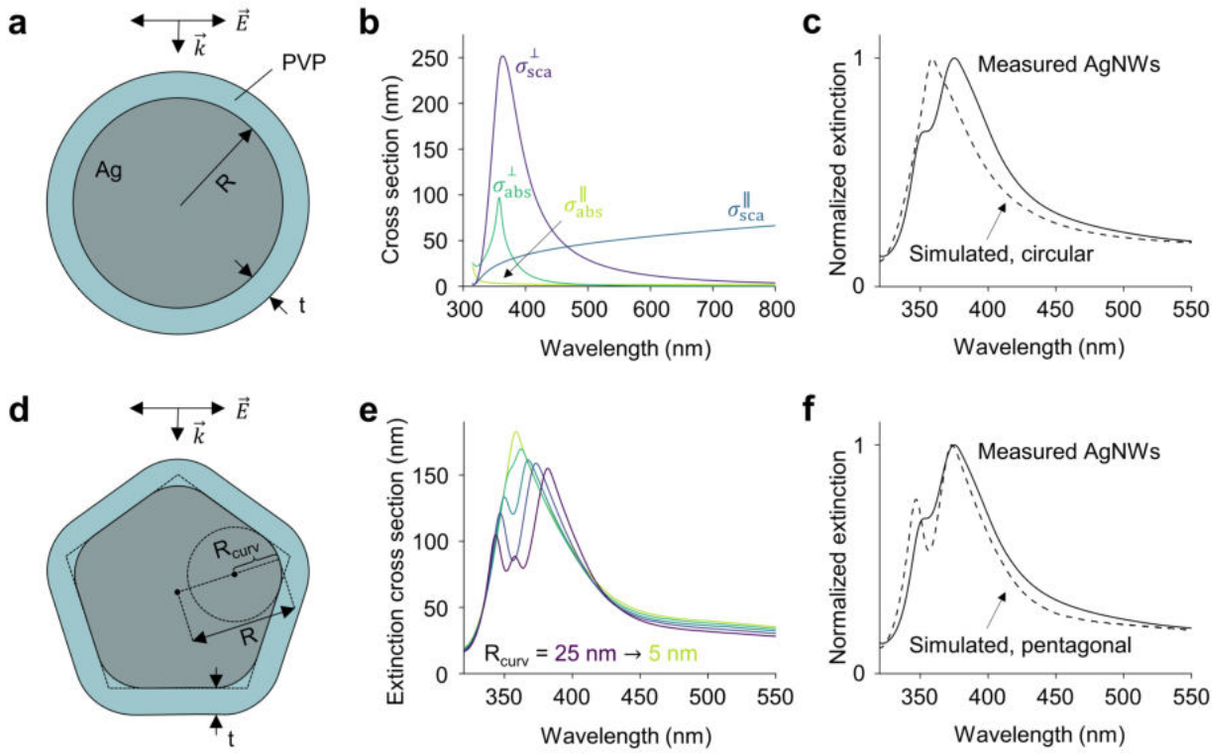

Figure 7.1: Optical response of infinitely long silver nanowires with circular and pentagonal cross sections. (a) Illustration of a circular infinite nanowire of radius R surrounded by a PVP layer of thickness t under perpendicular illumination. (b) Simulated scattering and absorption cross sections under parallel and perpendicular illumination for a circular infinite nanowire with $R = 25$ nm and $t = 5$ nm. (c) Comparison between the simulated (dashed) extinction spectrum of a circular infinite nanowire with the one measured experimentally for 25 nm radius PVP-stabilized AgNWs in water (solid).[204] The simulated extinction cross section is obtained by averaging over the two incoming parallel and perpendicular polarizations shown in panel (b). (d) Illustration of a pentagonal infinite nanowire of radius R and radius of curvature R_{curv}. (e) Simulated extinction cross sections of pentagonal infinite nanowires with $R = 25$ nm and R_{curv} varying from 25 nm (dark blue) to 5 nm (light blue) in steps of 5 nm. The cross sections are averaged over the two incoming polarizations $\vec{E}_{\parallel}$ and $\vec{E}_{\perp}$. (f) Comparison between the simulated (dashed) extinction spectrum of a pentagonal infinite nanowire ($R_{\text{curv}} = 10$ nm) with the experimental one shown also in panel (c) (solid).

The agreement between measured and simulated spectra demonstrates how UV-vis spectroscopy, when coupled to proper optical modeling, can be a powerful tool in assessing the quality of AgNW syntheses. For example, the quantity of synthetic byproducts can be properly estimated by comparing the UV extinction at the transverse resonance of the wires with the one measured in the visible. Furthermore, the radius of curvature of the wires' edges, which is a crucial parameter for near-field applications, can be determined with almost nanometer precision by looking at the shape and spectral position of the transverse resonance peaks. Such an accurate structural characterization would otherwise only be possible with the most advanced electron microscopy techniques.

7.3.2 Nanowire networks as transparent electrodes

Our improved optical model allows us to give several design rules for the use of AgNWs in specific applications. In particular, due to their plasmon resonance outside the visible and their high elec-

trical conductivity, networks of AgNWs can be used as transparent electrodes for smart windows, touch screens, solar cells, and organic light-emitting diodes (OLEDs).[213] For these applications, a minimal extinction in the visible is desired, while retaining a high conductivity of the network. Upon decreasing the radius of the wire, we observe a blueshift of the transverse plasmon resonance, together with a narrowing of the peak (Figure 7.2a). This blueshift toward the UV region of the spectrum has been used as a justification for the need of synthesizing thinner nanowires for applications in transparent electrodes.[214] Although this strategy is correct, it can be seen from Figure 7.2a that the blueshift of the extinction is only a few nanometers. The largest transparency gain upon decreasing the nanowire radius is due to the lower residual extinction above 500 nm which results from the decreased geometrical size of the wire.

To quantify the performance of AgNW networks in the context of transparent electrodes, we calculate the optical transparency and electrical sheet resistance as a function of the wire density and wire diameter. To calculate the transparency, we first pick an appropriate source spectrum $I_0(\lambda)$. If we take the example of smart windows, where the electrode needs to be transparent to the human eye, we can define $I_0(\lambda)$ as the product between the solar spectrum and the response of a typical human eye to light (Figure 7.2b). We then calculate the wavelength-dependent optical transmission of the network $T_{\text{network}}(\lambda)$ using[193]

$$T_{\text{network}}(\lambda) = \exp\left[-\sigma_{\text{ext}}(\lambda) L n\right], \tag{7.1}$$

where σ_{ext} is in the unit of meters due to the use of two-dimensional simulations, L is the length of the wire in meters and n is the wire density in #wires per square meter. The integrated transmission T of the network is then be expressed by

$$T = \frac{\int I_0 T_{\text{network}} \mathrm{d}\lambda}{\int I_0 \mathrm{d}\lambda}. \tag{7.2}$$

Note that due to the distinct spectral shape of the human eye response (Figure 7.2b), we expect T to be similar for all applications where the human eye is the sensor, such as touch screens and OLEDs. For solar cell applications, however, the electrode needs to be transparent to photon energies above the bandgap of the semiconductor. In this latter case, a more appropriate choice for $I_0(\lambda)$ would be the portion of the solar spectrum with photon energies above the bandgap. For the most widely-used semiconductor Si with a bandgap of 1.12 eV, this portion also includes the ultraviolet, which overlaps with the extinction peaks of the AgNW network. Therefore, for Si solar cells, we obtain slightly lower transmission values than for smart windows, touch screens, and OLEDs (Figure 7.8).

We also calculate the electrical sheet resistance.[192] The sheet resistance of an AgNW network has contributions from the resistance at the junctions between different NWs and from the resistance of the NW segments between the junctions. When the junctions have poor electrical conductivity, the sheet resistance of the network is merely determined by the number of junctions.[189] For the same wire length, a smaller radius results in an increased optical transparency (Figure 7.2a), but does not influence the amount of junctions and, therefore, also does not influence the sheet resistance, making the design recommendation straightforward. In practical applications, however, AgNW networks are often treated after deposition using, for example, thermal treatment[215] or mechanical pressing[216] to minimize junction resistance to the point where the internal resistance of the wires can no longer be neglected.[192,217,218] As the resistance of a single wire scales with the inverse of its cross-sectional area, a small radius is preferred for highly transparent networks and a larger radius for highly conductive networks.

Using a previously reported model, we obtain the sheet resistance in Ohm per square, here denoted using $\Omega/\square$ (see also Methods section 7.5).[192] We model a 30 × 30 µm^2 area with contacts on

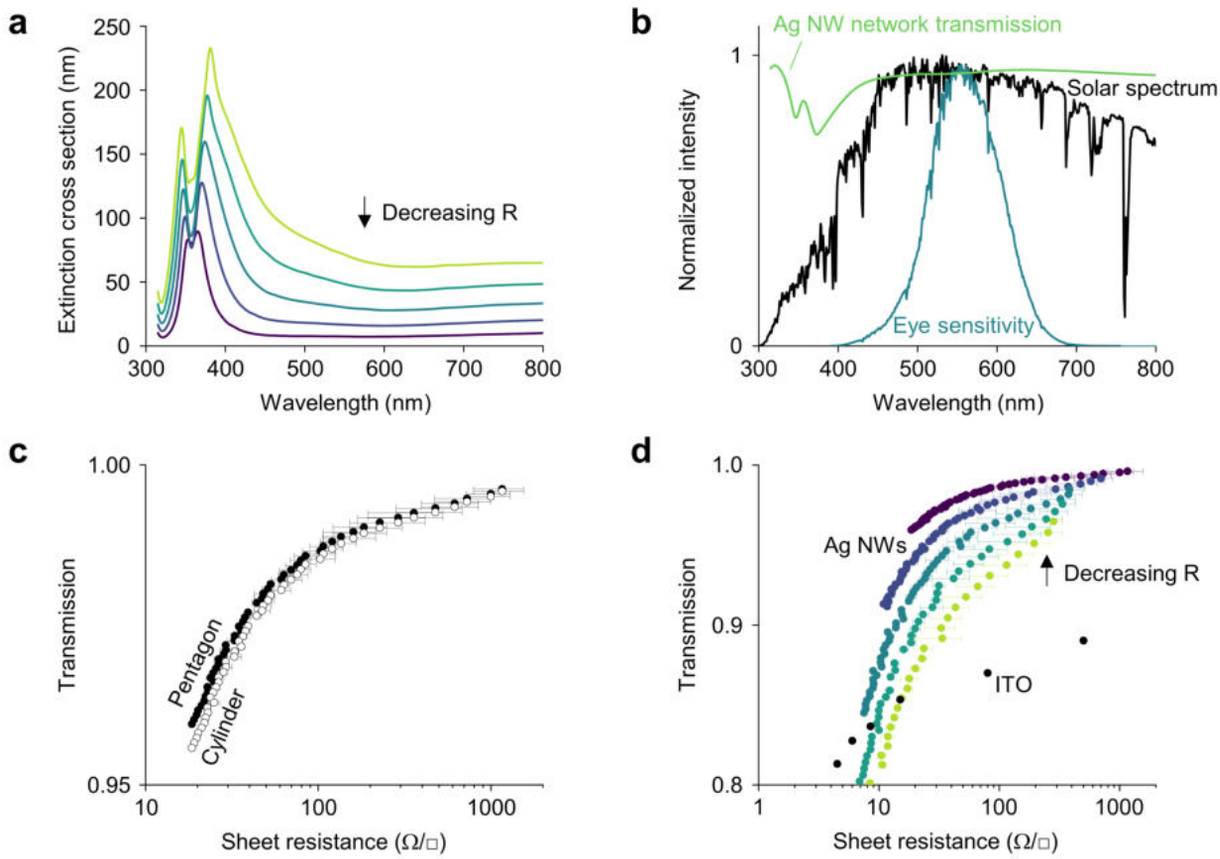

Figure 7.2: AgNWs for transparent electrodes. (a) Calculated extinction cross section of an infinite pentagonal wire. The radius R is decreased from 35 nm to 15 nm in steps of 5 nm. The radius of curvature $R_{\text{curv}} = 10$ nm. (b) Solar spectrum before (black) and after (blue) multiplying by the human eye sensitivity, and an example of the transmission $T_{\text{network}}(\lambda)$ of an AgNW network. (c) Transmission and sheet resistance for AgNW networks consisting of wires with a pentagonal (closed circles) or circular (open circles) cross section. (d) Transmission and sheet resistance of networks of pentagonal AgNWs with varying radii, as indicated using the same color scheme as panel (a). In panels (c,d), every point is a different wire density, which ranges from 0.05 µm^{-2} to 0.55 µm^{-2}. The junction resistance is 11 Ω and the wire length is 10 µm. The error bars are standard deviations resulting from simulating multiple samples (see Methods section 7.5).

either side along the whole edge. Wires with a length L and a cross-sectional area A are placed randomly at a density n. Each junction has a resistance R_{junc} and the segments between the junctions have a resistance R_{seg} that is calculated using

$$R_{\text{seg}} = \frac{\rho l}{A}, \tag{7.3}$$

where $\rho = 2.26 \cdot 10^{-8}$ Ωm is the resistivity of silver[219] and l is the length of the segment. We find that for fairly poor junctions ($R_{\text{junc}} = 1$ kΩ) the sheet resistance is indeed junction-dominated and depends mostly on the wire density n and only weakly on the wire radius R (Figure 7.9). For optimized junctions ($R_{\text{junc}} = 11$ Ω), however, we find that an increased radius significantly decreases the total sheet resistance of the network (Figure 7.9).

For these optimized junctions, we first compare infinite cylindrical and pentagonal wires by modeling the sheet resistance and transmission of networks consisting of wires with equal cross-sectional

areas (Figure 7.10). For example, we compare a pentagonal wire with $R = 15$ nm and $R_{\text{curv}} = 10$ nm to a cylindrical wire with $R = 14.6$ nm. The characteristic extinction peaks that differentiate these shapes lie in the UV part of the spectrum (Figure 7.1), where solar irradiation is not intense and where the human eye is not sensitive (Figure 7.2b). Therefore, when calculating T, the resulting transmission values are similar for pentagonal or circular geometries (Figure 7.2c). Due to this similarity, when altering the NW radius, our improved optical model yields results that agree with what has been reported previously for cylindrical wires (Figure 7.2d).[192] For touch screen applications, a sheet resistance below $\sim$100 $\Omega/\square$ is sufficient. In these cases, AgNW networks outperform indium tin oxide (ITO) already at moderate NW densities, especially for small radii (Figure 7.2d). Furthermore, to obtain these sheet resistances, the junction resistance does not need to be optimized down to 11 Ω, but is allowed to be higher (Figure 7.9). For OLEDs and solar cell applications, which require a lower sheet resistance of $\sim$10 $\Omega/\square$, the use of optimized junctions (Figure 7.9) and thin wires (Figure 7.2d) are instrumental.

7.3.3 Nanowires as near-field platforms

Whereas the transmission of an AgNW network mostly depends on the geometrical size of the AgNW rather than its exact shape, the spatial distribution and intensity of the electric field around the wire is expected to be strongly dependent on the nanowire cross section and on the radius of curvature at its edges. Therefore, when estimating the performance of AgNWs for applications where the electric field strength is a key figure of merit, such as in Raman spectroscopy, catalysis, and sensing,[199–203] it is important to simulate the right geometry and to understand which optical modes are supported by the AgNW and how these contribute to the near-field intensity and distribution.

The characteristic UV extinction peaks of AgNWs are associated with the excitation of transverse plasmon resonances (Figure 7.1a,b). In Figure 7.3, we compare the electric field distributions for infinite cylindrical and pentagonal wires under perpendicular light polarization. For infinite cylindrical wires we use two-dimensional Mie theory,[8,205] while for infinite pentagonal wires we obtain the electric fields via FDTD simulations. In the former case, the contributions to the electric field and to the extinction spectrum can be decomposed into dipolar, quadrupolar, and higher order modes. We find that for $R = 25$ nm, besides the dipolar mode, the quadrupolar mode also contributes to the extinction spectrum (Figure 7.3a). In fact, the energy range of the transverse resonances observed here is also the range in which higher order modes in large Ag nanoparticles occur.[220] However, contrary to nanoparticles, here the dipolar and quadrupolar modes appear at similar wavelengths and, therefore, do not appear as distinct peaks in the extinction spectrum. For wavelengths below the extinction maximum ($\lambda < 358$ nm), the quadrupole contribution is negligible (Figure 7.3a), resulting in near-field enhancement distributions with a dominant dipolar character, as indicated by the two opposite charges at the nanowire surface (Figure 7.3b). At the cylindrical wire resonance, both the quadrupolar ($\lambda = 358$ nm) and the dipolar ($\lambda = 364$ nm) resonances contribute to the overall extinction, resulting in an overall near-field distribution with a quadrupolar character (Figure 7.3c,d). For wavelengths above the extinction maximum ($\lambda > 364$ nm) the quadrupole contribution vanishes and the near-field enhancement distribution has again a simple dipolar character (Figure 7.3e).

The finite-difference time-domain method does not allow us to decompose the extinction spectrum into dipolar and quadrupolar contributions easily. However, in the near-field maps we observe two non-degenerate quadrupolar modes for both extinction peaks of the pentagonally twinned wire, as shown in Figure 7.3h,i, even though the low energy peak around 375 nm is often attributed to a dipolar resonance.[196,221] This confusion likely stems from the analogy with the optical properties of large metallic spheres, in which the strong dipolar peak is accompanied by a smaller quadrupolar peak at a lower wavelength. For wavelengths above and below the extinction maxima we again

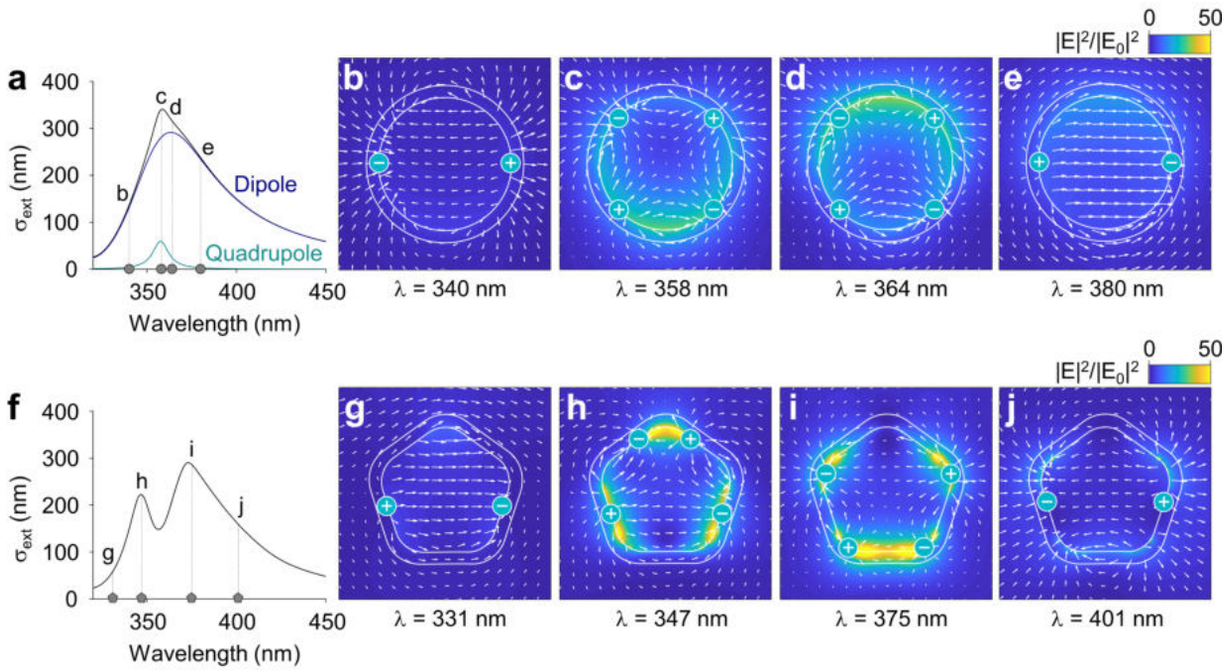

Figure 7.3: Extinction cross sections and electric field distributions for infinite cylindrical and pentagonal wires. (a) Extinction cross section calculated for an infinite cylindrical silver wire with a radius of 25 nm (black) and its decomposition into dipolar (dark blue) and quadrupolar (light blue) contributions. The dashed vertical lines correspond to the wavelengths of the field enhancement maps in panels (b) 340 nm, (c) 358 nm, (d) 364 nm, and (e) 380 nm. (f) Extinction cross section calculated for an infinite pentagonal silver wire with a radius of 25 nm and a radius of curvature of 10 nm. The dashed vertical lines correspond to the wavelengths of the field enhancement maps in panels (g) 331 nm, (h) 347 nm, (i) 375 nm, and (j) 401 nm. The white arrows in the field enhancement maps indicate the real components of the vectorial electric field and the plotted fields are total fields (incident + scattered).

observe a dipolar near-field distribution (Figure 7.3g,j). Most notably, in the transition from a cylinder to a pentagonally twinned wire we also observe roughly a twofold increase in the electric field strength, which can be attributed to the presence of sharper corners (Figure 7.3).[222] This observation highlights the importance of using an accurate geometrical description when predicting the performance of AgNW-based devices that rely on near-field enhancements.

7.4 Conclusion

In conclusion, we studied how the optical properties of AgNWs depend on the shape of their cross section. We demonstrated that comprehensive knowledge of the relationship between the optical properties and the geometry of AgNWs allows us to extract accurate structural information from simple UV-vis spectroscopy. We showed that the characteristic double extinction peak of colloidal AgNWs is a clear marker of a pentagonal cross section and that the exact shape of the peak is extremely structurally sensitive to the radius of curvature of the edges, which is a crucial structural parameter for accurately modeling near-fields. On the contrary, when modeling AgNWs for transparent electrode applications, a simple cylindrical approximation is sufficient to reproduce the optical and electrical performance of nanowire networks. Our results can help in assessing the yield of AgNW syntheses, as well as in choosing the right nanowire dimensions for maximizing the sensing and enhancing effects in applications like Raman spectroscopy.

7.5 Methods

7.5.1 Mie theory

Mie theory calculations of infinitely long cylinders are performed using MatScat[205] with a dielectric function from the literature.[44]

7.5.2 FDTD simulations

FDTD simulations are performed using Lumerical FDTD[123] with a dielectric function from the literature.[44] The nanowire has a pentagonal cross section (see main text and Figure 7.1d) and is assumed to be infinitely long due to the use of a two-dimensional simulation geometry. The simulation bandwidth ranges from 315 nm to 800 nm to ensure an accurate fit of the dielectric function over all simulated wavelengths (Figure 7.7). Around the AgNW a fine mesh of 0.25 × 0.25 nm^2 is used.

7.5.3 Sheet resistance model

The sheet resistance is modeled using a previously reported model.[192] The input variables (wire diameter, wire length, wire density, and simulation box size) are mentioned in the main text. The model maps the spatial coordinates of the nanowire junctions and assigns either a junction with a resistance R_{junc} or a segment with a resistance R_{seg}. The corresponding resistance matrix is solved using Kirchhoff's circuit law. To obtain accurate sheet resistances and their corresponding standard deviations, the number of samples is varied from 3, for high nanowire densities, to 100, for low nanowire densities.

7.6 Supporting information

7.6.1 Reflectivity of an Ag mirror

For polarizations parallel to the long axis of the wire ($\vec{E}_{\parallel}$) we observe a broadband response in the scattering cross section σ_{sca} of an Ag cylinder (Figure 7.1). To demonstrate the analogy with the reflectivity of an Ag mirror we simulate the transmission, reflection, and absorption of a 50 nm Ag film (Figure 7.4). We use a finite-difference time-domain method with a dielectric function taken from literature.[44]

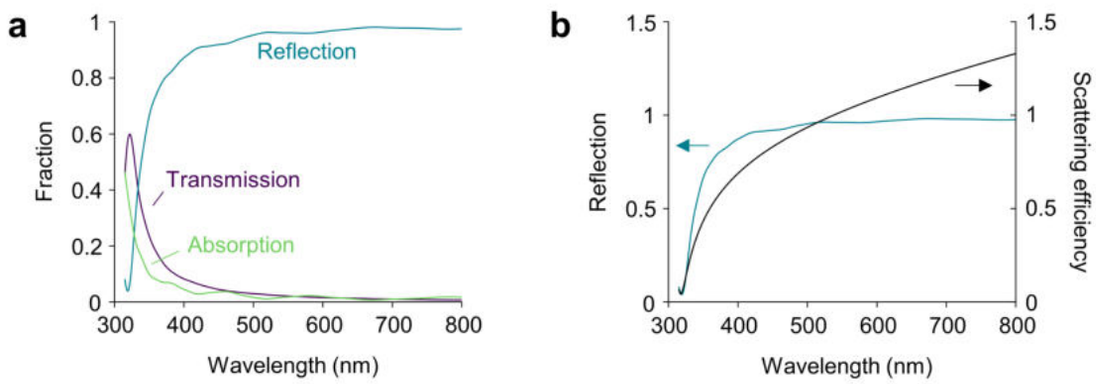

Figure 7.4: Analogy between the reflectivity of an Ag mirror and the scattering cross section of an Ag cylinder for longitudinal polarizations ($\vec{E}_{\parallel}$). (a) Transmission, reflection, and absorption of a 50 nm Ag film in air. (b) Comparison between the reflection of the 50 nm Ag film (black) and the scattering efficiency of an Ag cylinder with a radius of $R = 25$ nm illuminated with a polarization along its long axis (blue). The scattering efficiency is defined as $\sigma_{\text{sca}}/2R$.

7.6.2 Extinction of Ag cylinders with varying radii

The modeled extinction spectrum of an Ag cylinder with a radius $R = 25$ nm does not accurately reproduce the characteristic double peak that is experimentally observed (Figure 7.1). Also for other values of R the extinction spectrum of an Ag cylinder does not show a double peak in the UV (Figure 7.5).

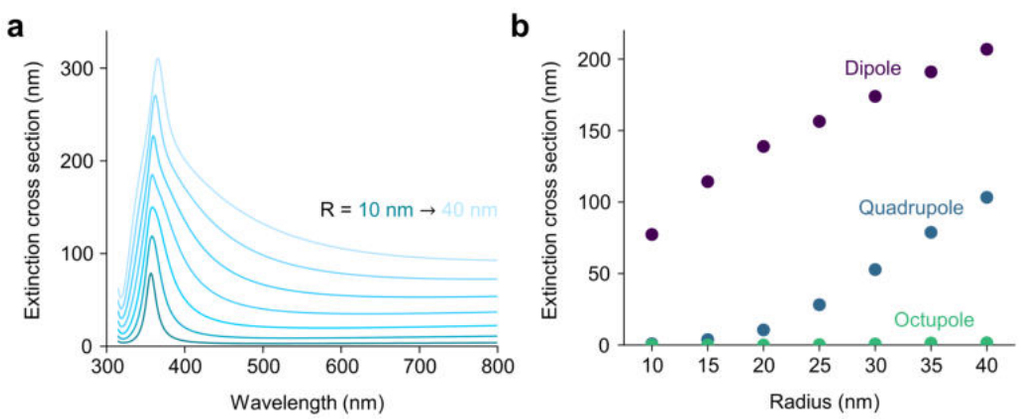

Figure 7.5: (a) Extinction spectra of Ag cylinders with different radii. The radius R is decreased from 10 nm (dark blue) to 40 nm (light blue) in steps of 5 nm. (b) Contributions from the dipolar (purple), quadrupolar (dark blue), and octupolar (light blue) modes to the extinction peaks in panel (a).

7.6.3 Full bandwidth comparison between circular and pentagonal cross sections

In Figure 7.1c,f we plot comparisons between simulated and measured extinction spectra for circular and pentagonal cross sections from 320 nm to 550 nm to highlight the transverse plasmon resonance. Below, in Figure 7.6, we plot the full simulated bandwidth (315 nm to 800 nm) to also highlight the residual extinction in the visible.

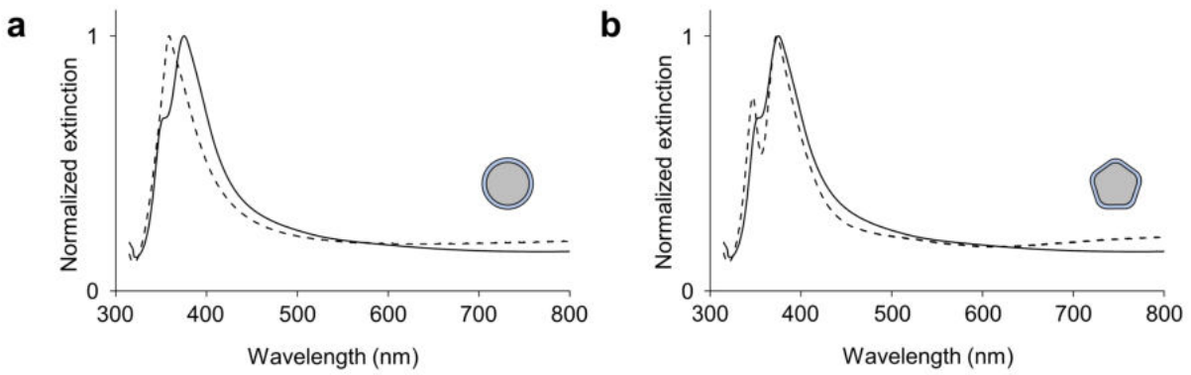

Figure 7.6: Comparison between the simulated (dashed) extinction spectrum of a circular (a) or pentagonal (b) infinite nanowire with the one measured experimentally for 25 nm radius PVP-stabilized AgNWs in water (solid).[204]

7.6.4 Fit of the dielectric function

For the finite-difference time-domain (FDTD) simulations the experimental dielectric function is fitted (Figure 7.7). As FDTD simulations take place in the time domain, the relation between the dielectric displacement and the electric field needs to be causal, i.e. materials cannot respond to fields in the future. This condition places some restrictions on the fitted dielectric function, known as the Kramers-Kronig relations.[42]

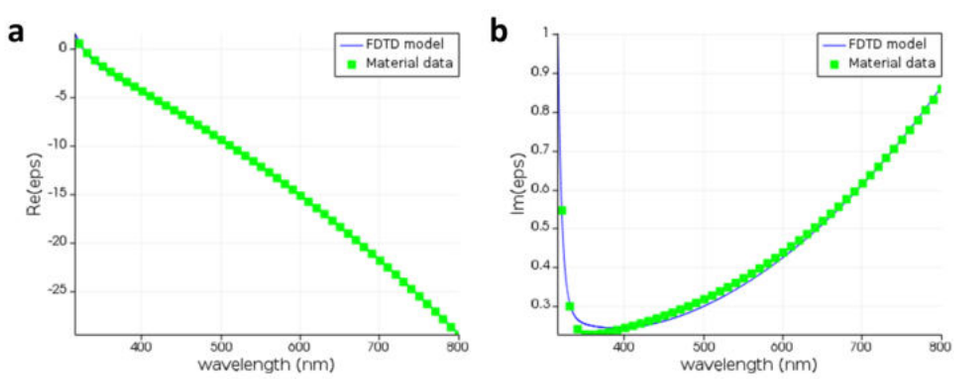

Figure 7.7: Fitted dielectric function for FDTD simulations. (a,b) Real (a) and imaginary (b) part of the experimental dielectric function (green squares) and the fit for the FDTD simulations (blue lines).

7.6.5 AgNW networks for solar cells

As can be seen in Figure 7.2b, the extinction peaks of AgNW networks lie outside the spectral range where the human eye is sensitive. Therefore, AgNW networks have a high transparency for transparent electrode applications (Figure 7.8a). However, solar cells also absorb in the UV, which coincides with the extinction peaks of the AgNW network. This overlap results in slightly lower transparency values when AgNW networks are used in solar cell applications (Figure 7.8b).

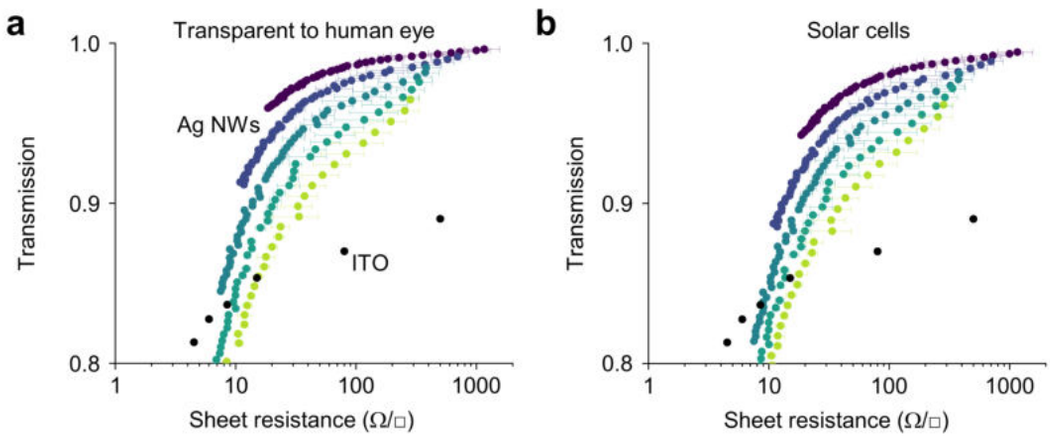

Figure 7.8: Transmission and sheet resistance values for AgNW networks for (a) transparent electrode and (b) solar cell applications. The simulation parameters are the same as those presented in Figure 7.2d.

7.6.6 AgNW network sheet resistance as a function of wire density

The model that we use for simulating the sheet resistance of an AgNW network takes into account both the resistance at the NW junctions and the resistance of the segments between the junctions.[192] When the junctions are poor, the resistance in the NW segments does not contribute significantly to the sheet resistance. Therefore, in these cases, the sheet resistance is mostly dependent on the NW density, which determines the amount of junctions, and only weakly on the NW diameter, which determines the resistance of the segments (Figure 7.9a).

As the junctions become better and R_{junc} becomes lower, the sheet resistance of the network decreases and the influence of the NW segments becomes more dominant, which is demonstrated by the dependency of the sheet resistance on the wire radius R in Figure 7.9b,c.

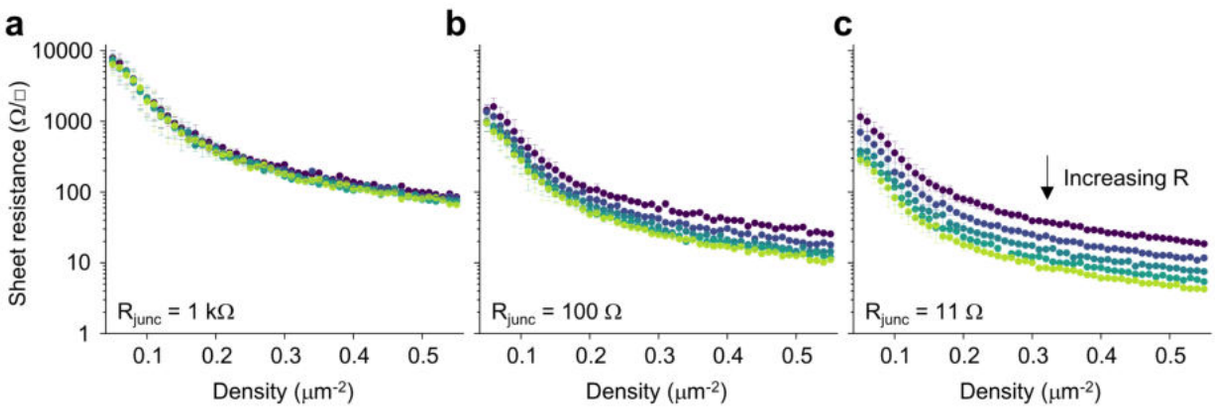

Figure 7.9: Simulated sheet resistance as a function of the AgNW density. The simulation parameters are the same as those presented in Figure 7.2d. The wire radius R is increased from 15 nm to 35 nm in steps of 5 nm. The junction resistance R_{junc} is (a) 1 kΩ, (b) 100 Ω, or (c) 11 Ω.

7.6.7 Pentagonal vs circular cross section comparison

To calculate the area of a pentagon with rounded corners, we first define a triangle at one of the corners (Figure 7.10a). The area A_1 of this triangle is

$$A_1 = \frac{1}{2} R_{\text{curv}}^2 / \tan 54° \tag{7.4}$$

The part of this triangle that is occupied with the rounded pentagon has an area

$$A_2 = \frac{36}{360} \pi R_{\text{curv}}^2 = \frac{\pi}{10} R_{\text{curv}}^2 \tag{7.5}$$

The amount of area that is taken away by rounding the corners then is

$$A_3 = 10(A_1 - A_2) \tag{7.6}$$

The initial unrounded pentagon has a radius R_{unr} that is larger than R (Figure 7.10a):

$$R_{\text{unr}} = R + R_{\text{curv}} \left(\frac{1}{\sin 54°} - 1 \right) \tag{7.7}$$

The area of the rounded pentagon then becomes

$$A_4 = \frac{5}{4} \sqrt{\frac{5+\sqrt{5}}{2}} R_{\text{unr}}^2 - A_3 \tag{7.8}$$

As can be seen in Figure 7.10b, when simulating cylinders and pentagons with equal cross-sectional areas, the resulting extinction spectra are similar for wavelengths above ~450 nm. The characteristic double peak of the pentagon lies in the UV part of the spectrum, where solar irradiation is not intense and where the human eye is not sensitive (Figure 7.2b). Therefore, simulating pentagonal rather than cylindrical wires has no added benefit when calculating the transmission of AgNW networks for solar cell or transparent electrode applications (Figure 7.2c).

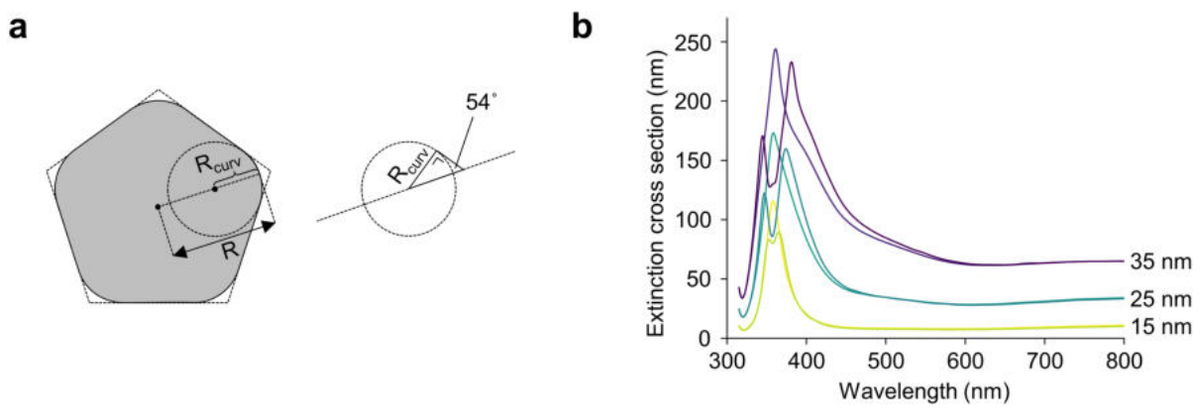

Figure 7.10: (a) Illustration indicating the radius R and radius of curvature R_{curv} of an AgNW with a pentagonal cross section. The triangle at one of the NW corners is used to calculate the cross-sectional area. (b) Extinction of wires with identical cross-sectional areas, but with a pentagonal (R_{curv} = 10 nm) or circular cross section. The radii R are 15 nm, 25 nm, and 35 nm (pentagonal cross section), or 14.6 nm, 23.5 nm, and 32.3 nm (circular cross section).

Chapter 8

Conclusion

8.1 Main findings

In this thesis we have reported a wide variety of studies on the optical properties of metallic nanoparticles, all linked by the work of plasmonic near-fields.

Here, we summarize the main findings of this thesis.

- In chapter 4 we showed that extended lattice resonances in plasmonic particle arrays have minimal influence on the spontaneous decay rate of single molecule emitters, but instead can be exploited to enhance the outcoupling and directivity of the emission. These results can guide the rational design of future optical devices based on plasmonic particle arrays.
- In chapter 5 we mapped the position of individual product molecules from a chemical reaction driven by plasmonic near-fields, with ∼30 nm spatial resolution. We demonstrated a clear correlation between the electric field distribution around individual nanoparticles and their super-resolved catalytic activity maps. These results can be extended to systems with more complex electric field distributions, thereby guiding the design of future advanced photocatalysts.
- In chapter 6 we disentangled every possible activation mechanism of a plasmon-driven chemical reaction. Using different illumination wavelengths combined with extinction spectroscopy, transmission electron microscopy, thermal characterization, and finite-difference time-domain simulations, we unequivocally identified interband holes as the main driving force behind a silver shell growth around gold nanorods. This strategy to discern between plasmon activation mechanisms can be extended to a variety of light-driven processes including photocatalysis, nanoparticle syntheses, and drug delivery.
- In chapter 7 we showed that accurately modeling the geometry of silver nanowires is crucial to deduce structural information from the extinction spectra of nanowire suspensions and to predict the performance of nanowire-based plasmonic near-field sensors. These results can help assess the quality of nanowire syntheses and guide in the design of optimized silver nanowire-based devices.

8.2 Future perspectives

In this section we propose some research directions that emerge from our work and that have the promise to answer remaining open questions in the generation, control, and utilization of plasmonic near-fields, non-equilibrium charge carriers, and photothermal effects in metal nanoparticles.

In chapter 5 we have seen how super-resolution microscopy could be used to study the role of plasmonic near-fields in activating photochemical conversions. In the future, super-resolution microscopy can be extended to study chemical reactions driven by non-equilibrium charge carriers. The nanometer spatial resolution that can be achieved with this technique can be used to compare the spatial distribution of catalytic reactions to calculated non-equilibrium charge carrier distributions.[132–134] This approach would result in a platform to study charge carrier-driven catalysis at the nanoscale under in-situ conditions, removing the necessity for ex-situ characterizations, for example using electron microscopy.[39,133,223]

Recently, Li et al. have shown that the turnover rate of the fluorogenic oxidation from Amplex Red to resorufin catalyzed by Au nanorods can be enhanced under 785 nm excitation.[140] This wavelength does not excite the reactant or the product, which excludes plasmonic near-fields from enhancing any direct excitation in these molecules, but only excites the plasmon resonance of the catalysts. A 532 nm laser is used simultaneously, at a low power density, to image the fluorescent products. Temperature-dependent characterizations of the turnover rate showed a change in the activation barrier for the first step of the reaction under plasmon excitation, whereas the activation barrier for the second and final step remained unaltered. The fact that only one of the two barriers changed under plasmon excitation, combined with temperature measurements and calculations, excludes plasmonic heating as an activation mechanism, making non-equilibrium charge carriers the main driving force.

The study by Li et al. unequivocally showed an activation mechanism due to non-equilibrium charge carriers. One can therefore envision the use of our super-resolution approach to study the same reaction. The usual figure of merit for the characterization of plasmonic enhancement in a chemical reaction is the increase in the turnover rate. However, the spatial position at which the chemical reaction takes place can give further insight in the underlying mechanism of the acceleration.[224] More specifically, the generation of non-equilibrium charge carriers is expected to follow the light polarization, whereas thermal contributions are expected to be homogeneous across the particle.[58] In practical terms, experiments could be performed on catalysts with an isotropic in-plane shape, such as nanodisks.[225] The catalyst can then be excited with different in-plane polarizations, without changing the scattering and absorption cross sections. Furthermore, using isotropic shapes minimizes intrinsic heterogeneities in the spatial distribution of catalytic activity, which typically happens when catalysts have sharp features such as tips or corners.[128] Plasmon excitation can then result in a control over where the chemistry takes place, if the reaction is driven by non-equilibrium charge carriers, or in an enhancement across the whole surface of the catalyst, if the reaction is driven by photothermal heating.

From a more general perspective, more research is required in the understanding of how photon absorption eventually results in the excitation of an adsorbate molecule or in charge transfer to an adjacent semiconductor. In the context of non-equilibrium charge carriers, photon absorption first results in the formation of an electron-hole pair inside the metal. The electron or hole is then 'put to work' only after being transferred to the adjacent species. This transfer process significantly limits the efficiency of non-equilibrium charge carrier-driven processes, due to the high recombination rates of the carriers involved.[60] However, as mentioned in chapter 5, several studies have proposed a different mechanism to explain their plasmon-driven catalysis enhancement, in which the plasmonic near-fields induce direct optical excitations of adsorbate molecules.[142–145] This mechanism is not limited by fast electron-electron scattering and could therefore result in high conversion efficiencies. Furthermore, recently, metal to semiconductor charge transfer efficiencies in excess of 80% have been observed, which is substantially higher than what has been previously reported.[26] While exciting, a proper understanding of a 'direct' mechanism requires a more extensive understanding of how electronic states hybridize at a metal-molecule or metal-

semiconductor interface and requires for experiments to be able to differentiate between this mechanism and the 'indirect' mechanism of electron transfer from the metal.[226]

One approach often used to characterize the existence of the direct mechanism is by measuring the change in the plasmon linewidth. Photon absorption via this mechanism adds an additional loss channel for the plasmon resonance, often referred to as 'chemical interface damping', resulting in a broadening of the plasmon. This broadening should be the largest when the plasmon resonance wavelength is matched to the energy of the direct transition that is made available by adsorbing a molecule. One can therefore envision experiments on nanoparticles with varying resonance wavelengths and the same adsorbate, or on similar nanoparticles and adsorbates with varying gaps between their highest occupied molecular orbital and their lowest unoccupied molecular orbital. The increase in linewidth should then peak when the energy of the plasmon is matched to that of the direct transition.[226] Another possibility would be to control the rate of energy exchange between a plasmonic nanoparticle and an adsorbate by modifying the coupling strength, for example by using spacer layers. Simultaneously, it is important to be aware of the fact that plasmon broadening by molecular adsorbates is not necessarily an indication of charge transfer. Their presence can also broaden the plasmon by inducing dipoles in the metal[227,228] or due to electron scattering caused by an adsorbate-induced effective roughness of the surface.[229] Understanding and being able to control all these mechanisms could then result in the rational design of photocatalysts with increased conversion efficiencies.

Bibliography

[1] File:GothicRayonnantRose003.jpg. https://commons.wikimedia.org/wiki/File:GothicRayonnantRose003.jpg.

[2] File:Brit Mus 13sept10 brooches etc 046.jpg. https://commons.wikimedia.org/wiki/File:Brit_Mus_13sept10_brooches_etc_046.jpg.

[3] Barber, D. J.; Freestone, I. C. An Investigation of the Origin of the Colour of the Lycurgus Cup by Analytical Transmission Electron Microscopy. *Archaeometry* **1990**, *32*, 33–45.

[4] Summers, H. *Nanomedicine*; Elsevier: Kidlington, 2013.

[5] Maxwell, J. C. VIII. A Dynamical Theory of the Electromagnetic Field. *Philosophical Transactions of the Royal Society of London* **1865**, *155*, 459–512.

[6] Maxwell, J. C. *A Treatise on Electricity and Magnetism*; Clarendon Press: Oxford, 1873.

[7] Mie, G. Beiträge zur Optik Trüber Medien, Speziell Kolloidaler Metallösungen. *Annalen der Physik* **1908**, *330*, 377–445.

[8] Bohren, C. F.; Huffman, D. R. *Absorption and Scattering of Light by Small Particles*; John Wiley & Sons: New York, 2008.

[9] Maier, S. A. *Plasmonics: Fundamentals and Applications*; Springer Science & Business Media: New York, 2007.

[10] Novotny, L.; Van Hulst, N. Antennas for Light. *Nature Photonics* **2011**, *5*, 83–90.

[11] Novotny, L. From Near-Field Optics to Optical Antennas. *Physics Today* **2011**, *64*, 47–52.

[12] Ueno, K.; Juodkazis, S.; Shibuya, T.; Yokota, Y.; Mizeikis, V.; Sasaki, K.; Misawa, H. Nanoparticle Plasmon-Assisted Two-Photon Polymerization Induced by Incoherent Excitation Source. *Journal of the American Chemical Society* **2008**, *130*, 6928–6929.

[13] Mack, D. L.; Cortés, E.; Giannini, V.; Török, P.; Roschuk, T.; Maier, S. A. Decoupling Absorption and Emission Processes in Super-Resolution Localization of Emitters in a Plasmonic Hotspot. *Nature Communications* **2017**, *8*, 1–10.

[14] Fleischmann, M.; Hendra, P. J.; McQuillan, A. J. Raman Spectra of Pyridine Adsorbed at a Silver Electrode. *Chemical Physics Letters* **1974**, *26*, 163–166.

[15] Jeanmaire, D. L.; Van Duyne, R. P. Surface Raman Spectroelectrochemistry: Part I. Heterocyclic, Aromatic, and Aliphatic Amines Adsorbed on the Anodized Silver Electrode. *Journal of Electroanalytical Chemistry and Interfacial Electrochemistry* **1977**, *84*, 1–20.

[16] Albrecht, M. G.; Creighton, J. A. Anomalously Intense Raman Spectra of Pyridine at a Silver Electrode. *Journal of the American Chemical Society* **1977**, *99*, 5215–5217.

[17] Haran, G. Single-Molecule Raman Spectroscopy: A Probe of Surface Dynamics and Plasmonic Fields. *Accounts of Chemical Research* **2010**, *43*, 1135–1143.

[18] Wilson, A. J.; Devasia, D.; Jain, P. K. Nanoscale Optical Imaging in Chemistry. *Chemical Society Reviews* **2020**, *49*, 6087–6112.

[19] Khurgin, J. B. How to Deal with the Loss in Plasmonics and Metamaterials. *Nature Nanotechnology* **2015**, *10*, 2–6.

[20] Brongersma, M. L.; Halas, N. J.; Nordlander, P. Plasmon-Induced Hot Carrier Science and Technology. *Nature Nanotechnology* **2015**, *10*, 25.

[21] Linic, S.; Aslam, U.; Boerigter, C.; Morabito, M. Photochemical Transformations on Plasmonic Metal Nanoparticles. *Nature Materials* **2015**, *14*, 567–576.

[22] Zhang, Y.; He, S.; Guo, W.; Hu, Y.; Huang, J.; Mulcahy, J. R.; Wei, W. D. Surface-Plasmon-Driven Hot Electron Photochemistry. *Chemical Reviews* **2018**, *118*, 2927–2954.

[23] Aslam, U.; Rao, V. G.; Chavez, S.; Linic, S. Catalytic Conversion of Solar to Chemical Energy on Plasmonic Metal Nanostructures. *Nature Catalysis* **2018**, *1*, 656–665.

[24] Zhang, Z.; Zhang, C.; Zheng, H.; Xu, H. Plasmon-Driven Catalysis on Molecules and Nanomaterials. *Accounts of Chemical Research* **2019**, *52*, 2506–2515.

[25] Knight, M. W.; Sobhani, H.; Nordlander, P.; Halas, N. J. Photodetection with Active Optical Antennas. *Science* **2011**, *332*, 702–704.

[26] Tagliabue, G.; DuChene, J. S.; Abdellah, M.; Habib, A.; Gosztola, D. J.; Hattori, Y.; Cheng, W.-H.; Zheng, K.; Canton, S. E.; Sundararaman, R., et al. Ultrafast Hot-Hole Injection Modifies Hot-Electron Dynamics in Au/P-GaN Heterostructures. *Nature Materials* **2020**, *19*, 1312–1318.

[27] Baffou, G.; Quidant, R. Thermo-Plasmonics: Using Metallic Nanostructures as Nano-Sources of Heat. *Laser & Photonics Reviews* **2013**, *7*, 171–187.

[28] Kamarudheen, R.; Kumari, G.; Baldi, A. Plasmon-Driven Synthesis of Individual Metal@Semiconductor Core@Shell Nanoparticles. *Nature Communications* **2020**, *11*, 1–10.

[29] Baffou, G.; Cichos, F.; Quidant, R. Applications and Challenges of Thermoplasmonics. *Nature Materials* **2020**, *19*, 946–958.

[30] Kamarudheen, R.; Castellanos, G. W.; Kamp, L. P. J.; Clercx, H. J. H.; Baldi, A. Quantifying Photothermal and Hot Charge Carrier Effects in Plasmon-Driven Nanoparticle Syntheses. *ACS Nano* **2018**, *12*, 8447–8455.

[31] Zhou, L.; Swearer, D. F.; Zhang, C.; Robatjazi, H.; Zhao, H.; Henderson, L.; Dong, L.; Christopher, P.; Carter, E. A.; Nordlander, P., et al. Quantifying Hot Carrier and Thermal Contributions in Plasmonic Photocatalysis. *Science* **2018**, *362*, 69–72.

[32] Zhang, X.; Li, X.; Reish, M. E.; Zhang, D.; Su, N. Q.; Gutieérrez, Y.; Moreno, F.; Yang, W.; Everitt, H. O.; Liu, J. Plasmon-Enhanced Catalysis: Distinguishing Thermal and Nonthermal Effects. *Nano Letters* **2018**, *18*, 1714–1723.

[33] Yu, Y.; Sundaresan, V.; Willets, K. A. Hot Carriers Versus Thermal Effects: Resolving the Enhancement Mechanisms for Plasmon-Mediated Photoelectrochemical Reactions. *The Journal of Physical Chemistry C* **2018**, *122*, 5040–5048.

[34] Aizpurua, J.; Ashfold, M.; Baletto, F.; Baumberg, J.; Christopher, P.; Cortés, E.; de Nijs, B.; Fernandez, Y. D.; Gargiulo, J.; Gawinkowski, S., et al. Dynamics of Hot Electron Generation in Metallic Nanostructures: General Discussion. *Faraday Discussions* **2019**, *214*, 123–146.

[35] Sivan, Y.; Baraban, J.; Un, I. W.; Dubi, Y. Comment on "Quantifying Hot Carrier and Thermal Contributions in Plasmonic Photocatalysis". *Science* **2019**, *364*, eaaw9367.

[36] Yu, Y.; Wijesekara, K. D.; Xi, X.; Willets, K. A. Quantifying Wavelength-Dependent Plasmonic Hot Carrier Energy Distributions at Metal/Semiconductor Interfaces. *ACS Nano* **2019**, *13*, 3629–3637.

[37] Dubi, Y.; Sivan, Y. "Hot" Electrons in Metallic Nanostructures — Non-Thermal Carriers or Heating? *Light: Science & Applications* **2019**, *8*, 1–8.

[38] Jain, P. K. Taking the Heat Off of Plasmonic Chemistry. *The Journal of Physical Chemistry C* **2019**, *123*, 24347–24351.

[39] Kamarudheen, R.; Aalbers, G. J. W.; Hamans, R. F.; Kamp, L. P. J.; Baldi, A. Distinguishing Among All Possible Activation Mechanisms of a Plasmon-Driven Chemical Reaction. *ACS Energy Letters* **2020**, *5*, 2605–2613.

[40] Hamans, R. F. *Super-Resolution Mapping of Plasmonic Hot Electrons*; Eindhoven University of Technology: Eindhoven, 2017.

[41] Hamans, R. F.; Kamarudheen, R.; Baldi, A. Single Particle Approaches to Plasmon-Driven Catalysis. *Nanomaterials* **2020**, *10*, 2377.

[42] Jackson, J. D. *Classical Electrodynamics*; John Wiley & Sons, 2007.

[43] Palik, E. D. *Handbook of Optical Constants of Solids*; Academic Press: Orlando, 1985.

[44] Yang, H. U.; D'Archangel, J.; Sundheimer, M. L.; Tucker, E.; Boreman, G. D.; Raschke, M. B. Optical Dielectric Function of Silver. *Physical Review B* **2015**, *91*, 235137.

[45] Johnson, P. B.; Christy, R. W. Optical Constants of the Noble Metals. *Physical Review B* **1972**, *6*, 4370.

[46] Drude, P. Zur Elektronentheorie der Metalle. *Annalen der Physik* **1900**, *306*, 566–613.

[47] Drude, P. Zur Elektronentheorie der Metalle; II. Teil. Galvanomagnetische und Thermomagnetische Effecte. *Annalen der Physik* **1900**, *308*, 369–402.

[48] Kittel, C. *Introduction to Solid State Physics*; John Wiley & Sons: Hoboken, 2005.

[49] Ehrenreich, H.; Philipp, H. R.; Segall, B. Optical Properties of Aluminum. *Physical Review* **1963**, *132*, 1918–1928.

[50] Christensen, N. E.; Seraphin, B. O. Relativistic Band Calculation and the Optical Properties of Gold. *Physical Review B* **1971**, *4*, 3321.

[51] Christensen, N. E. The Band Structure of Silver and Optical Interband Transitions. *Physica Status Solidi B* **1972**, *54*, 551–563.

[52] Vial, A.; Grimault, A.-S.; Macías, D.; Barchiesi, D.; De La Chapelle, M. L. Improved Analytical Fit of Gold Dispersion: Application to the Modeling of Extinction Spectra with a Finite-Difference Time-Domain Method. *Physical Review B* **2005**, *71*, 085416.

[53] Boyer, D.; Tamarat, P.; Maali, A.; Lounis, B.; Orrit, M. Photothermal Imaging of Nanometer-Sized Metal Particles Among Scatterers. *Science* **2002**, *297*, 1160–1163.

[54] Taylor, A. B.; Zijlstra, P. Single-Molecule Plasmon Sensing: Current Status and Future Prospects. *ACS Sensors* **2017**, *2*, 1103–1122.

[55] Gans, R. Über die Form Ultramikroskopischer Goldteilchen. *Annalen der Physik* **1912**, *342*, 881–900.

[56] Gans, R. Über die Form Ultramikroskopischer Silberteilchen. *Annalen der Physik* **1915**, *352*, 270–284.

[57] Yee, K. Numerical Solution of Initial Boundary Value Problems Involving Maxwell's Equations in Isotropic Media. *IEEE Transactions on Antennas and Propagation* **1966**, *14*, 302–307.

[58] Khurgin, J. B. Fundamental Limits of Hot Carrier Injection From Metal in Nanoplasmonics. *Nanophotonics* **2020**, *9*, 453–471.

[59] Sundararaman, R.; Narang, P.; Jermyn, A. S.; Goddard III, W. A.; Atwater, H. A. Theoretical Predictions for Hot-Carrier Generation from Surface Plasmon Decay. *Nature Communications* **2014**, *5*, 1–8.

[60] Bernardi, M.; Mustafa, J.; Neaton, J. B.; Louie, S. G. Theory and Computation of Hot Carriers Generated by Surface Plasmon Polaritons in Noble Metals. *Nature Communications* **2015**, *6*, 1–9.

[61] DuChene, J. S.; Tagliabue, G.; Welch, A. J.; Cheng, W.-H.; Atwater, H. A. Hot Hole Collection and Photoelectrochemical CO_2 Reduction with Plasmonic Au/P-GaN Photocathodes. *Nano Letters* **2018**, *18*, 2545–2550.

[62] Brown, A. M.; Sundararaman, R.; Narang, P.; Goddard III, W. A.; Atwater, H. A. Nonradiative Plasmon Decay and Hot Carrier Dynamics: Effects of Phonons, Surfaces, and Geometry. *ACS Nano* **2016**, *10*, 957–966.

[63] Baffou, G.; Quidant, R. Nanoplasmonics for Chemistry. *Chemical Society Reviews* **2014**, *43*, 3898–3907.

[64] Baffou, G.; Girard, C.; Quidant, R. Mapping Heat Origin in Plasmonic Structures. *Physical Review Letters* **2010**, *104*, 136805.

[65] Baffou, G.; Rigneault, H. Femtosecond-Pulsed Optical Heating of Gold Nanoparticles. *Physical Review B* **2011**, *84*, 035415.

[66] Arrhenius, S. Über die Dissociationswärme und den Einfluss der Temperatur auf den Dissociationsgrad der Elektrolyte. *Zeitschrift für Physikalische Chemie* **1889**, *4*, 96–116.

[67] Arrhenius, S. Über die Reaktionsgeschwindigkeit bei der Inversion von Rohrzucker durch Säuren. *Zeitschrift für Physikalische Chemie* **1889**, *4*, 226–248.

[68] Rayleigh, L. XXXI. Investigations in Optics, with Special Reference to the Spectroscope. *The London, Edinburgh, and Dublin Philosophical Magazine and Journal of Science* **1879**, *8*, 261–274.

[69] Chroma Spectra Viewer - Rhodamine 6G. `https://www.chroma.com/spectra-viewer?fluorochromes=10366`.

[70] File:Multicolor fluorescence image of living HeLa cells.jpg. https://commons.wikimedia.org/wiki/File:Multicolor_fluorescence_image_of_living_HeLa_cells.jpg.

[71] Moerner, W. E.; Orrit, M. Illuminating Single Molecules in Condensed Matter. *Science* **1999**, *283*, 1670–1676.

[72] Martin-Fernandez, M. L.; Tynan, C. J.; Webb, S. E. D. A 'Pocket Guide' to Total Internal Reflection Fluorescence. *Journal of Microscopy* **2013**, *252*, 16–22.

[73] Hecht, E. *Optics*; Pearson Addison-Wesley: Harlow, 2002.

[74] Airy, G. B. On the Diffraction of an Object-Glass with Circular Aperture. *Transactions of the Cambridge Philosophical Society* **1835**, *5*, 283–291.

[75] Thompson, R. E.; Larson, D. R.; Webb, W. W. Precise Nanometer Localization Analysis for Individual Fluorescent Probes. *Biophysical Journal* **2002**, *82*, 2775–2783.

[76] Mortensen, K. I.; Churchman, L. S.; Spudich, J. A.; Flyvbjerg, H. Optimized Localization Analysis for Single-Molecule Tracking and Super-Resolution Microscopy. *Nature Methods* **2010**, *7*, 377–381.

[77] Ovesnỳ, M.; Křížek, P.; Borkovec, J.; Švindrych, Z.; Hagen, G. M. ThunderSTORM: A Comprehensive ImageJ Plug-in for PALM and STORM Data Analysis and Super-Resolution Imaging. *Bioinformatics* **2014**, *30*, 2389–2390.

[78] Izeddin, I.; Boulanger, J.; Racine, V.; Specht, C. G.; Kechkar, A.; Nair, D.; Triller, A.; Choquet, D.; Dahan, M.; Sibarita, J. B. Wavelet Analysis for Single Molecule Localization Microscopy. *Optics Express* **2012**, *20*, 2081–2095.

[79] Xu, W.; Kong, J. S.; Yeh, Y.-T. E.; Chen, P. Single-Molecule Nanocatalysis Reveals Heterogeneous Reaction Pathways and Catalytic Dynamics. *Nature Materials* **2008**, *7*, 992–996.

[80] Zhang, Y.; Lucas, J. M.; Song, P.; Beberwyck, B.; Fu, Q.; Xu, W.; Alivisatos, A. P. Super-resolution Fluorescence Mapping of Single-Nanoparticle Catalysts Reveals Spatiotemporal Variations in Surface Reactivity. *Proceedings of the National Academy of Sciences* **2015**, *112*, 8959–8964.

[81] Zhou, X.; Xu, W.; Liu, G.; Panda, D.; Chen, P. Size-Dependent Catalytic Activity and Dynamics of Gold Nanoparticles at the Single-Molecule Level. *Journal of the American Chemical Society* **2010**, *132*, 138–146.

[82] Hamans, R. F.; Parente, M.; Castellanos, G. W.; Ramezani, M.; Gómez Rivas, J.; Baldi, A. Super-Resolution Mapping of Enhanced Emission by Collective Plasmonic Resonances. *ACS Nano* **2019**, *13*, 4514–4521.

[83] Zou, S.; Janel, N.; Schatz, G. C. Silver Nanoparticle Array Structures That Produce Remarkably Narrow Plasmon Lineshapes. *The Journal of Chemical Physics* **2004**, *120*, 10871–10875.

[84] Zou, S.; Schatz, G. C. Narrow Plasmonic/Photonic Extinction and Scattering Line Shapes for One and Two Dimensional Silver Nanoparticle Arrays. *The Journal of Chemical Physics* **2004**, *121*, 12606–12612.

[85] Garcia De Abajo, F. J. Colloquium: Light Scattering by Particle and Hole Arrays. *Reviews of Modern Physics* **2007**, *79*, 1267.

[86] Vecchi, G.; Giannini, V.; Gómez Rivas, J. Shaping the Fluorescent Emission by Lattice Resonances in Plasmonic Crystals of Nanoantennas. *Physical Review Letters* **2009**, *102*, 146807.

[87] Pirruccio, G.; Ramezani, M.; Rodriguez, S. R.-K.; Gómez Rivas, J. Coherent Control of the Optical Absorption in a Plasmonic Lattice Coupled to a Luminescent Layer. *Physical Review Letters* **2016**, *116*, 103002.

[88] Chu, Y.; Schonbrun, E.; Yang, T.; Crozier, K. B. Experimental Observation of Narrow Surface Plasmon Resonances in Gold Nanoparticle Arrays. *Applied Physics Letters* **2008**, *93*, 181108.

[89] Auguié, B.; Barnes, W. L. Collective Resonances in Gold Nanoparticle Arrays. *Physical Review Letters* **2008**, *101*, 143902.

[90] Kravets, V. G.; Schedin, F.; Grigorenko, A. N. Extremely Narrow Plasmon Resonances Based on Diffraction Coupling of Localized Plasmons in Arrays of Metallic Nanoparticles. *Physical Review Letters* **2008**, *101*, 087403.

[91] Wang, W.; Ramezani, M.; Väkeväinen, A. I.; Törmä, P.; Gómez Rivas, J.; Odom, T. W. The Rich Photonic World of Plasmonic Nanoparticle Arrays. *Materials Today* **2018**, *21*, 303–314.

[92] Kravets, V. G.; Kabashin, A. V.; Barnes, W. L.; Grigorenko, A. N. Plasmonic Surface Lattice Resonances: A Review of Properties and Applications. *Chemical Reviews* **2018**, *118*, 5912–5951.

[93] Purcell, E. M. Spontaneous Emission Probabilities at Radio Frequencies. *Physical Review* **1946**, *69*, 681.

[94] Schuller, J. A.; Barnard, E. S.; Cai, W.; Jun, Y. C.; White, J. S.; Brongersma, M. L. Plasmonics for Extreme Light Concentration and Manipulation. *Nature Materials* **2010**, *9*, 193–204.

[95] Giannini, V.; Fernández-Domínguez, A. I.; Heck, S. C.; Maier, S. A. Plasmonic Nanoantennas: Fundamentals and Their Use in Controlling the Radiative Properties of Nanoemitters. *Chemical Reviews* **2011**, *111*, 3888–3912.

[96] Anger, P.; Bharadwaj, P.; Novotny, L. Enhancement and Quenching of Single-Molecule Fluorescence. *Physical Review Letters* **2006**, *96*, 113002.

[97] Kühn, S.; Håkanson, U.; Rogobete, L.; Sandoghdar, V. Enhancement of Single-Molecule Fluorescence Using a Gold Nanoparticle as an Optical Nanoantenna. *Physical Review Letters* **2006**, *97*, 017402.

[98] Offermans, P.; Schaafsma, M. C.; Rodriguez, S. R. K.; Zhang, Y.; Crego-Calama, M.; Brongersma, S. H.; Gómez Rivas, J. Universal Scaling of the Figure of Merit of Plasmonic Sensors. *ACS Nano* **2011**, *5*, 5151–5157.

[99] Lozano, G.; Louwers, D. J.; Rodríguez, S. R. K.; Murai, S.; Jansen, O. T. A.; Verschuuren, M. A.; Gómez Rivas, J. Plasmonics for Solid-state Lighting: Enhanced Excitation and Directional Emission of Highly Efficient Light Sources. *Light: Science & Applications* **2013**, *2*, e66–e66.

[100] Zhou, W.; Dridi, M.; Suh, J. Y.; Kim, C. H.; Co, D. T.; Wasielewski, M. R.; Schatz, G. C.; Odom, T. W. Lasing Action in Strongly Coupled Plasmonic Nanocavity Arrays. *Nature Nanotechnology* **2013**, *8*, 506–511.

[101] Ramezani, M.; Halpin, A.; Fernández-Domínguez, A. I.; Feist, J.; Rodriguez, S. R.-K.; Garcia-Vidal, F. J.; Gómez Rivas, J. Plasmon-Exciton-Polariton Lasing. *Optica* **2017**, *4*, 31–37.

[102] Hakala, T. K.; Rekola, H. T.; Väkeväinen, A. I.; Martikainen, J.-P.; Nečada, M.; Moilanen, A. J.; Törmä, P. Lasing in Dark and Bright Modes of a Finite-sized Plasmonic Lattice. *Nature Communications* **2017**, *8*, 1–7.

[103] Schokker, A. H.; Koenderink, A. F. Lasing at the Band Edges of Plasmonic Lattices. *Physical Review B* **2014**, *90*, 155452.

[104] Adato, R.; Yanik, A. A.; Amsden, J. J.; Kaplan, D. L.; Omenetto, F. G.; Hong, M. K.; Erramilli, S.; Altug, H. Ultra-Sensitive Vibrational Spectroscopy of Protein Monolayers with Plasmonic Nanoantenna Arrays. *Proceedings of the National Academy of Sciences* **2009**, *106*, 19227–19232.

[105] Rodriguez, S. R. K.; Gómez Rivas, J. Surface Lattice Resonances Strongly Coupled to Rhodamine 6G Excitons: Tuning the Plasmon-Exciton-Polariton Mass and Composition. *Optics Express* **2013**, *21*, 27411–27421.

[106] Väkeväinen, A. I.; Moerland, R. J.; Rekola, H. T.; Eskelinen, A.-P.; Martikainen, J.-P.; Kim, D.-H.; Törmä, P. Plasmonic Surface Lattice Resonances at the Strong Coupling Regime. *Nano Letters* **2014**, *14*, 1721–1727.

[107] Liu, W.; Lee, B.; Naylor, C. H.; Ee, H.-S.; Park, J.; Johnson, A. T. C.; Agarwal, R. Strong Exciton–Plasmon Coupling in MoS_2 Coupled with Plasmonic Lattice. *Nano Letters* **2016**, *16*, 1262–1269.

[108] Tran, T. T.; Wang, D.; Xu, Z.-Q.; Yang, A.; Toth, M.; Odom, T. W.; Aharonovich, I. Deterministic Coupling of Quantum Emitters in 2D Materials to Plasmonic Nanocavity Arrays. *Nano Letters* **2017**, *17*, 2634–2639.

[109] Zakharko, Y.; Graf, A.; Zaumseil, J. Plasmonic Crystals for Strong Light-Matter Coupling in Carbon Nanotubes. *Nano Letters* **2016**, *16*, 6504–6510.

[110] Betzig, E.; Patterson, G. H.; Sougrat, R.; Lindwasser, O. W.; Olenych, S.; Bonifacino, J. S.; Davidson, M. W.; Lippincott-Schwartz, J.; Hess, H. F. Imaging Intracellular Fluorescent Proteins at Nanometer Resolution. *Science* **2006**, *313*, 1642–1645.

[111] Hess, S. T.; Girirajan, T. P. K.; Mason, M. D. Ultra-High Resolution Imaging by Fluorescence Photoactivation Localization Microscopy. *Biophysical Journal* **2006**, *91*, 4258–4272.

[112] Rust, M. J.; Bates, M.; Zhuang, X. Sub-Diffraction-Limit Imaging by Stochastic Optical Reconstruction Microscopy (STORM). *Nature Methods* **2006**, *3*, 793–796.

[113] Verschuuren, M. A. *Substrate Conformal Imprint Lithography for Nanophotonics*; Utrecht University: Utrecht, 2010.

[114] Abberior CAGE 552. `https://www.abberior.com/jtl-shop/Abberior-CAGE-552`.

[115] Ramezani, M.; Lozano, G.; Verschuuren, M. A.; Gómez Rivas, J. Modified Emission of Extended Light Emitting Layers by Selective Coupling to Collective Lattice Resonances. *Physical Review B* **2016**, *94*, 125406.

[116] Lozano, G.; Barten, T.; Grzela, G.; Gómez Rivas, J. Directional Absorption by Phased Arrays of Plasmonic Nanoantennae Probed with Time-Reversed Fourier Microscopy. *New Journal of Physics* **2014**, *16*, 013040.

[117] Rodriguez, S. R. K.; Arango, F. B.; Steinbusch, T. P.; Verschuuren, M. A.; Koenderink, A. F.; Gómez Rivas, J. Breaking the Symmetry of Forward-Backward Light Emission with Localized and Collective Magnetoelectric Resonances in Arrays of Pyramid-Shaped Aluminum Nanoparticles. *Physical Review Letters* **2014**, *113*, 247401.

[118] Yang, A.; Hryn, A. J.; Bourgeois, M. R.; Lee, W.-K.; Hu, J.; Schatz, G. C.; Odom, T. W. Programmable and Reversible Plasmon Mode Engineering. *Proceedings of the National Academy of Sciences* **2016**, *113*, 14201–14206.

[119] Rodriguez, S. R. K.; Murai, S.; Verschuuren, M. A.; Gómez Rivas, J. Light-Emitting Waveguide-Plasmon Polaritons. *Physical Review Letters* **2012**, *109*, 166803.

[120] Wertz, E.; Isaacoff, B. P.; Flynn, J. D.; Biteen, J. S. Single-Molecule Super-Resolution Microscopy Reveals How Light Couples to a Plasmonic Nanoantenna on the Nanometer Scale. *Nano Letters* **2015**, *15*, 2662–2670.

[121] Wertz, E. A.; Isaacoff, B. P.; Biteen, J. S. Wavelength-Dependent Super-Resolution Images of Dye Molecules Coupled to Plasmonic Nanotriangles. *ACS Photonics* **2016**, *3*, 1733–1740.

[122] Guo, K.; Verschuuren, M. A.; Koenderink, A. F. Superresolution Imaging of the Local Density of States in Plasmon Lattices. *Optica* **2016**, *3*, 289–298.

[123] Nanophotonic FDTD Simulation Software - Lumerical FDTD. `https://www.lumerical.com/products/fdtd/`.

[124] Hamans, R. F.; Parente, M.; Baldi, A. Super-Resolution Mapping of a Chemical Reaction Driven by Plasmonic Near-Fields. *Nano Letters* **2021**, *21*, 2149–2155.

[125] Buurmans, I. L.; Weckhuysen, B. M. Heterogeneities of Individual Catalyst Particles in Space and Time As Monitored by Spectroscopy. *Nature Chemistry* **2012**, *4*, 873.

[126] Chen, T.; Chen, S.; Song, P.; Zhang, Y.; Su, H.; Xu, W.; Zeng, J. Single-Molecule Nanocatalysis Reveals Facet-Dependent Catalytic Kinetics and Dynamics of Pallidium Nanoparticles. *ACS Catalysis* **2017**, *7*, 2967–2972.

[127] Zhou, X.; Andoy, N. M.; Liu, G.; Choudhary, E.; Han, K.-S.; Shen, H.; Chen, P. Quantitative Super-Resolution Imaging Uncovers Reactivity Patterns on Single Nanocatalysts. *Nature Nanotechnology* **2012**, *7*, 237.

[128] Andoy, N. M.; Zhou, X.; Choudhary, E.; Shen, H.; Liu, G.; Chen, P. Single-Molecule Catalysis Mapping Quantifies Site-Specific Activity and Uncovers Radial Activity Gradient on Single 2D Nanocrystals. *Journal of the American Chemical Society* **2013**, *135*, 1845–1852.

[129] Hansen, P. L.; Wagner, J. B.; Helveg, S.; Rostrup-Nielsen, J. R.; Clausen, B. S.; Topsøe, H. Atom-Resolved Imaging of Dynamic Shape Changes in Supported Copper Nanocrystals. *Science* **2002**, *295*, 2053–2055.

[130] Zugic, B.; Wang, L.; Heine, C.; Zakharov, D. N.; Lechner, B. A. J.; Stach, E. A.; Biener, J.; Salmeron, M.; Madix, R. J.; Friend, C. M. Dynamic Restructuring Drives Catalytic Activity on Nanoporous Gold–Silver Alloy Catalysts. *Nature Materials* **2017**, *16*, 558–564.

[131] Kumari, G.; Kamarudheen, R.; Zoethout, E.; Baldi, A. Photocatalytic Surface Restructuring in Individual Silver Nanoparticles. *ACS Catalysis* **2021**, *11*, 3478–3486.

[132] Manjavacas, A.; Liu, J. G.; Kulkarni, V.; Nordlander, P. Plasmon-Induced Hot Carriers in Metallic Nanoparticles. *ACS Nano* **2014**, *8*, 7630–7638.

[133] Cortés, E.; Xie, W.; Cambiasso, J.; Jermyn, A. S.; Sundararaman, R.; Narang, P.; Schlücker, S.; Maier, S. A. Plasmonic Hot Electron Transport Drives Nano-Localized Chemistry. *Nature Communications* **2017**, *8*, 1–10.

[134] Jermyn, A. S.; Tagliabue, G.; Atwater, H. A.; Goddard III, W. A.; Narang, P.; Sundararaman, R. Transport of Hot Carriers in Plasmonic Nanostructures. *Physical Review Materials* **2019**, *3*, 075201.

[135] Chen, G.; Zou, N.; Chen, B.; Sambur, J. B.; Choudhary, E.; Chen, P. Bimetallic Effect of Single Nanocatalysts Visualized by Super-Resolution Catalysis Imaging. *ACS Central Science* **2017**, *3*, 1189–1197.

[136] Zhang, X.; Li, X.; Zhang, D.; Su, N. Q.; Yang, W.; Everitt, H. O.; Liu, J. Product Selectivity in Plasmonic Photocatalysis for Carbon Dioxide Hydrogenation. *Nature Communications* **2017**, *8*, 1–9.

[137] Ye, X.; Zheng, C.; Chen, J.; Gao, Y.; Murray, C. B. Using Binary Surfactant Mixtures to Simultaneously Improve the Dimensional Tunability and Monodispersity in the Seeded Growth of Gold Nanorods. *Nano Letters* **2013**, *13*, 765–771.

[138] Burda, C.; Chen, X.; Narayanan, R.; El-Sayed, M. A. Chemistry and Properties of Nanocrystals of Different Shapes. *Chemical Reviews* **2005**, *105*, 1025–1102.

[139] Zou, N.; Chen, G.; Mao, X.; Shen, H.; Choudhary, E.; Zhou, X.; Chen, P. Imaging Catalytic Hotspots on Single Plasmonic Nanostructures Via Correlated Super-Resolution and Electron Microscopy. *ACS Nano* **2018**, *12*, 5570–5579.

[140] Li, W.; Miao, J.; Peng, T.; Lv, H.; Wang, J.-G.; Li, K.; Zhu, Y.; Li, D. Single-Molecular Catalysis Identifying Activation Energy of the Intermediate Product and Rate-Limiting Step in Plasmonic Photocatalysis. *Nano Letters* **2020**, *20*, 2507–2513.

[141] Zhang, Y.; Yam, C.; Schatz, G. C. Fundamental Limitations to Plasmonic Hot-Carrier Solar Cells. *The Journal of Physical Chemistry Letters* **2016**, *7*, 1852–1858.

[142] Wu, K.; Chen, J.; McBride, J. R.; Lian, T. Efficient Hot-Electron Transfer by a Plasmon-Induced Interfacial Charge-Transfer Transition. *Science* **2015**, *349*, 632–635.

[143] Boerigter, C.; Campana, R.; Morabito, M.; Linic, S. Evidence and Implications of Direct Charge Excitation as the Dominant Mechanism in Plasmon-Mediated Photocatalysis. *Nature Communications* **2016**, *7*, 1–9.

[144] Boerigter, C.; Aslam, U.; Linic, S. Mechanism of Charge Transfer from Plasmonic Nanostructures to Chemically Attached Materials. *ACS Nano* **2016**, *10*, 6108–6115.

[145] Seemala, B.; Therrien, A. J.; Lou, M.; Li, K.; Finzel, J. P.; Qi, J.; Nordlander, P.; Christopher, P. Plasmon-Mediated Catalytic O_2 Dissociation on Ag Nanostructures: Hot Electrons or Near Fields? *ACS Energy Letters* **2019**, *4*, 1803–1809.

[146] Taylor, A.; Verhoef, R.; Beuwer, M.; Wang, Y.; Zijlstra, P. All-Optical Imaging of Gold Nanoparticle Geometry Using Super-Resolution Microscopy. *The Journal of Physical Chemistry C* **2018**, *122*, 2336–2342.

[147] Chattopadhyay, S.; Biteen, J. S. Super-Resolution Characterization of Heterogeneous Light-Matter Interactions between Single Dye Molecules and Plasmonic Nanoparticles. *Analytical Chemistry* **2021**, *93*, 430–444.

[148] Gorelikov, I.; Matsuura, N. Single-Step Coating of Mesoporous Silica on Cetyltrimethyl Ammonium Bromide-Capped Nanoparticles. *Nano Letters* **2008**, *8*, 369–373.

[149] van der Hoeven, J. E. S. *Gold Based Nanorods: Tuning the Structure for Catalysis and Sensing*; Utrecht University: Utrecht, 2019.

[150] Yorulmaz, M.; Khatua, S.; Zijlstra, P.; Gaiduk, A.; Orrit, M. Luminescence Quantum Yield of Single Gold Nanorods. *Nano Letters* **2012**, *12*, 4385–4391.

[151] Zou, N.; Zhou, X.; Chen, G.; Andoy, N. M.; Jung, W.; Liu, G.; Chen, P. Cooperative Communication Within and Between Single Nanocatalysts. *Nature Chemistry* **2018**, *10*, 607–614.

[152] Alexander, G. B.; Heston, W.; Iler, R. K. The Solubility of Amorphous Silica in Water. *The Journal of Physical Chemistry* **1954**, *58*, 453–455.

[153] Chau, Y.-F.; Chen, M. W.; Tsai, D. P. Three-Dimensional Analysis of Surface Plasmon Resonance Modes on a Gold Nanorod. *Applied Optics* **2009**, *48*, 617–622.

[154] Barczak, M. Template Removal From Mesoporous Silicas Using Different Methods As a Tool for Adjusting Their Properties. *New Journal of Chemistry* **2018**, *42*, 4182–4191.

[155] Baffou, G.; Quidant, R.; García de Abajo, F. J. Nanoscale Control of Optical Heating in Complex Plasmonic Systems. *ACS Nano* **2010**, *4*, 709–716.

[156] Baffou, G.; Berto, P.; Bermúdez Ureña, E.; Quidant, R.; Monneret, S.; Polleux, J.; Rigneault, H. Photoinduced Heating of Nanoparticle Arrays. *ACS Nano* **2013**, *7*, 6478–6488.

[157] Chen, T.; Zhang, Y.; Xu, W. Single-Molecule Nanocatalysis Reveals Catalytic Activation Energy of Single Nanocatalysts. *Journal of the American Chemical Society* **2016**, *138*, 12414–12421.

[158] Li, C.; Cao, Q.; Wang, F.; Xiao, Y.; Li, Y.; Delaunay, J.-J.; Zhu, H. Engineering Graphene and TMDs Based Van Der Waals Heterostructures for Photovoltaic and Photoelectrochemical Solar Energy Conversion. *Chemical Society Reviews* **2018**, *47*, 4981–5037.

[159] Srituravanich, W.; Fang, N.; Sun, C.; Luo, Q.; Zhang, X. Plasmonic Nanolithography. *Nano Letters* **2004**, *4*, 1085–1088.

[160] Wadell, C.; Syrenova, S.; Langhammer, C. Plasmonic Hydrogen Sensing with Nanostructured Metal Hydrides. *ACS Nano* **2014**, *8*, 11925–11940.

[161] Anikeeva, P.; Deisseroth, K. Photothermal Genetic Engineering. *ACS Nano* **2012**, *6*, 7548–7552.

[162] Langille, M. R.; Personick, M. L.; Mirkin, C. A. Plasmon-Mediated Syntheses of Metallic Nanostructures. *Angewandte Chemie International Edition* **2013**, *52*, 13910–13940.

[163] Marimuthu, A.; Zhang, J.; Linic, S. Tuning Selectivity in Propylene Epoxidation by Plasmon Mediated Photo-Switching of Cu Oxidation State. *Science* **2013**, *339*, 1590–1593.

[164] Jin, R.; Cao, Y.; Mirkin, C. A.; Kelly, K. L.; Schatz, G. C.; Zheng, J. Photoinduced Conversion of Silver Nanospheres to Nanoprisms. *Science* **2001**, *294*, 1901–1903.

[165] Zhai, Y.; DuChene, J. S.; Wang, Y.-C.; Qiu, J.; Johnston-Peck, A. C.; You, B.; Guo, W.; DiCiaccio, B.; Qian, K.; Zhao, E. W., et al. Polyvinylpyrrolidone-Induced Anisotropic Growth of Gold Nanoprisms in Plasmon-Driven Synthesis. *Nature Materials* **2016**, *15*, 889–895.

[166] Kim, Y.; Smith, J. G.; Jain, P. K. Harvesting Multiple Electron-Hole Pairs Generated Through Plasmonic Excitation of Au Nanoparticles. *Nature Chemistry* **2018**, *10*, 763–769.

[167] Zhao, J.; Nguyen, S. C.; Ye, R.; Ye, B.; Weller, H.; Somorjai, G. A.; Alivisatos, A. P.; Toste, F. D. A Comparison of Photocatalytic Activities of Gold Nanoparticles Following Plasmonic and Interband Excitation and a Strategy for Harnessing Interband Hot Carriers for Solution Phase Photocatalysis. *ACS Central Science* **2017**, *3*, 482–488.

[168] Khurgin, J. B. Hot Carriers Generated by Plasmons: Where Are They Generated and Where Do They Go from There? *Faraday Discussions* **2019**, *214*, 35–58.

[169] Christopher, P.; Xin, H.; Linic, S. Visible-Light-Enhanced Catalytic Oxidation Reactions on Plasmonic Silver Nanostructures. *Nature Chemistry* **2011**, *3*, 467–472.

[170] Hogan, N. J.; Urban, A. S.; Ayala-Orozco, C.; Pimpinelli, A.; Nordlander, P.; Halas, N. J. Nanoparticles Heat Through Light Localization. *Nano Letters* **2014**, *14*, 4640–4645.

[171] Ye, X.; Jin, L.; Caglayan, H.; Chen, J.; Xing, G.; Zheng, C.; Doan-Nguyen, V.; Kang, Y.; Engheta, N.; Kagan, C. R., et al. Improved Size-Tunable Synthesis of Monodisperse Gold Nanorods Through the Use of Aromatic Additives. *ACS Nano* **2012**, *6*, 2804–2817.

[172] Rodríguez-González, B.; Burrows, A.; Watanabe, M.; Kiely, C. J.; Marzán, L. M. L. Multi-shell Bimetallic AuAg Nanoparticles: Synthesis, Structure and Optical Properties. *Journal of Materials Chemistry* **2005**, *15*, 1755–1759.

[173] Richardson, H. H.; Carlson, M. T.; Tandler, P. J.; Hernandez, P.; Govorov, A. O. Experimental and Theoretical Studies of Light-to-Heat Conversion and Collective Heating Effects in Metal Nanoparticle Solutions. *Nano Letters* **2009**, *9*, 1139–1146.

[174] Al-Zubeidi, A.; Hoener, B. S.; Collins, S. S. E.; Wang, W.; Kirchner, S. R.; Hosseini Jebeli, S. A.; Joplin, A.; Chang, W.-S.; Link, S.; Landes, C. F. Hot Holes Assist Plasmonic Nanoelectrode Dissolution. *Nano Letters* **2019**, *19*, 1301–1306.

[175] Guo, W.; Johnston-Peck, A. C.; Zhang, Y.; Hu, Y.; Huang, J.; Wei, W. D. Cooperation of Hot Holes and Surface Adsorbates in Plasmon-Driven Anisotropic Growth of Gold Nanostars. *Journal of the American Chemical Society* **2020**, *142*, 10921–10925.

[176] Kim, Y.; Dumett Torres, D.; Jain, P. K. Activation Energies of Plasmonic Catalysts. *Nano Letters* **2016**, *16*, 3399–3407.

[177] Zheng, Y.; Zhong, X.; Li, Z.; Xia, Y. Successive, Seed-Mediated Growth for the Synthesis of Single-Crystal Gold Nanospheres with Uniform Diameters Controlled in the Range of 5–150 nm. *Particle & Particle Systems Characterization* **2014**, *31*, 266–273.

[178] Hamans, R. F.; Parente, M.; Garcia-Etxarri, A.; Baldi, A. On the Optical Properties of Silver Nanowires. *ChemRxiv* **2022**, 10.26434/chemrxiv–2022–vw6vh.

[179] Li, B.; Ye, S.; Stewart, I. E.; Alvarez, S.; Wiley, B. J. Synthesis and Purification of Silver Nanowires to Make Conducting Films with a Transmittance of 99%. *Nano Letters* **2015**, *15*, 6722–6726.

[180] Zhang, P.; Wyman, I.; Hu, J.; Lin, S.; Zhong, Z.; Tu, Y.; Huang, Z.; Wei, Y. Silver Nanowires: Synthesis Technologies, Growth Mechanism and Multifunctional Applications. *Materials Science and Engineering B* **2017**, *223*, 1–23.

[181] van Hoof, N.; Parente, M.; Baldi, A.; Gómez Rivas, J. Terahertz Time-Domain Spectroscopy and Near-Field Microscopy of Transparent Silver Nanowire Networks. *Advanced Optical Materials* **2020**, *8*, 1900790.

[182] Yao, S.; Zhu, Y. Wearable Multifunctional Sensors Using Printed Stretchable Conductors Made of Silver Nanowires. *Nanoscale* **2014**, *6*, 2345–2352.

[183] Wang, J.; Jiu, J.; Nogi, M.; Sugahara, T.; Nagao, S.; Koga, H.; He, P.; Suganuma, K. A Highly Sensitive and Flexible Pressure Sensor with Electrodes and Elastomeric Interlayer Containing Silver Nanowires. *Nanoscale* **2015**, *7*, 2926–2932.

[184] Hu, W.; Niu, X.; Zhao, R.; Pei, Q. Elastomeric Transparent Capacitive Sensors Based on an Interpenetrating Composite of Silver Nanowires and Polyurethane. *Applied Physics Letters* **2013**, *102*, 38.

[185] Tao, A.; Kim, F.; Hess, C.; Goldberger, J.; He, R.; Sun, Y.; Xia, Y.; Yang, P. Langmuir-Blodgett Silver Nanowire Monolayers for Molecular Sensing Using Surface-Enhanced Raman Spectroscopy. *Nano Letters* **2003**, *3*, 1229–1233.

[186] Ni, K.; Chen, L.; Lu, G. Synthesis of Silver Nanowires with Different Aspect Ratios as Alcohol-Tolerant Catalysts for Oxygen Electroreduction. *Electrochemistry Communications* **2008**, *10*, 1027–1030.

[187] Kostowskyj, M.; Gilliam, R.; Kirk, D.; Thorpe, S. Silver Nanowire Catalysts for Alkaline Fuel Cells. *International Journal of Hydrogen Energy* **2008**, *33*, 5773–5778.

[188] Bergin, S. M.; Chen, Y.-H.; Rathmell, A. R.; Charbonneau, P.; Li, Z.-Y.; Wiley, B. J. The Effect of Nanowire Length and Diameter on the Properties of Transparent, Conducting Nanowire Films. *Nanoscale* **2012**, *4*, 1996–2004.

[189] Mutiso, R. M.; Sherrott, M. C.; Rathmell, A. R.; Wiley, B. J.; Winey, K. I. Integrating Simulations and Experiments to Predict Sheet Resistance and Optical Transmittance in Nanowire Films for Transparent Conductors. *ACS Nano* **2013**, *7*, 7654–7663.

[190] Fairfield, J. A.; Ritter, C.; Bellew, A. T.; McCarthy, E. K.; Ferreira, M. S.; Boland, J. J. Effective Electrode Length Enhances Electrical Activation of Nanowire Networks: Experiment and Simulation. *ACS Nano* **2014**, *8*, 9542–9549.

[191] Marus, M.; Hubarevich, A.; Lim, R. J. W.; Huang, H.; Smirnov, A.; Wang, H.; Fan, W.; Sun, X. W. Effect of Silver Nanowire Length in a Broad Range on Optical and Electrical Properties as a Transparent Conductive Film. *Optical Materials Express* **2017**, *7*, 1105–1112.

[192] Manning, H. G.; da Rocha, C. G.; O'Callaghan, C.; Ferreira, M. S.; Boland, J. J. The Electro-Optical Performance of Silver Nanowire Networks. *Scientific Reports* **2019**, *9*, 1–9.

[193] Khanarian, G.; Joo, J.; Liu, X.-Q.; Eastman, P.; Werner, D.; O'Connell, K.; Trefonas, P. The Optical and Electrical Properties of Silver Nanowire Mesh Films. *Journal of Applied Physics* **2013**, *114*, 024302.

[194] Dong, H.; Chen, Y.-C.; Feldmann, C. Polyol Synthesis of Nanoparticles: Status and Options Regarding Metals, Oxides, Chalcogenides, and Non-Metal Elements. *Green Chemistry* **2015**, *17*, 4107–4132.

[195] Fiévet, F.; Ammar-Merah, S.; Brayner, R.; Chau, F.; Giraud, M.; Mammeri, F.; Peron, J.; Piquemal, J.-Y.; Sicard, L.; Viau, G. The Polyol Process: A Unique Method for Easy Access to Metal Nanoparticles with Tailored Sizes, Shapes and Compositions. *Chemical Society Reviews* **2018**, *47*, 5187–5233.

[196] Gao, Y.; Song, L.; Jiang, P.; Liu, L. F.; Yan, X. Q.; Zhou, Z. P.; Liu, D. F.; Wang, J. X.; Yuan, H. J.; Zhang, Z. X., et al. Silver Nanowires with Five-Fold Symmetric Cross-Section. *Journal of Crystal Growth* **2005**, *276*, 606–612.

[197] Sun, Y.; Mayers, B.; Herricks, T.; Xia, Y. Polyol Synthesis of Uniform Silver Nanowires: A Plausible Growth Mechanism and the Supporting Evidence. *Nano Letters* **2003**, *3*, 955–960.

[198] Zhang, S.-H.; Jiang, Z.-Y.; Xie, Z.-X.; Xu, X.; Huang, R.-B.; Zheng, L.-S. Growth of Silver Nanowires from Solutions: A Cyclic Penta-Twinned-Crystal Growth Mechanism. *Journal of Physical Chemistry B* **2005**, *109*, 9416–9421.

[199] Pettinger, B.; Ren, B.; Picardi, G.; Schuster, R.; Ertl, G. Nanoscale Probing of Adsorbed Species by Tip-Enhanced Raman Spectroscopy. *Physical Review Letters* **2004**, *92*, 096101.

[200] Ayars, E. J.; Hallen, H. D.; Jahncke, C. L. Electric Field Gradient Effects in Raman Spectroscopy. *Physical Review Letters* **2000**, *85*, 4180.

[201] Stöckle, R. M.; Suh, Y. D.; Deckert, V.; Zenobi, R. Nanoscale Chemical Analysis by Tip-Enhanced Raman Spectroscopy. *Chemical Physics Letters* **2000**, *318*, 131–136.

[202] Li, K.; Hogan, N. J.; Kale, M. J.; Halas, N. J.; Nordlander, P.; Christopher, P. Balancing Near-Field Enhancement, Absorption, and Scattering for Effective Antenna-Reactor Plasmonic Photocatalysis. *Nano Letters* **2017**, *17*, 3710–3717.

[203] Acimovic, S. S.; Kreuzer, M. P.; González, M. U.; Quidant, R. Plasmon Near-Field Coupling in Metal Dimers as a Step Toward Single-Molecule Sensing. *ACS Nano* **2009**, *3*, 1231–1237.

[204] Parente, M.; van Helvert, M.; Hamans, R. F.; Verbroekken, R.; Sinha, R.; Bieberle-Hutter, A.; Baldi, A. Simple and Fast High-Yield Synthesis of Silver Nanowires. *Nano Letters* **2020**, *20*, 5759–5764.

[205] Schäfer, J.-P. *Implementierung und Anwendung Analytischer und Numerischer Verfahren zur Lösung der Maxwellgleichungen für die Untersuchung der Lichtausbreitung in Biologischem Gewebe*; Universität Ulm: Ulm, 2011.

[206] Hwang, J.; Shim, Y.; Yoon, S.-M.; Lee, S. H.; Park, S.-H. Influence of Polyvinylpyrrolidone (PVP) Capping Layer on Silver Nanowire Networks: Theoretical and Experimental Studies. *RSC Advances* **2016**, *6*, 30972–30977.

[207] Jia, C.; Yang, P.; Zhang, A. Glycerol and Ethylene Glycol Co-Mediated Synthesis of Uniform Multiple Crystalline Silver Nanowires. *Materials Chemistry and Physics* **2014**, *143*, 794–800.

[208] Gebeyehu, M. B.; Chala, T. F.; Chang, S.-Y.; Wu, C.-M.; Lee, J.-Y. Synthesis and Highly Effective Purification of Silver Nanowires to Enhance Transmittance at Low Sheet Resistance with Simple Polyol and Scalable Selective Precipitation Method. *RSC Advances* **2017**, *7*, 16139–16148.

[209] Sim, H.; Kim, C.; Bok, S.; Kim, M. K.; Oh, H.; Lim, G.-H.; Cho, S. M.; Lim, B. Five-Minute Synthesis of Silver Nanowires and Their Roll-to-Roll Processing for Large-Area Organic Light Emitting Diodes. *Nanoscale* **2018**, *10*, 12087–12092.

[210] Wang, H.; Wang, Y.; Chen, X. Synthesis of Uniform Silver Nanowires from AgCl Seeds for Transparent Conductive Films via Spin-Coating at Variable Spin-Speed. *Colloids and Surfaces A* **2019**, *565*, 154–161.

[211] Saw, M. J.; Ghosh, B.; Nguyen, M. T.; Jirasattayaporn, K.; Kheawhom, S.; Shirahata, N.; Yonezawa, T. High Aspect Ratio and Post-Processing Free Silver Nanowires as Top Electrodes for Inverted-Structured Photodiodes. *ACS Omega* **2019**, *4*, 13303–13308.

[212] Sun, Y.; Yin, Y.; Mayers, B. T.; Herricks, T.; Xia, Y. Uniform Silver Nanowires Synthesis by Reducing $AgNO_3$ with Ethylene Glycol in the Presence of Seeds and Poly(Vinyl Pyrrolidone). *Chemistry of Materials* **2002**, *14*, 4736–4745.

[213] Liu, C.-H.; Yu, X. Silver Nanowire-Based Transparent, Flexible, and Conductive Thin Film. *Nanoscale Research Letters* **2011**, *6*, 1–8.

[214] Da Silva, R. R.; Yang, M.; Choi, S.-I.; Chi, M.; Luo, M.; Zhang, C.; Li, Z.-Y.; Camargo, P. H.; Ribeiro, S. J. L.; Xia, Y. Facile Synthesis of Sub-20 nm Silver Nanowires Through a Bromide-Mediated Polyol Method. *ACS Nano* **2016**, *10*, 7892–7900.

[215] Langley, D. P.; Lagrange, M.; Giusti, G.; Jiménez, C.; Bréchet, Y.; Nguyen, N. D.; Bellet, D. Metallic Nanowire Networks: Effects of Thermal Annealing on Electrical Resistance. *Nanoscale* **2014**, *6*, 13535–13543.

[216] Tokuno, T.; Nogi, M.; Karakawa, M.; Jiu, J.; Nge, T. T.; Aso, Y.; Suganuma, K. Fabrication of Silver Nanowire Transparent Electrodes at Room Temperature. *Nano Research* **2011**, *4*, 1215–1222.

[217] Bellew, A. T.; Manning, H. G.; Gomes da Rocha, C.; Ferreira, M. S.; Boland, J. J. Resistance of Single Ag Nanowire Junctions and Their Role in the Conductivity of Nanowire Networks. *ACS Nano* **2015**, *9*, 11422–11429.

[218] O'Callaghan, C.; da Rocha, C. G.; Manning, H. G.; Boland, J. J.; Ferreira, M. S. Effective Medium Theory for the Conductivity of Disordered Metallic Nanowire Networks. *Physical Chemistry Chemical Physics* **2016**, *18*, 27564–27571.

[219] da Rocha, C. G.; Manning, H. G.; O'Callaghan, C.; Ritter, C.; Bellew, A. T.; Boland, J. J.; Ferreira, M. S. Ultimate Conductivity Performance in Metallic Nanowire Networks. *Nanoscale* **2015**, *7*, 13011–13016.

[220] Bastús, N. G.; Piella, J.; Puntes, V. Quantifying the Sensitivity of Multipolar (Dipolar, Quadrupolar, and Octapolar) Surface Plasmon Resonances in Silver Nanoparticles: The Effect of Size, Composition, and Surface Coating. *Langmuir* **2016**, *32*, 290–300.

[221] Song, J.; Huang, Y.; Fan, Y.; Zhao, Z.; Yu, W.; Rasco, B. A.; Lai, K. Detection of Prohibited Fish Drugs Using Silver Nanowires as Substrate for Surface-Enhanced Raman Scattering. *Nanomaterials* **2016**, *6*, 175.

[222] Garcia-Etxarri, A.; Apell, P.; Käll, M.; Aizpurua, J. A Combination of Concave/Convex Surfaces for Field-Enhancement Optimization: The Indented Nanocone. *Optics Express* **2012**, *20*, 25201–25212.

[223] Hobbs, R. G.; Putnam, W. P.; Fallahi, A.; Yang, Y.; Kärtner, F. X.; Berggren, K. K. Mapping Photoemission and Hot-Electron Emission from Plasmonic Nanoantennas. *Nano Letters* **2017**, *17*, 6069–6076.

[224] Baffou, G.; Bordacchini, I.; Baldi, A.; Quidant, R. Simple Experimental Procedures to Distinguish Photothermal from Hot-Carrier Processes in Plasmonics. *Light: Science & Applications* **2020**, *9*, 1–16.

[225] Zorić, I.; Zäch, M.; Kasemo, B.; Langhammer, C. Gold, Platinum, and Aluminum Nanodisk Plasmons: Material Independence, Subradiance, and Damping Mechanisms. *ACS Nano* **2011**, *5*, 2535–2546.

[226] Oksenberg, E.; Shlesinger, I.; Xomalis, A.; Baldi, A.; Baumberg, J. J.; Koenderink, A. F.; Garnett, E. C. Energy-Resolved Plasmonic Chemistry in Individual Nanoreactors. *Nature Nanotechnology* **2021**, *16*, 1378–1385.

[227] Westcott, S. L.; Averitt, R. D.; Wolfgang, J. A.; Nordlander, P.; Halas, N. J. Adsorbate-Induced Quenching of Hot Electrons in Gold Core-Shell Nanoparticles. *The Journal of Physical Chemistry B* **2001**, *105*, 9913–9917.

[228] Foerster, B.; Spata, V. A.; Carter, E. A.; Sönnichsen, C.; Link, S. Plasmon Damping Depends on the Chemical Nature of the Nanoparticle Interface. *Science Advances* **2019**, *5*, eaav0704.

[229] Khurgin, J. B.; Petrov, A.; Eich, M.; Uskov, A. V. Direct Plasmonic Excitation of the Hybridized Surface States in Metal Nanoparticles. *ACS Photonics* **2021**, *8*, 2041–2049.

Scientific output

Publications as first author on which this thesis is based

- **On the Optical Properties of Silver Nanowires**, Ruben F Hamans*, Matteo Parente*, Aitzol Garcia-Etxarri, Andrea Baldi, *Submitted*
  *Equal author contribution
- **Super-Resolution Mapping of a Chemical Reaction Driven by Plasmonic Near-Fields**, Ruben F. Hamans, Matteo Parente, Andrea Baldi, *Nano Letters* (2021), 21 (5), 2149-2155
- **Single Particle Approaches to Plasmon-Driven Chemistry**, Ruben F. Hamans, Rifat Kamarudheen, Andrea Baldi, *Nanomaterials* (2020), 10 (12), 2377
- **Distinguishing Among All Possible Activation Mechanisms of a Plasmon-Driven Chemical Reaction**, Rifat Kamarudheen*, Guus J.W. Aalbers*, Ruben F. Hamans*, Leon P.J. Kamp, Andrea Baldi, *ACS Energy Letters* (2020), 5 (8), 2605-2613
  *Equal author contribution
- **Super-Resolution Mapping of Enhanced Emission by Collective Plasmonic Resonances**, Ruben F. Hamans, Matteo Parente, Gabriel W. Castellanos, Mohammad Ramezani, Jaime Gómez Rivas, Andrea Baldi, *ACS Nano* (2019), 13 (4), 4514-4521

Other publications related to this thesis work

- **Dynamic Optical Tuning of Chemical Interface Damping**, Matteo Parente*, Ruben F Hamans*, Joost Reinders, Andrea Baldi, *In Preparation*
  *Equal author contribution
- **Hot! Hot! Hot! Plasmon-Assisted Heterogeneous Catalysis**, Rifat Kamarudheen*, Matteo Parente*, Ruben F Hamans, Gayatri Kumari, Andrea Baldi, *In Preparation*
  *Equal author contribution
- **Simple and Fast High-Yield Synthesis of Silver Nanowires**, Matteo Parente, Max van Helvert, Ruben F Hamans, Ruth Verbroekken, Rochan Sinha, Anja Bieberle-Hutter, Andrea Baldi, *Nano Letters* (2020), 20 (8), 5759-5764
- **Dynamics of Hot Electron Generation in Metallic Nanostructures: General Discussion**, Javier Aizpurua et al., *Faraday Discussions* (2019), 214, 123-146

Other publications not related to this thesis work

- **Fabrication of Scaffold-Based 3D Magnetic Nanowires for Domain Wall Applications**, Dédalo Sanz-Hernández, Ruben F Hamans, Johannes Osterrieth, Jung-Wei Liao,

Luka Skoric, Jason Fowlkes, Philip Rack, Anna Lippert, Steven Lee, Reinoud Lavrijsen, Amalio Fernández-Pacheco, *Nanomaterials* (2018), 8 (7), 483

- **Fabrication, Detection, and Operation of a Three-Dimensional Nanomagnetic Conduit**, Dédalo Sanz-Hernández, Ruben F Hamans, Jung-Wei Liao, Alexander Welbourne, Reinoud Lavrijsen, Amalio Fernández-Pacheco, *ACS Nano* (2017), 11 (11), 11066-11073

Oral contributions at conferences

- Euromat, 13-17 September 2021, Online. **Super-Resolution Mapping of a Chemical Reaction Driven by Plasmonic Near-Fields**
- Master Your Physics, 14-18 June 2021, Online. **Super-Resolution Mapping of a Chemical Reaction Driven by Plasmonic Near-Fields**
- London Plasmonics Forum, 9 June 2021, Online. **Super-Resolution Mapping of a Chemical Reaction Driven by Plasmonic Near-Fields**
- Dutch Days of Photochemistry, 10 & 17 May 2021, Online. **Super-Resolution Mapping of a Chemical Reaction Driven by Plasmonic Near-Fields**
- Physics@Veldhoven, 18-20 January 2021, Online. **Super-Resolution Mapping of a Chemical Reaction Driven by Plasmonic Near-Fields**
- CHAINS, 8-9 December 2020, Online. **Super-Resolution Mapping of a Plasmon-Driven Reaction**
- AMOLF International Nanophotonics Summerschool, 17-21 July 2019, Amsterdam, The Netherlands. **Super-Resolution Mapping of Plasmon-Enhanced Processes**

Poster contributions at conferences

- PEP2021 Summer School: Photothermal Effects in Plasmonics, 17-22 October 2021, Porquerolles, France. **Super-Resolution Mapping of a Chemical Reaction Driven by Plasmonic Near-Fields**
- Photonics Online Meetup, 22 June 2020, Online. **Super-Resolution Mapping of Plasmon-Enhanced Processes**
- CHAINS, 10-11 December 2019, Veldhoven, The Netherlands. **Super-Resolution Mapping of Plasmon-Enhanced Processes**
- MRS Fall, 1-6 December 2019, Boston, United States. **Super-Resolution Mapping of Plasmon-Enhanced Processes**
- Faraday Discussion - Hot-Electron Science and Microscopic Processes in Plasmonics and Catalysis, 18-20 February 2019, London, United Kingdom. **Super-Resolution Mapping of Plasmonic Hot Electrons**
- CHAINS, 4-5 December 2018, Veldhoven, The Netherlands. **Super-Resolution Mapping of Plasmonic Hot Electrons**
- XXV International Summer School 'Nicolás Cabrera': Manipulating Light and Matter at the Nanoscale, 10-14 September 2018, Miraflores de la Sierra, Madrid, Spain. **Super-Resolution Mapping of Plasmon-Enhanced Processes**

- SCOM, 16 April 2018, Eindhoven, The Netherlands. **Super-Resolution Microscopy on Single Molecules for Plasmon-Activated Catalysis and LDOS Mapping**
- PAC Symposium, 8 March 2018, Utrecht, The Netherlands. **Super-Resolution Mapping of Plasmonic Hot Electrons**

Theses supervision

- **Stability of Gold Catalytic Nanoparticles for the Super-Resolution Mapping of Plasmonic Hot Charge Carriers**, Margherita Minissi, 2021, Master Internship, Universiteit van Amsterdam, The Netherlands
- **Characterizing Catalytic Reactions at the Single Molecule Level**, Donna Sandtke, 2021, Bachelor Thesis, Universiteit van Amsterdam, The Netherlands
- **Temperature Mapping of Plasmonic Nanoparticles**, Bram van Kuyck, 2021, Bachelor Thesis, Fontys University of Applied Science, Eindhoven, The Netherlands
- **Discriminating the Mechanisms in Plasmon-Activated Chemical Reactions via a Light-Driven Au@Ag Core@Shell Nanorod Synthesis**, Guus J. W. Aalbers, 2020, Bachelor Thesis, Fontys University of Applied Science, Eindhoven, The Netherlands
- **Synthesis of Colloidal Nanoparticle for 2D and 3D Self-Assembled Arrays**, Mike Nuijen, 2020, Bachelor Internship, Fontys University of Applied Science, Eindhoven, The Netherlands

Acknowledgments

The other day I came across an interview with Arnold Schwarzenegger (oh the wonders of the Facebook algorithm), in which he said the following: 'It is not true that I am self-made. Like everyone, to get to where I am, I stood on the shoulders of giants. My life was built on a foundation of parents, coaches, and teachers.' Although the blockbuster movie genre is one I despise, I do find myself having to agree. A PhD project might seem like a lonely crusade through a vast desert, in which a brave person travels far and wide across a long and lonesome road to try and reach a singular goal. Needless to say, such a journey sounds very noble and dramatic. This picture is, however, far from the truth. This thesis would not have been possible without the support from many people, who I'll (try to) acknowledge in this final section. Even though I am blessed with a fairly decent memory, especially for funny and seemingly irrelevant details from events that happened a long time ago (don't ask me what I had for dinner yesterday though), writing acknowledgments is always done at the risk of forgetting people or thanking people to a lesser or greater extent than they would have liked to see. Therefore, I'll start with a general 'thank you' to whomever is reading this.

To try to avoid the above-mentioned issues to the best of my abilities, I have gone through what a regular work week, if such a thing even exists, could have looked like during my PhD. Monday, of course, is a day of work, which leads me to thanking my supervisor Andrea Baldi. Our journey has been a long one indeed. I can vividly remember seeing your guest lecture during my nanophotonics master course and thinking 'I need to work with this man'. Your ability to communicate scientific work with a balanced mix of enthusiasm, structure, depth, and slick slides is what attracted me at the time and it is something that I continue to admire. Although we ended up doing a different master thesis project than the one you advertised during the lecture, it was a choice that I never regretted. Furthermore, the project I did allowed me to spend way more of your money. After all, microscopes are expensive. Needless to say, when the opportunity came to continue with a PhD, there was no hesitation. We have seen a lot of meetings, experiments, discussions, lectures, conference talks (insulting other people's slides has become a hobby), writing sessions that sometimes turned philosophical (I know I still suck at summarizing my articles in one sentence and in actually guiding a reader through a story, but the combination of my purely-scientific-just-write-what-the-results-are approach and your mastery of making things actually sound interesting has proven to be effective I think), students, rejection letters, referee reports, acceptance letters, group outings, often-disappointing lunches, lab clean-ups, lab relocations, and what not. For all of this, I will forever be grateful.

During a day of work one of course spends a lot of time in the lab with colleagues, which brings me to thanking my NEA (DIFFER) and PCM (VU) colleagues. First of all, Matteo, you have transitioned from my Master thesis supervisor, to a colleague, to a great friend. Thanks for teaching me how to do a proper synthesis (one synth at a time, fellas), for renewing my appreciation for film (or, in some cases, hate, let's not name too many names), for teaching me how to express discontent in Italian, and, most of all, for this intuitive bond that links us; a bond of hatred. Rifat, thanks for all the chemistry-related help in the lab, for pushing my spice-tolerance limit while we were in London for the Faraday Discussion, and for all the great science we have done

together. Gayatri, thanks for all the scientific insights and for being a rare source of relaxedness. Ferry, I will remember our shared struggles of living in Eindhoven and working in Amsterdam for the last part of my PhD. Thanks for making them easier and many thanks for your sample fabrications and for designing the cover of this thesis. We still need to play a board game together, I believe. Francesco, thanks for always providing a good laugh mixed with some existential dread and for the climbing sessions. Sven, thanks for your unrelenting enthusiasm in performing good science, critiquing rubbish papers, and writing proposals. Gabi, thanks for all the beers we've shared (it's been too long, actually), and for your skills as a Lumerical instructor, as a tour guide in Madrid and Sevilla, and as a belaying partner. Quynh, you've only been in the group for a few months. It has been a pleasure helping you out in the lab. You're on your own now. You'll be fine. Thanks for carrying on the PCM legacy. Long may we reign.

I am also thankful for all my committee members: Emiliano Cortés, Giulia Tagliabue, Peter Zijlstra, Esther Alarcón Lladó, Jaime Gómez Rivas, and Erwin Peterman. Thanks for all your scientific insights, for taking the time to read my thesis, and for elevating my work to a higher level.

The beginning of this project would not have been possible without the support from the group of Jaime Gómez Rivas at DIFFER (now at TU/e, of course). Thanks in particular to Jaime, Mohammad, Stan, Niels, and Gabi for your support on everything optics-related. I am also grateful for technical and administrational support from the people at DIFFER (in particular, Jolanda, Henk, Ton, Stefan, Erwin, Casandra, and Frans) and the VU (in particular, Martin, for making our transition to the VU as smooth as can be, for your proactive attitude, and for your endless library of technical knowledge and of what I would call 'stuff', and Marja, for guiding Andrea and myself through the administrational 'system' of the VU).

Since we're still in the scientific realm, I would also like to express gratitude to our external collaborators at AMOLF. Thanks to Erik, Sven, Eitan, and Jenny for your scientific insights and for the fun we've had outside of work. Our shared group outing and the AMOLF International Nanophotonics Summerschool come to mind in particular. Thanks also to all the students that I've supervised over the years for the fun we've had inside and outside of the lab: Margherita, Donna, Bram, Guus (technically maybe I wasn't your supervisor, but I felt like one), and Mike. I also shouldn't forget all the people that have helped me in the other DIFFER labs or with whom I've just shared a coffee at the infamous DIFFER coffee corner. I can't possibly name (or remember, for that matter) you all, but people that come to mind are Rochan, Georgios, Devyani, Dozie, Sathiyaraj, Usman, Vasilis, Paola, Wendy, Simone, Diego, Ruth, Daphne, Thomas, Andrea F, Joost, Matteo M, ...

Outside of work, there have been a great many people that have kept me sane over the course of my PhD. Jean-Paul Sartre once said 'Three o'clock is always too late or too early for anything you want to do'. Similarly, Monday evening ended up being an evening in between the weekend and the evenings that are usually filled with recurring activities. This lack of purpose makes a Monday evening particularly suitable for all sorts of mischief or for just a relaxed evening of hanging out with friends, which bring me to two of my oldest friends Sander and Casper. Sander, I will never be able to understand how we can laugh uncontrollably about things that other people don't find even remotely funny. Similarly, it will forever remain a mystery to me why deep frying slavinken is not a nationwide culinary hit. Oh, and many thanks for essentially doing 90% of the manual labor in my new apartment. Casper, thanks for all of the computer-related help (I will learn how to use Python properly at some point) and, way more importantly, for our shared appreciation for the finer beers and the heavier musics, which I think has grown to be unparalleled. To both of you, thanks for the company and the welcome distractions. The remainder of the group of friends from my student days, infamously known as The Stoute Gijtjes,

also deserves a huge thanks. Kaylee, thanks for introducing me to all sorts of rubbish television, for providing snacks (or, snaaaaacks, pronounced loudly, with vigor and an edge of aggression) in times of need, for buying me a blanket for my couch, and for just being a nice person to be around. Maarten, thanks for all the jazz, for teaching us how to cook and how to be late, for turning my kitchen into what can only be described as a crime scene, and for introducing me to the greatest sport of all sports (no, not heavy beer lifting). When are we going to Fontainebleau? Stan, thanks for an odd combination of knowledgeability and unorthodox humor. Sanne, thanks for the relaxed company during our holidays and for teaching us that a holiday can be spent quite comfortably by just chilling around a swimming pool. I think the two of you, together with Amy, make a great family! Shannen, thanks for being a rare source of common sense in this group and for telling us why the holiday destination that we chose is interesting again. Marc, thanks for all the bar duties and all the drinks we've shared (including the ones you made yourself, you better not be giving me methanol poisoning).

Tuesday and Wednesday evenings have often been taken up by activities of ESMG Studentproof Jazz. It has been an honor and a pleasure to serve as the secretary of arguably the best board ever, the 30th board 'Board to be wild', in the academic year 2018-2019. Thanks to all my fellow board members for making this such a pleasant time. Mr. Chairman Arturs, thanks for providing our board with an overdose of charisma and non-pc humor. Mr. Treasurer Jerom, thanks for being the only one that actually knows how to play jazz. Mr. Combo Commissioner Maarten, thanks for catering our board meetings and making them way too long. We wouldn't have it any other way. Thanks also to my Hootie Tootie bandmates Afke, Arturs, Jerom, Matthijs, and Tom. All of our previous gigs are great memories and I'm looking forward to the next one. Perhaps we can play a blues that is not in the key of E soon. I'd also like to thank the other people that I've played music with over the years, with whom I've organized some of our activities, or with whom I've just listened to some jazz. In particular, the bands Kamphuis Kollektiv (Maarten, Jeff, Jerom, David) & Los Pidrillos (Annie, Arturs, Lars, Martin, Melvyn, Daniël, Luuc, Kristien), the activities Whisky & Jazz (Sarah, Maarten, Twan, Jerom, Pim) & JAZZLAB (Laurens, Maarten, Tristan, Lisa, Chris, Martin), and the remaining active and less-active-but-just-chill members (Arthur, Jorick, Lars, Jérôme, Rebecca, Thomas, Rick, Manon, Wei Hao, Kamil, Merel, Karlijn, ...) come to mind.

The work day on Thursday often had to be interrupted at 16h B.T. sharp (sorry Andrea) for the Borrel of the study association for Applied Physics 'J.D. van der Waals' in 'de Salon'. Thanks to all the bartenders I have served with over the years (particular people that come to mind are Casper, Marc, Robin, Pim, and Gijs) and to all the people I've had beers with (that'd be a long list). First time I visit after my defense, the first round will be on me. I recommend 'Stoute Gijt', a fine beverage indeed.

Come Friday evening, the weekend starts, which, when not spent in Eindhoven, quite often I have spent in my home town of Roosendaal, which leads me to thanking the 'Five Guys'. Thanks to Tim, Niels, Michiel, and Sebastiaan for all the fine evenings filled with barbecues, intense discussion, fine beers & whiskys, and poor jokes. Thanks also for our shared quest in finding which country serves the best meat-based dishes, none of which should be served 'to share'. I myself think that out of Portugal, Spain, Italy, Israel, and the United Arab Emirates, Portugal would probably be on the top of my list, currently. However, if you ask me again tomorrow, my opinion might be different and, therefore, our quest is not over. In fact, we should plan our next holiday soon. While thinking of Roosendaal, I also realize I'd like to acknowledge my high school physics teacher Ad, for your down-to-earth yet enthusiastic teaching approach and for also making us realize there's more to life than just physics.

Last, but most certainly not least, I'd like to thank my family for their unconditional love and support. For some reason, life always seems so much simpler when I'm 'back home'. The thought that I can just come home and do nothing for a while is a very comforting one and it has been a solid foundation from which I could draw my energy to do this PhD.

Finally then, I'd like to finish this thesis in the same way I started it and that is by dedicating this work to my parents. Thank you for everything.

Curriculum vitae

Ruben F. Hamans was born on February 26th 1994 in Roosendaal, The Netherlands.

He completed his bachelor's degree in applied physics at the Eindhoven University of Technology in 2015. He performed his thesis project "Electrical and optical characterization of single-photon detectors based on superconducting nanowires" under supervision of Giulia Digeronimo in the Photonics and Semiconductor Nanophysics group of prof. Andrea Fiore.

He then completed his master's degree in applied physics cum laude at the same university in 2017. During his master's he worked in the Thin Film Magnetism group of prof. Russell Cowburn in the subgroup headed by dr. Amalio Fernández-Pacheco at the University of Cambridge. He worked on a project titled "3D magnetic nanostrips: advanced fabrication and magneto-optical detection", under daily supervision of Dédalo Sanz-Hernández. He performed his thesis project "Super-resolution mapping of plasmonic hot electrons" in the Nanomaterials for Energy Applications group of dr. Andrea Baldi at DIFFER - Dutch Institute for Fundamental Energy Research, under daily supervision of Matteo Parente. For this thesis he received the second prize in the KNCV Golden Master Award.

In January 2018, he started a PhD in the same group. After relocation in March 2020, his PhD continued at the Vrije Universiteit Amsterdam, with the group now embedded in the Photo Conversion Materials group. The main focus of the project is to use super-resolution fluorescence microscopy to study plasmon-driven processes at the nanoscale. The results of these studies, combined with other work by the author performed during the project, are presented in this thesis.

In his spare time he plays drums & a bit of guitar, has opinions about music & craft beer & movies, and climbs things.